



THE UNIVERSITY *of* EDINBURGH

This thesis has been submitted in fulfilment of the requirements for a postgraduate degree (e.g. PhD, MPhil, DClinPsychol) at the University of Edinburgh. Please note the following terms and conditions of use:

This work is protected by copyright and other intellectual property rights, which are retained by the thesis author, unless otherwise stated.

A copy can be downloaded for personal non-commercial research or study, without prior permission or charge.

This thesis cannot be reproduced or quoted extensively from without first obtaining permission in writing from the author.

The content must not be changed in any way or sold commercially in any format or medium without the formal permission of the author.

When referring to this work, full bibliographic details including the author, title, awarding institution and date of the thesis must be given.

Assessment of Mid-Depth Arrays of Single Beam Acoustic Doppler Velocity Sensors to Characterise Tidal Energy Sites

Duncan R.J. Sutherland



Doctor of Philosophy

THE UNIVERSITY OF EDINBURGH

2015

“To achieve great things, two things are needed: a plan and not quite enough time.”

Leonard Bernstein

Abstract

Accurate characterisation of fluid flow at tidal energy sites is critical for cost effective Tidal Energy Converter (TEC) design in terms of efficiency and survivability. The standard instrumentation in tidal site characterisation has been Diverging acoustic-Beam Doppler Profilers (DBDPs) which remotely measure the flow over a range of scales, resolving up to three velocity vectors. However, they are understood to have several drawbacks particularly in terms of characterising turbulent aspects of the flow. This characterisation is generally based upon a small number of key transient metrics, the accuracy of which directly impacts TEC designs.

This work presents an optimisation and performance assessment of newly available Single Beam Doppler Profilers (SBDPs) mounted on a commercial-scale tidal turbine at mid-channel depth in a real operating environment. It was hypothesised that SBDPs would have advantages over DBDPs for site characterisation, in terms of reduced random error, reduced uncertainty in turbulence intensities and the ability to quantify the structure of the turbulent flow.

The relationship between random error, sensor orientation and flow speed is quantified for both single and diverging beam sensor types. Random error was found to increase with increasing flow velocity as a power law, the slope of which varies for different sensor orientations. Quantification of noise offers a practical method to correct turbulence metrics. To enable the use of multiple acoustic sensors mounted in close proximity, interference was quantified and mitigation techniques examined. Cross-talk between sensors of the same type were generally shown to bias measurements towards zero. In the presence of alternate types of acoustic sensors, interference caused an increase in standard deviation of velocity results. Implementing a timing offset control mechanism was able to mitigate this effect. This work has achieved a greater understanding of the drivers (spatial separation, inclination angle, pulse power) and effects on measurements of interference along with ambient-noise for users of acoustic instruments. Lessons learned of value to the industry, as site characterisation work intensifies ahead of next generation commercial scale devices, are presented.

Mid-channel depth mounted SBDPs were found to have advantages over seabed mounted DBDPs in resolving the key turbulent flow metrics. SBDPs were able to resolve integral length-scales of turbulence that show an anisotropic ratio of scales as predicted from theory and in work at similar sites, while the DBDPs results were similar for all directions. Turbulence intensity measurements were found to be similar after noise correction, with the SBDPs more able to accurately capture the turbulence dissipation rate. This evidence suggests that SBDP arrays present a significant improvement over bottom mounted DBDPs in discerning information about the nature of the turbulent flow, and thus future site characterisation work should consider the use of SBDPs alongside bottom mounted DBDPs for this purpose.

Acknowledgements

The author like to extend the most sincere gratitude to Brian Sellar for his tireless work for the University of Edinburgh on the ReDAPT project and for his guidance throughout my PhD. I would also like to thank the Alstom ocean energy team for their assistance and support during the data gathering campaigns. I would finally like to extend my thanks to the other ReDAPT consortium members and my colleagues at the Institute for Energy Systems who always provided a supportive and enjoyable environment to spend these years of my life.

Declaration

I declare that this thesis was composed by myself, that the work contained herein is my own except where explicitly stated otherwise in the text, and that this work has not been submitted for any other degree or professional qualification except as specified.

Duncan Sutherland

Contents

Abstract	iii
Acknowledgements	iv
Declaration	v
List of Figures	xi
List of Tables	xviii
Nomenclature	xx
Abbreviations	xxiii
1 Thesis Overview	1
1.1 Research Motivation	1
1.2 Hypothesis and Relevance within the Field	2
1.3 Scope of Work	3
1.4 Contribution to Knowledge	4
1.5 Thesis Structure	6
2 Research Motivation and The State of the Art	8
2.1 Chapter Overview	8
2.1.1 Motivation	8
2.2 The Importance of Renewable and Tidal Energy	8
2.2.1 The drivers for renewable energy	8
2.2.2 The advantages of tidal energy	10
2.3 Challenges to the Tidal Energy Sector	11
2.3.1 History	11
2.3.2 Gaps in knowledge	12
2.4 Tidal Energy Site Characterisation	15
2.4.1 The physics of tidal Flow	15
2.5 Site Characterisation Instrumentation	21
2.5.1 Tide gauge	21
2.5.2 Velocimeters	22
2.5.3 Differential pressure sensors	23
2.5.4 Sensor mounting solutions	24

2.6	Sub-sea Acoustic Velocity Sensors (Doppler Sensors)	25
2.6.1	Doppler theory	25
2.6.2	Range gating	27
2.6.3	Design variations	28
2.6.4	Pulse types	30
2.6.5	Relative advantages and limitations of DBDPs	31
2.7	Quantifying Tidal Sites	31
2.7.1	Use of DBDPs and ADVs	32
2.7.2	Mean flows: depth profiles	32
2.7.3	Definitions of isotropy and homogeneity	33
2.7.4	Quantifying turbulence magnitude and structure	33
2.8	Reducing Measurement Uncertainty	38
2.9	Chapter Summary	39
3	Overview of the ReDAPT Project	40
3.1	Chapter Overview	40
3.2	ReDAPT Project Aims	40
3.3	Project Structure and Participants	40
3.3.1	Project management	41
3.3.2	Machine	42
3.3.3	Environment	42
3.3.4	Modelling	43
3.4	University of Edinburgh: Scope of Work and Time-line	43
3.5	Instrumentation and Project Experimental Set-up	45
3.5.1	Acoustic instruments	46
3.5.2	Instrument placement on the turbine	49
3.5.3	Stand-alone deployments	53
3.6	Turbine Operation and Data Gathering Procedures	54
3.6.1	SBDP Application Program Interface (API)	55
3.7	Data Storage and Management	56
3.8	Work Contribution Map	57
3.9	Chapter Summary	57
4	Quantification and Mitigation of Noise in SBDP Measurements	59
4.1	Chapter Overview	59
4.1.1	Motivation	60
4.1.2	Author's contribution	60
4.2	Part A - Quantification of Random Error	60
4.2.1	Methodology and Theory	60
4.2.2	Results	67

CONTENTS	viii
4.2.3 Discussion of results	68
4.3 Part B - Inter-SBDP variation and LSNR results	69
4.3.1 Methodology and Theory	69
4.3.2 Results	71
4.3.3 Discussion of results	75
4.4 Part C - Quantification of Bias Error using the LSNR method	76
4.4.1 Methodology and Theory	76
4.4.2 Results	78
4.4.3 Discussion of results	82
4.5 Part D - Noise Mitigation using Power and Grounding Modifications	83
4.5.1 Methodology and Theory	83
4.5.2 Results	85
4.5.3 Discussion of results	88
4.6 Conclusions	88
4.7 Chapter Summary	90
5 Cross-talk Between Co-Located Acoustic Instruments	91
5.1 Chapter Overview	91
5.1.1 Motivation	91
5.1.2 Author's contribution	92
5.2 Methodology	92
5.2.1 Theory overview	92
5.2.2 Tests and data collection	94
5.2.3 Data restrictions and quality control	101
5.3 Results	102
5.3.1 Basic example and variation with separation	102
5.3.2 Power and signal to noise ratio	107
5.3.3 Effect of angle between instruments and measuring velocity components	112
5.3.4 Mitigating cross-talk with ping offsets	116
5.3.5 Surface reflections from vertical instruments	119
5.3.6 Cross-talk from other acoustic sensor types on SBDPs	119
5.4 Discussion of Results	125
5.5 Chapter Summary	128
6 SBDP and DBDP comparison - Part A: Introduction and Data Preparation	130
6.1 Chapter Overview	130
6.1.1 Motivation	131
6.1.2 Contribution	131
6.2 Theoretical background	131

6.3	Data Set Selection	133
6.4	DBDP Velocity Transforms	136
6.4.1	Introduction	136
6.4.2	Transform definitions	136
6.4.3	Angle to turbine	138
6.4.4	Discussion	140
6.5	Instrument Range-Bin Selection	141
6.5.1	Introduction	141
6.5.2	Results	141
6.5.3	Discussion	142
6.6	Defining DBDP Noise Variance to Axial Velocity Relationship	144
6.6.1	Introduction	144
6.6.2	Results	145
6.6.3	Discussion	151
6.7	A Discussion of Averaging Options	152
6.7.1	Introduction	152
6.7.2	Effect of spatial averaging on metrics	153
6.7.3	Discussion	154
6.8	Chapter Summary	156
7	SBDP and DBDP comparison - Part B Results	157
7.1	Chapter Overview	157
7.1.1	Motivation	157
7.1.2	Author's contribution	157
7.2	Methodology and Theory	158
7.2.1	Mean velocity	158
7.2.2	Turbulence intensity	158
7.2.3	Turbulent kinetic energy dissipation rate	159
7.2.4	Integral lengthscale	159
7.2.5	Reynold stresses	162
7.2.6	Quality control	164
7.3	Results	165
7.3.1	Axial metrics (x)	165
7.3.2	Transverse metrics (y)	169
7.3.3	Vertical metrics (z)	174
7.3.4	Reynolds Stresses	179
7.4	Discussion	182
7.4.1	Future work	188
7.5	Chapter Summary	189

8	Summary, Conclusions and Recommendations for Future Work	190
8.1	Chapter Overview	190
8.2	Quantification and Mitigation of Noise in SBDP Measurements	190
8.2.1	Summary of Contributions to Knowledge	190
8.2.2	Future Work	191
8.3	Crosstalk Between Co-Located Acoustic Instruments	191
8.3.1	Summary of Contributions to Knowledge	191
8.3.2	Future Work	192
8.4	SBDP and DBDP comparison - Part A: Introduction and Data Preparation . .	193
8.4.1	Summary of Contributions to Knowledge	193
8.4.2	Future Work	193
8.5	SBDP and DBDP comparison - Part B Results	194
8.5.1	Summary of Contributions to Knowledge	194
8.5.2	Future Work	195
8.6	Review of the Hypothesis	196
	Bibliography	197

List of Figures

1.1	Illustration of the Alstom 1MW DeepGen IV tidal turbine and a selection of acoustic instrument beams Sellar <i>et al.</i> (2015).	4
2.1	Scottish tidal resource based on peak flows of spring tides. Image: ABPmer (2008)	11
2.2	The Hammerfest HS300 during installation (Andritz Hydro Hammerfest, 2012). .	12
2.3	A decomposition of the drivers of unsteady velocities at tidal sites.	13
2.4	Illustration of the effects of the gravitational forces of the Moon and Sun causing Spring and Neap tides. Image adapted from Surachit.	16
2.5	Examples of principle direction plots for both asymmetrical (left) and near symmetrical (right) sites from (Gooch <i>et al.</i> , 2009).	17
2.6	Example of a basin Digby Gut in Nova Scotia (right) taken from Yellow Maps and the estimated peak flow velocities (left) taken from Karsten <i>et al.</i> (2012).	17
2.7	Overview of forces on a rotating lifting surface (Burton <i>et al.</i> , 2011).	18
2.8	Illustration of the energy cascade, highlighting the most important regions in tidal site characterisation. Adapted from Pope (2000).	21
2.9	Example of a tide gauge from Valeport. Image: Valeport (2001)	23
2.10	Example of a impeller mounted to a directional vane. Image: Valeport (2015) . .	23
2.11	Example of a single access hot wire probe. Image: SMV-Tec	23
2.12	Principle of operation of a magnetic flow meter. Image: Piping-engineering.com .	23
2.13	An RDI RiverRay DBDP boat mounting (left) (Image: RDI) and a gravity base with gimbal mounting for a DBDP as used on the ReDAPT project (right).	25
2.14	Shear probe and DBDP mounted on an AUV. Image: (Rockland Scientific)	26
2.15	Buoy and gravity base tethered sensor mounting (Kilcher <i>et al.</i> , 2014).	26
2.16	Example of range gating for a sensor with a bin size and blanking distance of 0.4m. Image adapted from Gordon (1996).	28
2.17	DBDP beam geometry.	29
2.18	ADV beam geometry. Image: SonTek.	29
2.19	Example of different acoustic pulse types.	30
3.1	Location of EMEC test sites. The Alstom 1MW turbine was deployed at the full scale tidal site. Image from: EMEC (2015).	41
3.2	Illustration of standard acoustic instrument setup. Green beams represent the directions of the acoustic beams of the Doppler velocimeters.	45
3.3	Turbine coordinate system	46

3.4	Admiralty charts showing locations of tide gauges (GN and GS) with turbine location (marked TGL) Image from: Stock-Williams and Gunn (2012)	47
3.5	The Alstom DeepGen iv 1MW turbine being lifted for deployment. The annotations show the locations of the UoE instrument frames. There is also a single SBDP mounted in the nose that is not visible from this angle. Image from: Alstom	49
3.6	Top instrument frame being prepared for turbine deployment 5. The starboard SBDPs are visible mounted along the near edge with the AWAC behind in the centre. The outriggers for the focus beam SBDPs have been installed but the sensors themselves are not yet mounted.	51
3.7	Locations and naming convention for instruments on the top instrumentation frame. Note that not all of these sensors were installed for every deployment. . .	51
3.8	Instrument placement and naming convention for rear frame turbine. Note that not all of these sensors were installed for every deployment.	52
3.9	Overview of top instrument frame with SBDPs used in the focus beam arrangement. Image from Sellar <i>et al.</i> (2015).	52
3.10	A DBDP mounted in a gimbal on a concrete gravity base during deployment. . .	53
4.1	Illustration of the components of a measured spectrum. Adapted from Richard <i>et al.</i> (2013).	62
4.2	Example of de-trended data before and after the application of a Hamming window. The blue line represents the original signal and the red the filtered signal. .	64
4.3	Example of the spectral curve fitting method of Richard <i>et al.</i> (2013), highlighting the region used for the fit and the individual curve components.	65
4.4	Variation of σ_{noise}^2 (top) and cut-off frequencies (bottom) with inflow (\bar{u}) for inflow, transverse and vertical for the SBDPs.	67
4.5	Comparison of amplitude returns of a horizontal SBDP at 0 dB and -100 dB power settings.	69
4.6	Velocity time series of the individual SBDPs in LSNR (-100 dB) pulse power setting. The grey shaded background indicates instruments mounted on the rear instrumentation frame.	71
4.7	Histogram of velocity distributions of all available SBDP velocities in LSNR (-100 dB) pulse power setting.	73
4.8	Mean and Standard deviation of velocity measurements of four parallel SBDPs in -100 dB LSNR power setting contrasted with instrument noise measured in 0 dB power setting, for a sub-set of four parallel SBDPs.	74
4.9	Spectra of SBDP velocity fluctuations at -100 dB power setting.	75
4.10	Overview of 'side-on to flow' instrument and turbine orientation.	76
4.11	Powered (0 dB) SBDP velocity time series sub-set for the bias case study, highlighting the sensors measuring broadly similar inflow values.	79

4.12	LSNR-mode velocity time series sub-set for the bias case study, highlighting small differences in mean and standard deviation of velocity values.	79
4.13	Differences in mean inflow velocity with time across four parallel sensors.	80
4.14	Resultant flow angle for case study data set. The light blue lines represent the 1 Hz data and the darker blue the 256 second mean values.	81
4.15	Velocity difference with resultant flow angle.	81
4.16	Test for bias in 0 dB pulse power mode compared with the LSNR measurements in four parallel SBDPs.	82
4.17	Circuit diagram for the hard-wired grounding modification and DC-DC isolated power-conditioning transformer, installed on the rear instrumentation frame.	84
4.18	Mean amplitude and correlation returns from 2 power supplies from SBDPs at 0 dB power setting.	86
4.19	Velocities from a single SBDP in 0 dB mode with and without the DC-DC isolated power-conditioning transformer.	86
4.20	Subset of velocity measurements from a single SBDP in 0 dB mode with and without the DC-DC isolated power-conditioning transformer at a single bin at a range of 20 m.	87
4.21	$\Delta\sigma_u(x)$ from SBDPs at 0 dB power setting. Blue dots represent the mean difference in standard deviation. The blue triangles represent the standard deviation in the difference around the mean value.	87
5.1	Cross talk illustration showing a subsection of the transmit/receive cycle of two parallel SBDs. The black pulse is from the powered sensor and the red the -100 dB pulse of the LSNR instrument. The timing of each phase is given at the top right of each panel and starts at the bottom left advancing anti-clockwise.	93
5.2	Transmit/receive cycle and range gating of an SBDP with the reflected signal from a 1 m separated neighbouring instrument super-imposed. Image adapted from (Gordon, 1996).	94
5.3	Instrument configuration on the top frame of the turbine for the parallel cross-talk test.	95
5.4	Amplitude and correlation for SBDP with no interference.	96
5.5	Instrument configuration on the top frame of the turbine for the angled cross-talk test.	98
5.6	Illustration of the theory of two angled sensors measuring a component of the free stream velocity along the angle intersecting the two beams.	99
5.7	Amplitude and correlation for SBDP in LSNR mode showing indications of interference from a 0 dB source sensor for three separation distances.	103
5.8	Effect on velocity measurements for SBDP set to LSNR mode showing indications of interference in response to a 0 dB source at three separation distances.	104

5.9	Effect on velocity measurements for SBDP set in normal operating mode showing indications of interference in response to a 0 dB source at three separation distances.	105
5.10	Effect on velocity measurements for SBDP set in normal operating mode showing indications of interference in response to a 0 dB source at three separation distances.	106
5.11	Mean PSD plot of velocity fluctuations in the three regions of SBDP at 0.9 m separation showing effects of interference in the near, spike and far regions. . .	107
5.12	Plot of mean amplitude with range for a range of pulse power settings in the source SBDP (top) on a 0.9 m parallel separated instrument (bottom). The circles mark the locations of the spikes along the range for each source power setting. .	108
5.13	The effect of 4 power settings in the source instrument on the affected SBDP velocity measurements, highlighting a bias towards zero in both mean and fluctuation of velocity readings in the spike region.	108
5.14	Signal to noise ratio in the receiving SBDP in response to a source instrument at 2.4m separation at a range of power settings. The dashed lines show the range of the amplitude spike and the black circles the values corresponding to the extreme amplitude.	110
5.15	An example of cross-talk causing a velocity spike in the receiving SBDP over a 2.4 m range with both SBDPs set to 0 dB pulse power.	111
5.16	Velocity spike steepness as a function of SNR for an affected sensor at 0 dB, 2.4 m from the source.	111
5.17	Example of the effect of cross-talk between angled sensors on the receiving LSNR-mode instrument QC metrics.	112
5.18	Effect of cross-talk on velocity measurements of two receiving LSNR mode SBDPs at two beam intersection angles.	113
5.19	Comparison of bi-static angled LSNR mode SBDP velocity measurements with $\overline{u_{DBDP}}$	114
5.20	Expected component of \bar{u} along each angle against the value measured by an angled SBDP in both modes.	115
5.21	Amplitude and correlation returns for a range of pulse offsets for a receiving SBDP in a bi-static array configuration.	116
5.22	Measurement accuracy comparison of the measured and component velocities for a range of pulse offsets.	117
5.23	Resulting gradient of Figure 5.22 and noise variance of component measurement for a range of pulse offsets.	117
5.24	The effect of increasing the ping offset in the affected SBDPs at three separations.	118
5.25	The correlation of co-pinging vertical and transverse SBDPs, with the vertical sensor being cycled through a range of power settings.	120

5.26	Velocity measurements by horizontal SBDP showing effects of surface reflections, for a range of power settings of the source vertical SBDP.	120
5.27	Amplitude returns for a SBDP set to LSNR mode, illustrating the complex effects due to a parallel oriented AWAC transmitting at full power.	121
5.28	Amplitude returns for a SBDP set to 0 dB pulse power mode, illustrating the complex effects due to a parallel oriented AWAC transmitting at full power.	122
5.29	Standard deviation of velocity measurements at each range bin of SBDP, highlighting interference caused by the AWAC.	122
5.30	Power Spectral Density for an affected and non-affected range bin of the vertical SBDP due to interference from the AWAC.	123
5.31	Amplitudes from SBDP set at 0 dB power setting, mounted parallel with a Continental-SBDP.	124
5.32	Standard deviation of velocities with range of SBDP set at 0dB power setting, mounted parallel with a Continental-SBDP.	124
5.33	Power spectral density of SBDP set at 0 dB power setting at two range bins, mounted parallel with a Continental-SBDP. A spike at the Nyquist frequency and higher energy across the remaining frequency range is clearly evident in the 14.4 m range velocity measurements.	125
6.1	Illustration of increased spatial averaging of DBDP measurements with separation from the instrument.	132
6.2	Illustration of the measurements from the two instruments.	133
6.3	Turbine and DBDP measurement bin heights for comparison	135
6.4	DBDP transform stage 1.	137
6.5	Example of DBDP pitch and roll measurements showing Flood data.	137
6.6	Gradients (top) and R^2 values (bottom) for linear fits of mean velocities for the NW DBDP and the AWAC for a variety of trial angles between DBDP and turbine. The green circles highlight the gradients closest to 1 and the highest R^2 of the v measurements.	139
6.7	One to one mean velocity plot for a DBDP heading to turbine angle of 148.7° between DBDP and turbine using AWAC.	139
6.8	Bin Selection for SBDP in x direction, showing \bar{u} with range.	143
6.9	Illustration of increasing gradient of one-to-one velocity plots between SBDP and increasing bin number of DBDP.	143
6.10	Gradients of one-to-one velocity plots between SBDP at bin 25 and u component of DBDP at a range of bins.	144
6.11	Example of the effect of the two stages of the velocity transform on the spectra and subsequent noise floor.	145
6.12	Example of the issues experienced with fitting to a DBDP PSD.	147

6.13	Comparison of spectra and noise floor for the streamwise SBDP data down sampled and the DBDP at the original sample-rate.	148
6.14	Relationship of DBDP noise variance and cut-off frequency with velocity.	150
6.15	An example of the issues with DBDP vertical velocity from transform to compute the PSD, for 2.65 ms^{-1} axial velocity data set.	151
6.16	The effect of spatial averaging on SBDP measured metrics. The circle indicates the number of averaged bins that reduces I to the value corrected for variance due to noise.	155
6.17	The effect of spatial averaging on the PSD. The circle indicates the number of averaged bins that represents the best estimation of the inertial sub-range slope.	155
6.18	The effect of temporal averaging on the PSD.	156
7.1	Example of de-trending methods of velocity time series data.	161
7.2	An example of the effect of de-trending method on the autocorrelation function.	161
7.3	Selected samples for the SBDP and DBDP for the axial comparison study.	165
7.4	Histogram of streamwise data availability by mean DBDP velocity bin centres.	165
7.5	Comparison of contemporaneous \bar{u} measurements by the SBDP and the DBDP.	166
7.6	Comparison of the I_x values from the SBDP and DBDP. The large dots mark the mean values and the small dots the standard deviation about the mean for each 0.1 ms^{-1} velocity range. The top plot is the uncorrected values and the lower those corrected for the contribution of random error.	167
7.7	ε measurements from the two sensor types based on axial velocity measurements.	168
7.8	Comparison of ℓ_x calculated via temporal autocorrelation method on measurements by the SBDP and DBDP. The large dots mark the mean values and the small dots the standard deviation about the mean for each 0.01 ms^{-1} velocity range.	169
7.9	Selected samples for the SBDP and DBDP for the transverse comparison study.	170
7.10	Histogram of transverse data availability by mean DBDP velocity bin centres.	170
7.11	Comparison of contemporaneous \bar{v} measurements by the SBDP and the DBDP.	170
7.12	Distribution plot of \bar{v} measurements with axial velocity. The large dots mark the mean values and the small dots the standard deviation about the mean for each 0.1 ms^{-1} velocity range.	172
7.13	Comparison of the I_y values from the SBDP and DBDP. The large dots mark the mean values and the small dots the standard deviation about the mean for each 0.1 ms^{-1} velocity range. The top plot are the uncorrected values and the lower those corrected for the contribution of random error.	172
7.14	ε measurements from the two sensor types mounted in the traverse orientation.	173

7.15 Comparison of ℓ_y calculated via temporal autocorrelation method on measurements by the SBDP and DBDP. The large dots mark the mean values and the small dots the standard deviation about the mean for each 0.01 ms^{-1} velocity range.	173
7.16 SBDP measurements of ℓ_y calculated via a spatial autocorrelation method. . . .	174
7.17 Selected samples for the SBDP and DBDP for the vertical comparison study. . .	175
7.18 Histogram of vertical data availability by mean DBDP velocity bin centres. . . .	175
7.19 Comparison of contemporaneous \bar{w} measurements by the SBDP and the DBDP.	176
7.20 Distribution plot of \bar{w} measurements with axial velocity. The large dots mark the mean values and the small dots the standard deviation about the mean for each 0.1 ms^{-1} velocity range.	177
7.21 Comparison of the I_z values from the SBDP and DBDP. The large dots mark the mean values and the small dots the standard deviation about the mean for each 0.1 ms^{-1} velocity range. The top plot is the uncorrected values and the lower those corrected for the contribution of random error.	178
7.22 ε measurements from the two sensor types mounted in the vertical orientation. .	178
7.23 Comparison of ℓ_z calculated via temporal autocorrelation method on measurements by the SBDP and DBDP. The large dots mark the mean values and the small dots the standard deviation about the mean for each 0.01 ms^{-1} velocity range.	179
7.24 SBDP measurements of ℓ_z calculated via a spatial autocorrelation method. . . .	180
7.25 Data set matched across three sensors for τ_{uw} comparison.	180
7.26 Estimates of the Reynolds stress two calculated via the beam-pair method and via $\langle u'w' \rangle$ from rotated DBDP velocities.	181
7.27 Reynolds stress estimates via a x - z SBDP pair averaged over all available flow speeds.	182
7.28 Hub height comparison of SBDP and DBDP Reynolds stress results across the available flow speeds.	183

List of Tables

3.1	ReDAPT Sub-project MP – Project Management work packages.	41
3.2	ReDAPT Sub-project A – Machine work packages.	42
3.3	ReDAPT Sub-project ME – Environment work packages.	42
3.4	ReDAPT Sub-project MD – Model work packages with UoE lead sub-packages highlighted.	43
3.5	UoE led MD2 and MD3 project deliverables	44
3.6	Time-line of turbine and associated instrumentation deployments.	45
3.7	Overview of Doppler sensors available	48
3.8	ReDAPT project - Author contribution map. Orange rows relate to pre-project planning, blue to project management, green to the experimentation and pink to data analysis. The work specifically relating to the analysis in the thesis is marked with *	58
4.1	Range bin at which relationship of noise variance with velocity is defined for each direction.	66
4.2	Instrument availability and configuration for the SBDP σ_{noise}^2 test.	70
4.3	SBDP LSNR-mode test settings.	71
4.4	Mean and Standard deviation of velocity measurements of SBDPs in LSNR (-100 dB) power setting, contrasted with instrument noise measured in 0 dB powered setting. Shaded cells correspond to the sub-set plotted in Figure 4.8.	72
4.5	Qualitative summary of the distributions in Figure 4.7.	73
4.6	Gradients of LSNR-mode PSD for each individual SBDP.	74
4.7	SBDP settings for the analysis of bias study.	78
4.8	Case study velocities by individual SBDP for 0 dB mode.	79
4.9	SBDP Settings for DC-DC isolated power-conditioning transformer and grounding modification test.	85
5.1	Data collection for basic LSNR test	95
5.2	Data collection for 0 dB pulse power test at three separations.	97
5.3	Data collection and instrument settings for varying source pulse power at 0.9m .	97
5.4	Data collection and instrument settings for varying source pulse power at 2.4m .	97
5.5	Data collection and instrument settings for the two tests for two angled SBDP. One with two SBDPs in in LSNR mode and a second with all instruments at 0 dB power.	99

5.6	Data collection and instrument settings for a range of pulse offset to assess accuracy velocity component in LSNR at 23.2°.	100
5.7	Data collection and instrument settings for mitigation of cross-talk by pulse offset test.	100
5.8	Data collection and instrument settings for test of effect of surface reflections. . .	103
5.9	Data collection and instrument settings for cross-talk between different sensor types.	103
5.10	Peak values of correlation and amplitude of LSNR SBDPs in response to parallel 0 dB signal.	104
5.11	Peak values of correlation and amplitude of fully powered SBDPs in response to parallel 0 dB signal.	105
5.12	Peak values of amplitude in the receiving sensor for a range source sensor power settings.	107
5.13	Velocity response to power increase in interference signal.	109
5.14	Peak values of correlation and amplitude of fully powered SBDPs in response to a 0 dB signal at two beam intersection angle.	113
6.1	SBDP and DBDP settings for comparison.	134
6.2	Gradients and associated R^2 values of linear fits for the heading to turbine angle given in Figure 6.7.	140
6.3	Turbine angles from alternate NW DBDP deployments.	140
6.4	Comparison of σ_{noise}^2 based on f_s for streamwise data from the SBDP and the DBDP.	148
7.1	Summary of the effect of de-trending on ℓ_x values.	160

Nomenclature

α	Amplitude
β	Beam inclination angle
Δr	Range from sensor
Δx	Length along the x vector
Δy	Length along the y vector
Δz	Length along the z vector
ℓ	Integral lengthscale
ε	Turbulent kinetic energy dissipation rate
ε'	Standard (random) error
Λ	Velocity peak sharpness
μ	Dynamic viscosity
∇	Gradient of slope
$\bar{\varepsilon}$	Systematic error (bias)
\bar{u}	Mean velocity in the x direction
\bar{v}	mean velocity in the y direction
\bar{w}	Mean velocity in the z direction
ϕ	Pitch angle
ψ	Roll angle
ρ	Density
σ	Standard deviation
σ^2	Variance
τ_{vw}	Vertical-streamwise Reynolds stress tensor
θ	Heading angle
Υ	Temporal lag
A	Aft (<i>SBDP position indicator</i>)
B	Bottom (<i>SBDP position indicator</i>)
F	Fore (<i>SBDP position indicator</i>)
M	Middle (<i>SBDP position indicator</i>)
P	Port (<i>SBDP position indicator</i>)
S	Starboard (<i>SBDP position indicator</i>)
T	Top (<i>SBDP position indicator</i>)
V	Vertical (<i>SBDP position indicator</i>)
A	Area
C	Speed of sound
c_i	Integral sub-range coefficient

c_k	Kolmogorov coefficient
c_L	Lift coefficient
c_p	Power conversion efficiency coefficient
c_s	Structure function coefficient
c_{vk}	Von Kármán coefficient
D	Structure function
D_h	Hydraulic diameter
E	Energy
f	Frequency
f_d	Doppler shifted frequency
f_n	Nyquist frequency
f_p	Frequency associated with a peak
f_s	Sample-rate
f_{pulse}	Pulse carrier frequency
H_s	Significant wave height
I	Turbulence intensity
K	Kinetic power density
k	Wave number
L_{FFT}	Number of data points in fast Fourier transform
N	Power spectral density of noise floor
P	Power
R	Autocorrelation coefficient
r	Position along acoustic beam vector
R^2	Goodness of fit statistic
Re	Reynolds number
S	Power spectral density
T	Period
T_p	Peak wave period
T_{Stat}	Period of stationarity
u	Instantaneous velocity in the x direction
u'	Velocity fluctuation about the mean in the x direction
v	Instantaneous velocity in the y direction
v'	Velocity fluctuation about the mean in the y direction
vel	Velocity not aligned to a Cartesian direction
w	Instantaneous velocity in the z direction
w'	Velocity fluctuation about the mean in the z direction
x	Vector associated with axial or stream-wise measurements
Y	Spectral periodogram
y	Vector associated with transverse or lateral measurements

z vector associated with vertical measurements and height above seabed

Abbreviations

ADV	Acoustic Doppler Velocimeter
API	Application Program Interface
AWAC	Acoustic Wave and Current Meter
CBDP	Converging Beam Doppler Profiler
CFD	Computational Fluid Dynamics
DC	Direct Current
DBDP	Diverging Beam Doppler Profiler
EMEC	European Marine Energy Centre
ETI	Energy Technologies Institute
FFT	Fast Fourier Transform
IPCT	Isolated Power Conditioning Transformer
LSNR	Low Signal to Noise Ratio
NW	North West
PPM	Parts Per Million
PSD	Power Spectral Density
QC	Quality Control
ReDAPT	Reliable Data Acquisition for Tidal
SBDP	Single Beam Doppler Profiler
SE	South East
TKE	Turbulent Kinetic Energy
UoE	University of Edinburgh

Thesis Overview

1.1 Research Motivation

The drivers for alternative energy sources: security of energy supply, finite fossil fuel resources and their contributions to accelerated climate change, are now well understood (MacKay, 2008). In order to meet an ever increasing global energy demand (BP, 2014) many options for alternative solutions must be explored. Tidal stream energy is one possible source of energy that is currently being developed, with the first commercial devices in the UK now deployed and the first array projects beginning construction. The UK's extractable tidal stream resource is estimated between 15.7 TWh/year (Black & Veatch, 2005) and 20.6 TWh/year (Carbon Trust, 2011) which has the potential to fulfil up to 5.8% of the UK's total 335TWh annual electricity consumption (UK Parliament, 2014).

Several large scale (> 1 MW) devices have been developed to extract this energy in sites across the UK (Alstom, 2014; MCT, 2008; OpenHydro, 2008; Atlantis, 2008). Many aspects of these devices are conservatively engineered to mitigate a lack of understanding of the environment at high energy sites (Marsh, 2009), particularly regarding the contribution of turbulent flow to fatigue loading and quality of power. In order to be commercially viable, tidal stream energy extraction technology has to be optimised for site-specific conditions. This in turn, requires sites to be characterised accurately and cost effectively and the metrics that are of highest benefit to device designers must be discerned and quantified.

Currently the vast majority of tidal site or potential site characterisation employs one or more seabed mounted Diverging Beam acoustic Doppler Profilers (DBDP). These devices are capable of providing three Cartesian vector velocity measurements throughout the water depth, and hence are able to characterise the relationship between depth and velocity. However, standard DBDPs were originally developed for oceanographic measurements rather than for turbulence measurements and they have several drawbacks when used with this aim:

- Limited sample rate for measuring turbulent characteristics (generally around 2 Hz);
- Require a velocity transform from measured beam velocities to Cartesian u , v and w ;
- Require assumption of homogeneous flow across large areas (~ 20 m scales);
- Restricted data storage;

- Limited by battery life;
- Require expensive vessel deployment;
- Inherently noisy technology.

The primary aim of this thesis is to assess whether Single Beam Doppler Profilers (SBDPs), which were newly available at the start of this project, can be used effectively in arrays at mid-channel depth to improve understanding of energetic tidal stream environments.

1.2 Hypothesis and Relevance within the Field

There is currently high uncertainty surrounding the measurements of turbulent fluctuations in the flow, due in part to the configuration of the sensors being used. Utilising multiple SBDPs mounted at mid-channel depth on a commercial scale tidal turbine, the most relevant turbulence information for device designers, i.e., those in the rotor plane, can be captured.

This work initially seeks to establish and parametrise the interaction between multiple SBDP devices operating in close proximity, as well as identifying other sources of noise on the sensors and developing mitigation strategies. This includes assessing noise due to the mounting of these sensors on a tidal turbine. This understanding will allow the optimisation of placement and instrument settings to ensure minimal unwanted interference between sensors.

With an established methodology for operating these devices in turbine mounted arrays, the ability of these arrays to measure the turbulent and mean parameters at the site can be assessed against the industry standard of a Diverging Beam Doppler Profiler (DBDP). This involved contrasting the results with those of other pre-existing technologies such as DBDPs. Of particular interest is the SBDP's ability to discern the magnitude and scale of the fluctuations and their variation within the tidal cycle and spatially across the site.

This project had several unique advantages over the majority of field measurement campaigns. Firstly the sensors were mounted on a commercial scale tidal turbine meaning they were at an ideal height for capturing inflow relevant for the turbine. Mounting on a turbine also allowed the sensors to be connected to a shore-based server via Ethernet and were supplied with power, meaning a large amount of continuous high frequency data could be collected without battery and storage issues. The SBDPs were synchronised by a GPS master clock and could be set up to transmit their acoustic pulses at offset intervals from each other; this is vital in minimising interference between acoustic pulses. However, there were unknown issues with how operating on a turbine might effect the sensors particularly in terms of electrical noise.

The formal hypothesis for this work is that:

“Single beam Doppler sensors used in arrays mounted at mid-channel depth will reduce uncertainty in turbulent flow metrics at tidal energy sites compared with standard seabed mounted diverging beam Doppler profilers.”

1.3 Scope of Work

This work took place as part of the Energy Technologies Institute (ETI) funded Reliable Data Acquisition Platform for Tidal (ReDAPT) project. The equipment was specified to meet a broad range of overall project goals and, as such, was not specified for or constantly available to this body of work. The broad scope of the University of Edinburgh's work within the project was to measure and characterise a representative inflow to the 1MW DeepGen IV tidal turbine. The turbine, developed, operated and owned by Alstom Ocean Energy, is situated in the Fall of Warness in the Orkney Isles, is part of the European Marine Energy Centre (EMEC). A further explanation of the structure of the ReDAPT project and where this work fits within it can be found in Chapter 3.

The University had six different types of acoustic Doppler sensor available over the course of the project covering a range of scales including:

- A Sontek acoustic Doppler velocimeter (ADV), which measures flow averaged over a range of 3 cm at 25 Hz sample-rate.
- A Nortek Continental long range single beam sensor, which could in theory measure up to ranges of 200 m at 1 Hz.
- Multiple Nortek SBDPs with an operating range of 15-20 m and a maximum sample rate of 2 Hz, later upgraded to 4 Hz.
- Multiple designs of DBDPs, with four to five beams, operating ranges in the order of 50 m and a maximum sample rate of 2 Hz.

An illustration of the turbine and the sensors mountings is given in Figure 1.1.

This work focuses on the single beam Doppler profilers which were newly available at the commencement of the ReDAPT project. The sensor, developed by manufacturer Nortek, is a broadband sensor with a maximum sample rate of 4 Hz, carrier frequency of 1 MHz and a maximum operational range of around ~ 20 m. There were 16 of these sensors available which were mounted in a variety of configurations on the top, rear and nose of the turbine.

The experimental testing can be separated into two broad categories:

1. Minimising noise and cross talk between the instruments to collect the best flow data.
2. Comparison of flow metrics between a seabed mounted DBDP and a mid-depth Cartesian SBDP array, particularly with regard to turbulence.

The former of the two can be further broken down into two main test types: In-situ noise measurements caused by power quality and instrument placement, and 'crosstalk' interference. The latter compares data from arrays of SBDPs with the alternative flow measurement instrumentation. Utilising optimised post-processing techniques it will be assessed if SBDP arrays possess advantages over the current best practice.

Due to the measurement range (typically 15-20m) of the SBDPs, tank facilities of an appropriate scale where tests of the array configurations could be conducted under repeatable

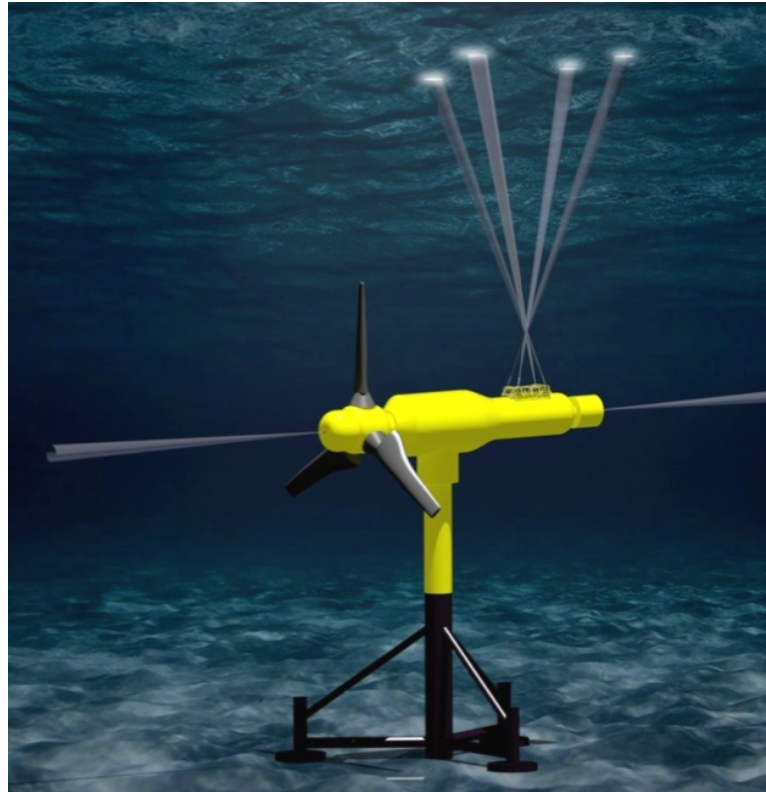


Figure 1.1: Illustration of the Alstom 1MW DeepGen IV tidal turbine and a selection of acoustic instrument beams Sellar *et al.* (2015).

conditions, are extremely limited. Thus configuration tests were required to be conducted in ‘real world’ non-steady-state environment which increases uncertainty in the results. Where possible, large data sets were collected in order that parameters would converge for a given test and ambient flow condition.

1.4 Contribution to Knowledge

As the SBDPs are a new sensor type, optimisation for and assessment of their ability to measure the flow represents an original piece of research. In addition, the sensors are mounted at mid-channel depth on a commercial scale turbine providing measurements from instruments within the rotor plane of the turbine; this reduces uncertainty compared with bottom or surface buoy mounted instrumentation requiring velocity transforms and spatial averaging. This mounting arrangement has potential drawbacks in terms of the additional sources of electrical noise. However, there are important benefits, such as being able to measure streamwise flow velocities with much reduced spatial averaging compared with DBDPs.

The most significant original contributions to knowledge of this work are summarised as:

- The relationship between random error and velocity was characterised for two instrument types for multiple orientations to the onset flow, highlighting hitherto unquantified variation between these parameters;
- The use of a novel Low Signal to Noise Ratio (LSNR) mode in the sensors showed promising results as a method of noise characterisation in acoustic sensors;
- Identification, effects and mitigation of cross-talk between similar and different sensor types is presented, which has not previously been quantified for such a large array of acoustic devices.
- A mitigation strategy to mitigate this cross-talk based on a pulse offset proves to effectively remove this issue;
- A methodology for aligning data to a common axis for sensors on the turbine and the seabed was presented and proven to be effective;
- Spatial averaging of a streamwise SBDP data sub-set was shown to reduce random error, increase accuracy of turbulence intensity and integral length-scale values, while still representing the integral sub-range spectrally; Conversely, temporal averaging (although still reducing random error) was shown to be inappropriate for turbulence metrics;
- The first field measurements using a SBDP array and a comparison with a seabed mounted DBDP are presented. Results for a comprehensive set of metrics demonstrating the superior performance of the SBDP array for detecting lengthscales and dissipation rates and as accurate in the other metrics, highlighting the value of this newly available sensor type.

It is expected the knowledge gained in this work will reduce uncertainty and guide methodologies for future site characterisation projects. It highlights the benefits of SBDP arrays and outlines the best practise for sensor orientation and configuration to minimise instrument noise and interference and to maximise capture of low uncertainty flow metrics.

1.5 Thesis Structure

This section gives a brief overview of what is detailed within each chapter of the work. Each of the technical chapters contains an introduction and motivation section, followed by the theory and experimental set-up used. The results of each experiment are then presented and discussed.

Chapter 2 Research Motivation and The State of the Art

This chapter investigates the literature relating to characterisation work for potential tidal energy sites based on field measurements. It gives an overview of the drivers for and the potential of tidal energy for electricity generation in the UK. The challenges in reducing the uncertainty regarding these field measurements and the metrics that must be captured to effectively quantify a tidal site are detailed. An overview of available sensors is given, with particular attention paid to the method of acoustic Doppler technology and the motivation for the use of single beam acoustic sensors.

Chapter 3 Overview of the ReDAPT Project

This work was conducted within a wider multifaceted and multi-million pound research project entitled “Reliable Data Acquisition Platform for Tidal” (ReDAPT). In order to understand the context and limitations of the experiments undertaken, an overview of the wider project is essential. This chapter gives an overview of the organisations involved and their individual goals. It also details the experimental set-up which was used for all the measurements taken in this work.

Chapter 4 Quantification and Mitigation of Noise in SBDP Measurements

This chapter looks at the noise in instruments both in terms of standard error and bias. Using a technique developed by Durgesh *et al.* (2014) and Richard *et al.* (2013) the variance attributable to noise in each SBDP is measured. An investigation to assess instrument bias is proposed and trialled. Two noise mitigation techniques are investigated and the effect on the quality control metrics and velocity measurements of these modifications is assessed.

Chapter 5 Cross-talk Between Co-Located Acoustic Instruments

The installation of so many acoustic Doppler sensors mounted so close together is unprecedented and interference between sensors was deemed probable. This chapter assesses the indicators and effects of ‘cross-talk’ between SBDPs. The effect of instrument separation and angle is investigated as are mitigation strategies such as source amplitude and pulse offsets. The effects of cross-talk from two other acoustic sensor types on the SBDPs are detailed and the effects of reflections at boundaries, such as the water surface, are examined. In addition,

the potential of utilising cross-talk between sensors to form a bi-static measurement system is investigated.

Chapter 6 SBDP and DBDP comparison - Part A: Introduction and Data Preparation

In this and the subsequent chapter the ability of an array of SBDPs, with one mounted along each Cartesian direction to measure a selection of turbulence metrics from the flow is compared with that of a bottom mounted DBDP. In order to make an accurate comparison of the two sensor types, the effects of data selection and processing methodology are assessed. This chapter discusses: What data is utilised; how different instruments data sets are aligned to a common axis; BDBP velocity transforms; the noise variance in DBDP velocity measurements for a range of orientations and flow conditions and the effects of ensemble averaging on turbulence metrics. The conclusions of this chapter are used in the data processing and calculation of results in Chapter 7 with the aim that the comparison and metrics are appropriate and as accurate as possible.

Chapter 7 SBDP and DBDP comparison - Part B Results

This chapter presents the methodology for processing turbulence metrics and in turn the results of the comparison between the mid-depth mounted Cartesian SBDP array and a bottom mounted DBDP. The results for each Cartesian direction are presented separately. The metrics compared include: mean velocity, turbulence intensity, turbulent kinetic energy dissipation rate, integral lengthscale and an initial study of the vertical-streamwise Reynolds stress tensor. The variation of these metrics for a range of streamwise flow speeds are presented and contrasted for both instruments for each vector.

Chapter 8 Summary, Conclusions and Recommendations for Future Work

The final chapter summarises the main findings of each of the experimental chapters as well as discussing any limitations and levels of uncertainty in the results. Recommendations for further site characterisation, novel array configurations and experiments to further reduce uncertainty of results are detailed.

Research Motivation and The State of the Art

2.1 Chapter Overview

This chapter gives an overview of the drivers for utilising renewable energy sources for electricity production and the merits of tidal energy as a contributor to the renewable energy mix. The importance of characterisation of potential sites are highlighted, as are the current knowledge gaps within this field of study. Previous work covering the techniques developed and quantifying field measurements are discussed. The various technologies available to measure tidal currents are reviewed with respect to their relative advantages and drawbacks, with special attention paid to the method of acoustic Doppler velocimeters, which were utilised during this project.

2.1.1 Motivation

In order to progress the field of tidal site characterisation, a good grounding in the available tools and previous work is essential. As well as outlining the key drivers for tidal energy, this chapter serves as a reference of the research and knowledge in this field available at the time of writing.

2.2 The Importance of Renewable and Tidal Energy

2.2.1 The drivers for renewable energy

The drivers for a move towards renewable energy sources are now well understood. MacKay (2008), highlights the three main motivations as:

1. Extractable fossil and fission fuel sources are finite.
2. Security of supply for any given nation is based on its ability to generate its own energy.
3. The effects of greenhouse gases (GHGs) produced by energy generation on the global climate.

At the time of writing new methods for fossil fuel extraction such as hydraulic fracturing ('Fracking') and directional drilling were leading to a reduction in the price of fossil fuels at the time of writing (ICIS, 2015). Meaning that even with ever increasing global demand (BP, 2014) the supply will outlast demand until a point where climate change will have adversely affected the lives of billions. A discussion on point 2 is beyond the subject matter of this introduction but at the time of writing several of the top 10 oil producing nations (particularly Russia, Iraq and Iran) were in areas of strained relations with the UK (CIA, 2014).

Climate change, and the effect of anthropogenic activities on it, is to say the least, a complex field of study. Here a brief summary is given to highlight the drivers and scale of this phenomenon. The planet's climate goes through a series of natural cycles of which it is currently in a inter-glacial warm period (NOAA, 2015a), within this there is a degree of natural fluctuation. There are many mechanisms that drive climate change and they can be split into two groups, fast feedback (acting over scales of less than 100 years) and slow feedback (acting over centuries to millennia) (Zeebe, 2013). Greenhouse gases (GHGs) fall in the latter which suggests that the planet is yet to adjust to the increase in post industrial revolution greenhouse gas emissions.

CO₂ emissions reported in September 2014 were 36 gigatonnes (GtCO₂) worldwide. This is 61% higher than 1990 (the Kyoto Protocol reference year) and an increased 2.3 % over the previous 2 years (Le Quéré *et al.*, 2013). Alternatively, the atmospheric CO₂ for December 2014 was 398.78 ppm (NOAA, 2015b), compared with 280 ppm pre industrial revolution (MacKay, 2008) and, looking further back, 290 ppm for previous inter-glacial periods of the planets history, as assessed from Vostok Ice Core Data (Petit *et al.*, 1999). Although average global temperature levels are not as high as they have been in previous interglacial periods, the effects of slow response climate systems to the rapid rise in CO₂ since the industrial revolution will cause greater temperature increases over this century (Hansen and Sato, 2011).

There are already many observed effects of climate change including a higher occurrence of: heavy precipitation events, droughts, cyclones and extreme sea level rises (IPCC, 2014). Predicted effects of climate change include further sea level rises (Rahmstorf, 2007), drought and desertification (Le Houérou, 1996), increase of extreme weather phenomenon (Meehl *et al.*, 2000), with some predictions that the planet would warm to a level where humans could not adapt to the increased heat stress (Sherwood and Huber, 2010).

In order to mitigate the issues with current energy sources, renewable energy (along with efficiency of energy use) is seen as the central alternative. Renewable energy for electrical, heat and other fuel production are sources of energy that are not depleted as they are used, or at least that the reductions are minimal. Renewable energy sources include: wind, solar, wave and tidal, bio-fuels, geo-thermal and others. The availability of these resources vary around the globe, thus it is important for different nations to identify the resources that are available to them.

The UK government has set targets to produce: 30% of its electricity, 12% of its heat and 10% of its fuels from renewable sources by 2020 (UK Parliament, 2009) and that there should be a 20 per cent reduction in emissions of GHGs from 1990 levels (UK Parliament, 2008). Scotland has been more ambitious in its targets: "an equivalent of 100% demand for electricity from renewable energy by 2020, as well as our target of 11% renewable heat" according to its 'Routemap for Renewable Energy in Scotland' (Scottish Government, 2011). The solution to this global energy crisis is complex and will require a diverse range of energy contributions based on the available local resources (DECC, 2011).

2.2.2 The advantages of tidal energy

The amount of kinetic energy in tidal driven movement of water globally is vast, but only a small portion of that is 'exploitable', i.e. can be feasibly converted to electricity. The main criteria for this are: the magnitude of the velocity of the flow, the depth of water, the wave climate at the site, the turbulence of the flow and proximity to, as well as strength of, potential grid connection. In addition to the physical extractable ratio that a turbine can remove from a moving fluid, I.E. the Betz limit (DNV, 2002).

The UK's extractable tidal stream resource is estimated to be between 15.7 TWh/year (Black & Veatch, 2005) and 20.6 TWh/year (Carbon Trust, 2011). This comprises 4.4% to 5.8% of the UK's total 335TWh electricity usage in 2014 (UK Parliament, 2014). Black & Veatch (2005) suggest that of the top 10 sites in the UK seven are in Scotland and it is estimated that 25% of the European resource is in Scotland (Scottish Government, 2003). Figure 2.1 highlights this resource via the available flow velocities around Scotland. The areas around Orkney (particularly the Pentland Firth) and around Islay and the Mull of Kintyre are particularly highly energetic.

One of the main advantages of tidal energy is the predictability of the resource. With suitable historic data the harmonic components of a tidal channel can be discerned and predictions of resource made for years into the future (Knauss, 1978). Wind and waves are driven by more complex meteorological effects and lack this predictability of resource. In order to have a large renewable contribution to the energy mix a large predictable component would ease the significant challenge of supply planning.

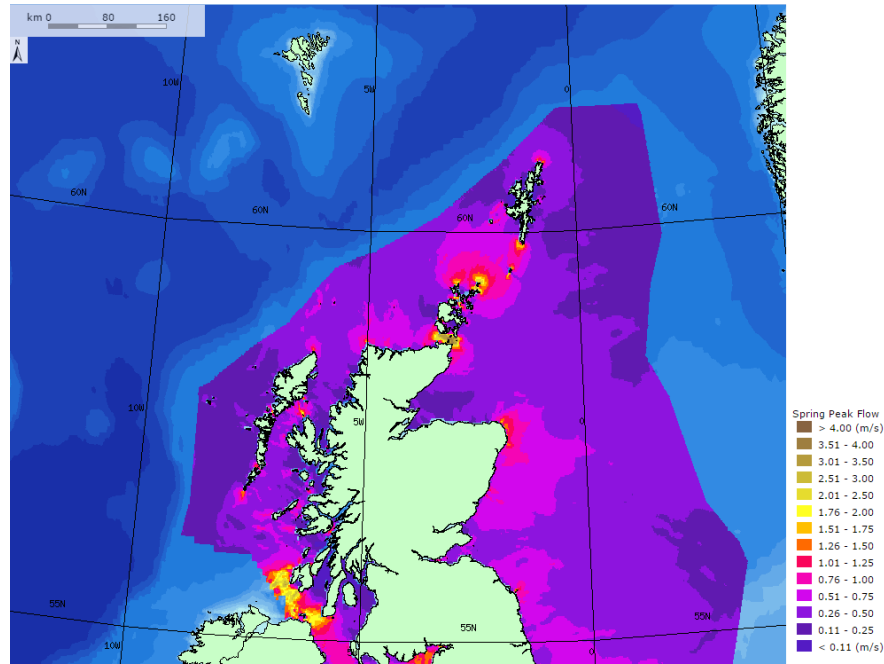


Figure 2.1: Scottish tidal resource based on peak flows of spring tides. Image: ABPmer (2008)

2.3 Challenges to the Tidal Energy Sector

2.3.1 History

Building a new energy sector from its infancy is an extremely challenging undertaking. First there is a limited understanding of the resource and limited tools to characterise it. Then there are the devices themselves which need an optimised source of energy capture, conversion and transmission along with a mechanism to mount them in the channel that can survive the harsh conditions. There are also challenges in the development of installation techniques as well as operation and maintenance planning. In the fledgling years of any technology where there is little or no supply chain infrastructure, there is the need for a large proportion of bespoke solutions to complex issues. This all leads to expensive development for a technology which will intrinsically be operated in harsh conditions.

Amongst the first grid connected tidal turbines was the 300kW HS300 prototype built by Hammerfest (now Andritz Hydro) which was first installed in Kvalsund in Finnmark, Norway. It has since been superseded by the HS1000 1MW commercial scale device, which had produced over 1.5GWh of electricity by the end of 2014 (Andritz Hydro Hammerfest, 2012). It is a single three-bladed rotor axial flow device based on a tripod support structure. Another early commercial (≥ 1 MW) scale grid connected tidal turbine was Seagen which was installed in Strangford Narrows (Northern Ireland) in June 2008. This 1.2 MW device employs two two-bladed rotors either-side of a surface piercing central pile. It had by the end of 2014 achieved over 8GWh of production (MCT). Since then other sizeable devices include: the



Figure 2.2: The Hammerfest HS300 during installation (Andritz Hydro Hammerfest, 2012).

Alstom DeepGen iv, the Open Hydro ‘Open-Centre’, the Atlantis ‘AR1000’ and Voith turbines, which are all rated at 1MW or greater and have been operated in real sea conditions.

At the time of writing, consent had been granted to begin development of the first tidal array projects. These were: MeyGen in the Pentland Firth, Scottish Power Renewables’ Sound of Islay project and France’s Agency for Environment and Energy Management project in Raz Blanchard, Normandy, France. It is hoped that these projects will significantly advance knowledge of the challenges to the sector, revealing detailed information regarding device interactions. In addition, it is hoped they will begin reducing the cost of tidal generated energy, through economies of scale related to multiple devices as well as sharing infrastructure and developing operation and maintenance strategies and other barriers to the development of the industry.

2.3.2 Gaps in knowledge

There has often been the assertion that the tidal industry can build on the knowledge of the more established wind industry, since they are founded on the same principles of fluid dynamics. However, a more dense fluid, more confined fluid depth compared with the device scale and the effects of waves at the upper boundary and their propagation down through water column, in addition to the challenges of installing equipment under the sea, mean tidal energy has a host of unique challenges. There are also difficulties in understanding the environmental impact of tidal turbines, but these will not be focused on here.

On the engineering side, the main areas of research are:

- The energy resource;
- The force loadings on a device;
- Wake interactions in arrays.

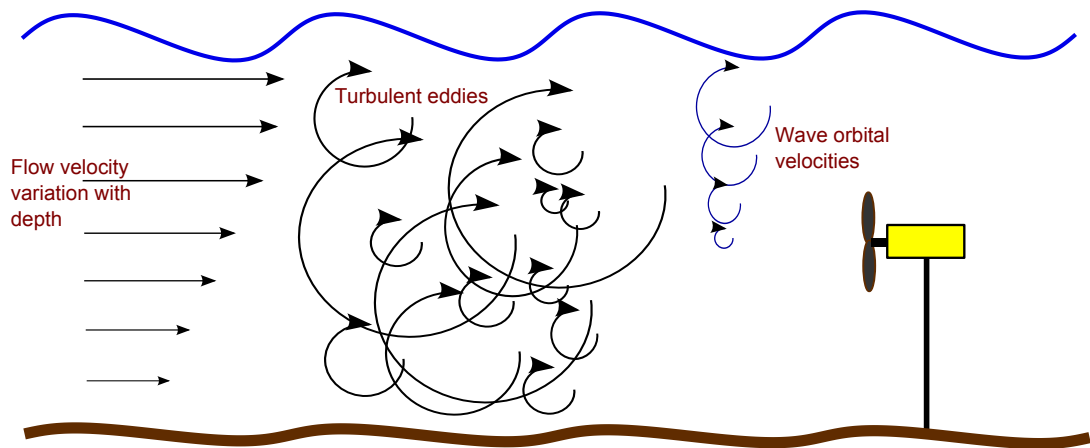


Figure 2.3: A decomposition of the drivers of unsteady velocities at tidal sites.

There is an urgent need for a reliable description of the fluid flow at potential tidal turbine sites to allow for predictions of potential power extraction as well as device and component life span. Although the main drivers of the flow which make them a predictable resource are understood at site-scale there is still uncertainty about local flow velocities. The flow at sub-site-scale is driven by local bathymetric features and coastline which can cause significant variation in flow over small (< 100 m) scales (Evans *et al.*, 2013). Literature sources for tidal velocities tend to vary in their estimate with one study showing a discrepancy of up to 2 ms^{-1} across different resource atlases for a single site (Black & Veatch, 2005). An additional motivation for a comprehensive understanding of the uninterrupted flow at a site, is to assess the effect of introducing a turbine or array of turbines to it. The wakes from tidal turbines is a key area of interest as array projects develop and expand.

The loading on devices at tidal stream sites are a complex combination of: mean flow, turbulence and wave orbital effects. Figure 2.3 highlights these components as decomposed two-dimensional phenomenon. In reality, these effects are superposed and three dimensional, creating a complex flow field, with other complex flow effects, such as the Ekman spiral which is a twist of flow through the water column (Knauss, 1978).

The drivers of turbulent flow are discussed in the Section 2.4.1, but since almost all tidal energy sites are turbulent, the fluctuations in flow velocity magnitude, direction and duration will affect the device loadings (Leishman, 2002). One of the key differences between wind turbines and tidal turbines is that for atmospheric wind flow, the most energetic turbulent structures are not restricted by an upper boundary layer and thus the highest energy containing structures can be very large, tending towards 280 m as separation from the boundary increases (Burton *et al.*, 2011). In a tidal channel the turbulent structures are limited by the channel depth. However, the limited size of the eddies is offset by the increased fluid density, which increases the energy within the eddies. In addition, since turbine blade diameters are often close in scale

to half the channel depth, the effect of turbulent structures of similar dimensions to the device on the loadings are an important factor and one that is not well understood. Finally, there is additional uncertainty over the effect of the smallest (dissipation) scales of the turbulence which are predicted to increase skin-friction drag and affect flow transition on blades (Clark, 2015).

In addition to turbulent flow induced fluctuations there is the added complication of surface waves. Waves induce orbital motions through the water depth, inducing further fluctuations around the mean velocity. The greater the amplitude and wavelength of a surface wave the greater the fluctuation at a given depth. The path of these orbital velocities is dependent on the ratio of wave length to total channel depth. (Sarpkaya and Isaacson, 1981). However, it should be noticed that for longer period waves the flow in a channel of this depth will experience shallow water effects with impact down to the seabed. The interaction between waves and currents particularly in turbulent environments is not well understood and thus is a source of uncertainty for device designers.

One technique of predicting these effects is via computational modelling. Computational models exist for all scales of fluid motion from global oceanography models to Computational Fluid Dynamics (CFD) which resolve flows at tiny scales. The advantage of these models is that they don't require expensive site surveys and can be modified for any site and used for the prediction of resource, with the inclusion of energy extracting devices in the form of tidal turbines. However these models all require high quality field data for validation. Furthermore, ideally data would be available from a range of sites so that the driving factors of site to site variation can be better understood. One of the fundamental goals of field velocity measurements (and the ReDAPT project of which this work is a part) is to gather data suitable to improve the confidence in these models.

A review of these modelling techniques is outwith the scope of this report, but it is mentioned to highlight the need for high quality turbulent flow data to validate these ever evolving techniques. For more information on use of what flow models are appropriate for which applications see Topper (2010) and for information on turbulent fluid solvers specifically see Nichols (2001).

The need for better understanding of the flow at potential tidal energy extraction sites is recognised by both academia and industry, and was one of the drivers in the formation of the 'Reliable Data Acquisition Platform for Tidal' (ReDAPT) Project. This project was commissioned and funded by the Energy Technologies Institute (ETI), which began in 2011. The central aim of the project is to accelerate the tidal industry and improve market confidence in the technology. A key aspect of this aim is the installation and testing of a 1MW tidal turbine at the European Marine Energy Centre (EMEC) tidal test site in the Orkney isles. This in turn provided an ideal mid-channel depth platform for flow measurement instrumentation. The data from the sensor array is then used as the input and validation of a range of computer models. The ReDAPT project of which this work is a part is discussed in detail in Chapter 3.

For information on BEM work within ReDAPT see Way and Thomson (2011); Way and Collier (2012); for information of the MIKE3 channel model see Stock-Williams and Gunn (2012) and for CFD models see Afgan *et al.* (2014).

2.4 Tidal Energy Site Characterisation

2.4.1 The physics of tidal Flow

The Moon and the Sun

The first recorded knowledge of the drivers for the tides dates back to Pytheas of Massalia, a 4th Century BC Greek explorer and geographer (Diels, 1879). He recognised the connection with the waxing and waning Moon with the rise and fall of the sea. Today the drivers of the tides are well understood. They are the result of the bodies the Moon and the Sun which exert the strongest gravitational forces on the Earth, pulling the Earth and thus the fluids on the surface towards them. The Moon rotates relative to the Earth once every 24 hours and 50 minutes (Knauss, 1978). As the Moon is the strongest of the forces this causes the largest of what are known as harmonic constituents, the M2. The harmonic constituents are the mathematical description of all the time varying forces on the tides, each with a magnitude and phase.

The M2 constituent has a phase causing high and low tides every 12 hours and 25 minutes. The next largest constituent (S2) is based on the position of the Sun relative to the Moon. When the gravitational forces of the two bodies are parallel the tide height is increased (Spring tides) and when the forces are normal the height difference is lessened (neap tides), as illustrated in Figure 2.4. There are at least 37 resolvable harmonic constituents (Knauss, 1978) which include complexities such as the elliptical nature of the Moon's orbit and the angle of the Earth relative to the Moon as it spins. The effect of these constituents is site-specific based on the longitude of the site and the effect of the land bounding it. In order to resolve tidal constituents data must be collected over a period considerably longer than that of the constituent. Thus the longer the deployment the greater the number of constituents that can be resolved and the more accurate the long term predictions.

Types of tidal site

Tidal sites applicable for energy extraction are generally defined as anywhere where flow velocities are sufficiently fast ($> 1 \text{ ms}^{-1}$) for extended periods of time. In order for these velocities to occur, the tides must be constrained by landmasses which cause the flow to accelerate. There are several conditions that can facilitate these speeds and the first stage in site characterisation is to qualitatively define the types of site. There are three basic types of

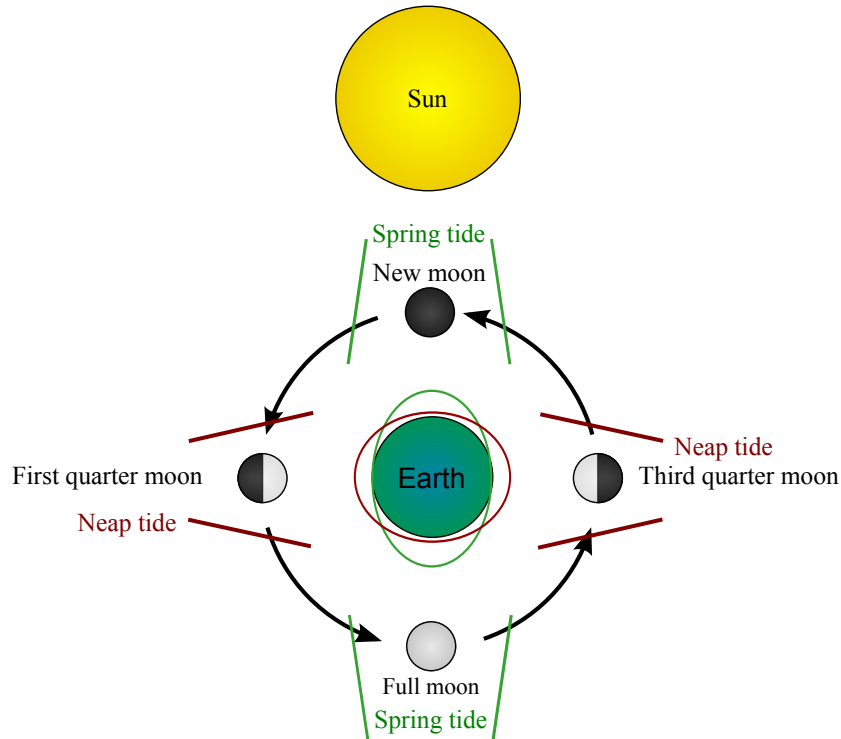


Figure 2.4: Illustration of the effects of the gravitational forces of the Moon and Sun causing Spring and Neap tides. Image adapted from Surachit.

site: tidal basins, symmetrical (also referred to as rectilinear) bi-directional channels and asymmetrical bi-directional channels. To differentiate between the latter two requires an introduction to the principle direction plot.

A principle direction plot presents the velocity magnitudes (as a radius) and directions (as a compass heading transformed to a radial co-ordinate) in polar co-ordinates. The velocity data points are generally 5 to 10 minute temporally-averaged and spatially-averaged over the channel depth (or over the predicted swept area of a turbine). The grouping of these plots helps determine the variation of flow direction at the site. Figure 2.5 gives an example of this from a characterisation study by Gooch *et al.* (2009). Where the fastest flow directions for Ebb and Flood are separated by $\sim 180^\circ$ the flow is described as symmetrical. Where the angle is significantly ($> 10^\circ$) off this value, the flow is described as asymmetrical.

A tidal basin occurs where the tide flows into and out of a reservoir through a single narrow channel. Examples of this include Strangford Loch where Seagen is deployed and Digby Gut shown in Figure 2.6 in Nova Scotia. These sites are ideal as the narrow channels restrict the variability of flow angle thus they have very symmetrical tidal ellipses.

Examples of rectilinear flow include Admiralty Inlet in Puget Sound as per the example in Figure 2.5 and the Fall of Warness Site in Orkney on which the core of this work reports. Rectilinear sites are desirable as turbines can be designed to be mounted in a fixed position,

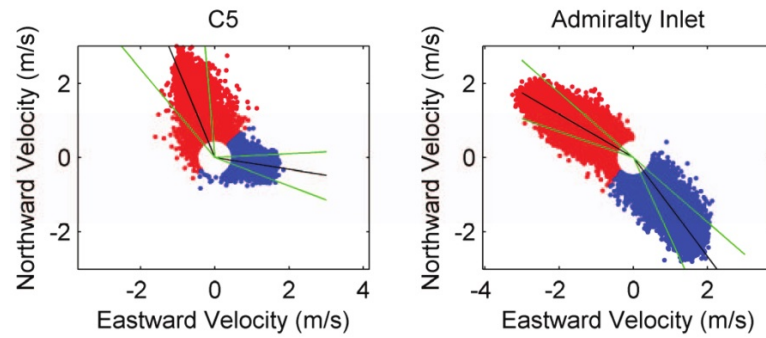


Figure 2.5: Examples of principle direction plots for both asymmetrical (left) and near symmetrical (right) sites from (Gooch *et al.*, 2009).

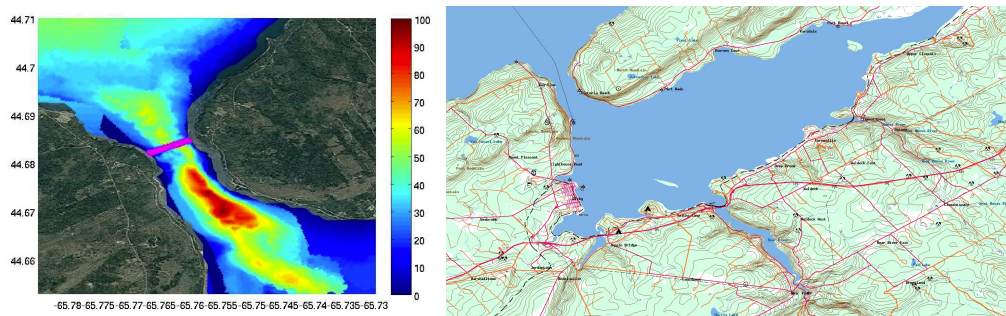


Figure 2.6: Example of a basin Digby Gut in Nova Scotia (right) taken from Yellow Maps and the estimated peak flow velocities (left) taken from Karsten *et al.* (2012).

pitching the blades to capture the tides from both directions. Sites with Ebb and Flood tides offset from symmetrical, like the C5 site example in Figure 2.5, would require a turbine which could yaw to capture both tides. The final detail of this high level characterisation is the equality of the magnitudes of the Ebb and Flood tides at a site. Some sites have one tide which is significantly faster than the other such as certain areas of Ramsey Sound off the coast of Wales (Evans *et al.*, 2013). This is generally undesirable as it usually means one tide is only at an extractable flow speed for a smaller proportion of the time if at all, reducing the availability of the turbine to generate and hence reducing the extractable resource.

Generating power

The complete systems through which tidal energy extraction devices convert the kinetic energy of a fluid to grid-specification electrical energy are complex and vary widely. It is important to underline the most basic principles which flow characteristics will affect. In the majority of devices a hydrofoil is employed, a surface which is designed to maximise the pressure difference across it, creating a force. The component of this force normal to the chord-line of the lifting surface is termed lift and that along chord-line drag. A basic example of this principle is illustrated in Figure 2.7. The equation for lift is:

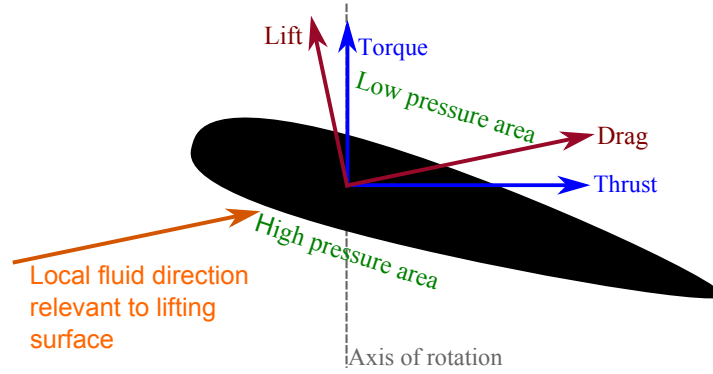


Figure 2.7: Overview of forces on a rotating lifting surface (Burton *et al.*, 2011).

$$F_L = \frac{1}{2} \rho A c_L u^2 \quad (2.1)$$

where F_L is the lift force, ρ is the fluid density, A the planform surface area of the lift surface and c_L is the lift coefficient which will vary for different angles of attack of the blade to the onset flow (Anderson, 2010). The drag force is identically defined but with a different coefficient. The lift force transfers the kinetic energy of the flow to the drive train of the device, a mechanism some times referred to as the ‘prime mover’. For wind and tidal turbines the resultant force of the lift and drag forces in the direction of rotation is termed torque and the force along the flow direction thrust. In the case of a turbine, the torque is used to power a generator (often via a gearbox). The lift and drag coefficients vary with angle of attack which is the resultant flow angle relative to the lifting surface. Thus the lift and drag forces are sensitive to both the magnitude and direction of the onset flow.

The force required to overcome the initial inertia of the device is related to a minimum flow speed, known as a cut-in velocity. In order to optimise the generator design a rated power is selected which is related to a maximum rotational speed of the generator for the common flow speeds at the site. A rated velocity is the minimum flow velocity needed to achieve this. As with most wind turbine designs, techniques such as adjusting the blade angle, are then employed to keep the rotational speed constant at higher flow velocities. The relationship of power extracted to inflow velocity is referred to as a "Power curve". The optimum power curve is site specific, hence the need for accurate long term resource predictions to enable designers to tailor a device for a specific site.

The theoretical extractable power (P) from the flow is defined as:

$$P = \frac{1}{2} \rho A c_p u^3 \quad (2.2)$$

where ρ is the fluid density, A the swept area of the device and c_p is the power coefficient for the specific device, which is limited by the requirement of the fluid to still have momentum on the downstream side of the prime mover, in the same way as the Betz limit is defined for wind (Burton *et al.*, 2011). For site characterisation the device specific terms can be removed to define the kinetic power density K (Polagye, 2009), given as:

$$K = \frac{\rho u^3}{2} \quad (2.3)$$

Polagye (2009) suggests a minimum kinetic power density of 1 kW/m² is required to make a site viable.

In reality the flow over a device is in a constant state of flux and thus so are the pressures and resulting lift forces. The response of lifting surfaces to velocity fluctuations is complex and responds to fluctuations of different sizes and magnitudes in different ways (Clark, 2015). This underlies the importance of characterising the turbulent flow at tidal sites across a range of scales.

Turbulent flow

Recorded observations of turbulent flow structures data back as far as Da Vinci (Richter, 1970) who observed that flowing water caused eddies to form. Pope (2000) describes a turbulent flow as one which “*varies significantly and irregularly in both position and time*”. Generally this is found in flows whose Reynolds number is above 4000 (Çengel and Turner, 2005). The equation of the Reynolds number, which is a ratio of the inertial to the viscous forces in a flow, is given as:

$$Re = \frac{\rho \bar{u} D_h}{\mu} \quad (2.4)$$

where μ is the dynamic viscosity of the fluid and D_h is the hydraulic diameter which, for an open top rectangular cross section channel, is given as:

$$D_h = \frac{area}{perimeter} = \frac{2 \cdot \Delta y \cdot \Delta z}{2 \cdot \Delta z + \Delta y} \quad (2.5)$$

where Δy is the channel width and Δz the depth (Çengel and Turner, 2005). Most tidal channels are well above this number, for example; a representative cut in speed for a commercial turbine of 1 ms⁻¹, a hydraulic diameter of 91 m (representative of a rectangular cross-section tidal channel 1 km wide and 50 m deep) the Reynolds number would be 9.1×10^7 .

The most basic explanation of the physical process which causes a flow to become turbulent is due to the friction caused by water flow at the seabed. The flow infinitely close to this boundary

layer is $\sim 0 \text{ ms}^{-1}$ and, with the higher flow speed away from this boundary, causes a gradient in the flow velocity. This gradient causes the faster higher flow to ‘spill over’ the lower flow causing large turbulent eddies to form. These large eddies then transfer energy via inertia to increasingly smaller eddies down to the scale where viscous forces dissipate the kinetic energy to heat. This effect is increases with the roughness of this bottom boundary layer and with the velocity of the ‘free’ flow.

The rate at which large eddies transfer energy to smaller scales is captured in the dimensional analysis work of Kolmogorov (1962) and the minus five-thirds law according to:

$$E(k) = c_k \varepsilon^{2/3} k^{-5/3} \quad (2.6)$$

where $E(k)$ is the kinetic energy per unit mass per wavenumber, c_k is a constant, ε is the dissipation rate of kinetic energy and k is the wavenumber which assuming a frozen turbulence field can be defined as:

$$k = \frac{2\pi f}{\bar{u}} \quad (2.7)$$

where f is frequency and \bar{u} is the mean velocity over a period of stationarity (T_{stat}) (Kolmogorov, 1962).

This transfer of energy ratio is part of what is known as the turbulent cascade and the $-5/3$ slope region is known as the inertial sub-range. The turbulent cascade covers all regions of turbulent motion and a diagram illustrating the various scales is presented in Figure 2.8. In tidal site analysis there have been studies and measurement of the magnitude of turbulence. However, there is uncertainty regarding the size and effect of the largest turbulent structures in the flow, how much kinetic energy they contain and what their impact on devices will be. It has been estimated that the scales of turbulence in tidal sites would be approximately one third the channel depth (Blackmore *et al.*, 2011). Studies by Kilcher *et al.* (2014) of lengthscales have found an average streamwise integral lengthscale of approximately 17 m for a 55 m deep channel for a site (Admiralty Inlet) with flow speeds of 1.5 ms^{-1} which supports this estimate. In addition, the smaller scales of turbulence are thought to affect lift and drag of blades as discussed in Section 2.4.1.

A final important theory in turbulence measurements is that of the ‘frozen field hypothesis’ developed by Taylor (1938). It is an assumption that the largest turbulent structures evolve significantly more slowly than they are advected and thus the flow past a given point can be considered as a snapshot of the structure moving with velocity \bar{u} . The metrics used to quantify turbulence are discussed in detail later in this chapter in Section 2.7.

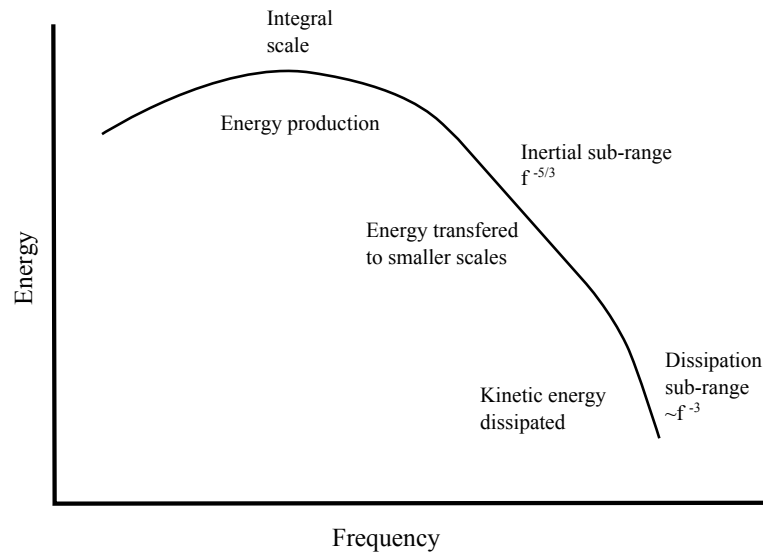


Figure 2.8: Illustration of the energy cascade, highlighting the most important regions in tidal site characterisation. Adapted from Pope (2000).

2.5 Site Characterisation Instrumentation

There are a wide variety of established techniques for measuring fluid velocities. This section introduces these techniques, the theory behind them and their main advantages and relative drawbacks. Acoustic sensors which are used throughout this work are discussed in more detail in Section 2.6.

2.5.1 Tide gauge

A tide gauge or water level meter, is a sensor which records surface elevation while averaging out variation due to waves. Sensors use a variety of technologies including pressure which are mounted on the seabed and radar which are mounted on the shore. If the cross-section of the channel is known this elevation can be used to inform the average volume flowrate. It cannot give information about variation of flow with depth or any smaller scale motions. Figure 2.9 shows an example of a pressure sensor tide gauge.

2.5.2 Velocimeters

Rotational anemometer/impeller

For the wind industry one of the most common velocity measurement devices is a rotational cup anemometer, a positive displacement meter which responds to the fluid causing multiple cups to rotate around a fixed axis. This is a cheap and effective system that calibrates a rotational speed to a given wind speed. It captures wind from all directions so is often paired with a vane to give directional information. A common adaptation for in oceanography is to replace the rotating cups with an impeller mounted on a directional vane such as in the device shown in Figure 2.10. For tidal applications it is a significant challenge to mount such a device in the appropriate part of the water column.

Hot wire/film

Hot wire anemometers use a heated wire which is cooled by convection as fluid flows over it. The resistance of the wire changes with temperature and the wire is installed in a Wheatstone bridge and calibrated such that the voltage output causes a change commensurate with flow velocity. Hot wire probes have been used in tidal turbulence analysis such as in work by Grant (1958). However, the sensor calibration can drift and it is only capable of measuring a single point. Multiple wires can be used to calculate flow velocities in multiple directions, but the individual filaments can not be completely isolated from convection due to off angle flow. An example of a single axis hot wire anemometer is shown in Figure 2.11.

Electromagnetic induction sensors

As water (and in particular brackish water) has electrical conductive properties, it is able to influence magnetic fields (Fondriest, 2015). Electromagnetic induction sensors use this effect by creating a magnetic field which, as the water flows through it, induces a potential difference by an amount directly proportional to the flow velocity perpendicular to the flux lines. Multiple electromagnetic fields can resolve fluid flows across multiple axes. The diagram in Figure 2.12 highlights an example of how this flowmeter works, in this example measuring fluid in a pipe. The direction of the electro-magnetic fields generated by these devices is often alternated inducing a voltage that also changes in polarity which counteracts interfering voltage effects. This technique has also been adapted for tidal velocity measurements, but is limited to a single point measurement at the location of the sensor. As an example, the Valeport 803 ROV Current Meter can measure at 16 Hz with an accuracy of 0.01 ms^{-1} (Valeport, 2001).



Figure 2.9: Example of a tide gauge from Valeport. Image: Valeport (2001)



Figure 2.10: Example of a impeller mounted to a directional vane. Image: Valeport (2015)

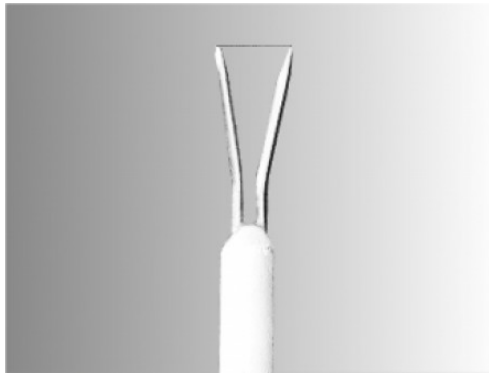


Figure 2.11: Example of a single access hot wire probe. Image: SMV-Tec

Magnetic Flowmeter Operating Principle

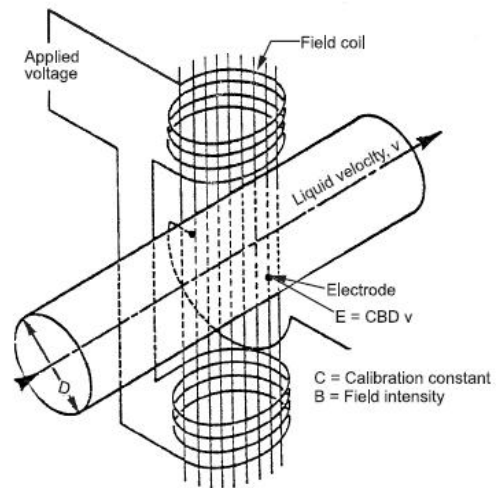


Figure 2.12: Principle of operation of a magnetic flow meter. Image: Piping-engineering.com

2.5.3 Differential pressure sensors

Pressure driven flow meters cover a whole range of sensor technologies that would exceed the scope of this technology review. Included are a subset of those most applicable to the tidal industry. Most flow sensors work on Bernoulli's principle whereby a moving fluid will create a pressure difference that increases proportionally with the square-root of the velocity, assuming no changes to the ambient pressure. This is often measured by the difference between the pressure due to the fluid flow (the dynamic pressure) and the pressure of the stagnate flow (the static pressure). These devices are generally referred to as differential pressure gauges such as the Pitot tube, commonly used in the aerospace industry.

Piezo-electric probes

A piezo-electric sensor is composed of a solid surface (often a ceramic) that generates an electrical charge when subjected to mechanical strain. As the pressure increases due to the dynamic pressure the strain on the probe surface will increase creating a voltage. Multiples of these probes at different angles can be used to measure the velocity fluctuations in multiple axes. One advantage of these devices is that the probe face can be very small allowing measurements of the smaller scales of turbulent flow, particularly as they can operate at sample rates of up to 200 Hz (Rockland Scientific). A drawback is that they do not measure the mean velocity thus a secondary sensor is required to give a reference flow velocity for these fluctuations. Similar devices can use a piezo-resistive strain gauge where a deformable diaphragm is strained by dynamic pressure. When attached to a Wheatstone bridge they can be calibrated to calculate a change in output voltage to correspond to a commensurate change in velocity.

2.5.4 Sensor mounting solutions

Tidal channel flows vary with separation from solid boundaries, where the frictional processes cause stresses which cause a velocity gradient (Thorpe, 2007). With tidal channels being of the order of 50 m deep flow sensors must be mounted ~ 25 m from either the sea surface or the seabed. In the absence of an existing superstructure in the channel to mount to, there are various solutions for taking measurements at the required depths. A selection of the most common solutions are presented : Seabed gravity frames, buoy suspended lines, boat mounted and sub-sea gliders.

Seabed gravity frames and boat mounted systems require instruments that can measure remotely to the ~ 25 m range. A gravity frame is a heavy non-buoyant structure designed such that the frictional force of the frame exceeds the drag force caused by the flow over it. Instruments are sometimes mounted in a two axis of rotation gimbal to allow them to sit horizontal on an uneven seabed. However, the trade off is that forces induced by the fluid (which is often very turbulent in the boundary layer) on the sensor can cause extreme pitching and tilting, thus the stiffness of gimbals (which can be affected by bio-fouling over long deployments) is important. The effect of small dynamic pitching and tilting on velocity measurements can be corrected for in post processing if they are accurately measured. Boat mounted sensors require correction for the boat's pitch, roll and yaw in a similar fashion but with the additional requirement of measuring and subtracting the boat velocity. Small boat designs (like the one shown in Figure 2.13) can also be tethered to a mooring system and used as a surface measurement platform.

An autonomous Underwater Vehicle (AUV) is another option for mounting flow measurement equipment. However, it is only capable of operating in limited flow speed environments. A buoy suspended line requires a gravity base as previously described as a tether point for a buoy which provides the up-force and resulting tension in a line to which measurement sensors can

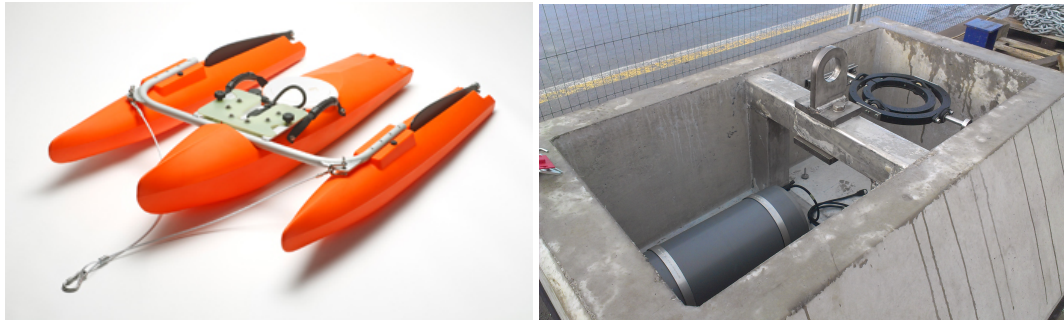


Figure 2.13: An RDI RiverRay DBDP boat mounting (left) (Image: RDI) and a gravity base with gimbal mounting for a DBDP as used on the ReDAPT project (right).

be mounted. An acoustic release can be employed to release the equipment without needing to retrieve the gravity base.

Examples of these mounting systems are shown in in Figures 2.13, 2.14 and 2.15. All these solutions (with the exception of a non-gimbaled gravity base) have multiple degrees of freedom for the sensor to move which is undesirable and will affect the velocity measurements. This is frequently achieved with a combination of tilt sensors, to measure the instrument's angle in the three rotational degrees of freedom and/or accelerometers to measure the speed of the sensor's movements in up to 6 degrees of freedom. This allows correction of the magnitude of the initial measurement and the direction of resolved velocity vectors where required.

2.6 Sub-sea Acoustic Velocity Sensors (Doppler Sensors)

The final sensor technology discussed here for measuring flow velocities, is acoustic Doppler velocimetry. These sensors are the most commonly used in tidal channels as, unlike all the other technologies discussed, they can measure the flow remotely at a significant range from the device. This means they can be mounted on the seabed, which is the mounting option in the lowest flow speeds and furthest removed from the surface waves, and still give hub-height flow measurements. This section gives an overview of the technology and the variety of available device configurations which utilise it.

2.6.1 Doppler theory

A Doppler sensor has a transducer that transmits an ultrasonic pulse or 'ping' into the water. The path of this pulse through the water is referred to as the 'beam'. As this pulse passes through the water it is reflected by particulate matter (of the order of 1-30 mm in size) suspended in the water. These particulates are known as back-scatterers. As the reflected pulse is not reflected by the water itself, it is a key assumption that the back-scatterers move with the same velocity as the water. At the end of transmitting the pulse, the transducer acts as a receiver

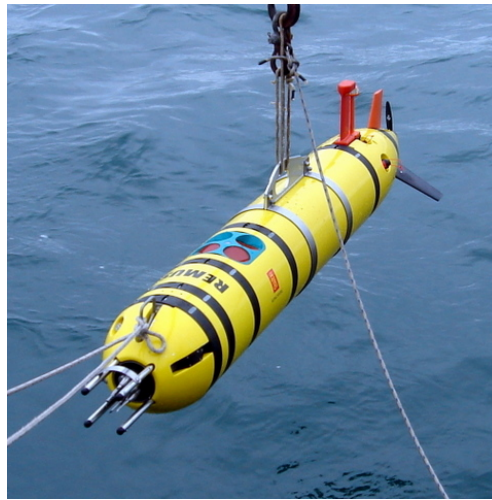


Figure 2.14: Shear probe and DBDP mounted on an AUV. Image: (Rockland Scientific)

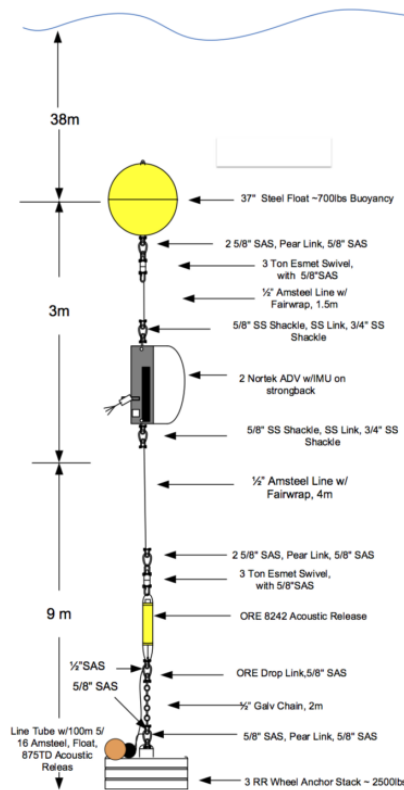


Figure 2.15: Buoy and gravity base tethered sensor mounting (Kilcher *et al.*, 2014).

and listens for the response from the reflections back along the beam axis. The reflected beam will be affected by an effect known as the Doppler shift.

The Doppler shift is a phenomenon discovered by Austrian physicist Christian Doppler. It states that if the source of a wave is moving relative to an observer, the observed wave is compressed or expanded as a function of the velocity component along the observer's line of sight (Gordon, 1996). A commonly given example of this is a siren on an ambulance which is raised in pitch (frequency) as it comes towards an observer (as the waves are compressed) and falls in pitch as it moves away as the waves are stretched.

The change in frequency ratio is proportional to that of the flow speed relative to the speed of sound in that medium. The relation is given as:

$$f_d = f_{pulse} \left(\frac{u_{beam}}{C} \right) \quad (2.8)$$

where f_d is the difference in frequency between the transmitted and received pulses, f_{pulse} is the transmitted pulse frequency, u_{beam} is the fluid velocity along the beam axis and C is the speed of sound in the appropriate medium, in this case sea water. It is this frequency shift in the reflected signal that allows Doppler velocimeters to estimate the velocity along each beam.

2.6.2 Range gating

The acoustic pulse will theoretically travel on indefinitely through the water, with the signal amplitude decreasing as an inverse square of distance. As the beam travels it will continuously be reflected back with weaker and weaker pulses returned towards the transducer. This continuous returned signal has to be processed in sections in order that each section is representative of a small volume of water along the beam path. The receiving phase of the transmit-receive cycle is divided into even sections based on a fixed time period. This time period corresponds to the reflections from even measurement volumes. Each of these volumes is referred to as a range bin. This process is illustrated in Figure 2.16.

The gap between the end of the transmitting of the pulse and the start of the first listening period is known as the 'blanking distance'. Figure 2.16 shows that the cells are weighted towards the centreline of the measurement volume for a cell. In reality the beam will spread out with separation from the sensor and thus measurement volumes increase slightly with range.

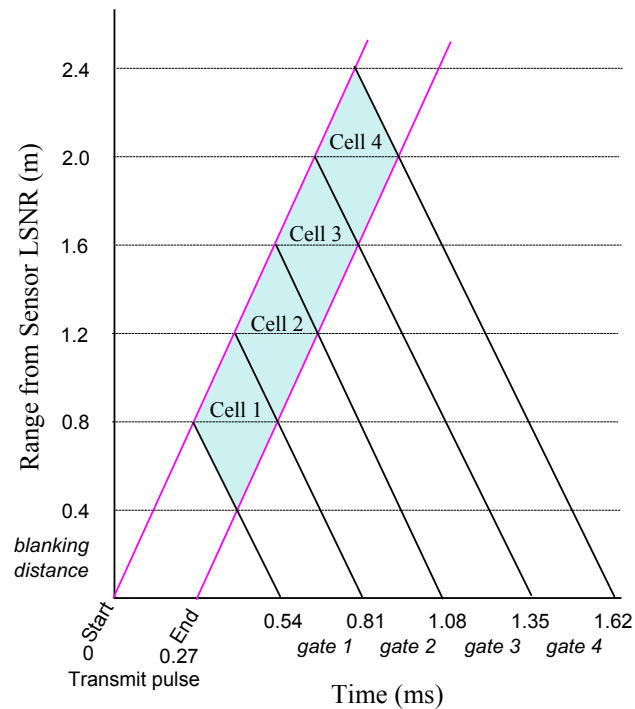


Figure 2.16: Example of range gating for a sensor with a bin size and blanking distance of 0.4m. Image adapted from Gordon (1996).

2.6.3 Design variations

Doppler sensors come in a variety of configurations for a range of applications. Some sensors have only a single range bin, others can have up to one hundred depending on the design. The general design trade off is range versus resolution at the expense of increased random error. A lower frequency pulse will travel further through the water but requires larger cell sizes to process the received pulse without increasing noise. A higher frequency instrument can resolve very small spatial scales and has a lower random error associated with it, but the range can be limited to a few centimetres.

In addition to range, the main design variation is the number of transducers used. A single beam can only resolve one velocity component along the angle of the beam. With three beams, three velocity vectors can be resolved, although many designs employ a fourth beam in order to generate an additional vertical velocity estimate. Having two measurement of the same velocity vector allows an error velocity to be calculated which is a good indicator of measurement quality. Finally, where wave measurements are of interest an additional vertical beam can be used to track the surface elevation.

Subsea Doppler sensors can be split into two basic types: Diverging Beam Doppler Profilers (DBDP) and Acoustic Doppler Velocimeters (ADV). DBDPs are short to long range field sensors that employ three to five transducers, each of which act both as a transmitter and a

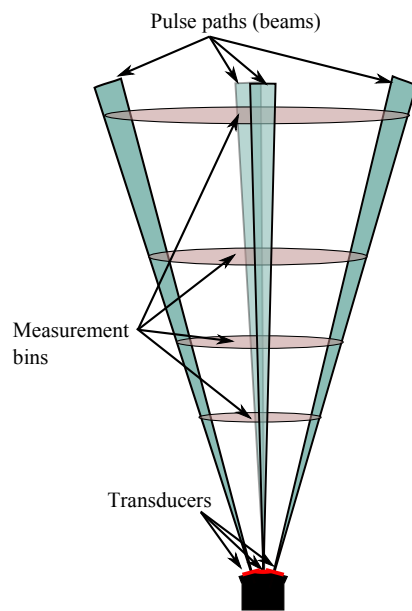


Figure 2.17: DBDP beam geometry.

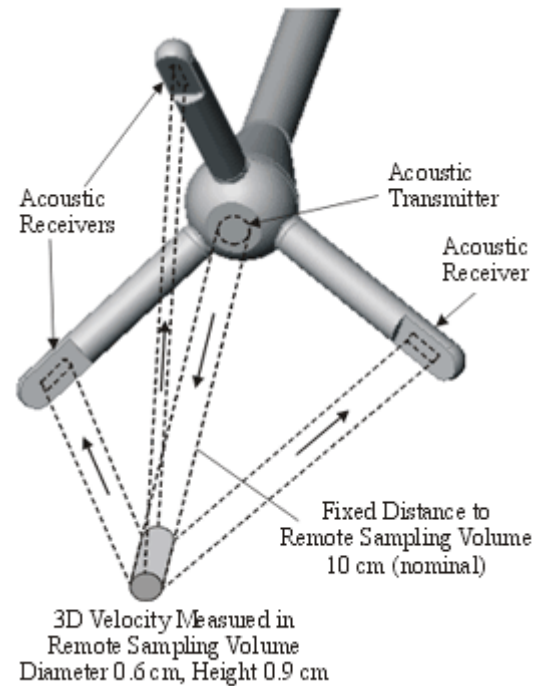


Figure 2.18: ADV beam geometry. Image: SonTek.

receiver. They are able to resolve three velocity vectors and are available in configurations optimised for different range and accuracy trade offs: from 8 Hz sample rate, 2 MHz pulse frequency over 1 m range (Nortek-AS, 2015a), to 1 Hz sample rate, 190 kHz pulse frequency over 300 m (Nortek-AS, 2015b).

The ADV has one transmitting transducer and three to four receiving transducers around it, all angled to focus on a single measurement volume, generally resolved into a single cell as illustrated in Figure 2.18. They can operate at high sample rates (up to 200 Hz) but are limited in range to $\sim 3 - 10$ cm (Nortek-AS, 2015c). Thus if they are to be used in mid-depth in a tidal channel a solution to mount them at the appropriate depth must be devised.

In addition to these two sensor types, single beam variants of the DBDP have recently been released. These are designed for situations where they can be easily mounted in the centre of the water column such as on a tidal turbine. These sensors were the focus of this work.

ADVs utilise a bi-static system, where a single transducer transmits the pulse and a series of other transducers inclined towards the measurement volume, listen for the reflected pulse. Figure 2.18 shows an example configuration for such a sensor. Having a single pulse removes the risk of cross-talk between pulses and the single measurement volume reduces the range over which the sensor requires the flow to be homogeneous.

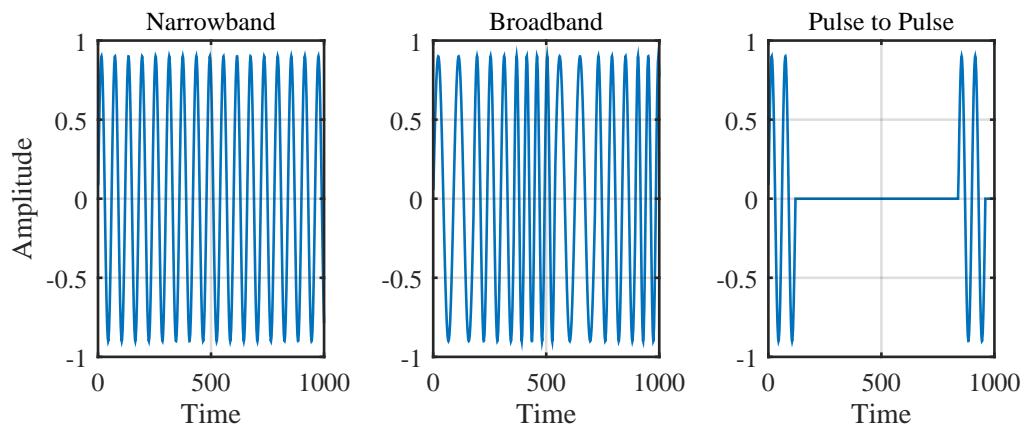


Figure 2.19: Example of different acoustic pulse types.

2.6.4 Pulse types

There are three types of pulse generally used in these devices, each with their advantages and drawbacks. These are: narrowband, broadband and pulse-to-pulse. Narrowband consists of a single frequency pulse, Broadband is formed from a repeated series of frequencies and pulse to pulse is performed by one short pulse then a gap long enough for any ‘ringing’ effects to dissipate then a second pulse is transmitted. An illustration of these different pulses is given in Figure 2.19. Narrowband pulses work over the longest range, while pulse to pulse only works over short distances but with lowest noise and broadband pulses are a trade off between these characteristics (Lohrmann, 2015).

Since 1991 Doppler sensors have greatly improved with the use of ‘broadband’ technology in many instruments, as supposed to the precursor ‘narrowband’. A broadband pulse is composed of a repeated pattern of changing frequencies allowing a more accurate assessment of the Doppler shift compared with the single frequency narrowband pulse. This advancement allows the velocities to be resolved with far greater accuracy. Device developer RDI, claims that it reduces the variance in measurements by a factor of ~ 100 (Gordon, 1996). There is a third type of pulse processing which is called ‘coherent’ where two or more very short pulses are sent with silence between them to allow any ‘ringing’ of the transducer to dissipate before sending the next pulse or listening for the reflected pulse. Sensor manufacturer Nortek have suggested that this technique reduces sensor noise by up to 4 orders of magnitude compared with narrowband technology, but it is limited to short ranges of $\leq 1\text{m}$.

For a comprehensive guide to the workings of DBDP it is recommended that the reader refer to (Gordon, 1996).

2.6.5 Relative advantages and limitations of DBDPs

A key advantage of acoustic technology, in particular of DBDPs, is the ability to take readings remotely and throughout the water column. Devices can be mounted on the seabed in a relatively fixed position and take three vector water measurements up to the surface. The uncertainty involved with constantly moving floated sensors is high and only gives a single point in the water column. Having a fixed body is often impractical and (if large enough) will impede the flow. This has made DBDP a standard technology for characterising potential tidal sites.

In order to deploy a DBDP a solution for power and data storage must be devised. Most devices use batteries and memory cards, which limit deployment goals. Data readings must often be taken less frequently to maximise the deployment length, which is often desirable as the cost of deploying devices is high. Alternatively a higher data sample-rate can be used at the expense of longevity. The data capture set up along with the range and spatial resolution are decisions site surveyors face to get the most appropriate data for their requirements.

The primary drawback of DBDPs in site characteristics for tidal power, is their limited ability to capture turbulence metrics. This is due to two main factors: Firstly they require a transformation of the measured beam velocities to a Cartesian system. This transformation increases noise and is expected to limit the accuracy of structural information that can be captured. Secondly, the diverging beam configuration requires the assumption that the flow is homogeneous over large scales.

These limitations were the drivers for the development of the Single Beam Doppler Profilers SBDPs. These devices, newly available at the commencement of the ReDAPT project, could be mounted at mid depth to measure the flow with much reduced spatial averaging and no velocity transforms required (depending on mounting orientation).

2.7 Quantifying Tidal Sites

Oceanography is an ancient science as already discussed with the discoveries of Pytheas (Diels, 1879) and turbulence has been studied in earnest since the start of the 20th Century with Taylor (1938), although there is evidence of Di Vinci discussing the phenomenon (Richter, 1970). As the concept of tidal power became pertinent in the 1990s the study of ocean turbulence has become more prevalent. Almost all the studies in this field have employed some sort of acoustic instrumentation, particularly DBDPs, to assess the resource and turbulence.

2.7.1 Use of DBDPs and ADVs

Prior to the development of DBDPs, early work by Grant *et al.* (1962) using hot-wire anemometers and Bowden and Howe (1963) using induction sensors, measured velocity fluctuations in field measurements of the bottom boundary layer. However, since the 1990s Doppler velocimeters have been ubiquitous in tidal analysis.

Early work on tidal site characterisation was conducted by instrument developers. Lohrmann *et al.* (1990) took measurements with an early 307 kHz pulse-to-pulse four beam DBDP, in the North Sea between the Orkney Isles and Norway. Although they were primarily concerned with optimising the instrument they also calculated the Reynolds stresses and Turbulent Kinetic Energy (TKE) of the flow. Lu and Lueck (1999a,b) produced a two part paper on using a DBDP to measure both mean values and turbulence. They developed tests to quantify the homogeneity of the flow to assess the applicability of various techniques as well as quantifying velocity errors. In addition to DBDPs the use of ADVs have also been adopted to assess turbulence measurements. Thomson *et al.* (2010) make a comparison with DBDP measurements, being one of the first to use an ADV for field measurement rather than in the lab.

Other recent papers which utilise Doppler sensors to measure turbulent structures include: Osalusi *et al.* (2009) in Orkney, Milne *et al.* (2013) in the sound of Islay, Thomson *et al.* (2014) at Admiralty Inlet and Togneri and Masters (2012) who assess three different sites using DBDP measurements.

2.7.2 Mean flows: depth profiles

Legrand (2009) recommends that to estimate long term resource, mean velocities should be collected and a harmonic analysis performed. The flow measurement should either be at predicted hub height of a device or averaged over the probable rotor diameter. For early feasibility studies the two largest constituents are sufficient, but for an ‘advanced’ tidal project site assessment, a minimum of 3 months of continuous field data are required, in order to resolve 20 of the Harmonic Constituents. The longer period constituents are of up to 2191 hours and as they combine can cause variation in yield predictions over a period of years. Unfortunately most resource work is project specific and is therefore unpublished.

As tidal channel flows vary vertically as previously discussed, flow measurements throughout the water column are recommended (Legrand, 2009). The tidal industry uses a variety of curves to describe how the flow varies with depth, known as velocity depth profiles. Equation 2.9 gives the general form of the relationship of velocity with depth ($u(z)$):

$$u(z) = \left(\frac{z}{H}\right)^{1/n} \cdot u_H \quad (2.9)$$

where n is empirically calculated, normally in the range of 7 to 10, u_H is the velocity at the surface, z is a point along the vertical axis and H is the total depth (Legrand, 2009).

This is only a rule of thumb and field measurements are recommended. Osalusi *et al.* (2009), took depth profile measurements for the EMEC site, which showed good agreement with the form of 2.9. It should be noted that Equation 2.9 assumes no wind and wave driven surface effects, which would be expected to significantly affect the depth profile in the upper part of the water depth.

2.7.3 Definitions of isotropy and homogeneity

Two concepts that appear regularly in turbulence analysis, particularly with DBDPs are isotropy and homogeneity. Therefore for clarity a quick definition is included.

- Isotropy is defined as being the same in all directions. I.e., if the turbulence at a given point is isotropic it would have the same fluctuation magnitude in the streamwise as in the transverse and vertical.
- Homogeneity is defined as a metric that has the same quantity of a defined area or volume. I.e., if the mean flow velocity at one point is the same 100 m downstream, this quantity can be described as homogeneous over that length.

2.7.4 Quantifying turbulence magnitude and structure

The first metric that needs to be defined in order to derive subsequent turbulence measures is the period of stationary (T_{stat}) of the flow. All turbulence metrics require the assumption that the flow is statistically stationary over the period the metric is being calculated. As, in reality, the flow is always evolving this can only be done in a statistical sense. Thomson *et al.* (2012) looked at a series of periods from 1 to 20 minutes, finding that 5 minutes was the longest period that could be considered stable in terms of mean and variance. It should be noted that this result is based on measurements at only two locations and may be site specific.

Velocity perturbations

As turbulence analysis involves analysis of fluctuations around the mean value \bar{u} , the mean and fluctuations around it must be clearly defined. Here \bar{u} is defined as the mean velocity value along the x vector over the T_{Stat} period. A velocity perturbation u'_n for a single velocity sample (n), is defined as (Pope, 2000):

$$u'_n = \bar{u} - u_n \quad (2.10)$$

with the average perturbation being defined as:

$$u' = \frac{1}{T_{Stat} \cdot f_s} \sum_{n=1}^{T_{Stat} \cdot f_s} u'_n \quad (2.11)$$

where f_s is the sample frequency.

The same equation is used to define the transverse and vertical velocity perturbations v' and w' .

Turbulence intensity

One of the metrics commonly used to quantify the magnitude of turbulence is the Turbulence Intensity (I). This term is adopted from the wind industry as a measure of the magnitude of fluctuation as a percentage of the mean flow velocity. It is defined as the root-mean-square (rms) of the velocity perturbations divided by the mean velocity over a period of stationarity as given by:

$$I = \frac{\sqrt{\frac{1}{3} \langle u'^2 + v'^2 + w'^2 \rangle}}{\bar{u}} \times 100 \quad (2.12)$$

where u' , v' and w' are the velocity perturbations along the three Cartesian vectors and the angled brackets denote an average over T_{stat} to calculate \bar{u} . If the turbulence is assumed to be isotropic (i.e. equal in all directions) only a single velocity perturbation measurement is required (Burton *et al.*, 2011):

$$I = \frac{\sqrt{\langle u'^2 \rangle}}{\bar{u}} \times 100 \quad (2.13)$$

where u' can be interchanged with the velocity component in any direction.

Generally isotropy can't be assumed in such environments. Here the individual turbulence intensity contributions in each directions are independently defined:

$$I_x = \frac{\sqrt{\langle u'^2 \rangle}}{\bar{u}} \times 100 \quad (2.14)$$

$$I_y = \frac{\sqrt{\langle v'^2 \rangle}}{\bar{u}} \times 100 \quad (2.15)$$

$$I_z = \frac{\sqrt{\langle w'^2 \rangle}}{\bar{u}} \times 100 \quad (2.16)$$

noting that the numerator corresponds to the corresponding velocity vector but this is always normalised by the streamwise value.

An alternate expression for the magnitude of turbulence is the Turbulent Kinetic Energy (E_{TKE}) which is based on the standard kinetic energy equation. The key difference between it and the

turbulence intensity is that it is not normalised by \bar{u} . The definition is given as (Thomson *et al.*, 2010):

$$E_{TKE} = \frac{1}{2} \langle u'^2 \rangle \quad (2.17)$$

assuming isotropic turbulence.

Reynolds stresses

To quantify the driving forces that generate turbulence the standard metric set are the Reynolds stresses. First introduced by Reynolds (1895), they are a measure of the shear forces which generate the turbulent flow conditions, again calculated from velocity perturbations. They are defined by the Reynolds stress tensors, for example for the transport of the horizontal fluid momentum in the vertical:

$$\tau_{uw} = -\rho \langle u'w' \rangle \quad (2.18)$$

where τ_{uw} is the Reynolds stress tensor and ρ is the density of the fluid. These stresses are strictly defined as a matrix of three momentum components in the three Cartesian planes. The density term can be omitted (and often is in tidal site characterisation work) for a fluid where the variation in density is negligible (Thorpe, 2007).

Several of the site characterisation reports referred to in this section include a measure of the Reynolds stress including: Grant (1958), Lu and Lueck (1999b) and Stacey *et al.* (1999) who also measured integral lengthscales in the flow as well as Togneri and Masters (2012). Lu and Lueck (1999b) found values of the order of 0.1 Pa at a depth of 15.6 m for a channel with a peak flow of 1 ms⁻¹. Togneri and Masters (2012) using results from peak flows at EMEC (estimated at 3 ms⁻¹) found longitudinal Reynolds stresses of up to 12.70 Pa with smaller (5.12 Pa) transverse values.

Integral lengthscale

The integral lengthscale (ℓ) is defined qualitatively as the average size of the largest eddies in a turbulent flow (Pope, 2000). There are several methods of estimating this value. The most robust method is the Spatial Correlation method, where velocities at multiple points are measured at the same instant in time. The correlation coefficient is then calculated for a range of spatial separations or ‘lags’

$$R(\Delta x) = \frac{\langle (u_x - \bar{u})(u_{x+\Delta x} - \bar{u}) \rangle}{\sigma_u^2} \quad (2.19)$$

where $R(\Delta x)$ is the correlation coefficient, x is a location along the streamwise axis, Δx is a spatial separation and σ_u^2 is the variance of the velocity (Pope, 2000). The integral lengthscale is then calculated via:

$$\ell_x = \sum_{\Delta x=0}^{R(\Delta x)=0} R(\Delta x) d\Delta x \quad (2.20)$$

The integration is only performed on R values up to the first zero axis crossing as recommended by O'Neill *et al.* (2004).

The drawback of this method is that the maximum spatial range must be ~ 7 times that of the desired lengthscale or the value calculated will be biased low (O'Neill *et al.*, 2004). Stacey *et al.* (1999) used this method and found lengthscales of ~ 2 m for a 9 m deep channel.

A variation on this method utilises the timescale (\mathfrak{S}) of turbulence which is calculated from the time based autocorrelation function given by:

$$R(\Upsilon) = \frac{\langle (u_t - \bar{u})(u_{t+\Upsilon} - \bar{u}) \rangle}{\sigma_u^2} \quad (2.21)$$

$$\mathfrak{S} = \sum_{\Upsilon=0}^{R(\Upsilon)=0} R(\Upsilon) d\Upsilon \quad (2.22)$$

where Υ is a temporal lag and other terms are as per Equation 2.19.

Assuming the largest turbulent structures are frozen as proposed by Taylor (1938) the timescale multiplied by the mean velocity advecting the structures will yield the lengthscale as:

$$\ell_x = \bar{u} \cdot \mathfrak{S} \quad (2.23)$$

This method has been used by Kilcher *et al.* (2014) where an ADV suspended in the channel on a buoyant line was used to measure the velocities. The lengthscales for the fastest flow speeds were approximately 17 m for a 55 m deep channel 10.5 m above the seabed at $\sim 1.5 \text{ ms}^{-1}$.

Alternatively the integral lengthscale can be estimated by the maximum turning point of the Power Spectral Density (PSD). The PSD uses a Fast Fourier Transform (FFT) of a de-trended statistically stationary velocity sample defined as:

$$Y(f) = \int_{-\infty}^{\infty} y(t) e^{-i2\pi ft} dt \quad (2.24)$$

where $y(t)$ is a time series, f is the frequency, t is time and $Y(f)$ spectral periodogram. This is

then modified to give the PSD ($S(f)$) via :

$$S(f) = \frac{2}{(L_{FFT})\Delta t} |Y(f)|^2 \quad (2.25)$$

where L_{FFT} is the number of points in $Y(f)$ and Δt is the period (Emery and Thomson, 2001). The maximum turning point of $S(f)$ represents the frequency at which there is most energy (see Figure 2.8) in the velocity, which is by definition the frequency of the integral lengthscale. Assuming the frozen field hypothesis, This can be stated as:

$$\ell = \frac{\bar{u}}{f_{S-max}} \quad (2.26)$$

where the frequency f_{S-max} is the frequency corresponding to the maximum value of $S(f)$, to calculate the integral lengthscale ℓ .

Integral lengthscales can be calculated for any of the Cartesian directions (ℓ_x, ℓ_y and ℓ_z). The magnitude of each term will not be equal. This is discussed in more detail in Chapters 6 and 7.

Turbulent kinetic energy dissipation rate

The turbulent kinetic energy dissipation rate describes the rate at which the viscous forces in the flow transfer the kinetic energy to heat at the smallest scales of the turbulent cascade. There is uncertainty surrounding the effect of such small-scale turbulence effects on of lifting surfaces but it is predicted that they effect the surface boundary layer in terms of both skin-friction drag and the transition point of laminar to turbulent flow over the blade (Clark, 2015).

The slope of the PSD that follows the inertial sub-range slope can also be used to calculate the turbulent kinetic energy dissipation rate. In theory the PSD is related to the dissipation rate by:

$$S(f) = 0.5 \cdot \varepsilon^{2/3} \cdot f^{-5/3} \quad (2.27)$$

where ε is the turbulent kinetic energy dissipation rate, f is the frequency, 0.5 is an empirical factor and $S(f)$ is the PSD (Richard *et al.*, 2013). In practice the measured PSD will also contain an energy contribution due to random error in the signal, which is discussed further in Chapter 4. Regardless, the measured PSD can be used to estimate ε .

Alternatively, Wiles *et al.* (2006) introduced the Structure function, $D(z, r)$ as a method to estimate ε . The structure function which is a version of the two point spatial autocorrelation is defined as:

$$D(z, r) = \overline{(u'(z) - u'(z+r))^2} \quad (2.28)$$

where z is a location or bin along the DBDP beam and r is a separation or lag between two

bins. Calculating $D(z, r)$ from Equation 2.28 for a range of Δr values allows the use of the calculation of ϵ :

$$D(z, r) = c_s^2 \epsilon^{2/3} r^{2/3} \quad (2.29)$$

where c_s is a constant. Thomson *et al.* (2010) showed that for a site in Puget Sound, ϵ could vary in order of magnitude from 10^{-6} Wm^{-3} at slack water to 10^1 Wm^{-3} at peak flow velocities.

2.8 Reducing Measurement Uncertainty

In addition to post-processing resource and turbulence metrics, an important field of study for tidal site characterisation is reducing uncertainty associated with instrument error. Errors are ubiquitous in any measurements but provide some unique challenges in using acoustic instruments. The two main types of error are defined as random error, fluctuations around the mean, and systematic error or bias where the measured mean is offset from its true value (Smith, 1999). Acoustic instruments are an inherently noisy technology and in a field where measuring fluctuations around the mean are an important factor, this means identifying and minimising random errors are of primary importance.

Lhermitte and Lemmin (1990) produced a report on calculating the noise in these devices and there has been research in the United States at sites centred around Puget Sound. This work started with directional assessment of sites (Gooch *et al.*, 2009), then went on to quantifying turbulence (Thomson *et al.*, 2010; Harding *et al.*, 2011; Thomson *et al.*, 2012), then building on this by developing techniques to remove instrument noise to improve reading of the high frequency turbulent fluctuations (Durgesh *et al.*, 2014; Richard *et al.*, 2013).

A key method for investigating noise involves the PSD function described in Equation 2.25. Assuming $S(f)$ follows the $-5/3$ slope according to Kolmogorov's Theory of the Turbulent Cascade, and that noise is white and thus distributed equally over the frequency range, there will be a point where the energy due to noise is significantly greater than that in the turbulent scales of motion. At this point the slope of $S(f)$ will tend to zero. The area under the $S(f)$ value of this zero gradient across the frequency range serves as an estimate of the variance attributable to noise (σ_{noise}^2) in the signal. This is explained in greater detail in Chapter 4.

2.9 Chapter Summary

This chapter has underlined the drivers for tidal energy extraction and the challenges surrounding this emerging technology. It has also detailed the reasons site characterisation in this field is important and challenging. The strengths of acoustic Doppler profilers for measuring the velocities at such sites has been argued and the metrics that can be utilised at these sites cited, including results from previous characterisation work at various sites. The motivation for use of single beam Doppler profilers, with their expected advantages of DBDPs has been outlined.

In this next chapter the specific instrumentation available and experimental setup for this work is explained. It gives an overview of the ReDAPT project and how this work fits in that wider context.

Overview of the ReDAPT Project

3.1 Chapter Overview

The work presented formed part of a wider, multi-faceted, multi-partner project. An understanding of the role of the author, and how the work presented in this thesis fitted into the wider project goals, is essential for the reader to appreciate the specification of instrumentation, limitations of the experimental work and other constraints relevant to the work presented. This chapter gives an overview of the project structure and the sub-projects and goals relating to each of the partner organisations. It also details the standard experimental set up which was used to gather the data used in the analysis in this thesis.

3.2 ReDAPT Project Aims

The ReDAPT (Reliable Data Acquisition Platform for Tidal) project is a UK-based consortium commissioned and funded by the Energy Technologies Institute (ETI), led by Alstom Ocean Energy and including Plymouth Marine Laboratory (PML), Det Norske Veritas - Germanischer Lloyd (DNV GL), the University of Edinburgh (UoE), Électricité de France (EDF) Energy, E.ON, and the European Marine Energy Centre (EMEC). The project aims to install and test a 1MW tidal turbine at the EMEC full-scale tidal test site in the Orkney Isles, illustrated in Figure 3.1, delivering detailed environmental and performance information not previously achieved at this scale in real sea conditions.

3.3 Project Structure and Participants

The ReDAPT project as a whole was managed by Alstom. The project is subdivided into four sub-projects:

- The machine sub-project centred around the turbine;
- The environmental sub-project ;
- The modelling sub-project;

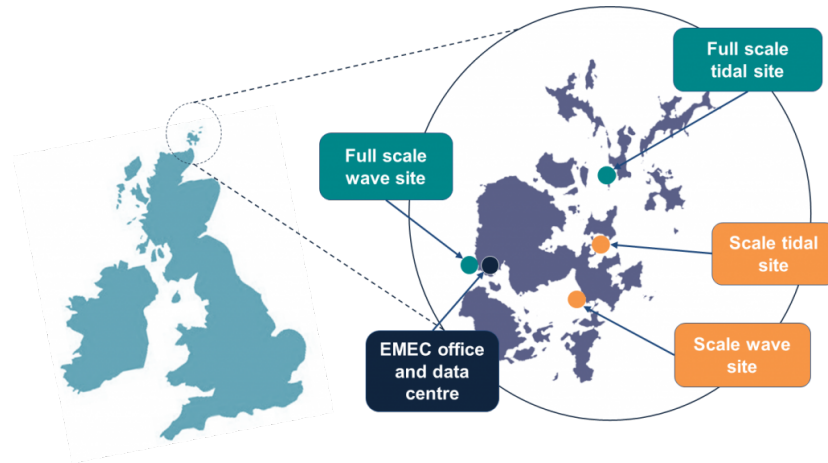


Figure 3.1: Location of EMEC test sites. The Alstom 1MW turbine was deployed at the full scale tidal site. Image from: EMEC (2015).

- The project management sub-project.

Each of these is led by a different project partner. Within these, there are work-packages which have project deliverables associated with them. This section gives a brief overview of the overall project structure with detail aimed at the modelling sub-project which encapsulated the vast majority of the University of Edinburgh’s work.

It should be noted that two of the partner organisations were involved in mergers over the course of the project. Tidal Generation Limited which was a wholly-owned subsidiary of Rolls Royce was acquired by Alstom and merged into their ocean energy division. Garrad Hassan was acquired by Germanischer Lloyd who were then in turn merged with Det Norske Veritas. Here the organisations are referred to by their current titles throughout.

3.3.1 Project management

The goal of the project management sub-project was to co-ordinate the different partners and technical activities, to set and work to (and where necessary update) target completion dates and to ensure a safe and productive working environment throughout the project. The main work packages within the project management sub-project are listed in Table 3.1.

Participants	Alstom Ocean energy (Leader) with UoE, EDF, E.ON
Main Work Packages	<ul style="list-style-type: none"> • MP1 Manage programme and technical aspects of project • MP2 Incorporate lessons learnt from 500kW machine • MP3 Develop tidal stream course material • MP4 CDM coordination, HS&E support

Table 3.1: ReDAPT Sub-project MP – Project Management work packages.

3.3.2 Machine

The machine sub-project covered the design, build, installation, commissioning, operation and ultimately the decommissioning of the Alstom DeepGEN iv turbine. The main work packages associated with the Machine sub-project are listed in Table 3.2.

Participants	Alstom Ocean Energy (Leader) with DNV.	
Main Work Packages	<ul style="list-style-type: none"> ● MC1 Design 1MW machine ● MC2 Procure components for fully instrumented 1MW tidal turbine ● MC3 Obtain GL Level C Prototype Certification ● MC4 Develop SCADA system ● MC5 Assembly and shoreline test programme ● MC6 Install and operate turbine on grid-connected foundation ● MC7 Generate and publish public domain data ● MC8 Develop certification design guidelines with DNV GL ● MC9 Develop standards and protocols ● MC10 Develop EHM system recommendations ● MC11 Supply Chain Report 	

Table 3.2: ReDAPT Sub-project A – Machine work packages.

3.3.3 Environment

The environmental sub-project was split into two parts. PML designed and conducted experimental work into anti-fouling coatings. This involved the deployment of two benthic landers as well as mounting several panels of coating on the turbine nacelle. EMEC originally had work packages relating to radar coverage of the turbine with the goal of capturing large mammal interactions. However, the work packages affiliated with that line of work were removed during the course of the project. The original list of work packages within the Environmental sub-project are listed in Table 3.3.

Participants	EMEC (Leader) and PML	
Main Work Packages	<ul style="list-style-type: none"> ● ME 1.1 Procurement of the radar system ● ME 1.2 Deployment of the radar system ● ME 1.3 Year 1 Monitoring ● ME 1.4 Year 2 Monitoring ● ME 1.5 Year 3 Monitoring ● ME 8 Anti fouling systems for tidal & wave energy devices 	

Table 3.3: ReDAPT Sub-project ME – Environment work packages.

3.3.4 Modelling

The modelling sub-project involved three different types of modelling work conducted by three different partners. The University of Manchester (sub-contracted by EDF) conducted CFD of the turbine for two specified flow conditions. This was done both to validate the turbulence modelling techniques used and to assess the accuracy of the predicted blade loads. DNV-GL used flow measurements to adapt and validate their blade element momentum based design tool ‘Tidal Bladed’. E.ON constructed a MIKE3 model of the wider channel bounded by the tide gauge deployments.

Participants	EDF (Leader)with UoE, E.ON and DNV GL
Main Work Packages	<ul style="list-style-type: none"> • MD1 Turbulence modelling (led by EDF) • MD2 Characterisation of far field boundary conditions (led by UoE) • MD3 Near field flow characterisation (led by UoE) • MD5 Channel flow modelling (led by E.ON) • MD6 Validation of Tidal Bladed (led by DNV GL)

Table 3.4: ReDAPT Sub-project MD – Model work packages with UoE lead sub-packages highlighted.

All these modelling packages required accurate flow data on a range of scales, from the surface elevation across the channel to the turbulence fluctuations. The University of Edinburgh’s work on ReDAPT was centred around this role and the two work packages highlighted in Table 3.4.

3.4 University of Edinburgh: Scope of Work and Time-line

The University of Edinburgh’s remit within ReDAPT covered two work-packages: MD2 – Characterisation of Far Field Boundary Conditions, specifying appropriate instrumentation and methodology to measure inflow and outflow through the channel; and MD 3 – Near Field Flow Characterisation, specifying appropriate instrumentation and methodology to generate and iterate a parametric description of the near field site. The central aim of this work was to measure and characterise the tidal flow surrounding the Alstom 1MW turbine at the far (~ 8000 m) and particularly focusing on the detail at near (~ 50 m) scales. The turbine is located within EMEC’s tidal test site in the Fall of Warness in the Orkney Isles, illustrated in Figure 3.4. The data gathered was used both to improve understanding of the flow environment, through deliverables relating to near and far flow characterisation, and to provide input parameters to a variety of numerical modelling activities being conducted by project partners.

This work spanned 4 years, 2 turbines and 8 separate turbine deployments with up to 22 acoustic instruments. Table 3.5 lists the project deliverables that the UoE was responsible for

and Table 3.6 gives a time line of the different turbine deployments (starting with a preliminary campaign centred around the pre-existing 500kW turbine) and marine operations over which data was gathered. Before each turbine deployment there was a period of procurement followed by a refit of the sensors and, finally, alterations could be made to the instrument set up. Between deployments the turbine was lifted onto a stand at Alstom's quay-side facility on the Orkney mainland.

Deliverables	Date delivered
MD2.9 Instruments acquired and frames built	June 2011
MD2.10 Existing ADP data sets prepared and delivered	August 2011
MD2.11 Far-field instrument deployments in support of channel flow modelling	October 2011
MD3.2 Instruments specified & procured.	July 2011
MD3.4 Report: Interim parametric model	January 2012
MD3.8 Report: Characterisation of near field turbulence	September 2015
MD3.15 Measurement campaigns completed	May 2014

Table 3.5: UoE led MD2 and MD3 project deliverables

Activity & Description	Date
Tide Gauge Deployments Far field velocity measurements in and out of the wider channel.	Jul 2011 - Aug 2011
500kW Turbine Deployment First data gathering from deployed turbine. Deployed with 7 acoustic instruments.	Feb 2012 - May 2012
1MW Turbine Deployment 1 Initial 1MW turbine deployment featured bespoke top and rear instrument frames as well as a sensor mounted on the nose. Power issues meant no data was collected during this deployment.	Jan 2012
1MW Turbine Deployment 2 Second Turbine Deployment	Feb 2012 - Mar 2012
1MW Turbine Deployment 3 Third Turbine Deployment	Jun 2012 - Jul 2012
1MW Turbine Deployment 4 Fourth Turbine Deployment	Oct 2012 - Dec 2012
1MW Turbine Deployment 5 Fifth Turbine Deployment	Apr 2014 - May 2014
1MW Turbine Deployment 6	Jun 2014 - Aug 2014

Sixth Turbine Deployment	
1MW Turbine Deployment 7	Sep 2014 - Jan 2015
Seventh Turbine Deployment	

Table 3.6: Time-line of turbine and associated instrumentation deployments.

3.5 Instrumentation and Project Experimental Set-up

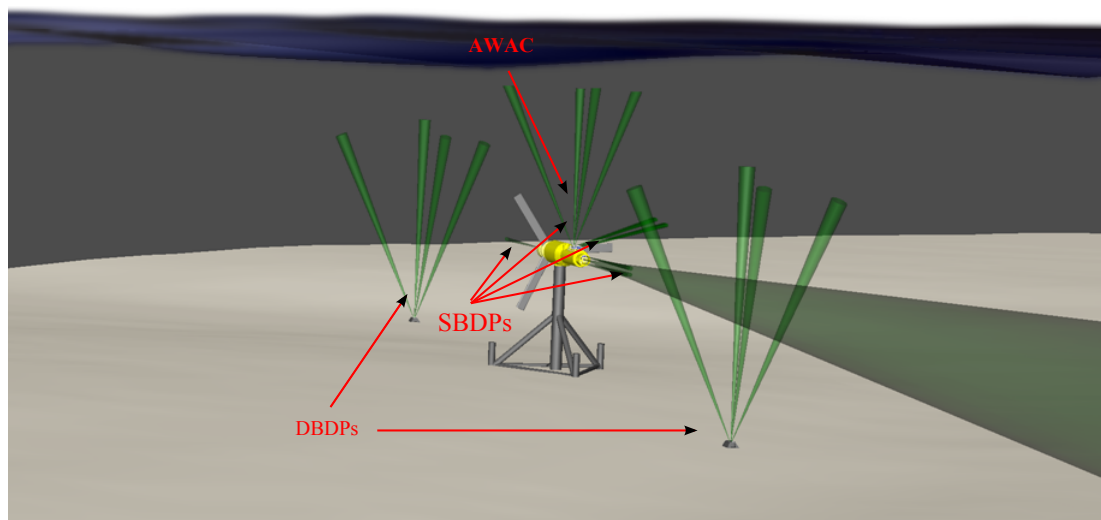


Figure 3.2: Illustration of standard acoustic instrument setup. Green beams represent the directions of the acoustic beams of the Doppler velocimeters.

A basic instrumentation methodology for turbine deployments was devised with two diverging beam doppler profilers (DBDPs), one either side of the turbine in-line with the expected principal flow direction, to provide un-interrupted depth profile velocity measurements. One acoustic wave and current meter (AWAC) was mounted on top of the turbine to measure waves and turbine to surface depth-profiles. This could then be used to investigate the correlation of the depth profile with that of the up-stream and down-stream stand-alone DBDP measurements. Single beam Doppler profilers (SBDPs) were directed along the primary, transverse and vertical axes (relative to the turbine nacelle) allowing the measurement of velocity, turbulence magnitude and turbulence scale along each of the Cartesian vectors of the flow. Where possible more than one SBDP was placed on each axis to assess spatial variation and provide redundancy. Figure 3.2 provides an illustration of the standard instrument configuration.

The turbine has the ability to yaw through approximately 270° . This allows the sensors to be oriented at a variety of angles. Figure 3.3 shows how the turbine yaw is measured as a rotation about the z axis. Generally the turbine nacelle was aligned to the flow direction either facing

it or reversed to it. The convention with the Cartesian co-ordinate system is for x to be fixed along the angle of the turbine nacelle rather than the mean flow direction. One exception to this is when the turbine is yawed side on to the flow when the nacelle axis is then termed the y axis and so the starboard sensors are measuring along the x axis.

The velocity components u , v and w correspond to velocities along the x , y and z directional vectors. The acoustic sensors indicate a flow towards the transducer as a negative velocity and a flow away from the transducer as a positive velocity.

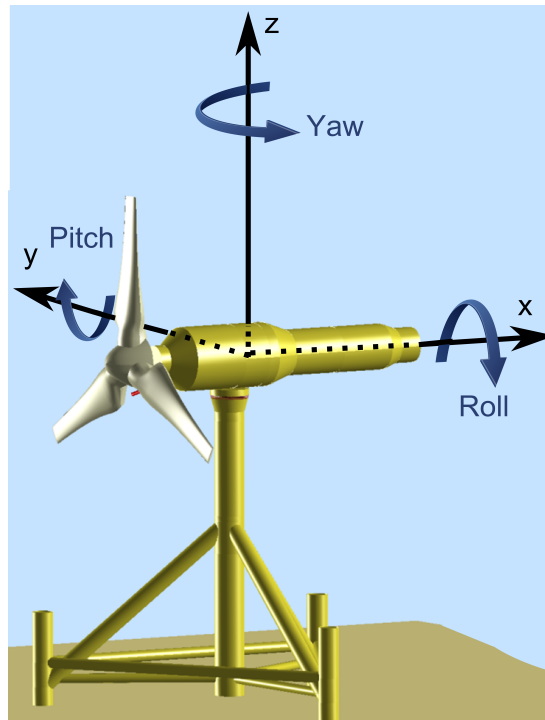


Figure 3.3: Turbine coordinate system

Figure 3.4 shows the locations of the turbine in the Fall of Warness. It also shows the location of the two far field tide gauges, which were the earliest field measurements taken within the ReDAPT project. The channel is approximately 1km wide where the turbine is deployed between Muckle Green Holm and Eday.

3.5.1 Acoustic instruments

An overview of how acoustic Doppler velocity sensors work can be found in Section 2.6. Table 3.7 lists all the acoustic velocity sensors available during the project. All the instruments except the acoustic Doppler velocimeter (ADV) are capable of taking measurements at multiple 'points' up to the stated range. The AWAC has a vertical beam for measuring surface elevation. It can operate in two modes: 'Wave' or 'Current'. 'Wave' mode will give a time averaged depth profile of the velocities over a period of a minimum of a minute. It then measures the

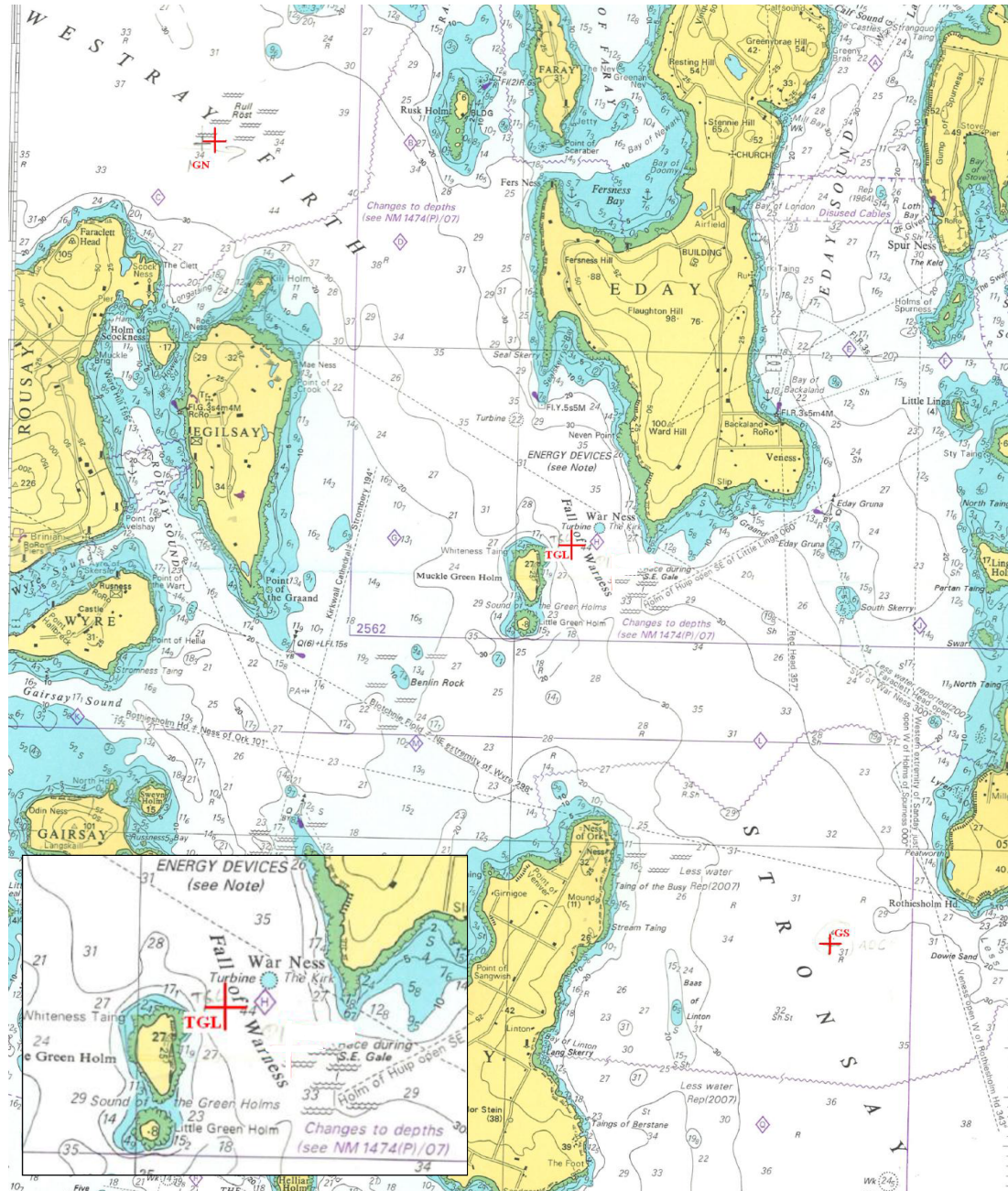


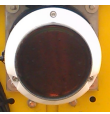




Figure 3.4: Admiralty charts showing locations of tide gauges (GN and GS) with turbine location (marked TGL) Image from: Stock-Williams and Gunn (2012)

surface elevation by minimising the cell-size but only processing cells near the expected surface height to measure a wave elevation time series. The AWAC also houses a pressure sensor, thermometer, pitch, roll and yaw sensors.

SBDPs and ‘Continental’ are single beam devices that measure the velocity along the beam axis. The SBDPs are effective to a range of ~ 20 m while the Continental was designed to measure long range variations up to ~ 150 m. The SBDPs also have thermometers and a subset are equipped with pressure sensors. The Workhorse Sentinal DBDPs have pitch, roll and yaw sensors and thermometer functionality. The ADV is designed for a different application and has a different transducer configuration with a single pinging transducer and three separate receiving transducers all focused on a single measurement volume approximately 3 – 10 cm from the transmit transducer face. The smaller measurement volume and higher samplerate are much better suited to capture turbulence, with the challenge being to mount it outwith the retarding influence of the turbine body on the flow.

Name	Sample rate (Hz)	Pulse freq (kHz)	No of beams	Range ¹ (m)	Number Available	
Nortek AWAC	2	1000	4	30	1	
Nortek SBDP	4	1000	1	25	16	
Nortek Continental	1	190	1	50	1	
RDI Workhorse	2	600	4	50	2	
Sontek ADV	25	10000	1 ²	0.1	1	

¹ Operational range in deployed configuration

² With one transmitting and three independent receiving transducers

Table 3.7: Overview of Doppler sensors available

3.5.2 Instrument placement on the turbine

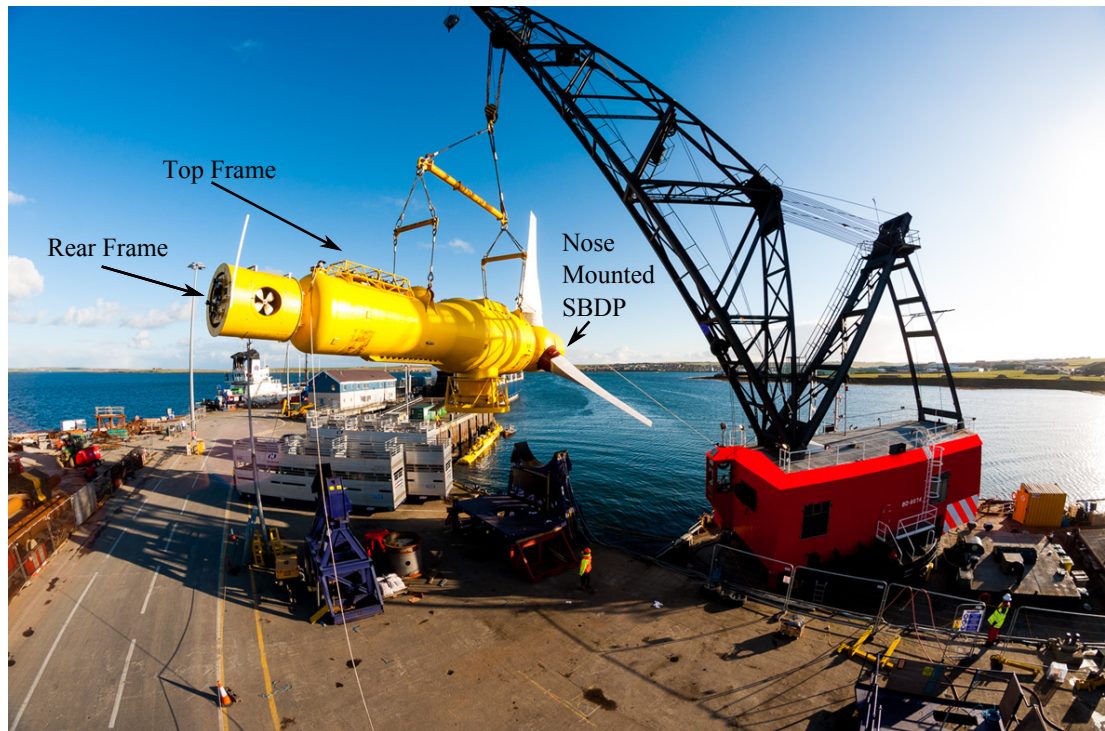


Figure 3.5: The Alstom DeepGen iv 1MW turbine being lifted for deployment. The annotations show the locations of the UoE instrument frames. There is also a single SBDP mounted in the nose that is not visible from this angle. Image from: Alstom

Mounting sensors on a turbine presents some advantages over a standard seabed mounted deployment. The turbine itself is installed ~ 25 m deep in a ~ 45 m channel (depending on the tide). Sensors mounted on the nacelle are all within the swept plane of the turbine and thus taking measurements representative of the flow the blades are experiencing. This combined with the turbine's ability to yaw through roughly 270° , allows the sensors to be oriented at a variety of angles to the onset flow. The turbine's power and communications infrastructure also allows instruments to be hard wired with power (12 V and 24 V DC) and Ethernet. However, the effects of electrical noise and turbine vibrations particularly during generating periods were an unquantified source of uncertainty.

The 1 MW turbine had three locations allocated for the University of Edinburgh's use during the ReDAPT project. A single sensor on the nose of the turbine and space for instrument frames (designed by the university) on the top and rear. Figure 3.5 shows the 1 MW turbine being lifted with the rear and top instrument frames positions visible. Figures 3.6 and 3.8 show the layout of these frames, which are designed to allow flexible instrument placements with hole patterns allowing multiple mounting points. All of the data presented in this thesis was collected during deployments of the 1 MW turbine. The sensor configuration on the 500 kW turbine was similar to the 1 MW turbine with four instruments mounted on the top of the turbine and two on the

rear.

As there are up to sixteen SBDPs used within the project, a naming convention is used based on position rather than the specific unit. The first letter declares the axis along which the beam of the sensor was pointing relative to the turbine and subsequent letters the order from fore to aft:

- V denotes vertical (always looking up towards the surface);
- S denotes Starboard (i.e. the right hand side treating the nose of the turbine as the fore);
- R denotes instruments on the rear frame;
- The letter P is used for instruments in the ‘Pyramid’ of focus-beam array (explained below) with the second letter giving its position as Port (P) or Starboard (S);
- The additional letters specify the order of instruments as Fore (F), Aft (A), Top (T) or Bottom (B) with an M interjected before to indicate a sensor in the middle of the order.

So for example the starboard sensor nearest the blades would be referred to as: $SBDP_{SF}$. Figures 3.7 and 3.8 illustrate the naming principle applied to the configuration of Turbine Deployment 6, which provided the vast majority of data presented in this thesis. These naming conventions are illustrated in Figures 3.7 and 3.8.

First installed for turbine deployment 5, an additional instrument array was retrofitted on the top frame, with four SBDPs focused at a single point approximately 4 m above the turbine nacelle and the vertical SBDP ($SBDP_{VA}$). This array of converging independent sensors could be used to transform the velocity measurements from the individual sensors into three Cartesian velocity components (u , v and w), in a similar way to how a DBDP would resolve them from its multiple diverging beams. If the velocities and turbulence metrics proved accurate, it would remove the amount of spatial averaging compared with a DBDP measurement significantly. This is discussed in more detail in Sellar *et al.* (2015). The outriggers to the frame are visible in unpainted stainless steel in Figure 3.6 and the pyramid beams compared with those of the AWAC are illustrated in Figure 3.9.

In addition, from Turbine deployment 5, the ADV was installed on the top frame. This was designed to give higher frequency measurement of the turbulence. However, as the instrument is a short (~ 10 cm) range device, the flow measured was known to be influenced by its proximity to the turbine nacelle.



Figure 3.6: Top instrument frame being prepared for turbine deployment 5. The starboard SBDPs are visible mounted along the near edge with the AWAC behind in the centre. The outriggers for the focus beam SBDPs have been installed but the sensors themselves are not yet mounted.

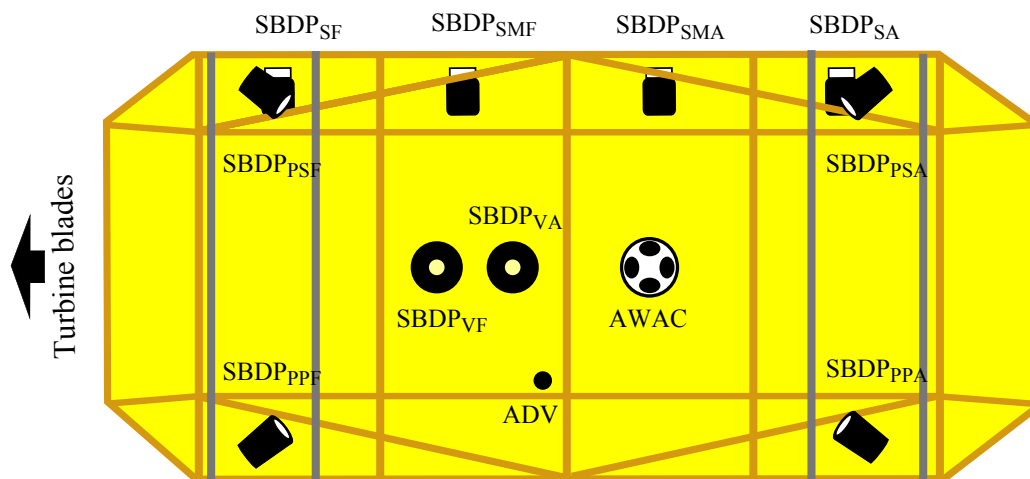


Figure 3.7: Locations and naming convention for instruments on the top instrumentation frame. Note that not all of these sensors were installed for every deployment.

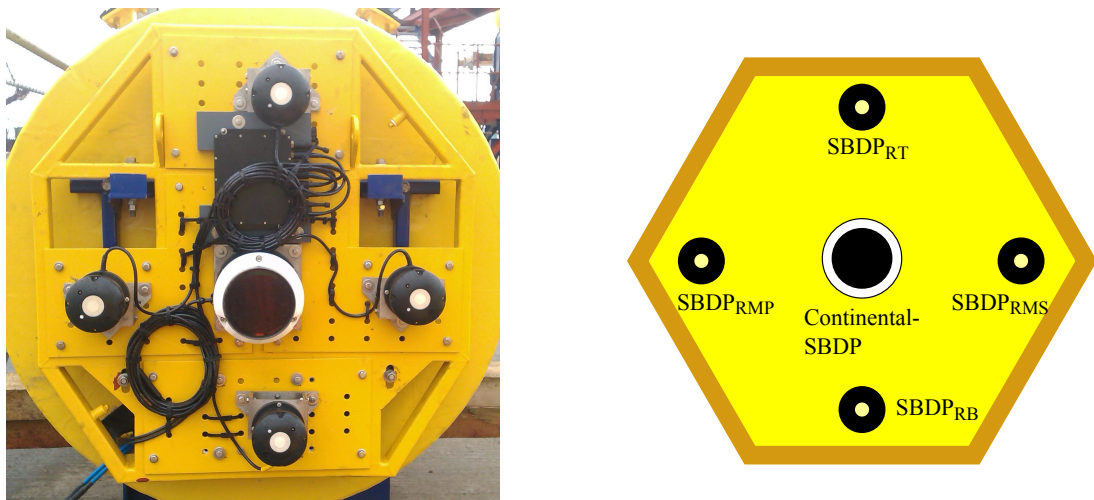


Figure 3.8: Instrument placement and naming convention for rear frame turbine. Note that not all of these sensors were installed for every deployment.

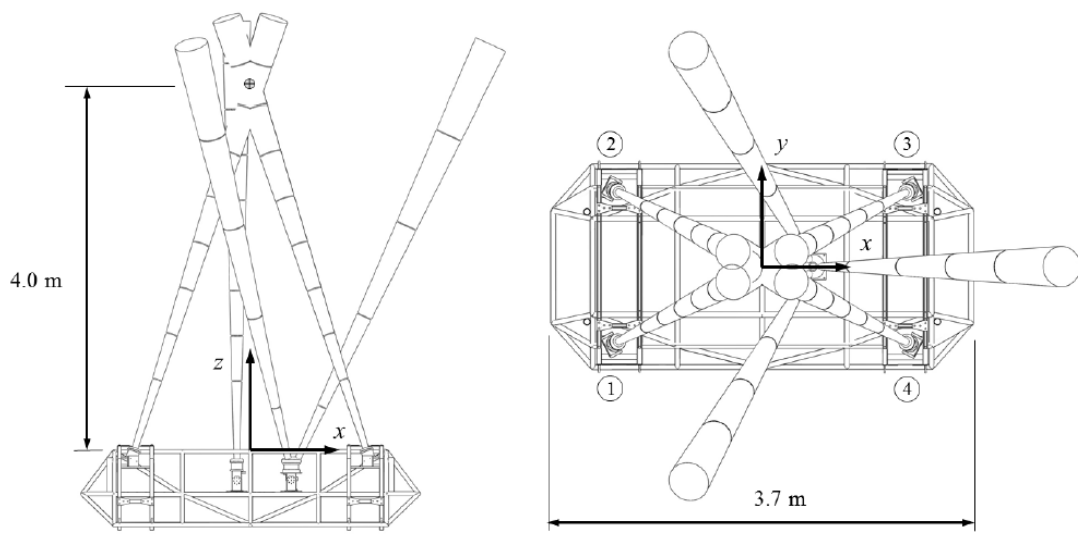


Figure 3.9: Overview of top instrument frame with SBDPs used in the focus beam arrangement. Image from Sellar *et al.* (2015).

3.5.3 Stand-alone deployments

In addition to the turbine mounted instruments, the UoE had access to four DBDP concrete gravity bases (see section 2.5.4 for more information) over the course of the project, some constructed from an in-house design. These deployments allowed the measurement of the full depth profile inflow to the turbine from seabed to surface at a distance great enough to avoid any impeding effects of the turbine on the flow. The majority of deployments placed the sensors at a distance of approximately 50 m either side of the turbine, aligned with the expected principal direction of the flow through the channel.

In order to extend the effective deployment period of the DBDP, part of the UoE's work was spent on improving the battery life and storage capabilities of these DBDPs, as well as an improved gimbals design to minimise vibration. Figure 3.10 shows a DBDP in its gimbal with a battery extension pack being deployed in a UoE designed concrete base.



Figure 3.10: A DBDP mounted in a gimbal on a concrete gravity base during deployment.

3.6 Turbine Operation and Data Gathering Procedures

The turbine and its use in experimental work was controlled by the turbine operator Alstom. The methodology covering this took the form of Test Request Notices (TRNs) which specify individual tests in terms of: equipment required, time/resource required and completion criteria based on the quantity and quality of data captured. The machine work-package generated TRNs associated with turbine commissioning, as well as targets for continuous and cumulative generation that covered every turbine deployment. The TRNs covering use of the turbine to meet the requirements of the modelling sub-project were split into three sets:

- Commissioning;
- Core;
- Advanced.

Commissioning Tests

The commissioning tests involved assessing which sensors were working upon deployment and to what level of functionality. This involved: testing that the instrument could be communicated with over the network, the Precision Time Protocol (PTP), used to accurately synchronise measurements between the SBDPs, was functioning and was connected to the GPS master clock, and that sample data sets appeared to be within expected parameters.

Core Tests

The Core tests involved capturing the flow data to meet the requirements of the modelling packages. This centred around capturing as many data points as possible within two sets of specified flow parameters. Specifically: mean flow speeds of 1.8 ms^{-1} and $2.8 \text{ ms}^{-1} \pm 0.1 \text{ ms}^{-1}$ with low wave conditions (significant wave height $< 1 \text{ m}$).

During turbine generation periods the effect of the blades on the flow is significant. Thus metrics for these modelling flow conditions could not be collected during operating periods. In order to capture these conditions the TRNs allowed the scheduling of tides where the turbine would not operate in order to capture the required flow data. These tests also requested a turbine yaw orientation with many requesting it be either reversed or transverse to the onset flow. In this way the rear frame or starboard mounted instruments on the top frame could measure the flow uninterrupted by the blades, which even when not operating were often allowed to rotate idle.

Advanced Tests

Finally the 'Advanced' MD work package TRN was designed to capture data that was not essential to the modelling work but would provide further insight to the flow characterisation or instrumentation limits and measurement techniques. The majority of the data collected for this thesis was captured within this TRN. Thus a balance had to be struck between operating the turbine, gathering the required quality and quantity of the critical flow metrics and scheduling in the advanced tests. As the 'Advanced' TRN was not on the critical path for project deliverables, the tests within it were low priority and thus some were not able to be carried out and others were left with incomplete data sets.

Beyond the official TRN scheduling there was a level of opportunism required to gain valuable measurements. For example, non-velocity dependent tests could be conducted at near slack water when the turbine was not operating. Sometimes precautionary turbine shut-down allowed a window for collection with the turbine in a fixed position. The scheduling of tests and monitoring of data collection was a large part of this project and is understood to have produced one of the largest collections of flow data at a single site.

However, the Advanced TRN tests did represent the lowest priority to the project and thus for specific tests less than optimum quantities of data were collected. The nature of the experimental set-up, newly available sensors with new software still undergoing debugging on a prototype turbine in a harsh environment, meant data gathering for tests was not a straightforward activity. This required development of in house codes to control instrumentation, data quality upon capture procedure and a high level of monitoring while also liaising with the sensor manufacturer on software revisions, such that reliability of instruments and data did increase throughout the project, with the exception of physical wear and tear.

3.6.1 SB DP Application Program Interface (API)

One of the key pieces of work within the data acquisition of the ReDAPT project was the development of an Application Program Interface (API) to control the SB DP settings and collection timings. This software allowed the real-time updating of the SB DP configuration remotely via Ethernet. Codes to update the settings were written in Matlab which then connected to the instruments via an SSH connection to a server connected to the turbine. The variables included: instrument pulse power, pulse offset, cellsize and blanking distance, sample rates and number of data points to collect.

Where variations of settings were required the API allowed a pre-programmed test schedule to be run, where a variety of settings could be cycled through, collecting a prescribed number of samples. The majority of the data collected for the results in this work were gathered via this software.

3.7 Data Storage and Management

The project generated over 1 TB of data from across multiple sensors in a variety of orientations, many mounted on a turbine rotated at multiple yaw angles in different operational states. In order to manage this complex data set an in-house database was developed. All metrics in the database were processed over a T_{stat} period of 5 minutes. Work by Thomson *et al.* (2012) suggested 5 minutes was an appropriate length for a stable mean without underestimating the variance. This was verified by analysis early within the ReDAPT project. Within this database for each five minute time step there was:

- A record of which instruments were on;
- The configuration and orientation of each instrument;
- The mean velocity over the T_{stat} period for each range bin for each instrument;
- The Turbulence Intensity over the T_{stat} period for each range bin for each instrument;
- The original file from which a data point was generated;
- The significant wave height over the T_{stat} period;
- A reference velocity;
- The turbine status in terms of, power generation and yaw angle;
- The tide direction, Ebb or Flood.

For the work presented within this thesis, the database was used primarily to establish what the turbine status was for a given test and to locate file sets for given conditions. The original data was then loaded and reprocessed for the individual test. This way any spurious data could be identified through quality control and more complex metrics calculated.

The wave height reference was generated by estimations from a series of sensors including the AWAC in 'Wave' mode, the vertical oriented SBDPs and the upstream and downstream DBDPs. The method of this calculation did not involve the author and an overview is outwith the scope of this work. For more information on the generation of wave metrics on the project see Sellar and Sutherland (2015).

With different sensors measuring the velocities in different locations angled at different orientations, a reference velocity was required to compare metrics. This was done using the DBDP upstream of the turbine for the applicable tide at a height 10 m above the turbine hub. This was correlated with the AWAC reading at the same height which showed good agreement of mean velocities. For more information on the calculation of a reference velocity see Sellar and Sutherland (2015).

3.8 Work Contribution Map

Within the ReDAPT project at the UoE there were two full-time members: The project manager and technical lead, Dr Brian Sellar and the author. At various times throughout the project this was augmented by other researchers, some working on very specific research questions or design work, others providing wider input. With such a multi-faceted project it is important to highlight the significant contributions of the author and where the work presented in this thesis fits into the wider goals of the ReDAPT modelling sub-project.

This thesis focuses on the SBDPs and their limits and prospective advantages when used in arrays to capture flow metrics. It must be stressed that all the analysis in this thesis is the author's own work, unless directly referenced otherwise. However, the project management, design and implementation of the experimental setup and database design and implementation, was shared throughout the UoE team. This section aims to highlight the author's contributions to the background work that made this data available for the analysis presented.

The project can be split up into four areas of work:

1. Pre-project planning;
2. Project management and ongoing infrastructure development;
3. Experiment specification and execution;
4. Data selection and analysis.

Table 3.8 gives an approximate quantification of the author's contributions to these areas of work within the ReDAPT project. The items are colour grouped into project logistics, data collection and data analysis. The original contributions to knowledge presented in this work (as detailed in section 1.4) utilise the infrastructure and instrumentation of the project to specify experiments to test the abilities of SBDP sensors (newly available at the initiation of the project) in arrays. The aim being to maximise the accuracy of the metrics being collected and to compare them with the current industry best practise to see if there are advantages to a SBDP array system.

3.9 Chapter Summary

This chapter has detailed the structure of the wider ReDAPT project, of which the work presented in this thesis forms a part. It has highlighted how data acquired for this work has to work in a framework of providing flow data for other project partners. It has also explained the instrumentation available which was utilised to gather the data for the work presented in the subsequent chapters. The next chapter investigates the effects of mounting instruments on a commercial-scale tidal turbine. In particular, the effects of instrument noise and its main drivers which it is desirable to reduce.

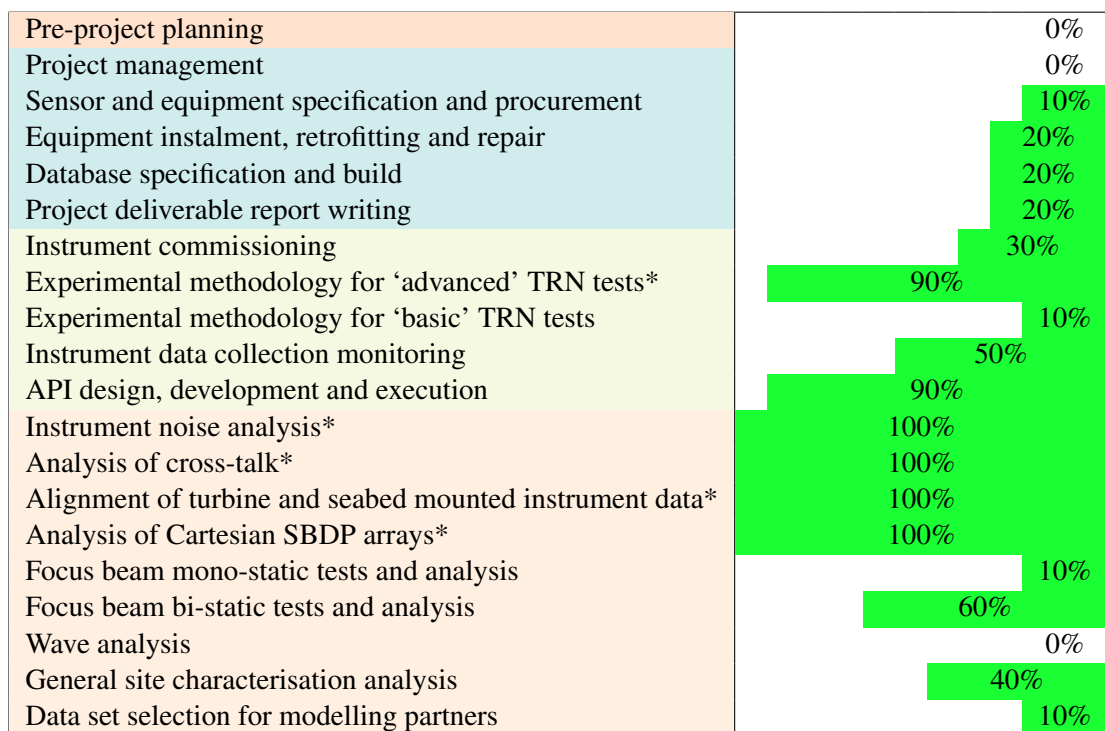


Table 3.8: ReDAPT project - Author contribution map. Orange rows relate to pre-project planning, blue to project management, green to the experimentation and pink to data analysis. The work specifically relating to the analysis in the thesis is marked with *.

Quantification and Mitigation of Noise in SBDP Measurements

4.1 Chapter Overview

In order to reliably utilise acoustic Doppler sensors mounted in close proximity on a commercial scale tidal turbine, an assessment into their performance was required. This was particularly pertinent in regard to the Single Beam Doppler Profilers (SBDPs) which were newly available and untested in the field at the start of this project. Instrument noise is a common problem in experimental analysis (Taylor, 1997) and presents some particular challenges in tidal characterisation work as the contributions of random error and turbulence fluctuations are difficult to separate.

This chapter investigates the following topics:

1. Quantification the variance due to random error in the SBDPs for a variety of flow conditions and sensor orientation using a spectral method;
2. Introduction of a Low Signal to Noise Ratio (LSNR) mode to highlight the differences in random error based on individual sensor locations;
3. A novel method to assess standard error (bias) between sensors using the LSNR mode;
4. Mitigation of random error using power conditioning and grounding modifications.

These methods are investigated in turn in order to minimise and quantify the affects of errors on velocity measurements for this and future site characterisation work.

This chapter does not investigate noise caused by crosstalk between multiple acoustic instruments which is covered in Chapter 5.

4.1.1 Motivation

Random and standard error will affect turbulence and mean velocity measurements respectively. With acoustic sensors not having been previously mounted on a commercial scale turbine and with the instruments employed being newly available it is important that the errors be quantified and where possible mitigated. This will increase confidence in the tidal site characterisation metrics acquired with these sensors which as highlighted in Chapter 2 is key to the development of the industry.

4.1.2 Author's contribution

With the multifaceted work on the ReDAPT project including contributions by both colleagues within the University of Edinburgh and project partners it is important to highlight to author's specific contribution to each chapter.

In this chapter the author's wholly attributable contribution comes in the form of:

- Specification of data collection campaigns specifically designed to assess the noise variation between instruments;
- Development of custom application program interface to control SBDP configuration and schedule measurement collection;
- Coordinating of test schedule with turbine operators;
- Selection of appropriate data from measurements taken across the four year project;
- The post processing methodologies and analysis presented.

The specification of the sensors, their integration (including the installation of grounding and power supply treatment) with turbine systems and high level project management were all the responsibility of the project manager at the University of Edinburgh. Instrument placement on the turbine was a joint decision between the author and the project manager, with the selected positions chosen to fulfil both internal and external data capture requirements.

4.2 Part A - Quantification of Random Error

4.2.1 Methodology and Theory

In analysis of tidal sites, velocity metrics can be defined as being the sum of a mean value (that can be considered stationary over a period of minutes) and a fluctuating (turbulent) component (Thomson *et al.*, 2012; Milne *et al.*, 2013):

$$u = \bar{u} + u' \quad (4.1)$$

where \bar{u} is the mean velocity over a period of assumed stationarity (T_{stat}) as discussed in section 2.7.4, and u' is the velocity perturbation about this mean value.

Noise can be divided into two types: random error (increased signal variance), ϵ' , and systematic error (bias), $\bar{\epsilon}$ (Smith, 1999). This makes analysis of noise in turbulent flows particularly difficult as bias and mean velocity values are amalgamated, as are random error with turbulence induced fluctuations. Thus any given measurement of u can be described as a sum of four components, with both error and physical subdivisions having a mean and fluctuating element:

$$u = \bar{u} + u' + \bar{\epsilon} + \epsilon' \quad (4.2)$$

Spectral Slope Fitting Method

There are many factors that could introduce random error to a Doppler profiler. These include: density of back-scatterers in the flow, poorly correlated signal returns, uncertainty in measuring the Doppler-shift, high spatial variability of the flow and electrical noise (Nystrom *et al.*, 2002; Gordon, 1996; DiMassa *et al.*, 2001). In this section the relationship between the random error with: instrument orientation, flow speed and electrical noise are investigated. These were the parameters unique to this experimental setup and would allow optimisation of site characterisation metrics. Investigation into the effects of other drivers have either previously been investigated (Nystrom *et al.*, 2002; DiMassa *et al.*, 2001) or were not possible with the available experimental setup.

In order to quantify the variance that is attributable to random error (σ_{noise}^2), a method developed by Durgesh *et al.* (2014) and Richard *et al.* (2013) was applied for the first time to the newly available SBDPs. The technique uses de-trended velocity measurements which form the basis of a spectral analysis. It utilises the principle that the variance of the measured velocity ($\sigma_{measured}^2$) can be sub-divided such that:

$$\sigma_{measured}^2 = \sigma_{physical}^2 + \sigma_{noise}^2 \quad (4.3)$$

where $\sigma_{physical}^2$ is the physical (i.e. attributable to velocity perturbations) component and σ_{noise}^2 is the noise component, as per the principle of Equation 4.2.

In order for this theoretical method to correctly fit the spectra of the measured data, two assumptions must be valid: That the noise is spread evenly across the frequency range, an assumption (which is examined in Section 4.3), and that the flow measured, and thus $\sigma_{physical}^2$, is turbulent.

As discussed in Chapter 2 the Reynolds number of the flow at the Fall of Warness site is of the order of 10^7 and thus a fully developed turbulent flow (Çengel and Turner, 2005). In

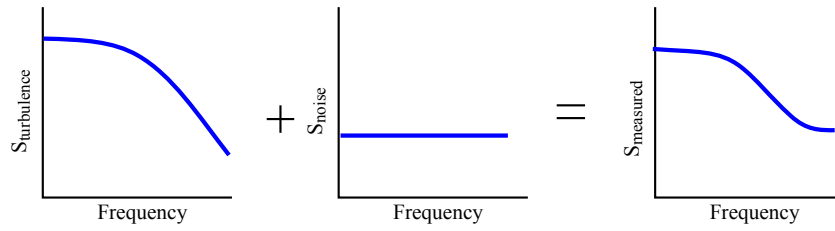


Figure 4.1: Illustration of the components of a measured spectrum. Adapted from Richard *et al.* (2013).

a turbulent flow the frequency spectrum of the velocities should follow the energy cascade as detailed in Section 2.4.1. At the scales measured by these devices at this site, the kinetic energy of the fluctuations would be expected to show evidence of the inertial sub-range, i.e. the energy varying with frequency (f) with a $f^{-5/3}$ slope (Pope, 2000). Thus the transition from the $f^{-5/3}$ slope to the ‘noise-floor’, where (as per the first assumption) the gradient is zero, can be easily identified. This is illustrated in Figure 4.1. The area under this noise floor represents the variance of the velocity due to noise as per Parseval’s theorem (Beauchamp, 1987), which can be used to correct turbulence intensity (I) measurements via the following equation (Thomson *et al.*, 2010):

$$I_u = \frac{\sigma_{measured}}{\bar{u}} = \frac{\sqrt{\langle u^2 \rangle - \sigma_{noise}^2}}{\bar{u}} \quad (4.4)$$

where $\sigma_{measured}$ is the standard deviation of the velocity u . Angled brackets denote the expected value over a period of stationarity (T_{stat}).

These two slopes for the theoretical sources of perturbation in the velocity time series can be summed together:

$$S_{measured}(f) = c_i \cdot f^{-5/3} + N \quad (4.5)$$

where $S_{measured}(f)$ is the Power Spectral Density (PSD) as a function of frequency (f), c_i is a constant (which is theoretically a function of the turbulent dissipation rate ε) and N is the PSD due to random error. The frequency at which these two components cross is termed the cut-off frequency (f_{cut}) after which the signal is considered to be dominated by noise.

The PSD has been previously defined in Section 2.7.4. It is calculated from the velocity perturbation time series, via the matlab Fast Fourier Transform (FFT). This is then used to calculate the PSD ($S(f)$) via Equation 2.25.

In order to calculate the FFT a T_{stat} value must be chosen. A T_{stat} of 256 seconds was selected as it is the closest power of two to 5 minutes, which is suggested to have a stable mean and variance over that period (Thomson *et al.*, 2010; Milne *et al.*, 2013). Using a number that is equal to a whole power of two means the data series for the PSD does not have to be padded which increases accuracy of results (Emery and Thomson, 2001).

The first stage of data separation was to divide sets with a long (greater than 30 second) gap in the timestamp between consecutive samples into separate sets. Sample-sets where the timestamps covered more than 256 seconds were then divided into sub-sets of that length with a 50% overlap between sub-sets. After this process if a sub-set was less than 90% of T_{stat} (i.e. less than 231 seconds) it was removed. The remaining data sets were passed for further processing with missing timestamp values padded with the mean value of that sample set. Thus all data sub-sets covered 256 seconds. Data sub-sets were de-trended to remove the mean value. Note, that the padded values become zeros upon de-trending, as this method is reported to smooth the FFT results and reduce quantisation error (Emery and Thomson, 2001).

A periodic Hamming filter was then applied to each data set in order to smooth the FFT output (Emery and Thomson, 2001). Figure 4.2 shows an example of a de-trended data set before and after windowing. The data sets are then passed to a FFT to obtain the PSD ($S(f)$) via equations 2.24 and 2.25. Where possible, $S(f)$ results were averaged over multiple sample-sets (with sample-sets binned by a specified mean velocity range detailed in the relevant results section) before the curve fit method was calculated. This was done in order to have the most accurate representation of the inertial sub-range slope.

As the windowing process removes energy from the spectra this must be corrected to satisfy Parseval's theorem that the energy under the PSD is equal to the variance of the time series (Beauchamp, 1987). The variance of the signal is calculated both before (σ_u^2) and after ($\sigma_{S(f)}^2$) windowing. This leads to the empirical correction factor used to correct the $S(f)$ value:

$$S_{corrected}(f) = S(f) \cdot \frac{\sigma_u^2}{\sigma_{S(f)}^2} \quad (4.6)$$

The theoretical two-line curve given in Equation 4.5 was fitted to the data by method of least squares linear regression. This is based on minimising the error (ΔS) based on the difference between the measured and fitted theoretical slope ($S_{theory}(f)$). This can then be solved numerically for c_i and N :

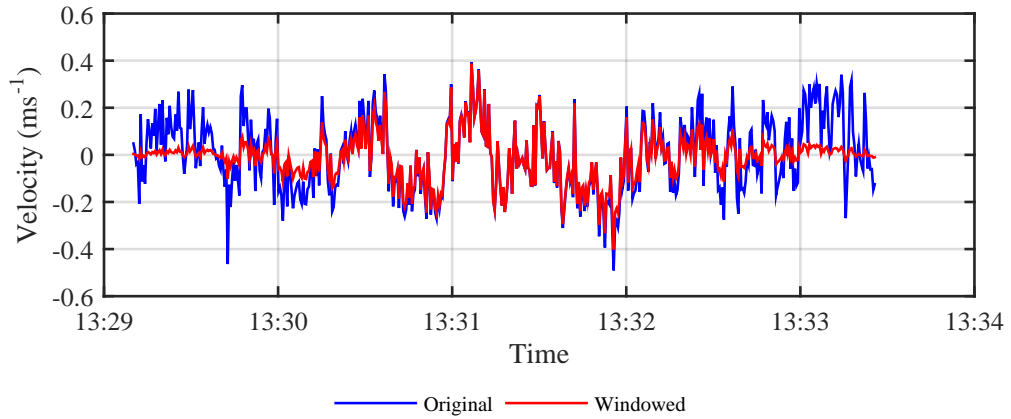


Figure 4.2: Example of de-trended data before and after the application of a Hamming window. The blue line represents the original signal and the red the filtered signal.

$$\Delta S = S_{measured}(f) - S_{theory}(f) \quad (4.7)$$

$$= S_{measured}(f) - c_i \cdot f^{-5/3} + N \quad (4.8)$$

$$E(N, c_i) = \sum_{i=1}^{f_n} \Delta S \quad (4.9)$$

At the lower frequencies captured with this method, the scale of the turbulent cascade is likely not within the inertial sub-range. Rather, it is expected that the integral range of motions which should theoretically centre around a maximum turning point that will dominate at this frequency range as per Figure 2.8. In order to avoid this region affecting the curve fit, designed for the inertial sub-range, only $S(f)$ values for frequencies greater than 10^{-1} Hz are used in the fitting process described, although for flow speeds $< 0.85 \text{ ms}^{-1}$ this band is raised to include frequencies greater than $10^{-0.8}$ Hz as this was found to improve estimates. The variance due to noise can then be estimated, by calculating the area under the N line across the frequency range:

$$\sigma_{noise}^2 \approx N \cdot f_{Nyquist} \quad (4.10)$$

An example of this method for a single 256 second SBDP data set collected at a sample rate of 2 Hz is given in Figure 4.3. It highlights the two individual curve components, the instrument noise and the turbulent slope, as well as the combined summation. The region used for the fit is highlighted between frequencies of 10^{-1} Hz and 1 Hz.

When both components are not present the fit technique will fail. This is manifested in a complex number result for f_{cut} and a vertical noise asymptote. These values and their associated

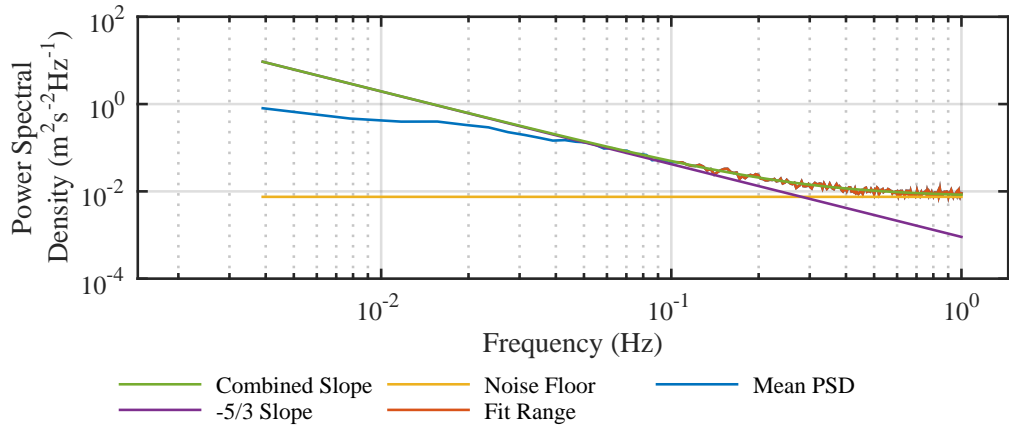


Figure 4.3: Example of the spectral curve fitting method of Richard *et al.* (2013), highlighting the region used for the fit and the individual curve components.

noise floors are removed from the results. These results are normally associated with relatively flat spectra and are more likely to occur at lower flow speeds.

The method of calculating the relationship between σ_{noise}^2 and \bar{u} , is implemented differently to the method in Richard *et al.* (2013), who calculated a PSD and thus a σ_{noise}^2 for each T_{stat} sample. Here the results are binned by velocity range as it has been suggested by many reports investigating the use of Doppler sensors in tidal environments that random error increases with flow velocity (Brumley *et al.*, 1991; Voulgaris and Trowbridge, 1998; Thomson *et al.*, 2012; Richard *et al.*, 2013). The relationship between mean stream-wise velocity (\bar{u}) and σ_{noise}^2 is assessed by calculating the mean PSD over a minimum of 20 sample sets for each 0.1 ms^{-1} velocity range as measured by an upstream DBDP at equivalent depth in the channel.

The spectra for each T_{stat} length sample-set within the velocity-range were calculated then the results averaged together. The σ_{noise}^2 of the fit method of the resulting averaged spectra was used to define the random error for that velocity range. This was done partly due to the large spread in results of σ_{noise}^2 which increased greatly with flow speed. Also at lower flow speeds where the turbulent structures were low an average spectra gave a better estimate of the inertial sub-range slope. This is done for three sensors: one mounted facing the onset flow, one normal to the flow oriented horizontally and one orientated vertically towards the surface. In this way the relationship between σ_{noise}^2 and both sensor orientation and flow velocity can be assessed. The goal is to calculate the most accurate correction value for Equation 4.4 for a range of flow conditions.

	Direction		
	<i>x</i>	<i>y</i>	<i>z</i>
Sensor used	Nose	Starboard mid fore	Vertical aft
Range bin	23	23	15
Range (m)	9.2	9.2	6

Table 4.1: Range bin at which relationship of noise variance with velocity is defined for each direction.

Data collection

This section uses data collected during turbine deployment 6 over June and July 2014 when 14 SBDPs were consistently available. A single SBDP in each direction with the most available data was selected. These were: the nose SBDP, SBDP_{VA} on the top frame orientated vertically and SBDP_{SMF} mounted on the top frame facing along the transverse axis as per Figure 3.7 were used. These measurements were not concurrent. Inflow velocities of less than 0.5 ms^{-1} were omitted due to the fluctuating nature of the velocity direction around slack water. Data points where the turbine was operating or not aligned with the flow were not included.

Only one range-bin was used for the data analysis with no spatial averaging. Bin selection was required to not be too close to the turbine nacelle, where the flow will be impeded, not too far that it is outwith the effective range of the sensor, and not too close to the surface in the vertical sensors. It was also desirable to use the same bins as would be used in the comparison study with the DBDP (this is discussed in greater detail in Section 6.5). The bins selected are detailed in Table 4.1.

Quality control

The SBDP data Quality Control (QC) on data matching the prescribed flow and turbine conditions covered four indicators:

1. The time-stamp associated with each data point are checked for repetition. All data associated with all but the first value of a non-unique time-stamp are removed. Experience suggests that velocity readings corresponding to non-unique time-stamps represent spurious data.
2. The SBDP sensors have an internal error detection system, that stores error information in an 8 bit code. This covers any combination of 8 types of error. All data points where an instrument recorded any type of error were removed as recommended by the instrument manufacturer (Nylund, 2013a).
3. The instrument configuration for the captured data is checked to ensure that the Precision Time Protocol (PTP) option was enabled to control the timing of the acoustic pulses.
4. Data points where the velocity reading in any bin exceeded the velocity range are excluded, as this should not be possible for the instrument to measure.

Once data had been divided into 256 second sample sets, velocity measurements with absolute values greater than four times the standard deviation were removed as these represent spurious results and had a significant effect on the de-trending and thus the spectra. Gaps of three or less consecutive samples were interpolated via a cubic spline method. Subsets with larger gaps were removed.

4.2.2 Results

Figure 4.4 shows the variation of σ_{noise}^2 , as calculated by the spectral line fit method, and the cut-off frequency (f_{cut}) for each 0.1 ms^{-1} \bar{u} bin. The red dots show the results for the sensor oriented along the y axis normal to the flow, the blue dots the sensor orientated to the inflow along the x axis and the green dots the sensor orientated vertically along the z axis.

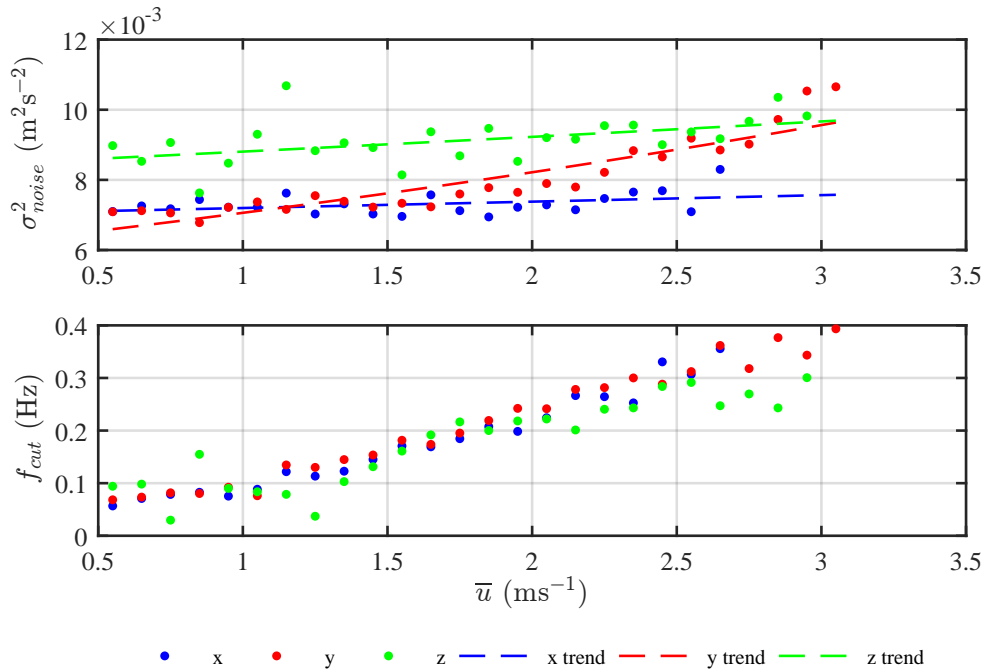


Figure 4.4: Variation of σ_{noise}^2 (top) and cut-off frequencies (bottom) with inflow (\bar{u}) for inflow, transverse and vertical for the SBDPs.

Figure 4.4 illustrates that for the three directions there are quite distinct curves. The x and z directions have similar slopes but with the z results at a higher value across the velocity range. The results for the y direction are steeper starting at a similar level as the x results at the lowest speeds and increasing to the highest value of $11 \times 10^3 \text{ m}^2\text{s}^{-2}\text{Hz}^{-1}$ at the highest flow speeds. This signifies that in the horizontal and vertical there is significantly less variation of noise with flow speed than in the transverse. However, the cut-off frequency is similar for all three orientations, increasing as the energy associated with turbulent structures increases in size with flow speed. This phenomenon is discussed further in Chapter 5. There is a little more variation in f_{cut} in the z direction compared with the x and y , suggesting the fit method might not be

capturing the two parts of the vertical spectra as accurately for the two horizontal directions. This could be due in part to increase noise from surface reflections and/or small wave orbital motions affecting the spectra.

Fitting a line of best fit by least squares regression for each orientation, leads to the following correction factors which can be applied to the SBDPs:

$$x : \quad \sigma_{noise}^2 = 10^{-2.15} \cdot 10^{0.01 \cdot \bar{u}} \quad (4.11)$$

$$y : \quad \sigma_{noise}^2 = 10^{-2.22} \cdot 10^{0.07 \cdot \bar{u}} \quad (4.12)$$

$$z : \quad \sigma_{noise}^2 = 10^{-2.08} \cdot 10^{0.02 \cdot \bar{u}} \quad (4.13)$$

where the R^2 goodness of fit respectively are 0.16, 0.84 and 0.23. The low values correspond to the fits with the shallowest gradients indicating that a constant value would be an acceptable correction factor in these two cases. A power law was selected as it was the best fit across the three directions.

4.2.3 Discussion of results

Figure 4.4 shows negligible increase in σ_{noise}^2 with stream-wise velocity as indicated by the low R^2 value for the fit. A mean value of $7.31 \times 10^3 \text{ m}^2\text{s}^{-2}$ would provide a good approximation, although more data at higher flow speeds would increase confidence in this value. For the individual beams of a DBDP sampled at 2 Hz, Richard *et al.* (2013) showed a relatively constant value of $6.4 \times 10^3 \text{ m}^2\text{s}^{-2}$ across the velocity range (although no fit was given). This variation in value could be down to the different sensor types as well as the density of scatterers in the flow between the two sites.

The differences between the three beam directions is surprisingly high. There is no evidence of this disparity in the results of Richard *et al.* (2013) between the four beams of the DBDP which, even though angled to the flow, would be expected to show some evidence of this, as generally one DBDP beam pair is more closely aligned with the x direction and the other with the y . The y orientation shows the greatest sensitivity to axial flow speed, indicating that as the flow moves past the sensor the reflected pulses are less easily resolved. The f_{cut} values in the y orientation are very similar to those in the x orientation following a smooth upward trend; this is an indication the method is working well.

It was expected that the two sensors orientated normal to the flow would give similar results for $\sigma_n^2(\bar{u})$. It was thought that the variation of σ_{noise}^2 with orientation would only vary with offset angle to the flow direction. The $\sigma_{noise_z}^2$ values are high across the flow range compared with those in the x orientation and higher than the results in the y direction at low flow speeds. The f_{cut} results in the vertical show more variation around the upward trend seen in the other orientations but still follow the same basic relationship with axial velocity. In summary, there

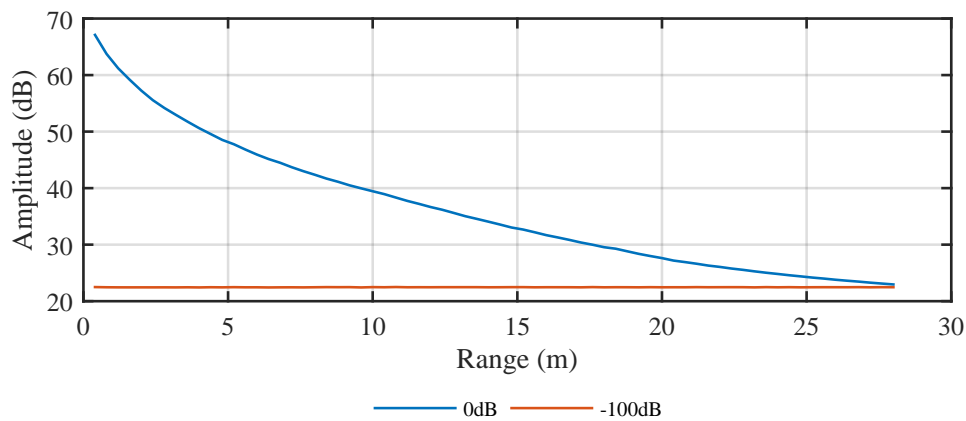


Figure 4.5: Comparison of amplitude returns of a horizontal SBDP at 0 dB and -100 dB power settings.

is more uncertainty associated with vertical results. There is the option to use the y correction curve for all sensors normal to the flow. However, the results of the vertical were not deemed excessive and thus are used in this work.

4.3 Part B - Inter-SBDP variation and LSNR results

4.3.1 Methodology and Theory

This project was the first time acoustic Doppler sensors have been mounted on a commercial-scale tidal turbine. Mounting electrical equipment in close proximity to a 1 MW generator and associated electrical infrastructure was predicted to be a source of noise that has not previously been characterised. The most likely manifestation of this noise was predicted to be a degree of spatial variation of noise, based on sensor location on the turbine.

In normal SBDP operating configuration, a difference in concurrent averaged velocity measurements between two or more instruments, even when measuring broadly the same inflow, could be due to a physical phenomenon or a systematic error, or a combination of the two. By decreasing the SBDP's pulse power to its lowest available setting (-100 dB), thus maximising the noise to signal ratio it is proposed to characterise the noise in each sensor by removing the influence of the flow on results. The premise was to investigate if the magnitude of the variance in the Low Signal to Noise Ratio (LSNR) measurements for a given SBDP was related to that of the same instrument in 'powered' (0dB) mode. An example of the variation in signal return amplitude between 0 dB (powered mode) and -100 dB (LSNR mode) power settings is given in Figure 4.5.

The hypothesis was that the LSNR mode SBDP velocity measurements would reveal information about the instrument noise. For each individual SBDP, a LSNR mode mean velocity value

across a 5 minute sample was calculated. These results were then contrasted with the σ_{noise}^2 from the powered test to assess if there is a correlation between the powered and LSNR mode measurements in terms of both mean value and fluctuations. For this inter-instrument variation, the data sets used were restricted to those corresponding to stream-wise flow velocities in the range of 0.0 ms^{-1} to 0.5 ms^{-1} . This was done to minimise the difference in along beam velocities in the sensors of mixed orientation found in Section 4.2.1, to assess if the noise floor of the instrument is specific, based on instrument build or electrical noise influenced by mounting position on the turbine.

In order to assess the validity of the spectral method and discern information about the nature of the noise, the PSD of the LSNR mode velocity measurements are calculated. It is predicted that in the LSNR mode the resulting PSD will be flat over the frequency range, indicating the noise is white.

Data collection

This section uses data collected during turbine deployment 6 over June and July 2014 when 14 SBDPs were consistently available. Data was not collected specifically for these tests, rather data from throughout the project was used to ensure the largest number of data sets over the velocity range of the channel, while not introducing the uncertainty of multiple instruments or mounting locations. The sensor locations and the configuration used in this test are listed in Table 4.2. An illustration of the sensor positions on the turbine and naming conventions are given in Section 3.5.2.

Sensors available: Nose, SA, SMA, SMF, SF, VA, VF, PPF, PSF, PPA, PSA, RT, RMS, RB					
Power (dB)	Sample Rate (Hz)	Cell Size (m)	Number of Cells	Blanking Distance (m)	Velocity Range (ms^{-1})
0	2	0.4	70	0.4	4

Table 4.2: Instrument availability and configuration for the SBDP σ_{noise}^2 test.

For the powered (0dB) mode, only data corresponding to stream-wise velocities in the range of 0.0 ms^{-1} to 0.5 ms^{-1} was used. All available data for each sensor matching this criterion was used. However, this was at the expense of high variation in the number of samples available for each instrument.

For the LSNR mode tests, a 5 minute data set was acquired for each of the available SBDPs. The instrument settings used for the LSNR mode tests are displayed in Table 4.3. As data collection time was limited, test sets for a range of sample rates and configurations were not possible in this case and data was captured during one slack tide on an opportunistic basis. The assumption must therefore be made that noise due to electrical interference does not vary with time, while the turbine is not operating.

The stream-wise in-flow velocities were calculated from upstream diverging beam Doppler profilers (DBDPs) mounted on the seabed either side of the turbine, as described in Section 3.5. These were averaged temporally across T_{stat} and spatially across the turbine rotor plane.

Power (dB)	Sample Rate (Hz)	Cell Size (m)	Number of Cells	Blanking Distance (m)	Velocity Range (ms ⁻¹)
-100	4	0.4	70	0.4	4

Table 4.3: SBDP LSNR-mode test settings.

4.3.2 Results

Figure 4.6 shows the LSNR velocity time series for a single range bin (4.0 m from the sensor) covering the available 12 SBDP sensors. It illustrates the variation between sensors in both mean values and standard deviation. The sensors on the rear frame are highlighted as these show the most distinct variation, while the top frame sensors (with the exception of SBD_{PSA}) have similar mean value and standard deviation. The values are presented in Table 4.4 along with the mean σ_{noise}^2 results for the low flow speed powered case.

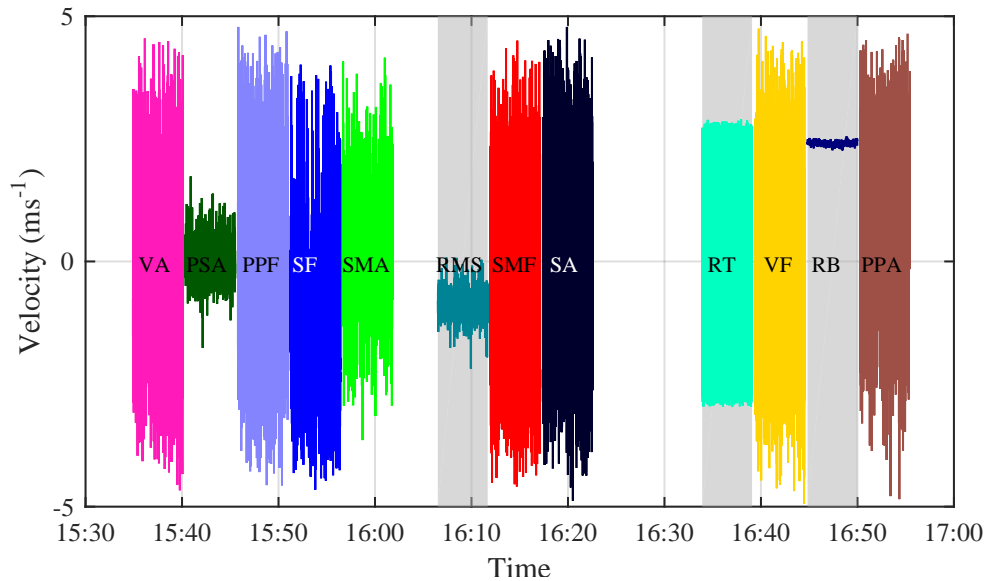


Figure 4.6: Velocity time series of the individual SBDPs in LSNR (-100 dB) pulse power setting. The grey shaded background indicates instruments mounted on the rear instrumentation frame.

The range of results is much greater than would be expected for instruments of the same design. In order to further analyse these differences, an investigation into the type of distributions of the velocity measurements was conducted. A histogram of each instrument is plotted in Figure 4.7, showing the averaged distribution for each SBDP. This plot shows that there are several types

Instrument	Mean velocity (ms ⁻¹)	Velocity standard deviation (ms ⁻¹)	$\sigma_{noise}^2 \times 10^{-3}$ (m ² s ⁻² Hz ⁻¹)
SF	-1.50	1.42	6.92
SMF	-1.08	1.98	7.02
SMA	0.27	1.14	6.75
SA	0.22	2.01	7.07
VF	-0.19	2.21	7.11
VA	-0.02	2.03	Not Available
PSA	-0.04	0.38	6.91
PPF	-0.05	2.08	6.77
PPA	1.31	1.70	6.68
RT	0.91	2.42	7.14
RMS	-0.89	0.25	7.22
RB	2.41	0.04	6.75

VA SBDP not included due to lack of data

Table 4.4: Mean and Standard deviation of velocity measurements of SBDPs in LSNR (-100 dB) power setting, contrasted with instrument noise measured in 0 dB powered setting. Shaded cells correspond to the sub-set plotted in Figure 4.8.

of distribution with some distributions being clearly bi-modal (generally non-symmetrically) and several showing skew to one side or the other. Table 4.5 gives a high level qualification of these different features in the available SBDP sensors. It is possible to assess the specific type of distribution through tests such as the χ^2 test. However, this was not deemed necessary as there was no obvious application for the results.

These results show a significant range in the velocity measurements taken when the noise is maximised relative to the pulse signal strength. In order to assess what effect, if any, this has on the sensors in a normal operating configuration, these results are compared with the results of the σ_{noise}^2 results for each SBDP. The LSNR mean velocities and standard deviations with the powered σ_{noise}^2 are given in Table 4.4. They show no direct correlation between the two metrics. Thus if there is an effect it is insignificant compared with other factors such as sensor orientation as suggested in Section 4.2.2.

In order to reduce this uncertainty the comparison was then limited to the four parallel SBDPs which were oriented along a common direction. Figure 4.8 shows the LSNR pulse power mean velocities and standard deviation for each of these SBDPs against their respective mean σ_{noise}^2 values. The mean LSNR mode velocity appears to have no obvious correlation. However, there is evidence that the fluctuations in the LSNR mode are related to the random error in powered mode.

A linear trend fitted to the relationship of LSNR velocity standard deviations as a function of σ_{noise}^2 by a least squares method, gives a gradient of 2.92 Hzsm⁻¹. This indicates that LSNR mode may be used to measure random error in sensors. It should be noted that in both cases

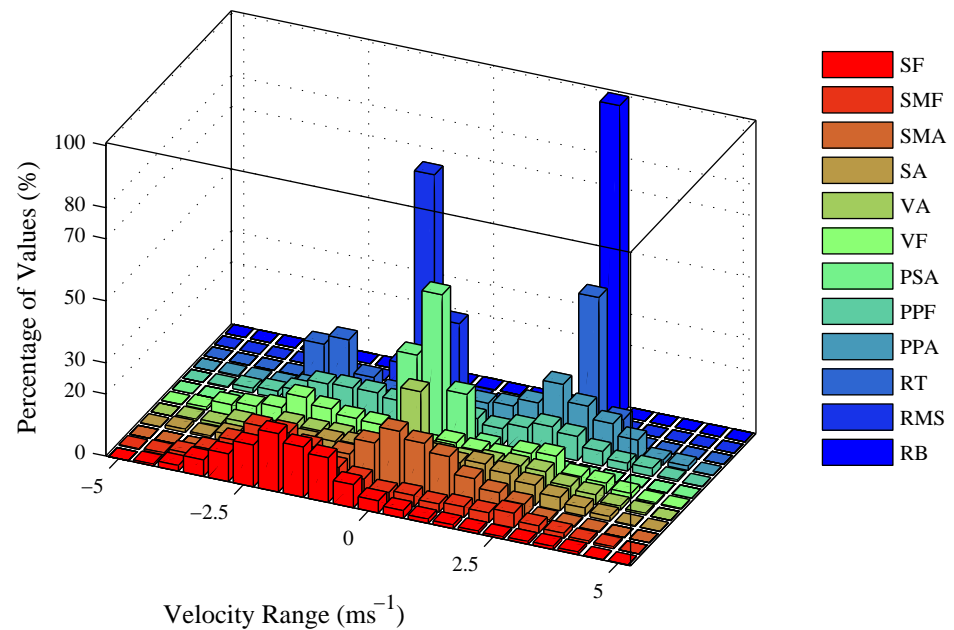


Figure 4.7: Histogram of velocity distributions of all available SBDP velocities in LSNR (-100 dB) pulse power setting.

Instrument	Mode	Skew
SF	single	right
SMF	bimodal	negative bias
SMA	single	right
SA	single	left
VF	bimodal	negative bias
VA	bimodal	negative bias
PSA	single	insignificant
PPF	bimodal	negative bias
PPA	single	left
RT	bimodal	positive bias
RMS	single	insignificant
RB	single	insignificant

Table 4.5: Qualitative summary of the distributions in Figure 4.7.

Instrument	Linear Gradient ($\text{m}^2\text{s}^{-2}\text{Hz}^{-2}$)	$R^2 \times 10^{-3}$
SF	0.15	5.69
SMF	-0.10	1.03
SMA	0.05	1.75
SA	-0.08	0.51
VA	-0.25	4.07
VF	0.23	3.00
PSA	0.00	0.08
PPF	-0.61	21.55
PPA	0.06	0.60
RT	0.21	1.56
RMS	0.00	1.71
RB	0.00	26.27

Table 4.6: Gradients of LSNR-mode PSD for each individual SBDP.

there is a limit to the fluctuations around a mean value that can be generated, based on the measurement parameters of the instrument which in this setting are limited to $\pm 4 \text{ ms}^{-1}$.

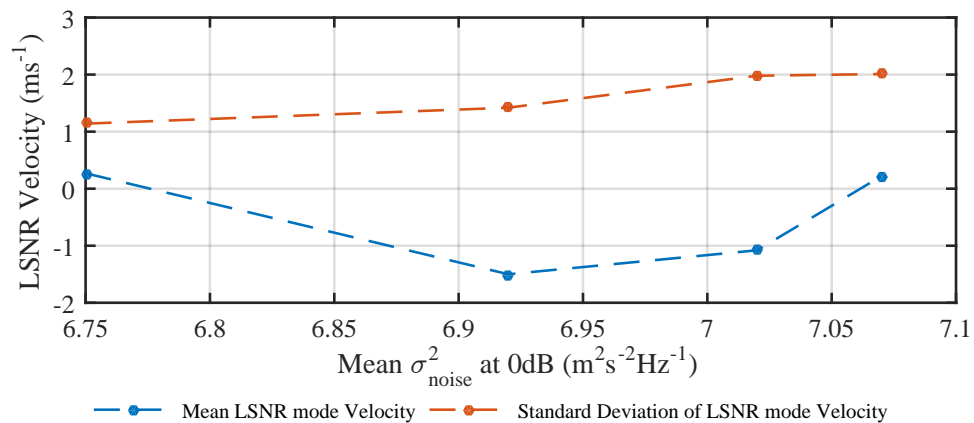


Figure 4.8: Mean and Standard deviation of velocity measurements of four parallel SBDPs in -100 dB LSNR power setting contrasted with instrument noise measured in 0 dB power setting, for a sub-set of four parallel SBDPs.

LSNR mode spectral analysis

Spectral analysis was carried out to discern if the energy in the velocity measurements in LSNR mode was spread evenly over the frequencies. Figure 4.9 shows the PSD for each instrument in LSNR mode across the frequency range. These were fitted to a linear slope with the gradients and goodness of fit reported in Table 4.6. The linear gradients range from $-0.38 \text{ m}^2\text{s}^{-2}\text{Hz}^{-2}$ to $0.10 \text{ m}^2\text{s}^{-2}\text{Hz}^{-2}$. It is noticeable that the SBDPs with the larger gradients in their LSNR spectra correspond to those with the higher random error in 0 dB mode.

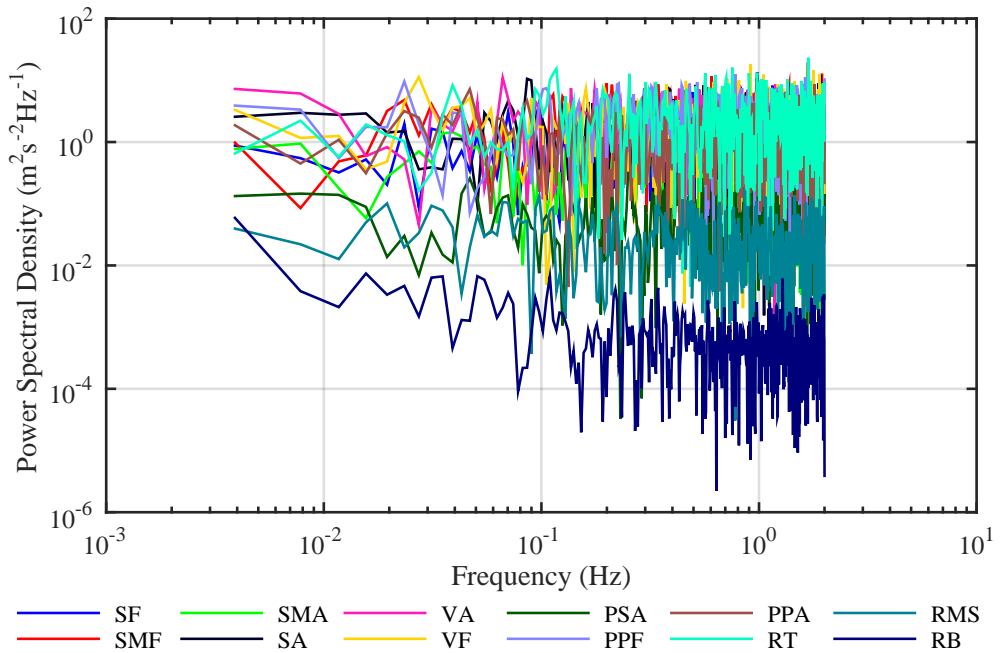


Figure 4.9: Spectra of SBDP velocity fluctuations at -100 dB power setting.

4.3.3 Discussion of results

The tests to maximise the noise relative to the signal produced highly contrasting results across the SBDPs in terms of: mean velocity, standard deviation and velocity distribution. With the exception of one of the focus beam SBDPs on the starboard aft quarter, the SBDPs on the top frame showed a relative similarity compared with those on the rear instrumentation frame. This suggests that sensor placement on the turbine did have an effect on sensor noise and that the source is most likely a form of electrical interference. Additional tests (not presented here) showed that in LSNR power mode noise did not vary significantly with range unless affected by crosstalk from other instruments, an effect which is discussed in Chapter 5.

When the LSNR mode velocity fluctuations across all the SBDPs are compared with the σ_{noise}^2 values of the 0 dB (maximum pulse-power) mode results, there is little evidence of a correlation. This suggests that the effects of electrical noise are minor compared with the effects of instrument orientation. However, for the starboard sub-set, Figure 4.8 showed evidence of a correlation between fluctuations in LSNR velocity measurements and σ_{noise}^2 in the measured results. With so few data points there is a high level of uncertainty in this assertion. With evidence of such wide variation in instrument noise in LSNR mode, further work in understanding the types and effects of noise to reduce these uncertainties is important for future flow measurement campaigns.

The LSNR PSD plots were calculated to assess if random error was constant over the frequency range. The slope that shows the greatest variation with frequency is the Bottom SBDP on

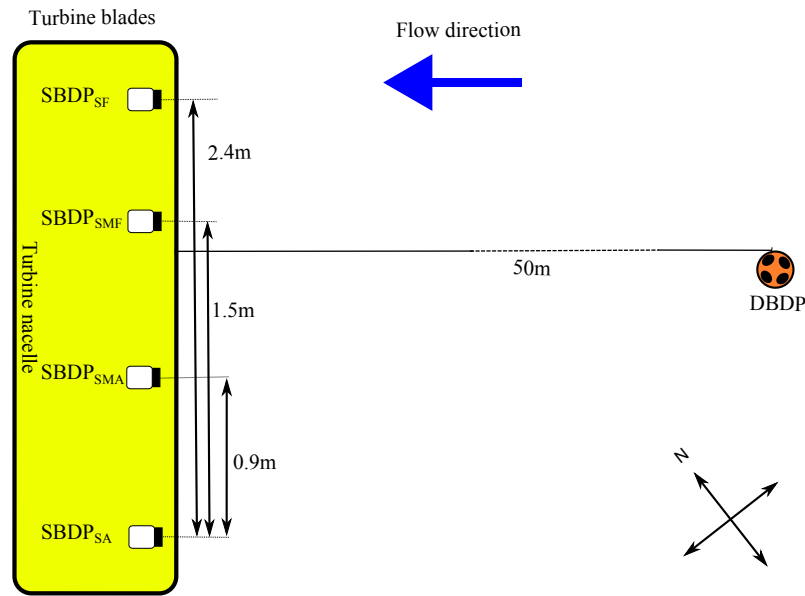


Figure 4.10: Overview of ‘side-on to flow’ instrument and turbine orientation.

the rear frame. This same sensor produced LSNR velocity results with the highest absolute mean value and lowest standard deviation. The bottom rear frame SBDP sensor had different grounding to the other two rear sensors which is explained further in Section 4.4. $SB DP_{RB}$ did not show a particularly high σ_{noise}^2 value in the powered tests, but the PSD result suggests that noise is not white for this instrument and noise could be higher at the lower frequencies. This will affect turbulence measurements but cannot be quantified and thus corrected by the line fit method, as a non-Gaussian noise distribution violates one of the stated assumptions. Therefore measurements taken by this sensor are excluded from the remainder of this work.

4.4 Part C - Quantification of Bias Error using the LSNR method

4.4.1 Methodology and Theory

Theory

In order to test if the LSNR mode velocity measurements could be extended to discern a measurement bias, a case study was undertaken. It utilised the four parallel SBDPs on the starboard side of the top instrumentation frame. For this test to be completed a data collection period was negotiated with the turbine operator Alstom to provide a turbine yaw angle such that the sensors were facing the undisturbed inflow (\bar{u}). The instrument and turbine orientation to the flow are illustrated in Figure 4.10.

Differences between velocity measurements from these four sensors with the measurements by the same instruments in LSNR mode were contrasted. This required a benchmarking instrument and the results of \bar{u} of all the instruments are de-trended by subtracting $\bar{u}_{SBDP_{SF}}$ for each sample set. To quantify the difference in velocity measured by the different SBDPs, $\Delta\bar{u}$ is defined:

$$\Delta\bar{u} = \bar{u}_n - \bar{u}_{SBDP_{SF}} \quad (4.14)$$

where n represents the measurements from one of the other three starboard facing parallel sensors and \bar{u} is the mean velocity over a 256 second sample.

It should be noted that there are other sources of variation in velocity measurements between sensors. This includes: spatial variation in the flow across the lateral separation, which in this case is a maximum of 2.4 m. In addition the alignment of the individual sensors to the flow provides an additional source of error. Sutherland *et al.* (2013) presents results calculated from data attained early in the ReDAPT project at the same site, indicates that the principal direction of the mean flow varies over the course of each 6.2 hour tide. For this experiment the turbine yaw and thus SBDP angle is fixed for each tide, allowing the onset flow angle relative to the acoustic beam to vary. If the starboard oriented SBDPs were at different angles significant enough to affect the velocity measurement, a variation in tide angle over the cycle will correspond to a variation in which sensor measures the highest velocity as the flow aligns with different angles.

In order to estimate if the angle of the sensors was affecting the bias calculations, the principle flow direction across the data set was calculated via the upstream DBDPs. For each of the two tidal cycles selected the corresponding data from the DBDPs were loaded for comparison. First the time stamps were matched to those of the SBDP data and data was divided into Ebb and Flood tides. Then the resultant flow angle is calculated as the angle of the resultant of the North and East DBDP velocities. The resultant flow heading angle is defined via:

$$\theta = \tan^{-1} \left(\frac{vel_{North}}{vel_{East}} \right) \quad (4.15)$$

where θ in the resultant flow angle from North, and vel_{North} and vel_{East} are the velocities measured by the DBDP along the stated compass vector. The quadrant of the angle (i.e. 0-90°, 90-180° etc) was preserved based on the sign of the vel_{North} and vel_{East} .

A key assumption in this work is that LSNR results are not time varying when the turbine is not operating and that the 5 minute sample of data is representative of the long term noise levels.

Data collection

For the case study a standard 0 dB pulse power setting data set was required from the four parallel SBDPs to contrast with the LSNR mode results. A roughly 11 hour period of data when the turbine was side on to the flow was utilised. The sensor's pulses were offset by 39 ms to ensure there was no interaction between the beams. The reason for selecting 39 ms is discussed in Section 5.3.4. Other instrument settings are detailed in Table 4.7. Data was used from a single range bin, 8.0 m from the instrument. Once the data set was selected it was divided into T_{stat} sub-sets, with a 50% overlap where sub-sets were concurrent.

The requirement to use the same sensors for both modes meant it was impossible to take concurrent measurements in both power settings. Thus the LSNR mode results are taken from the previous section. It must therefore be assumed that the LSNR velocity measurements are time and flow condition invariant.

Power (dB)	Sample Rate (Hz)	Cell Size (m)	Number of Cells	Blanking Distance (m)	Velocity Range (ms^{-1})
0	2	0.4	70	0.4	4

Table 4.7: SBDP settings for the analysis of bias study.

Quality control

Quality control was carried out as described in Section 4.2.1.

4.4.2 Results

Figure 4.11 shows the velocity measurements for the 11 hour data set available with the four parallel SBDPs facing the onset flow. The LSNR mode results from the previous section for the four relevant sensors are presented in Figure 4.12. The mean velocity value and standard deviation of velocity for the four SBDPs are detailed in Table 4.8 for both power modes. It shows that the largest magnitude velocity at a 0 dB power setting corresponds to the lowest velocity magnitude in the LSNR power mode. In addition, the standard deviation is highest in both modes in the same sensor.

In order to assess how the velocity measurements between the sensors vary with time and with \bar{u} , the velocity measurement differences ($\Delta\bar{u}$) are plotted alongside the reference velocity from SBD_{SF} in Figure 4.13. It shows a consistent pattern, with the greater the separation between sensors the greater $\Delta\bar{u}$. The differences can be seen to increase with inflow velocity, although there is a significant amount of fluctuation. $\Delta\bar{u}$ in SBDP_{SA} which shows the largest values, varies by a range of 0.14 ms^{-1} over the available data set.

In order to assess if the angle of the sensors were offset from parallel, the relationship between $\Delta\bar{u}$ and the principal flow direction (θ) was plotted. The principal flow direction was calculated

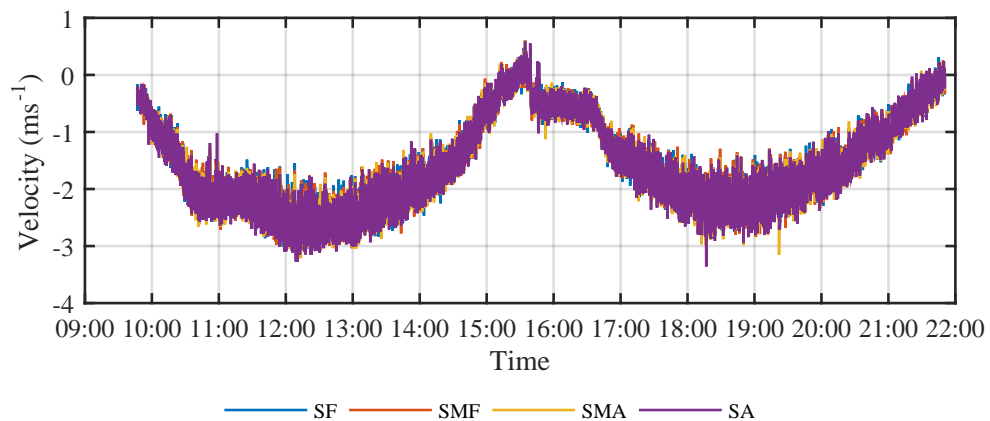


Figure 4.11: Powered (0 dB) SBDP velocity time series sub-set for the bias case study, highlighting the sensors measuring broadly similar inflow values.

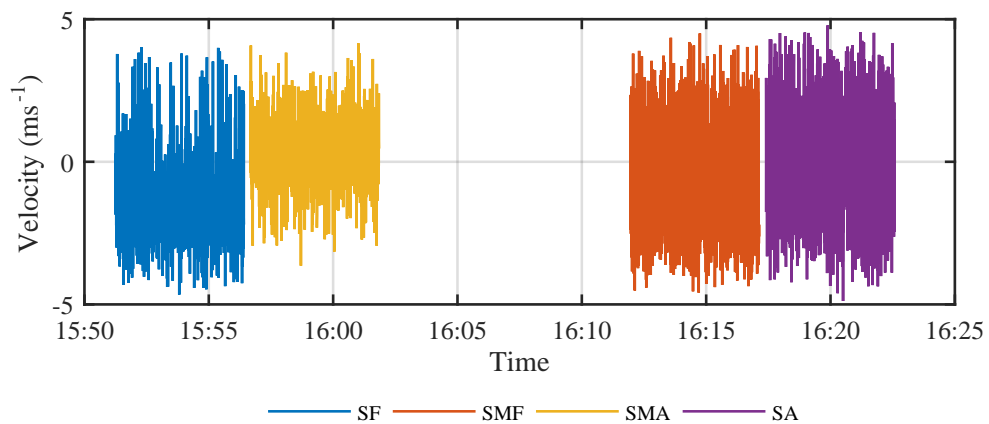


Figure 4.12: LSNR-mode velocity time series sub-set for the bias case study, highlighting small differences in mean and standard deviation of velocity values.

Power Setting		SBDP			
		SF	SMF	SMA	SA
0 dB	Mean	-1.55	-1.56	-1.58	-1.59
0 dB	σ	0.76	0.77	0.78	0.89
-100 dB	Mean	-1.50	-1.08	0.27	0.22
-100 dB	σ	1.42	1.98	1.14	2.01

Table 4.8: Case study velocities by individual SBDP for 0 dB mode.

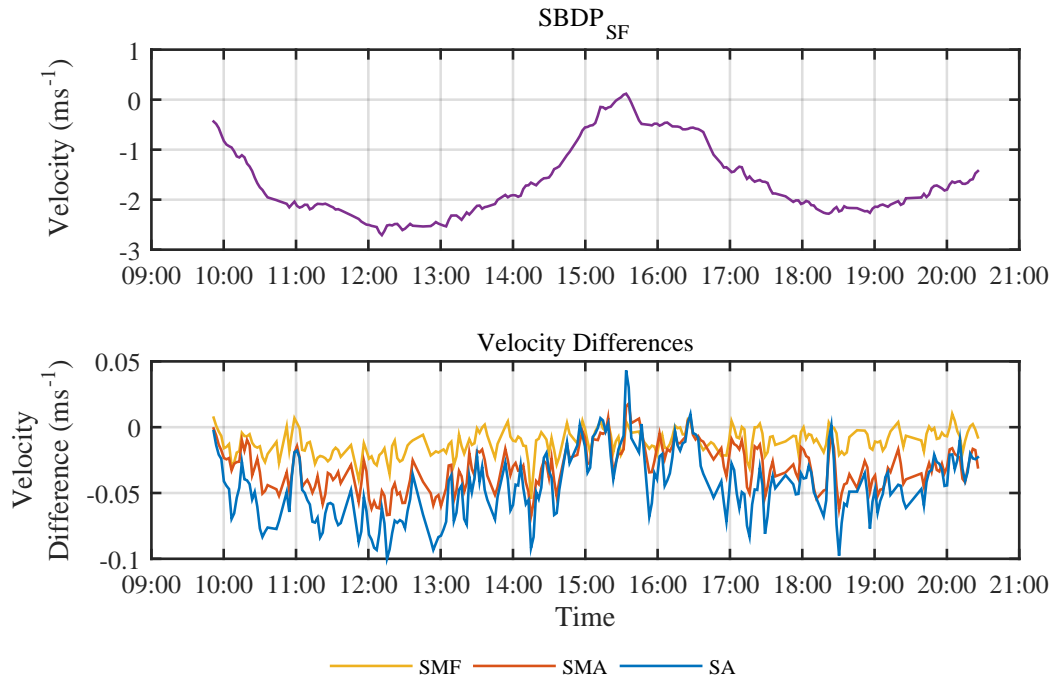


Figure 4.13: Differences in mean inflow velocity with time across four parallel sensors.

via the upstream DBDPs with the resulting angles presented in Figure 4.14. The light blue lines represent the 1 Hz data and the darker blue the 256 second mean values. The flow angles are limited to a range of 0° to 360° . However, here values for the Ebb tide where the resulting direction was greater than $0, 360^\circ$ is added to the values in order to compute the mean value correctly.

It can be seen that the noticeable variation in tide angle for both Ebb and Flood occur at the start and end of the tide. As the turbine was required to yaw between the two tides, there is a region of missing data over the start of the Flood tide.

One point of interest to highlight is the results for $SBDP_{SA}$ (and to a lesser extent $SBDP_{SMA}$) in Figure 4.15, is that at the lowest flow angles (50 to 120) $\Delta\bar{u}$ is positive, but as the angle changes as the tide velocity increases the velocity difference becomes negative.

The mean value and standard deviation of $\Delta\bar{u}$ across the four instruments, are contrasted with the mean values from the LSNR mode results in Figure 4.16. There is evidence of a correlation with an increase in magnitude in LSNR results relating to an increase in magnitude of the inflow measurement. Although with only four instruments the uncertainty in this relationship is high. Fitting a linear slope to these mean values constricted to pass through the origin gives a gradient of -0.022. The extra uncertainty associated with the result of $\Delta\bar{u}$ between the $SBDP_{SA}$ and $SBDP_{SF}$ sensors due to a probable angle offset may explain the greater spread of results and greater magnitude mean value.

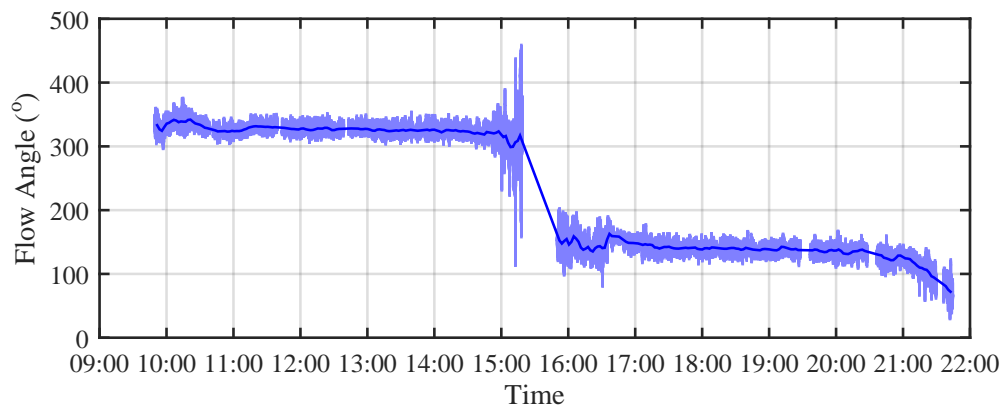


Figure 4.14: Resultant flow angle for case study data set. The light blue lines represent the 1 Hz data and the darker blue the 256 second mean values.

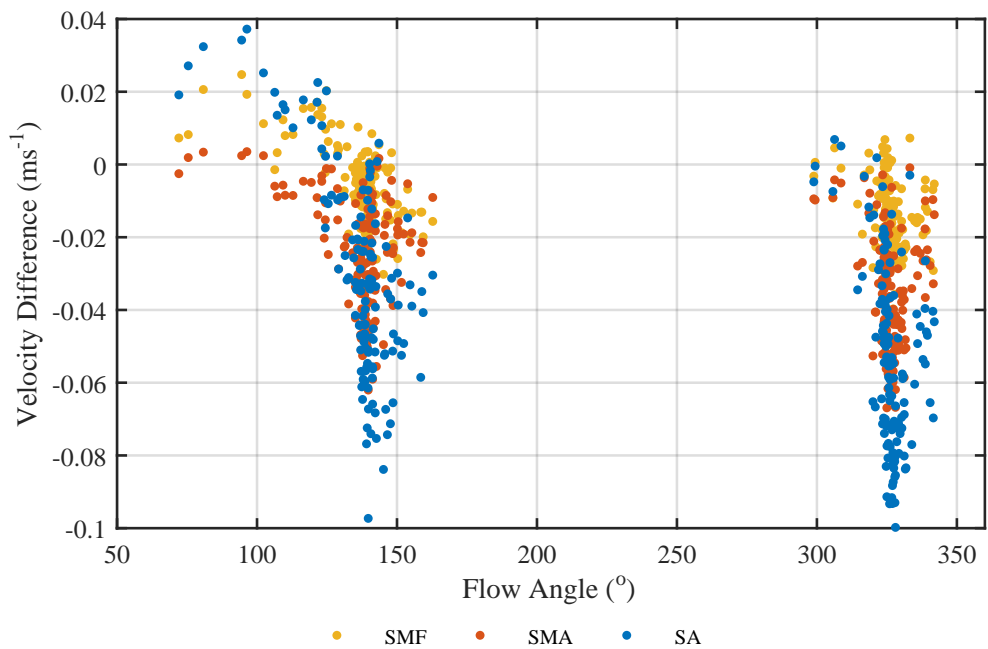


Figure 4.15: Velocity difference with resultant flow angle.

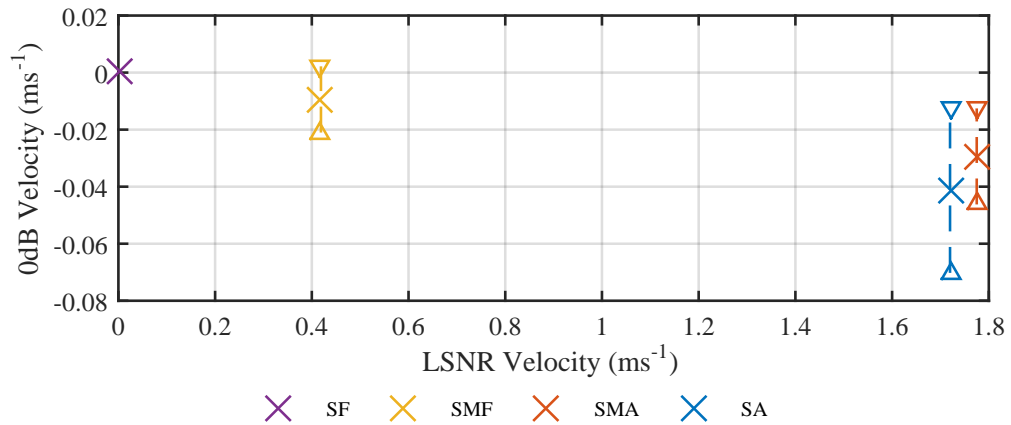


Figure 4.16: Test for bias in 0 dB pulse power mode compared with the LSNR measurements in four parallel SBDPs.

4.4.3 Discussion of results

Figure 4.16 shows evidence of a correlation between LSNR velocity measurements and a bias in 0 dB power mode, with increased magnitude in one corresponding to the other. However, with only four instruments the data set is limited and the gradient of -0.022 associated with the mean differences is, at best, a guide.

For the largest difference in measured velocity in 0 dB pulse power mode, the turbine angle was shown to be offset in Figure 4.15. Other causes of this velocity difference cannot be ruled out. These include: Spatial variation along the 2.4 m separation, however, a consistent difference in flow magnitude is unexpected over such a small lateral separation. Another is the angle of the Turbine to the flow (rather than the sensors individually) which could be offset.

A turbine angle offset of the turbine to the flow, would mean each sensor in effect measures a slightly different range from the turbine nacelle. Measuring further from the impeding effect of the turbine on the flow could cause the SBDPs to measure different inflows. However, a range-bin was selected where the velocity measurements are relatively stable with range and small offset angles would not make a large difference in effective range, thus the effect is assumed to negligible.

The final source of uncertainty is the angle of the SBDPs. Sensor misalignment would be expected to be manifested in the results as a change in which sensor measured the highest velocity value as the onset flow direction changes over the tidal cycle. Figure 4.15 shows that as the tide angle changed a difference in which sensor measured the largest value which would suggest an angle offset. The greatest offset appeared to be between SBDP_{SF} and SBDP_{SA}. This corresponded to a larger variance in the 0 dB mean velocity results highlighted in Figure 4.16.

It is likely that the differences in velocity are the combination of bias, spatial variation and sensor misalignment.

A final source of uncertainty is the temporal variation of the LSNR measurements, which was by necessity assumed to be time and flow condition invariant. Due to pressures on turbine time and data collection requirements discussed in Chapter 3, only a single 5 minute sample of these low priority data sets could be captured. A useful further study would be to monitor a long term variation in noise through this technique on turbine mounted sensors. including operating and non-operating conditions.

4.5 Part D - Noise Mitigation using Power and Grounding Modifications

4.5.1 Methodology and Theory

With evidence presented in Section 4.2.1 that the noise in the SBDPs may be in part caused by electrical interference, possible methods of mitigating this were investigated. The University of Edinburgh undertook the installation of an Isolated Power-Conditioning Transformer (IPCT) and a modification to the instrument grounding utilising a filtering capacitor. This trial was undertaken with the aim of decreasing random error and effectively increasing instrument measurement range.

Figure 4.17 shows the wiring of the capacitor grounding and IPCT modifications. The IPCT was a QUINT-PS/24DC/24DC/5 DC-DC converter, and was installed as, prior to deployment 6, the instruments had been recording operating voltages more than 1 V below the specified supply of 24 V despite multiple maintenance and mitigation steps. A below voltage specification power supply will limit the power of the transmitted acoustic pulse which will affect the effective range of the sensor and a noisy supply was theorised to affect the velocity measurements. The IPCT is supplied with a voltage over a large tolerance and transforms it to the specified output voltage, as well as providing electrical isolation between loads (Phoenix-Contact, 2014). There was no installed instrumentation to measure the magnitude and noise on the power supply to the sensors. The SBDPS (like most Doppler sensors) record Quality Control (QC) indicators based on both returned-pulse correlation and amplitude. The affect of the IPCT on the SBDP was assessed via the recorded voltage, the QC metrics and the velocity measurements.

Another potential source of noise in the instruments is the grounding method. Following correspondence during the project, it was recommended by the instrument manufacturer that the sensors be grounded to the seawater via a filtering capacitor to remove high frequency noise from the power supply. A 100 μF capacitor was selected as per instrument manufacturers recommendation (Nylund, 2013b). The 0 V line was connected via a cable attached to a 316 stainless steel rod approximately 10 cm long and 3 cm² cross-section, in contact with the seawater. Capacitors are used to increase impedance acting as a high pass filter so that high frequency signals will pass to ground while the lower frequencies will travel along the low

impedance path to the device. Figure 4.17 shows the setup of the IPCT and filtering capacitor on the turbine.

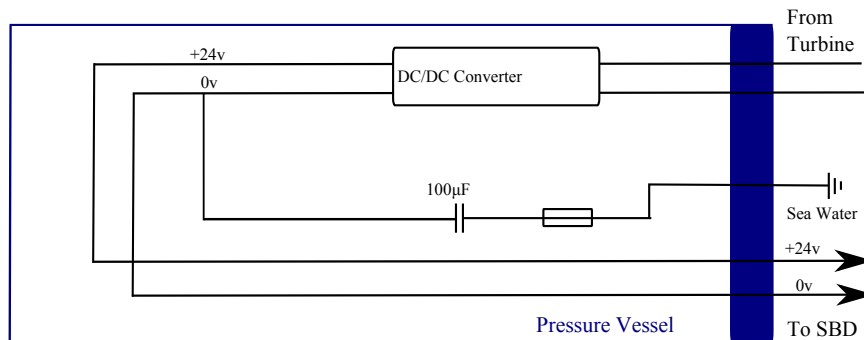


Figure 4.17: Circuit diagram for the hard-wired grounding modification and DC-DC isolated power-conditioning transformer, installed on the rear instrumentation frame.

A relay switch allowing the remote selection of grounding and power supply options, including multiple selectable sizes of capacitors to select different filtering frequencies, was installed on the top instrument frame prior to deployment 6. However, it was discovered upon recovery the cable connecting the stainless steel grounding rod had eroded. A second system (which was non-switch-able due to time constraints) of these IPCT and capacitor grounding option was installed (and intact) on two of the rear frame instruments. The third instrument was fed power directly from the turbine 24 V DC supply. Thus the effect of both noise mitigation methods combined was investigated but it was not possible to discern the effects of the individual techniques. In addition, as two different sensors were required, dissimilarities between instruments and their locations could not be ruled out and provide an additional source of uncertainty.

Differences between the results of the two sensors were quantified firstly through the QC metrics; amplitude and correlation of returned pulses. Then the standard deviation of the velocity measurements along the range are contrasted.

Data collection

Both sets of tests used two SBDPs mounted on the rear instrumentation frame on the turbine. Specifically the Top and Bottom mounted sensors $SBDP_{RT}$ and $SBDP_{RB}$, which are vertically separated by 1 m (see Section 3.5 for more information on instrument locations). $SBDP_{RT}$ was equipped with the power supply conditioning and grounding and $SBDP_{RB}$ was powered straight from the turbine 24 V DC supply. 540 minutes of coincident data were measured over the 24th of June to the 1st of July 2014. This was part of turbine deployment 6 which commenced on the 22nd of June. The sensors pulses were off-set by 39 ms to ensure there was no interaction

between the beams (the reason for selecting 39 ms is discussed in Section 5.3.4). Other SBDP settings for this test are detailed in Table 4.9. Once the data set was selected it was divided into T_{stat} bins as described in section A, with a 50% overlap where sub-sets were concurrent.

Power (dB)	Sample Rate (Hz)	Cell Size (m)	Number of Cells	Blanking Distance (m)	Velocity Range (ms^{-1})
0	2	0.4	70	0.4	4

Table 4.9: SBDP Settings for DC-DC isolated power-conditioning transformer and grounding modification test.

Quality control

Quality control was carried out as described in Section 4.2.1.

4.5.2 Results

The effect of the IPCT is evident in the operating voltages measured by the sensors. The Top SBDP fitted with the IPCT measured a mean voltage of 23.5V while the bottom sensor without power supply treatment measured 22.4V.

The effect of the modifications on the mean correlation and amplitude measurements with range, are illustrated in Figure 4.18. The modifications have the effect of decreasing the mean amplitude by 0.10 dB and increasing the mean correlation of the return pulse by 4.63 %_{unit}. The most noticeable difference being in the correlation in the range beyond 11 m. Note that ‘%_{unit}’ is used to represent a direct difference to the original percentage value as distinct from a percentage increase.

The effect of the noise mitigation modifications on velocity with range over the available data set is illustrated in Figure 4.19. Over the majority of the range the measurements are relatively well matched. However, at the region where the noise starts to dominate at around 20 m there is a disparity in results. Without the modifications there is a large number of measurements at spuriously high velocity values compared with the measurements in the SBDP with the modifications.

In order to highlight this effect a ‘snapshot’ of an hour of data at a range of 20 m for both instruments is presented in Figure 4.20. It shows the increased number of non-physical velocity spikes in the SBDP with standard power supply and grounding. This phenomenon is not present in the close (< 3.2m) range bins and increases more rapidly with range in the SBDP with standard power supply and grounding, although it does appear to a degree in the modified SBDP, as can be seen in Figure 4.20 with the spike between 23:25 and 23:30.

This increase of noise manifesting as non-physical velocity spikes with range is investigated via the difference in standard deviation of velocity measurements between the two sensors

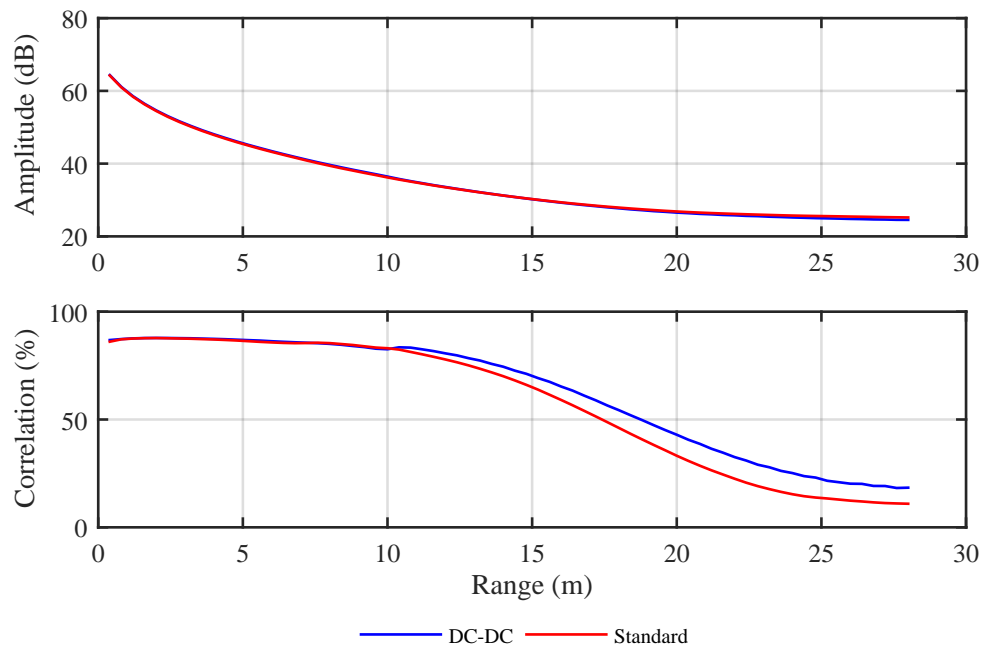


Figure 4.18: Mean amplitude and correlation returns from 2 power supplies from SBDPs at 0 dB power setting.

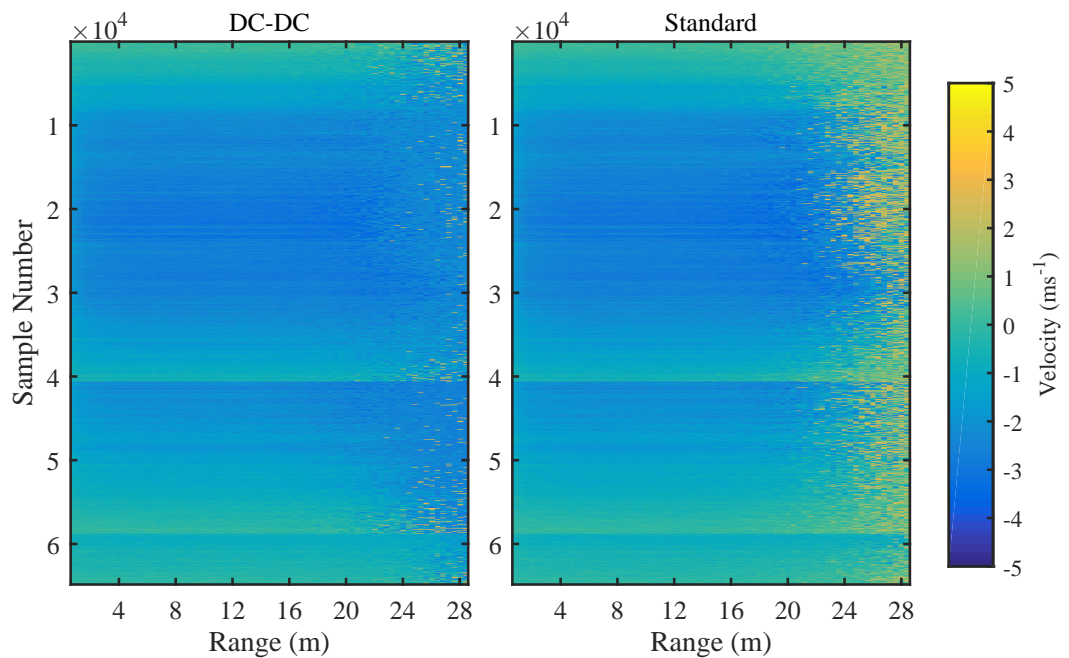


Figure 4.19: Velocities from a single SBDP in 0 dB mode with and without the DC-DC isolated power-conditioning transformer.

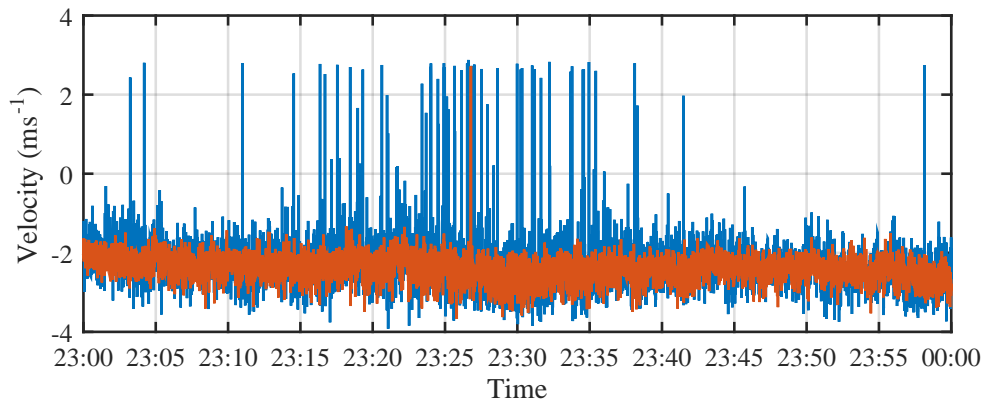


Figure 4.20: Subset of velocity measurements from a single SBDP in 0 dB mode with and without the DC-DC isolated power-conditioning transformer at a single bin at a range of 20 m.

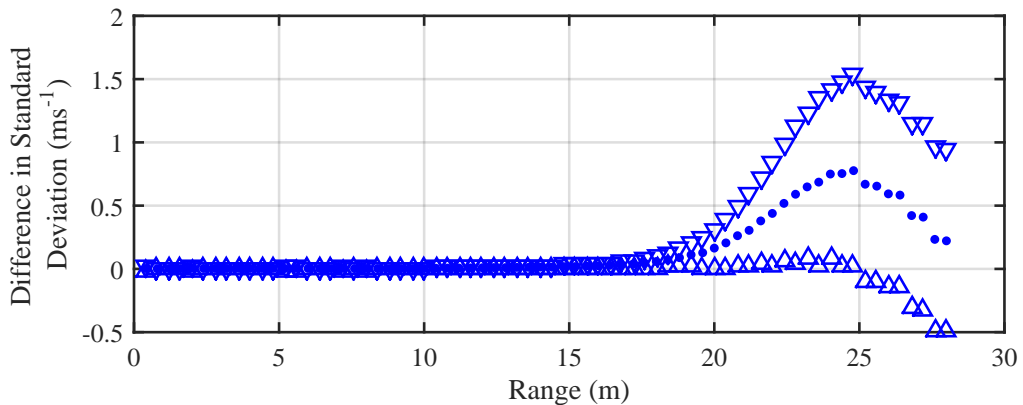


Figure 4.21: $\Delta\sigma_u(x)$ from SBDPs at 0 dB power setting. Blue dots represent the mean difference in standard deviation. The blue triangles represent the standard deviation in the difference around the mean value.

($\Delta\sigma_u(x)$). Figure 4.21 illustrates the mean standard deviation in velocity measurements for each range bin (blue dots), as well as that standard deviation around that mean value (blue triangles). It shows that up to 10 m range there is very little difference in the standard deviation measurements. The SBDP with the modifications has a smaller standard deviation by $3.27 \times 10^{-3} \text{ ms}^{-1}$ over this range. Beyond this range that difference in standard deviation increases significantly up to a maximum of 0.78 ms^{-1} at 24.8 m range. At the extreme of the range the difference decreases towards zero. Mean difference in standard deviation is lower across the range with the addition of the IPCT and grounding modifications.

The addition of the modifications is significantly reduced instrument noise across the 17 m to 24 m range and increases the effective range of the sensor by approximately 4m. In turbine mounted application where sensors are required to measure remotely at ranges outwith the

effect of the turbine nacelle impeding the flow, a 20% increase is a useful improvement.

4.5.3 Discussion of results

Of the two rear instrument frame SBDPs analysed, the one fitted with the grounding and power supply modifications has an increased effective range compared with the SBDP with a hard-wired path to seawater to ~ 20 m. The regular occurrence of non-physical spikes in velocity measurements are moved from 17.2 m to 20 m range after which the occurrence increases significantly which is highlighted by the standard deviation increase illustrated in Figure 4.21. The quality control metrics show very similar amplitudes and an increase in correlation in the > 10 m range with the modifications. It is clear that noise is more prevalent in the extreme of the range as the strength of the returned acoustic pulse is weaker.

These differences in noise can not be ruled out as being due to sensor placement, but the results do provide evidence that the modifications have been effective in mitigating noise and thus increasing the effective range of the sensor.

Due to the timing of the installation of these upgrades at the start of turbine deployment 6, which coincided with a period of high opportunity to measure flow conditions required for the Core Tests, these power supply conditioning tests were de-prioritised. A follow up study with the grounding and IPCT on separate switches would help reveal the effects of the individual techniques. In addition, the effect of different capacitor sizes may help reveal the frequency range of the noise on the electrical line that needs to be removed to most effectively improve velocity measurements.

4.6 Conclusions

There are several uncertainties associated with the results of this chapter. Primarily that the data was not collected in a controlled and repeatable environment. The flow and ambient conditions are constantly fluctuating. In addition the turbine has a number of operating conditions which could affect the levels of noise that could not be monitored. As discussed in Chapter 3 there were limitations on data collection throughout the project. This meant cases such as Section 4.3 where a single Ebb and Flood tide had to be assumed to be representative of all flow conditions. In addition the 5 minute LSNR data sets assumed no variation in electrical noise over time when the turbine was not operating, which is an unquantified uncertainty.

The results of Section 4.2.1 shows a large discrepancy in the results of the relationship between variance due to noise and flow velocity based on sensor orientation as presented in Figure 4.4. The two relationships in Equations 4.11 and 4.12 can be defined based on these results to estimate the correction factor for Equation 4.4. The contrast in the relationship between the

variance attributable to noise and velocity based on sensor orientation is an important outcome of this work utilising this newly available technology.

Section 4.3 presents velocity readings taken with LSNR power mode so as to maximise the effects of noise, which revealed very different velocity measurements in terms of: magnitude, distribution and fluctuation based on sensor location. In particular, there was a contrast in results between instruments mounted on the top and rear instrumentation frames. There is some evidence that the variance in the LSNR mode is indicative of increased variance due to noise in normal operating power settings, looking at a sub-set of parallel sensors, as illustrated in Figure 4.8. However, further work is needed to capture more data to assess long term variations, particularly for the LSNR mode data. It is also evident that this is not as prevalent a source of noise as the orientation to the flow, as demonstrated by the range of σ_{noise}^2 values over the top frame sensors listed in Table 4.4. It seems likely that there are different noise sources causing different effects, which would explain the differences in LSNR velocity measurements across the two frame locations. However, this could not be quantified. The results suggest that this effect is minimal compared with the effect of instrument orientation and can be assumed to be negligible in terms of I correction. The LSNR mode results suggest that in all but the case of one sensor the noise was relatively evenly spread across the frequency range as predicted.

Section 4.4 showed evidence in Figure 4.16 that LSNR ratio results can also be used to indicate instrument bias, using a sub-set of parallel sensors measuring the same onset flow. However, with other effects which were unquantifiable only a very rough indicator to quantify the relationship could be generated, which is: $\bar{u}_{0dB} = -0.022 \cdot \bar{u}_{-100dB}$. This methodology shows potential but has not been fully validated and requires further work.

Section 4.5 showed evidence that a combination of grounding via a filtering capacitor and power supply treatment could be used to reduce noise and increase the effective range of the SBDPs. There was an increase in correlation over the range above 10 m as shown in Figure 4.18. This led to in a reduction in instrument noise which manifested itself as non-physical spikes in velocity measurements as illustrated in figures 4.19 and 4.20. A repeat test of the remotely selectable IPCT, grounding and multiple capacitor sizes, which suffered a hardware failure as discussed in section 4.5.1, would be valuable. Preliminary ad-hoc trials of this system showed clear improvements in effective range. Collecting a large quantity of data over a range of flow conditions within this test, would increase knowledge of the best noise mitigation strategy for mounting sensors on a tidal turbine.

The transient nature of the noise in the LSNR measurements needs to be investigated. For future turbine mounted acoustic velocimeter campaigns it is recommended that as part of the commissioning phase a series of LSNR tests over a period of the M2 tidal harmonic components is undertaken. This will improve the understanding of long term noise variation. As part of this it would be recommended to cycle through high powered turbine operations to gain a deterministic understanding of the effects of these operations. If acoustic velocimeters

on turbines are to play a key role in site characterisation and turbine operation confidence in their ability to work effectively in these environments must be increased.

An improved LSNR mode velocity data set could help improve the study of instrument bias. The same experimental set up with sensors aligned to the flow to a high level of accuracy could measure alternative 0 dB and -100 dB sample sets in ~5 minute bursts. This would lead to two data sets for statistically very similar flow conditions. Any differences in velocity between the sensors for each mode can then be assessed for a range of flow conditions

The specification of appropriate grounding for turbine mounted system requires collaboration with turbine engineers to optimise the power supply for sensors, as retro-fitting such systems is challenging. Electrical interacting sub-systems in seawater require very careful design and further studies are required to optimise sensors for turbine mounted operation. A series of tests utilising a remote switch to alternatively select either filtering capacitor grounding, IPCT or both for a range of flow conditions and turbine operational states, would increase confidence in best practise for using acoustic sensors mounted on a turbine. Further to this, a remote relay switch system like that installed on the top instrumentation frame, would allow the effect of a series of capacitors of different sizes to be tested. As part of this experimental set-up, it is recommended that an automated system for recording relay switch position be installed, as this would increase accuracy of data recording by reducing human error. As the capacitance is linked to the frequency of the filtering of the noise this would allow analysis of the best value to be used for this application. A test to analyse the DC power signal before and after these treatments would help identify the sources of noise as quantify the effect of the mitigation procedures.

4.7 Chapter Summary

The goal of this chapter was to quantify the different types of noise in individual SBDPs. It has detailed the derivation of a correction factor for turbulence metrics that can be used throughout the rest of this thesis. The bias detection requires further work and is not used in any further work herein. Recommendations for use of noise mitigation technology has been made for future turbine mounted Doppler measurement campaigns. The next chapter focuses on noise caused by cross talk between closely located acoustic instruments.

Cross-talk Between Co-Located Acoustic Instruments

5.1 Chapter Overview

In order to assess the potential benefits of operating multiple acoustic sensors in close proximity, the effects of cross-talk must be investigated and, if possible, mitigated. Cross-talk is a well known phenomenon whereby a signal emitted on one channel of a transmission system creates an undesired effect when received by a separate channel. Acoustic pulses from sub-sea Doppler sensors are known to interact (Yu and Gordon, 1995) but these interactions will vary with pulse frequency, sensor angle and separation. This section investigates and, where possible, quantifies this effect. This is achieved by analysis of both the quality control metrics (amplitude and correlation) and the velocity measurements.

The effects on SBDPs are considered in a range of sensor configurations. With tests designed to quantify the sensitivity to:

- Instrument separation;
- Power of source signal;
- Angles between acoustic beams;
- Measurement of velocity components by cross-talk;
- Mitigation by ping offsets;
- Surface reflections and
- Interference from other sensor types.

5.1.1 Motivation

The use of SBDPs as part of arrays of acoustic sensors provides potential advantages over single sensor deployments in flow characterisation work. In order to use multiple sensors in close proximity the effects of cross-talk must be understood so that they can be: identified, predicted and mitigated. This chapter aims to provide a comprehensive review of these effects and make recommendations on instrument placement, as well as power and timing settings to minimise the effects of cross-talk on velocity measurements in acoustic sensor arrays.

5.1.2 Author's contribution

The instrumentation set-up and data collection was a collaborative effort between the author and the project principle investigator as discussed in Chapter 3. The author was responsible for the specification and carrying out of data collection for these tests. The processing algorithms, analysis and results are the sole work of the author unless specifically cited.

5.2 Methodology

5.2.1 Theory overview

Cross-talk is a common phenomenon in acoustic instruments with interactions between pulses known to adversely effect results (Appell *et al.*, 1991). In DBDPs, noise in measurements is most often due to side-lobe interference between the beams, where energy not concentrated in the main acoustic beam interacts with the signal of a second beam (Nystrom *et al.*, 2002). However, as the sensor beam angle converges the interactions between devices is expected to increase significantly. In order to give some context to the results of this investigation into the effects of cross-talk, it is worth detailing the underlying processes, in particular, with regard to the expected effects in the context of the transmit-receive cycle of the SBDPs, first discussed in Chapter 2. For the purposes of this chapter the instrument whose beam is causing interference is defined as the 'source', and the one experiencing it as 'affected' or 'receiving' regardless of the instrument type, setting or orientation.

The SBDP instruments are connected by a GPS clock which allows the co-ordination of the transmit receive cycle via Precision Time Protocol (PTP), the timings of which are accurate to $\sim 10 \mu\text{s}$.

An example is given in Figure 5.1 of two parallel instruments. One is set to full pulse power (0 dB) mode as per normal operating conditions. The other is set to Low Signal to Noise Ratio (LSNR) as defined in Chapter 4. A LSNR sensor follows the same transmit-receive cycle as it would in a normal operating power mode. Thus if the blanking distance and cell-size are equal (as they were for the tests in this chapter) across two instruments, they will initiate the same transmit-receive cycle and gate the responses at the same times.

The two sensors are separated by 1 m and Figure 5.1 illustrates 'snap shots' in time up until the transmitted pulse first reaches the receiving LSNR sensor. The LSNR sensor is on the right, with the red pulse representing the -100 dB signal it expects to process, and the sensor on the left is the source in normal 0 dB power mode transmitting, with the black pulse representing its acoustic pulse. In this example, the blanking distance and cell-size are both 0.4 m. Thus the pulse lengths of the two instruments are also equal. For a speed of sound in sea water of 1490 ms^{-1} , the pulse and each receiving gait lasts 0.27 ms.

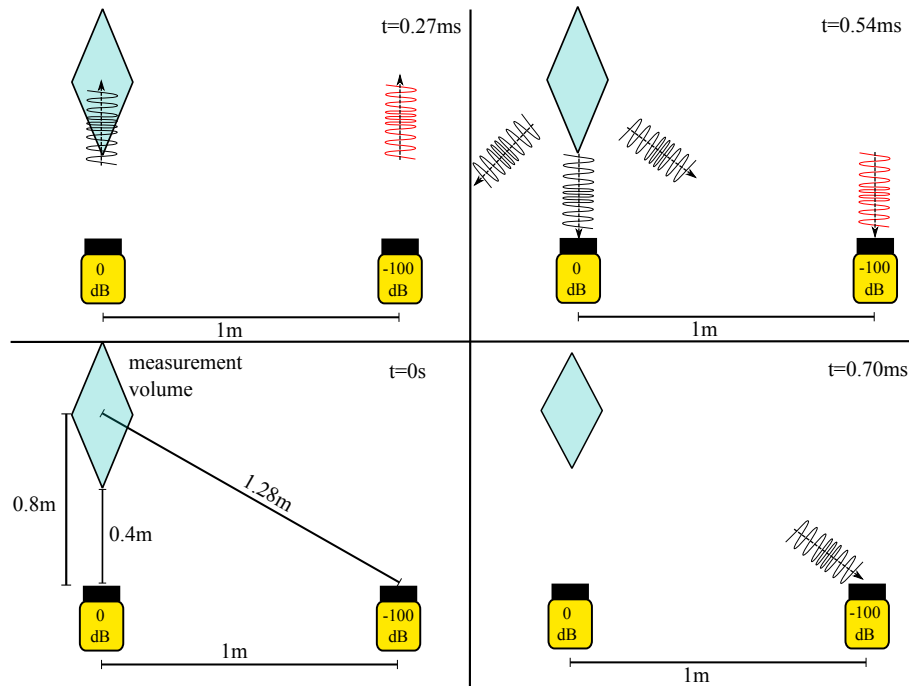


Figure 5.1: Cross talk illustration showing a subsection of the transmit/receive cycle of two parallel SBDs. The black pulse is from the powered sensor and the red the -100 dB pulse of the LSNR instrument. The timing of each phase is given at the top right of each panel and starts at the bottom left advancing anti-clockwise.

The first (bottom left) panel shows the instrument setup. The second (top left) panel shows the complete transmit part of the cycle with a pulse of 0.27 ms covering the blanking distance and the leading edge of the pulse just reaching the centre of the first sample volume. The third (top right) panel the leading edge of the 0 dB pulse has reflected off the scatterers in the first cell measurement volume and reflected in multiple directions. The leading edge of the along beam reflection has reached the transducer of the 0 dB SBDP at the start of the first gating of its receive cycle. The trailing edge will have just reached the centre of the measurement volume and the first gating of the receive cycle will continue from 0.54 ms to 0.81 ms. The -100 dB sensor does not receive the leading edge of the reflected pulse until 0.70 ms. Thus the pulse overlaps the first and second gating of the receive phase of its cycle.

Figure 5.2 illustrates this final panel from the point of view of the LSNR SBDP as a graph tracking the pulse in range and time. The two magenta lines represent the leading and trailing edges of the transmitted pulse heading away from the sensor. The solid black lines represent the reflected signal back to the transmitting SBDP with the blue shaded cells representing the measurement volumes of each range cell. This highlights the weighting and overlapping of measurement cells as detailed in Section 2.6. The red lines show the leading and trailing edges of the 0 dB pulse as experienced by the LSNR instrument. This delay will increase with parallel instrument separation for the other two LSNR sensors.

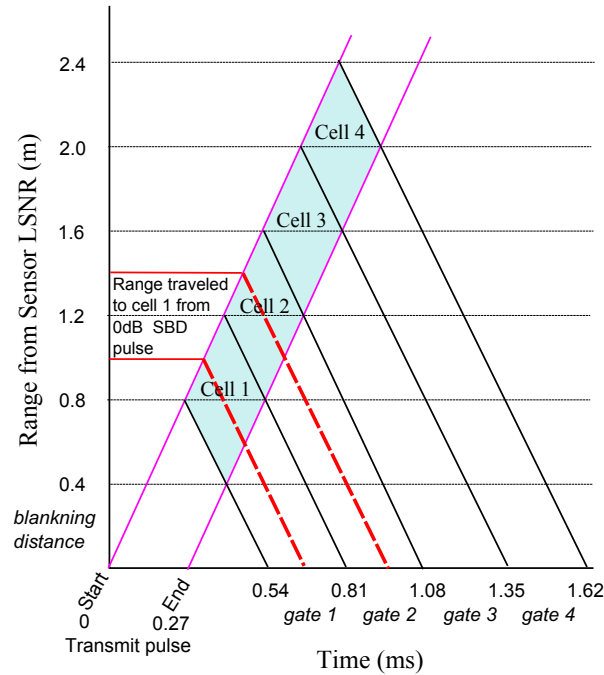


Figure 5.2: Transmit/receive cycle and range gating of an SBDP with the reflected signal from a 1 m separated neighbouring instrument super-imposed. Image adapted from (Gordon, 1996).

Thus in theory the starting point of any interference for a given instrument separation can be predicted. However, what effect this will have on the velocity and any variation with the magnitude of the interference is not known. In addition it should be noted that if the leading edge of the source signal is well aligned with the expected receiving instrument the resulting effect may be different to that of a poorly aligned signal.

5.2.2 Tests and data collection

Basic example and variation with separation and power

In order to test both that the theory of interference location are valid and how it is manifested in the QC metrics, a test was devised to maximise evidence of cross-talk. This utilised four parallel SBDPs with one instrument set to a 0 dB pulse power setting (mounted on one extreme of the set) and the other three in LSNR mode. An illustration of the instrument configuration is presented in Figure 5.3 and the instrument settings for this test are given in Table 5.1.

For a LSNR mode sensor the correlation and amplitude should be flat across the range bins corresponding to background noise levels, as shown for amplitude in Figure 4.5 in Section 4.2.1. Thus for this test, any variation in the amplitude or correlation over the range in the LSNR instruments would be evidence of cross-talk. By including multiple instruments in LSNR mode at multiple separations from the source of the signal, the relationship with separation from the

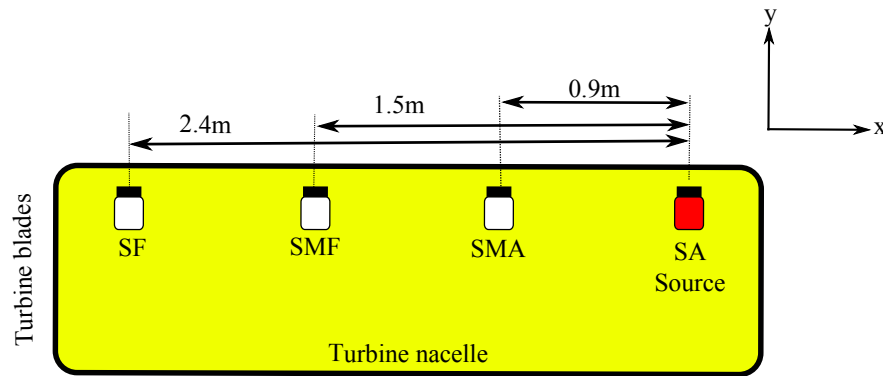


Figure 5.3: Instrument configuration on the top frame of the turbine for the parallel cross-talk test.

	Instruments			
	SBDP _{SA}	SBDP _{SMA}	SBDP _{SMF}	SBDP _{SF}
Power (dB)	0	-100	-100	-100
Pulse offset (ms)	28.6	9.5	9.5	9.5
Sample Rate (Hz)	2	2	2	2
Dates collected	08/08/2014 13:39 - 16:53			
Samples	2401			

Table 5.1: Data collection for basic LSNR test

source could also be investigated.

For this test the source SBDP was offset from the receiving SBDPs by 19.1 ms, with the transmit pulse delayed from the listening sensor. This was done in order to have the effect of the first indications of interference, being received at a later gating, i.e. as further along the range. With 19.1 ms chosen due to the offset in range being approximately in the middle of the sensor range, (the use of offsets is discussed in more detail in Section 5.3.4). In terms of the range gating illustration in Figure 5.2, this configuration would have the effect of moving the red lines to the right. This was done to move the evidence of cross-talk away from the edge of the range of the sensor to ensure it would be clearly visible.

Once the regions of interference have been identified the affected sensors were reconfigured with an acoustic pulse power of 0 dB, so that the indicators and effect of cross-talk in an operational configuration can be assessed. Again this requires a baseline for comparison. The standard correlation and amplitude returns for a single SBDP at a pulse power setting of 0 dB, with no evidence of interference are given in Figure 5.4.

This configuration represents that of the SBDPs normal operating pulse power setting. Thus the variation of velocity with range can be analysed in the identified regions of cross-talk against

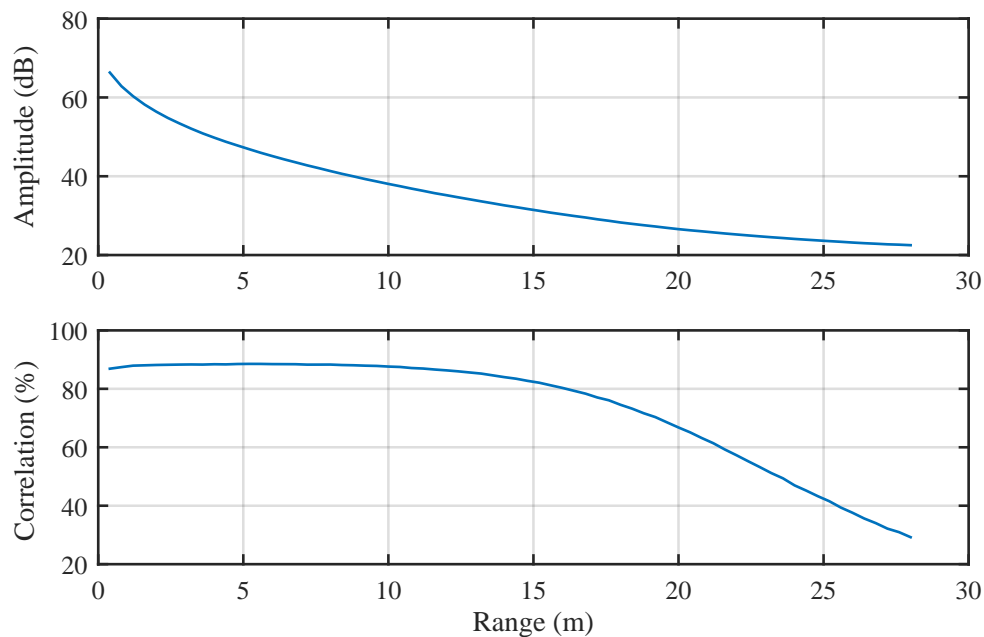


Figure 5.4: Amplitude and correlation for SBDP with no interference.

the baseline. Utilising the three parallel SBDPs the effects can be compared for three separation distances. Beyond this, the power of the source instrument can be varied to quantify a critical signal to noise ratio (SNR) below which the effects of cross-talk are negligible. The instrument configurations for the separation and source power tests can be found in Table 5.2 for variation with separation and Tables 5.3 and 5.4 for two tests of varying source power at 0.9 m and 2.4 m parallel separations.

Effect of angle between instruments with bisecting beams and measuring velocity components

The previous test was then repeated for three sensors aligned along one axis but orientated at an angle such that their beam paths cross, creating two angles. The sensors are mounted on the top instrumentation frame of the turbine. They form a transect of a five SBDP focus beam ‘pyramid’ set-up (as used in Sellar *et al.* (2015)) as illustrated in Figure 5.5. The angles between the acoustic beams were 23.2° and 46.4° . Due to the construction of the instrumentation frame, which had structural beams running along the centre, it was not possible to mount the vertical SBDP exactly half way between the two outer SBDPs.

A first test is conducted with a single source sensor set to 0 dB pulse power, and the other two in LSNR mode to identify interference locations in the amplitude and correlation measurements. A second test was then carried out with all the sensors configured with a pulse power of 0 dB to quantify effects in an operational configuration. This second test focused on effects on

Separation (m)	Instruments					
	SBDP _{SA}	SBDP _{SMA}	SBDP _{SMA}	SBDP _{SF}	SBDP _{SA}	SBDP _{SF}
	0.9		1.5		2.4	
Power (dB)	0	0	0	0	0	0
Pulse offset (ms)	19.060	0	19.060	0	28.6	19.1
Sample Rate (Hz)	2	2	2	2	2	2
Dates collected	01/07 - 01/08 2014		01/07 - 25/07 2014		28/07 - 19/07 2014	
Samples	12735		7323		5425	

Table 5.2: Data collection for 0 dB pulse power test at three separations.

Separation (m)	Instruments	
	SBDP _{SA}	SBDP _{SMA}
	0.9	
Power (dB)	-5, -3, -1, 0	0
Pulse offset (ms)	28.6	9.5
Sample Rate (Hz)	2	2
Dates collected	01/07 - 01/08 2014	
Samples	5209, 5448, 6036, 12735	

Table 5.3: Data collection and instrument settings for varying source pulse power at 0.9m

Separation (m)	Instruments	
	SBDP _{SA}	SBDP _{SF}
	2.4	
Power (dB)	-100, -10, -5, -3, -1, 0	0
Pulse offset (ms)	23.8	0
Sample Rate (Hz)	2	2
Dates collected	28/07 - 09/08 2014	
Samples	5425, 5432, 5109, 5012, 4839, 3782	

Table 5.4: Data collection and instrument settings for varying source pulse power at 2.4m

velocity measurements and its standard deviation along the range. Again a pulse offset of 19.1 ms was utilised in the receiving sensors, in order to increase the ease of identification of affected regions. Information of instrument configuration and data collection are given in Table 5.5.

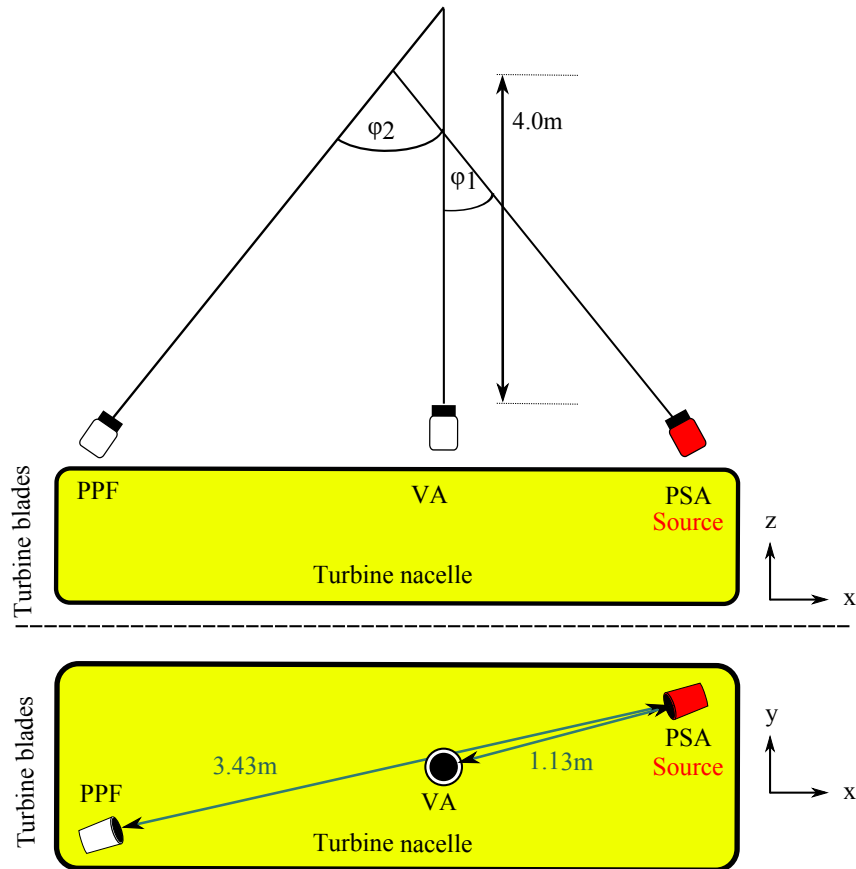


Figure 5.5: Instrument configuration on the top frame of the turbine for the angled cross-talk test.

One of the possible effects of cross-talk is that the receiving sensor will measure the component of the flow. As all the SBDPs send an identical coded pulse, any SBDP should be able to process the signal of a neighbouring instrument's signal as it would its own. Figure 5.6 shows a basic example of this process for two SBDPs separated by 1m. One mounted normal to the primary flow direction and one inclined by an arbitrary angle θ . It shows that the signal from the source sensor reaches its first measurement volume, part of the pulse is reflected along the angle of the affected SBDP. As the reflected pulse is along a component of the free stream velocity u it will experience a Doppler shift. The component relating to this shifted frequency is the bisecting angle of the two sensor beams (Lohrmann *et al.*, 1994). The accuracy of this method is likely to depend on the alignment of the source pulse with the expected receiver pulse.

This would allow a sensor in LSNR mode to measure a component of the flow speed. If this process is shown to be possible there are applications for the technique. One suggestion is

	Instruments		
	SBDP _{PSA}	SBDP _{VA}	SBDP _{PPF}
Angle(°)	0	23.2	46.4
Power (dB)	0	-100/0	-100/0
Pulse offset (ms)	9.6	29.7	29.7
Sample Rate (Hz)	2	2	2
Dates collected	24/07 - 28/08 2014		
Samples	3124		

Table 5.5: Data collection and instrument settings for the two tests for two angled SBDP. One with two SBDPs in LSNR mode and a second with all instruments at 0 dB power.

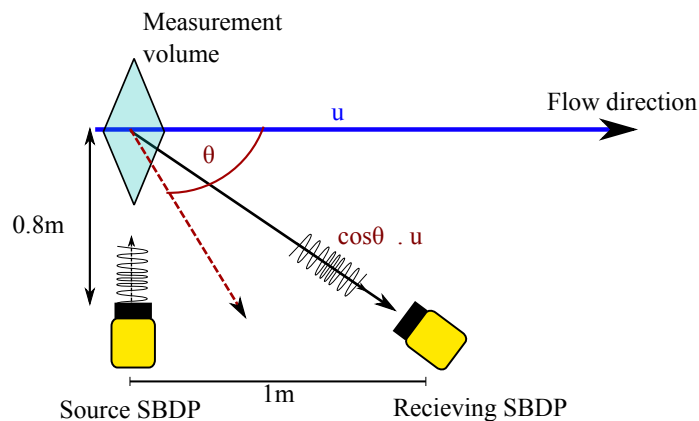


Figure 5.6: Illustration of the theory of two angled sensors measuring a component of the free stream velocity along the angle intersecting the two beams.

that multiple SBDPs in LSNR around a single powered vertical SBDP would allow velocity measurements which are resolvable into multiple components. This bi-static set-up would allow three Cartesian velocity measurements to be made remotely from the instrument position, but with a significantly smaller sample volume required compared with a standard DBDP. This would significantly decrease reliance on the spurious assumption of a homogeneous flow, which is particularly inappropriate for measuring turbulence metrics.

In order to assess this theory a test was designed utilising two SBDPs, one vertical and one on the 23.2° angle. The power settings of the two instruments was alternated between -100 dB and -3 dB, with each sensor configured at the opposite power setting for a given sample. 2.5 minute samples were taken in this interleaved manner, with the assumption that velocity in the flow would be of stable mean and variance over a 5 minute period and thus consecutive samples covering the two sets of configurations would be comparable. The data of the angled sensor would thus give: a consecutive along beam in powered mode data set and a bisecting component from the LSNR mode data set, which could be compared.

It is anticipated that the accuracy of this method will be affected both by the angle between the

sensors, with an optimal condition such that the transducer is facing the intended measurement volume, and with the coinciding of the leading edge of the pulse with the start of a range gating period. Thus the test trialled a range of pulse offsets to try and maximise the accuracy of the results. The settings for the test are given in Table 5.6.

	Instruments	
	SBDP _{PPF}	SBDP _{VA}
Power (dB)	-3 and -100*	-100 and -3*
Pulse offset (ms)	0.0, 0.1, 0.2, 0.3, 0.4, 0.5, 0.6, 0.7 and 78.0*	0.3 and 0.0*
Sample rate (Hz)	2	2
Blanking distance (m)	0.4	0.8
Dates collected	11/07 to 24/07 2014	
Samples	5272, 5279, 5029, 4293, 4195, 3785, 3375 and 23515*	

*The settings for the interleaved powered tests are marked *.*

Table 5.6: Data collection and instrument settings for a range of pulse offset to assess accuracy velocity component in LSNR at 23.2°.

Mitigating cross-talk with ping offset

The SBDPs are configurable to offset the start of their transmit-receive cycles from one another. Thus in theory it should be possible to increase this offset to a point where the pulse transmitted by the source sensor is not reflected and received by the neighbouring sensor until it has finished its transmit-receive cycle. Once the final range gating period is complete in the cycle the SBDPs enter a processing phase where no signals are emitted or recorded. The offset time required will be a function of the travel time, based on the instrument separation and the speed of sound in water. A test is conducted to assess this theory with one 0 dB pulse power setting and three LSNR sensors all mounted parallel at separations of 0.9 m, 1.5 m and 2.4 m as per Figure 5.3 with pulse offsets of 0.0 ms to 38.1 ms in eight even increments. The instrument settings for this test are given in Table 5.7.

	Instruments			
	SBDP _{SA}	SBDP _{SMA}	SBDP _{SMF}	SBDP _{SF}
Power (dB)	0	-100	-100	-100
Pulse offset (ms)	0	0.0, 4.8, 9.5, 14.3, 19.1, 23.8, 28.6, 33.4, 38.1		
Sample Rate (Hz)	2	2	2	2
Dates collected	24/06 to 08/08 2014			
Samples	13548, 8054, 4038, 2402, 2401, 1800, 600, 2398, 2403			

Table 5.7: Data collection and instrument settings for mitigation of cross-talk by pulse offset test.

Surface reflection effects

Vertically mounted sensors present a special case in the analysis of cross-talk in sub-sea acoustic sensors. When an acoustic pulse reaches a change of medium there is a very strong reflection (Appell *et al.*, 1991; Visbeck, 1995). This means that even horizontally mounted sensors may experience interference from vertically mounted sensors. A test is conducted to assess the magnitude to this interference, utilising one vertical and one transverse SBDP. Data sets are taken for the vertical sensor at a range of power settings given in Table 5.8, along with other instrument settings, so that the effect of the reflections on the transverse sensor could be quantified.

Cross-talk from other acoustic sensor types on SBDPs

While the majority of this chapter focuses on the interactions between multiple SBDPs, it will often be desirable to have sensors of multiple types mounted in close proximity in site characterisation instrumentation arrays. Tests were conducted to assess the effect of two other instrument types, an Acoustic Wave And Current profiler (AWAC) and a Continental single beam Doppler profiler.

The AWAC is a four beam instrument which sends its pulses at the same carrier frequency as the SBDPs. However, its pulse is narrowband rather than broadband as detailed in Section 2.6. The test instrument configuration consists of the AWAC mounted vertical, parallel to an SBDP separated by 0.9 m, with both sensors mounted on the top instrument frame. Data sets were collected with the SBDP in both LSNR and 0 dB pulse power modes. Thus the effects of the sensors can be identified via the QC metrics and quantified in the velocity measurements as per other tests. In addition, spectral analysis in the form of the power spectral density (PSD) as defined in Chapter 2, is utilised to assess the frequency of these effects. The Continental-SBDP tests follow the same methodology. The Continental-SBDP is mounted on the rear instrument frame of the turbine alongside SBDP_{RT}. Instrument settings and data collection information for both these tests are given in Table 5.9.

5.2.3 Data restrictions and quality control

Individual instrument settings for each test are listed in the previous section. With the exception of the Continental-SBDP data set which was collected during turbine deployment 5, all the data was collected over turbine deployment 6. The data were collected over a range of tide and flow conditions which were assumed not to affect the results of instrument interaction tests. The only universal stipulation was that the turbine not be operating due to the complex flow effects and increased uncertainty of possible electrical noise generated during turbine operation.

Quality control was undertaken as per other sections. Velocities exceeding the ambiguity range are removed as are: data points with sensor errors and measurements with non-unique times-

tamps. Gaps of up to two points are replaced by linear interpolation. Only data points with timestamps common to both instruments (within any PTP offset) are passed for processing, except in the case of the non-PTP AWAC and Continental data sets.

5.3 Results

5.3.1 Basic example and variation with separation

For the basic example of three SBDPs in LSNR mode parallel to a 0 dB sensor at three separations (offset from the source by 13.1 ms to clearly highlight the interference region) the response is analysed through the QC metrics: amplitude and correlation. Figure 5.7 shows the amplitude and correlation returns for the LSNR SBDPs. The response in both cases can be split into three regions: a flat response where there is no evidence of interference over the 0 m to 14 m range. A sharp spike at the 14 m to 16 m range. And finally a smaller less steep peak with a gradual negative gradient curve from 18 m onwards. The responses in both amplitude and correlation are greatest in the closest instrument to the source and fall off with separation. These three identified regions will be referred to throughout the chapter as: near, spike and far.

The location and magnitude of the spikes for both correlation and amplitude are given in Table 5.10. It should be noted that the peak of the 3.2 m separated SBDP is less sharp than in the other two cases. This is possibly due to the return pulse on that angle being less well aligned with the gating of that instrument.

The primary goal of investigating cross-talk is the effect it has on velocity measurements. The SBDPs set at such a low pulse power is generally not used in taking velocity measurements. However, it was theorised that it might provide insight into the likely effects on a fully powered sensor experiencing interference. Figure 5.8 shows the velocity results corresponding to Figure 5.7. The three defined regions are evident with noise in the near bins, a sharp spike at the same range as for amplitude and correlation and a region where the interference is causing an effect that appears to be a combination of the two nearest regions. The sensors each experience their own individual background noise levels as discussed in Chapter 4. For all three separations the velocity at the range bin responding to the peak in the amplitude is biased close to zero, regardless of whether the background velocity reading is positive or negative. The far range is biased towards zero by a smaller amount but also shows signs of the background noise pattern in the early bins.

The standard deviation of the velocity also responds differently in each of these three regions. The spike corresponding to the first indication of interference reduces the standard deviation, biasing towards zero. In the velocity plots it is evident that the greater the instrument separation the less this effect of biasing velocity and decreasing standard deviation is experienced, due to the interfering source pulse decreasing with power across the separations.

	Instruments	
	SBDP _{VA}	SBDP _{SMA}
Power (dB)	-100, -10, -5, -3, -1, 0	0
Pulse offset (ms)	0	0
Sample Rate (Hz)	2	2
Dates collected	30/07 to 07/08 2014	
Samples	837, 3345, 5664, 6432, 7410, 1209	

Table 5.8: Data collection and instrument settings for test of effect of surface reflections.

	Instruments			
	SBDP _{VA}	AWAC	SBDP _{RT}	Continental-SBDP
Power (dB)	-100, 0	'high'	-100, 0	'high'
Pulse offset (ms)	0	N.A.	0	N.A.
Sample Rate (Hz)	4	2	2	1
Bin Sizes (m)	0.4	1.0	0.4	2
Dates collected	01/07/2014		08/05/2014	
SBDP Samples	233, 2408		601, 601	

Table 5.9: Data collection and instrument settings for cross-talk between different sensor types.

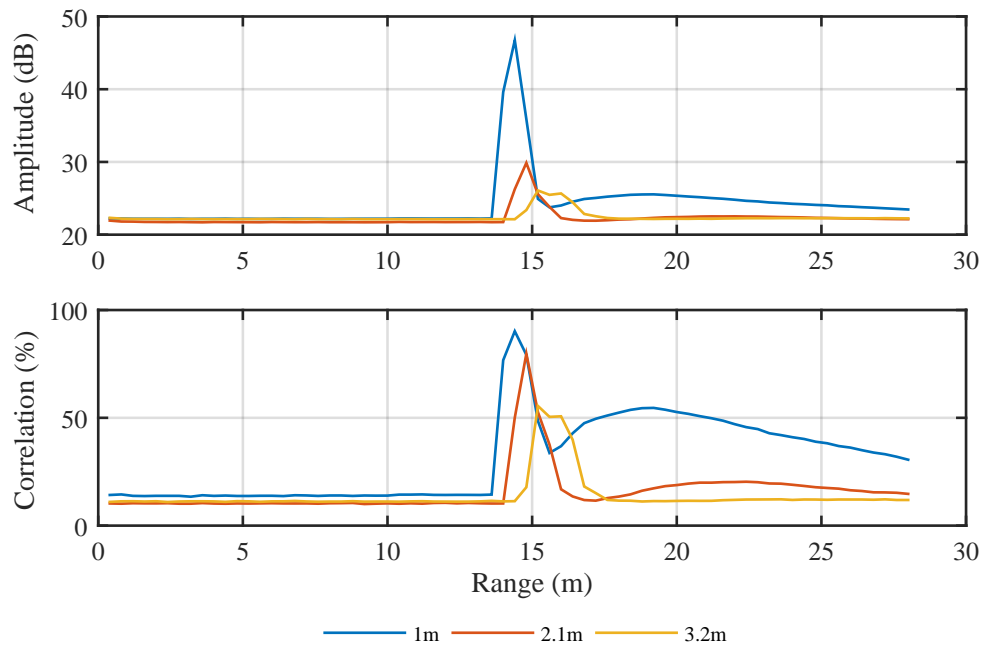


Figure 5.7: Amplitude and correlation for SBDP in LSNR mode showing indications of interference from a 0 dB source sensor for three separation distances.

	Instrument separation from source (m)		
	0.9	1.5	2.4
Peak location in range (m)	14.4	14.8	15.2
Peak amplitude value (dB)	46.73	29.87	26.07
Peak correlation value (%)	90.17	79.75	55.51

Table 5.10: Peak values of correlation and amplitude of LSNR SBDPs in response to parallel 0 dB signal.

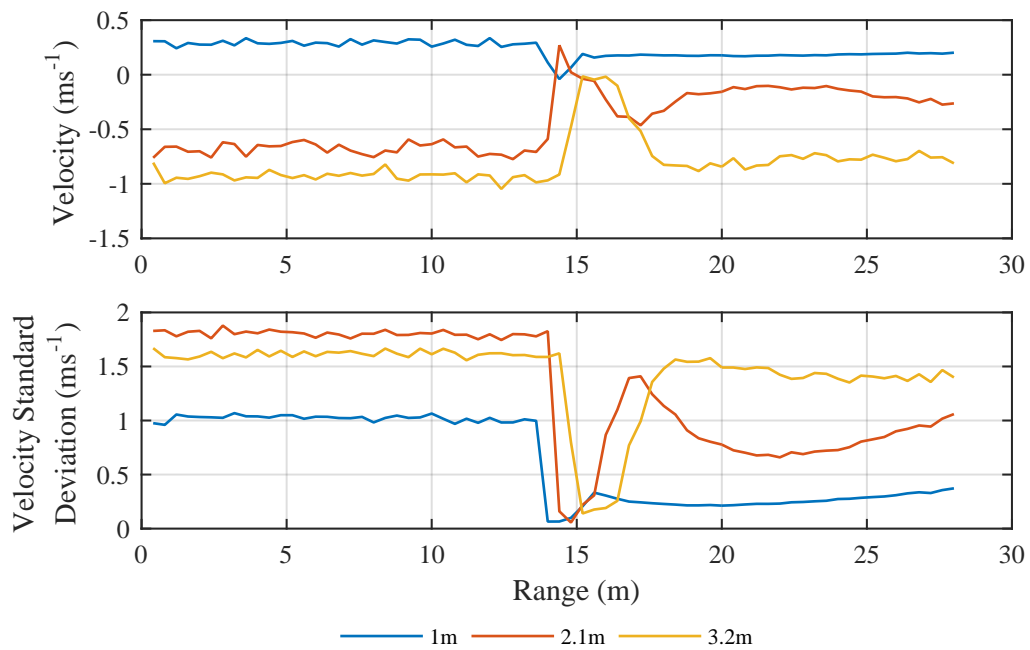


Figure 5.8: Effect on velocity measurements for SBDP set to LSNR mode showing indications of interference in response to a 0 dB source at three separation distances.

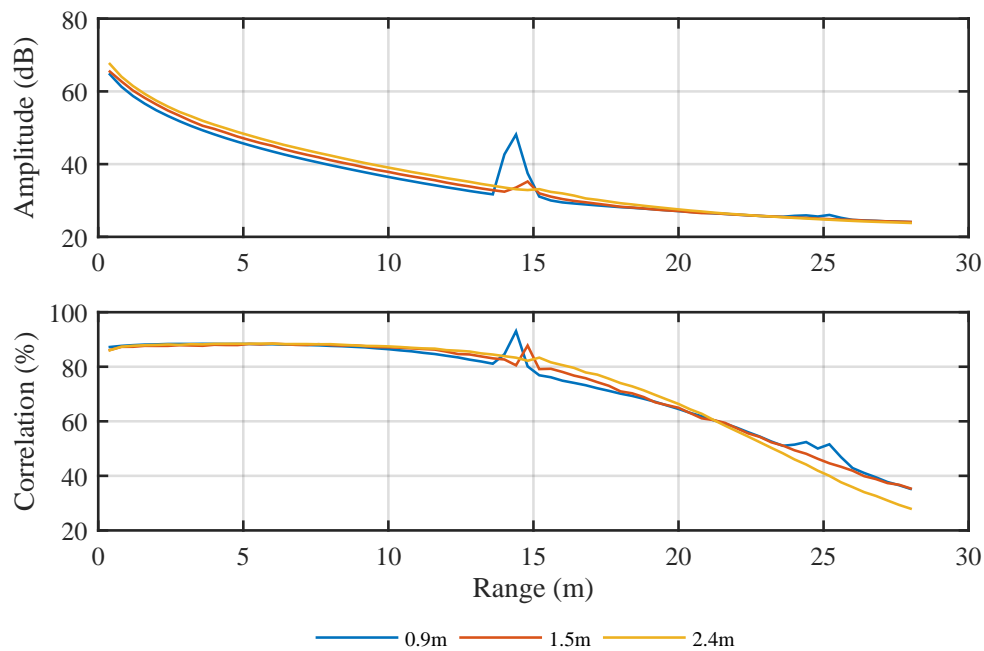


Figure 5.9: Effect on velocity measurements for SBDP set in normal operating mode showing indications of interference in response to a 0 dB source at three separation distances.

	Instrument separation from source (m)		
	0.9	1.5	2.4
Peak location in range (m)	14.4	14.8	15.2
Peak amplitude value (dB)	48.13	35.22	33.12
Peak correlation value (%)	93.05	87.77	83.34

Table 5.11: Peak values of correlation and amplitude of fully powered SBDPs in response to parallel 0 dB signal.

Powered mode results

With the regions of interference identified and defined for this timing configuration, data from the test with pulse power in all the sensors at 0 dB can be analysed to quantify the effects. Figure 5.9 presents the mean amplitude and correlation plots for the three separations with all four SBDPs at 0 dB. The spikes are again present in the same locations but with the far region of interference not clearly distinguishable. There is a secondary spike at 25 m range which maybe due to vertical sensors reflecting off the sea surface. The values and locations of the spikes are given in Table 5.11. The main amplitude spikes values are very similar to those in the LSNR results, with a mean increase of 13.8 %.

Figure 5.10 illustrates the velocity and standard deviation of velocity with range for the same data set as Figure 5.9. Each of the instruments has a different velocity reading in the clean near range. This is possibly due to bias as discussed in Chapter 4 or to instrument angles. There is

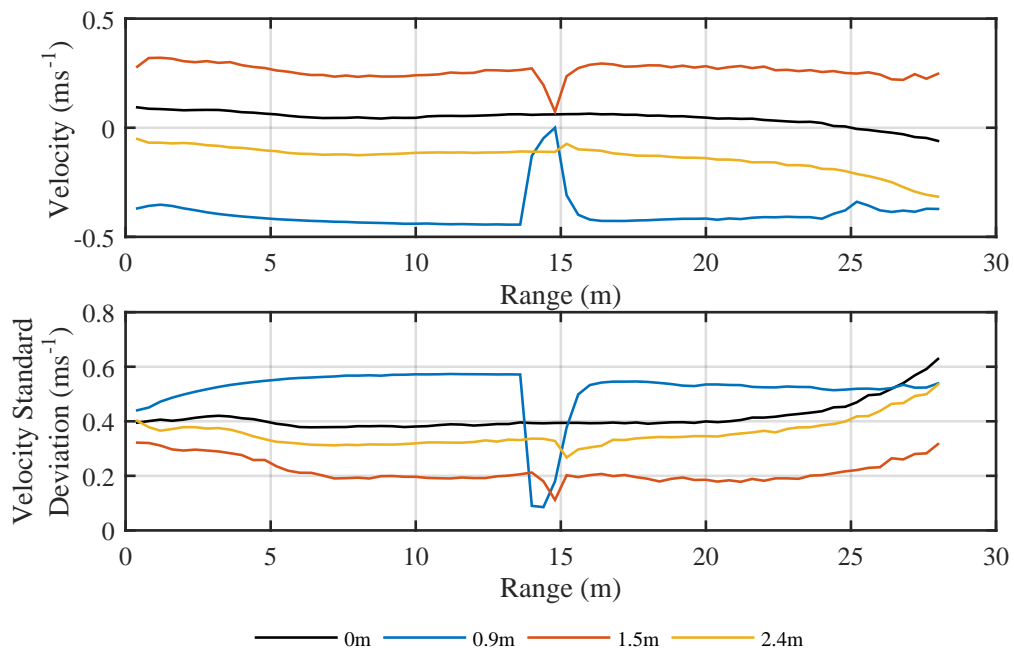


Figure 5.10: Effect on velocity measurements for SBDP set in normal operating mode showing indications of interference in response to a 0 dB source at three separation distances.

a biasing towards zero at the locations of the amplitude and correlation spikes which is most pronounced in the nearest SBDP and falls off with separation. The standard deviation is again biased towards zero at all three separations with the greatest effect in the nearest instrument. In the region beyond the spike there is little evidence of the velocity measurements changing due to interference.

In order to reveal more information about the frequency content of the velocity measurements due to these effects, the velocity power spectral density (PSD) was calculated for range bins representative of each of the three regions; 12.0 m for the near range, 14.4 m for the interference spike and 16.0 m for the far. For more information on how the PSD is calculated see Section 2.7.4. The results for the SBDP at 0.9 m separation from the source are displayed in Figure 5.11. At the range bin of the spike (14.4 m) the vast majority of the energy in the signal is at the Nyquist frequency range, with a relatively flat response throughout the rest of the frequency range, showing no evidence of capturing the turbulent structures. The bins either side show evidence of capturing turbulence structures with the greatest energy at the lower frequencies and a noise floor starting to dominate around $10^{-1.2}$ Hz region. The PSD of the furthest of these bins shows a slightly higher noise floor than that of the unaffected bin.

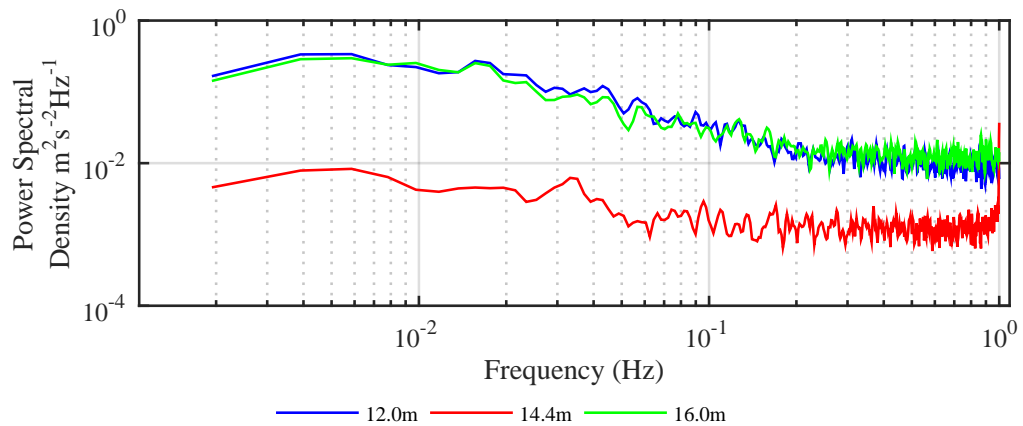


Figure 5.11: Mean PSD plot of velocity fluctuations in the three regions of SBDP at 0.9 m separation showing effects of interference in the near, spike and far regions.

5.3.2 Power and signal to noise ratio

One possible mitigation strategy is to reduce the pulse power of the source instrument. The effect of four power settings on the amplitude returns at 0.9 m parallel separation is given in Figure 5.12, with the peak values given in Table 5.12. It shows a reduction in spike amplitude consistent with the reduction with source power.

	Source power setting (dB)				
	none	-5	-3	-1	0
Peak amplitude value (dB)	30.89*	37.75	41.33	45.29	48.14

* value taken from top plot of 0 dB sensor

Table 5.12: Peak values of amplitude in the receiving sensor for a range source sensor power settings.

Figure 5.13 shows the response in the velocity measurements to the power of the interference source. The peak of the spike in the interference region at range of 14.4 m is biased close to zero on all cases. The standard deviation is also biased low at 14.4 m range, which for all power settings is between 0.08 ms^{-1} and 0.09 ms^{-1} . In the more extreme range there is little evidence of interference until 20 m range, where the instrument's own signal is very weak ($< 25 \text{ dB}$). An interesting effect is that the standard deviation drop is most evident over range of 14.0 m to 14.4 m while the velocity spike is most evident over 14.4 to 14.8 m region. The higher power settings induce a bias that passes zero into the positive at the 14.8 m range. This is possibly an effect of the range gating of the signal, causing a wrapping of the velocity reading.

It is evident from the results of both separation and power that as the amplitude of the interfering source signal in the affected sensor drops so velocity bias decreases. Thus at some level the power of the cross-talk must be so weak compared to the instruments own signal that the effect

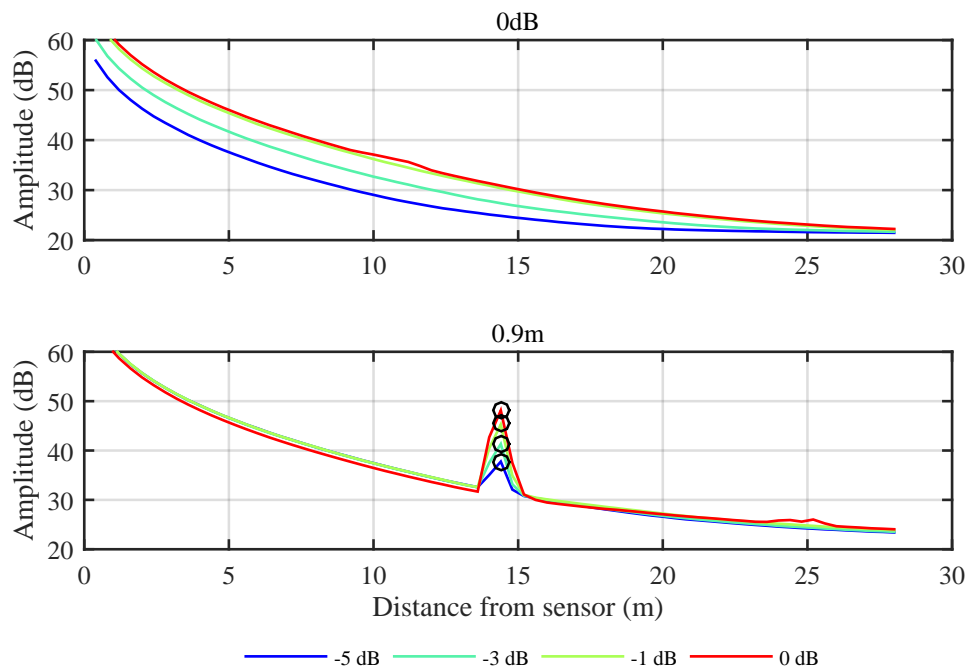


Figure 5.12: Plot of mean amplitude with range for a range of pulse power settings in the source SBDP (top) on a 0.9 m parallel separated instrument (bottom). The circles mark the locations of the spikes along the range for each source power setting.

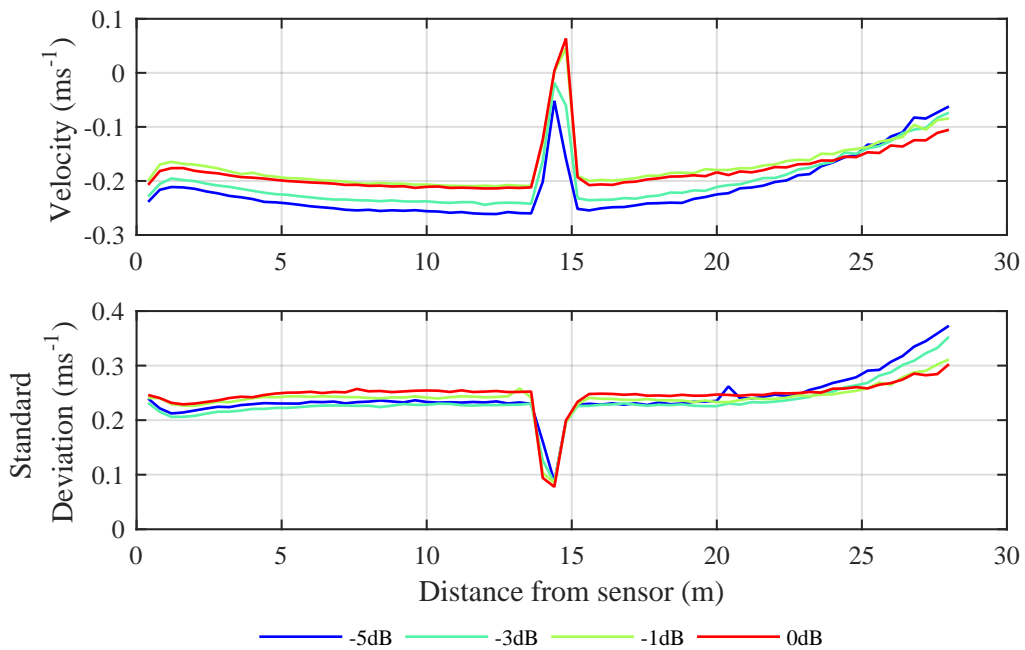


Figure 5.13: The effect of 4 power settings in the source instrument on the affected SBDP velocity measurements, highlighting a bias towards zero in both mean and fluctuation of velocity readings in the spike region.

	Source power setting (dB)			
	$-\infty$	-5	-3	-1
Velocity at 14.4 m range ms^{-1}	-0.05	-0.02	0	0
Velocity standard deviation at 14.4 m range ms^{-1}	0.09	0.09	0.09	0.08

Table 5.13: Velocity response to power increase in interference signal.

on the velocity measurements is minimal. Indeed, this is already in evidence from the figures in Section 5.3.1 that at the far range, where the LSNR results show the source signal is increasing the amplitude and correlation returns, with an effect evident in the velocity. However, the 0 dB tests show that the amplitude is low compared with the receiving instrument's signal amplitude return at that range and there is no evidence of an effect on the velocity measurements.

It is assumed that the effect of the velocity measurement (established as a bias towards zero which also reduces signal variance) is proportional to the signal to noise ratio. Comparing the amplitude spikes in Figures 5.7 and 5.9 there is a mean percentage increase in the magnitude of the amplitude spikes from the LSNR to the 0 dB results of 13.8 %. The assumption can be made that the amplitude of the interference spike represents only the source signal. The amplitude of the bin when no cross-talk is present is taken from a clean data set as a baseline for comparison. In this way a Signal to Noise Ratio can be calculated from:

$$SNR = \frac{\alpha_{baseline}(x = peak)}{\alpha_{affected}(x = peak)} \quad (5.1)$$

where $\alpha_{baseline}$ is the amplitude return of a SBDP with no interference, $\alpha_{affected}$ is the amplitude return of a SBDP with interference and x is a point along the range of the sensor.

To carry out this analysis, a data set of the 2.4 m separated SBDPs, for a range of power setting in the source instrument was selected. The 2.4 m range was selected as it was the only data set where velocity effects from cross-talk were clearly evident to be diminishing to negligible quantities. The SNR results with range for each source power setting are given in Figure 5.14. It shows the baseline data set as a straight line through a SNR of one, as per the definition, and decreasing SNR in the affected instrument in response to the increasing source pulse power.

A challenge in quantifying the effect of cross-talk as it diminishes is that the effects in the velocity will tend towards the size of natural fluctuations. Real sea flow conditions measured with acoustic instruments provide several sources of fluctuation in velocity measurements particularly with instrument range. In order to quantify the effect of the SNR on the velocity a metric is required. Changes in mean velocity bias, standard deviation and variance attributable to noise were all investigated, with the mean velocity giving the best indications of interference at low SNR amplitude returns.

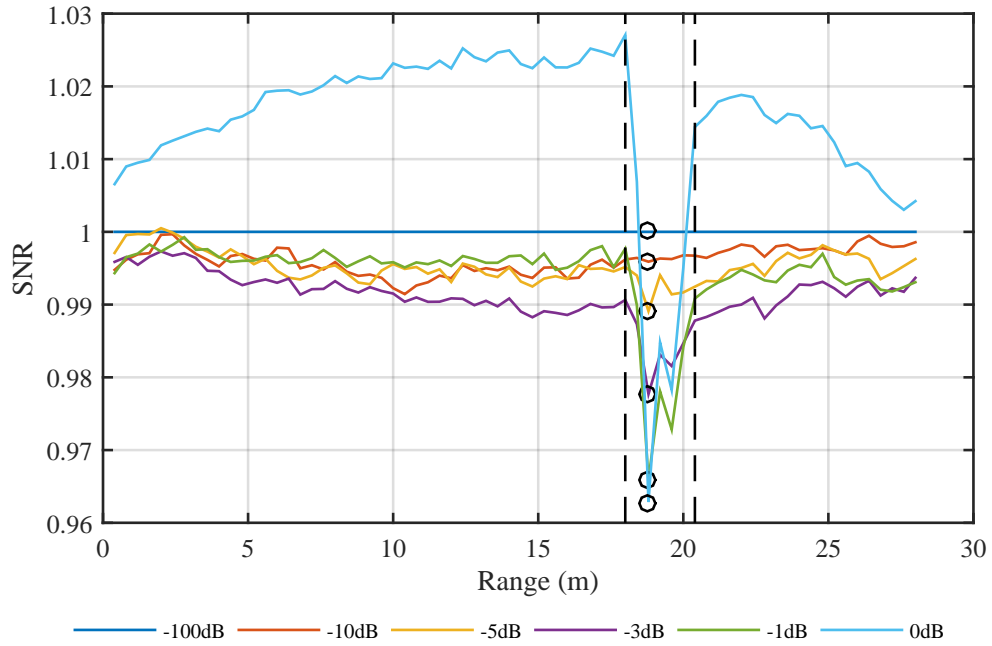


Figure 5.14: Signal to noise ratio in the receiving SBDP in response to a source instrument at 2.4m separation at a range of power settings. The dashed lines show the range of the amplitude spike and the black circles the values corresponding to the extreme amplitude.

It can be seen in Figure 5.14 that the amplitude spikes act over an approximately 2.4 m range highlighted by the black dashed vertical lines. For the velocity time series there is no baseline value to compare to, as the ambient flow conditions are in continual flux. Hence, the comparison must be made between velocity measurements in the affected region and the velocity measurements outwith it.

Here the velocity sharpness (Λ_v) is defined as the mean velocity value at the peak of the affected region $v_{y=peak}$, minus the mean of the values either side of the affected range. An example of the velocity sharpness is given in Figure 5.15. In this case the peak is at $y = 18.4$ m and the other values are at $y = 17.6$ m and $y = 20.4$ m resulting in the definition:

$$\Lambda_v = \left| v(y = 18.4) - \frac{v(y = 17.6) + v(y = 20.4)}{2} \right| \quad (5.2)$$

For the example in Figure 5.15, $\Lambda_v = 30.6 \times 10^{-3} \text{ ms}^{-1}$ for the highest power setting of the source pulse. It is likely the steepness of this peak is a function of the timing of the pulse within the range gating of the receiving sensor. However, the effect remains constant for a constant instrument separation and pulse offset. The Λ_v and SNR values for each power setting of the source SBDP were calculated, and the results are presented in Figure 5.16. A trend line of a

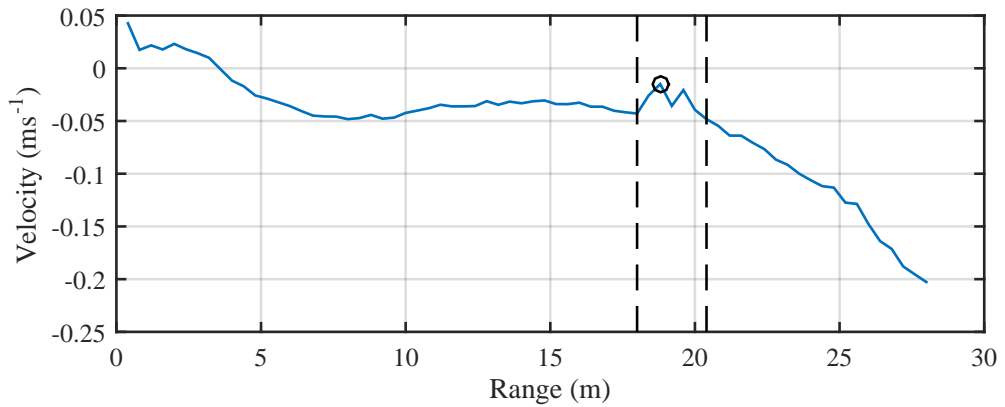


Figure 5.15: An example of cross-talk causing a velocity spike in the receiving SBDP over a 2.4 m range with both SBDPs set to 0 dB pulse power.

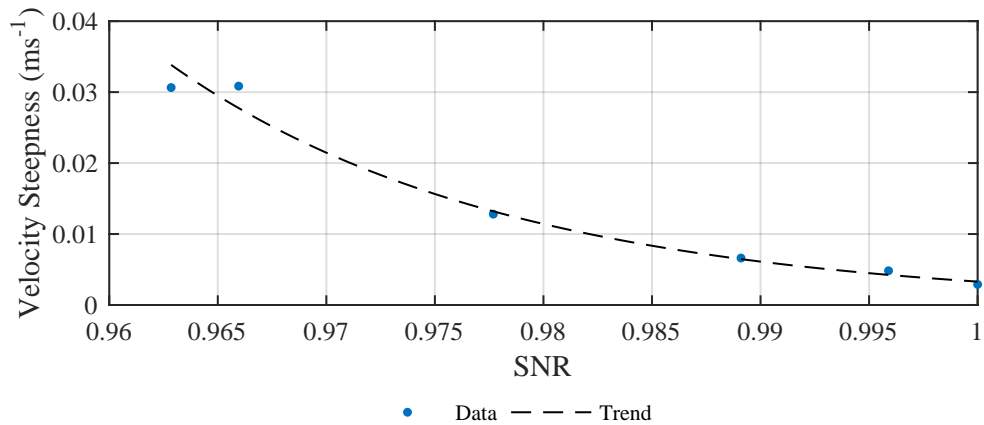


Figure 5.16: Velocity spike steepness as a function of SNR for an affected sensor at 0 dB, 2.4 m from the source.

power law of the form:

$$\Lambda_v = 3.3 \times 10^{-3} \cdot SNR^{-61.53} \quad (5.3)$$

is fitted to the data with an R^2 goodness of fit value of 0.98, representing the best goodness of fit of several trailed curve types. As would be expected the velocity steepness falls off as the source signal power decreases.

Figure 5.16 suggests that the velocity spikes are decreasing with SNR as a power law to a high goodness of fit. The velocity steepness never reaches zero due to the natural fluctuations in velocity measurements with range. The accuracy of the SBDPs is only $\pm 0.01 \text{ ms}^{-1}$ thus the SNR where $\Lambda_v < 0.005$ (half the velocity accuracy) is a good estimate for when cross-talk

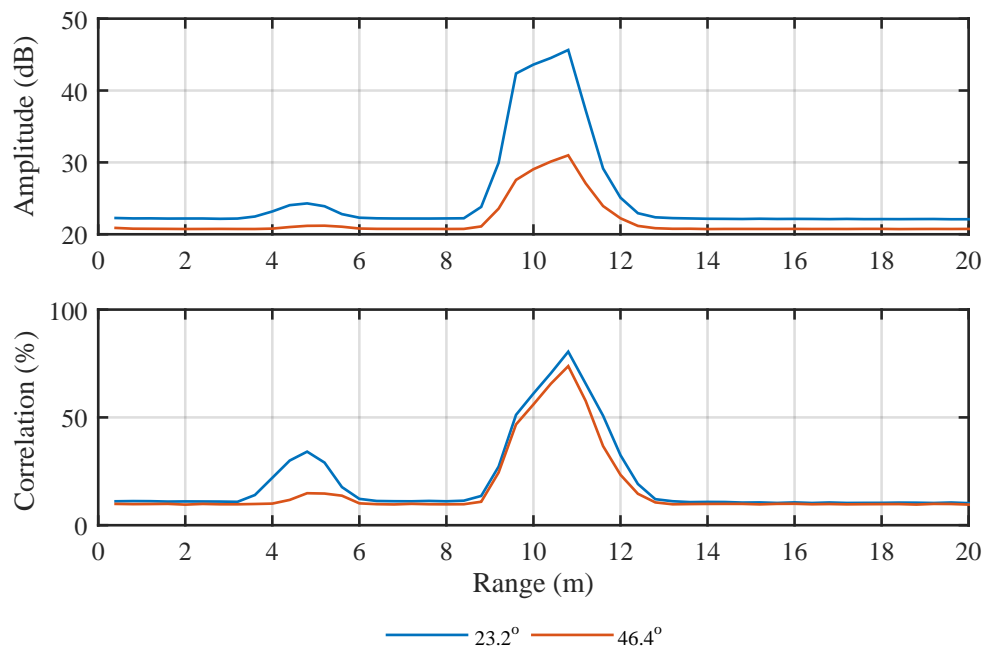


Figure 5.17: Example of the effect of cross-talk between angled sensors on the receiving LSNR-mode instrument QC metrics.

stops affecting the measurements. Using Equation 5.3 gives a minimum SNR of 0.9933 for that threshold.

5.3.3 Effect of angle between instruments and measuring velocity components

Figure 5.17 illustrates the effect of narrowing the angle between the beam paths from parallel to 23.2° and 46.4° for two LSNR mode sensors, as per the instrument layout illustrated in Figure 5.5. The response pattern, compared with the equivalent parallel test with a 19.1 ms offset, is altered in several ways: First there are two sets of spikes, a smaller one centred at 4.8 m range, and a larger one at the 10.8 m range. In addition the spikes are spread over a larger range than was the case for the parallel arrangement. For the parallel sensors the main spike was contained within a 1.2 m range, here the larger of the two spikes covers a 4.0 m range for both sensor angles. Other than the two spikes, there is little evidence of interference at the extreme, near or inter-spike ranges.

The effect of the angle between beams is evident, with the higher amplitude and correlation returns corresponding to the narrower angle. The magnitudes of the maximum correlation and amplitude values for both angles are given in Table 5.14, along with the equivalent data for the same settings from the equivalent parallel sensor test.

As with the basic parallel test, once the region of interference was defined, the three sensors were reconfigured to 0 dB pulse power mode, with the receiving pair offset from the

	Instrument separation from source (°)		
	0*	23.2	46.4
Peak location in range (m)	14.8	10.8	10.8
Peak amplitude value (dB)	29.87	45.64	30.98
Peak correlation value (%)	79.75	80.48	73.77

* taken from Table 5.10

Table 5.14: Peak values of correlation and amplitude of fully powered SBDPs in response to a 0 dB signal at two beam intersection angle.

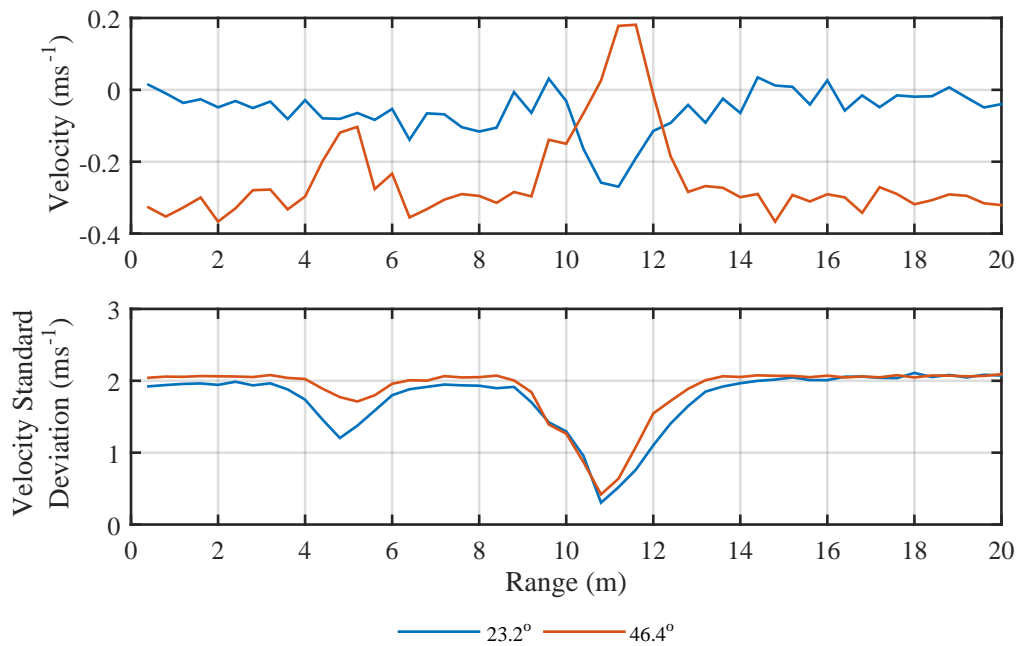


Figure 5.18: Effect of cross-talk on velocity measurements of two receiving LSNR mode SBDPs at two beam intersection angles.

source by 19.1 ms. Figure 5.18 illustrates the effect of the angled interference on the velocity measurements for the two receiving sensors. Again the response is different from that of the parallel sensors. At the range corresponding to the interference spikes, rather than being biased towards zero the measurements are offset towards different values roughly equal in magnitude but opposite in sign for each sensor. The standard deviation is very high across the range relative to the velocity measurements. In the regions of interference the standard deviation is closer to an expected magnitude for the corresponding velocity measurement.

As the velocity readings for the angled sensors are not being biased towards zero, it is possible they are measuring a component of real flow velocity as suggested in Section 5.2.2. In order to assess this, an interleaved data set of two sensors on two alternating power modes was utilised. With this method a powered SBDP can be compared with the response due to cross-talk of a

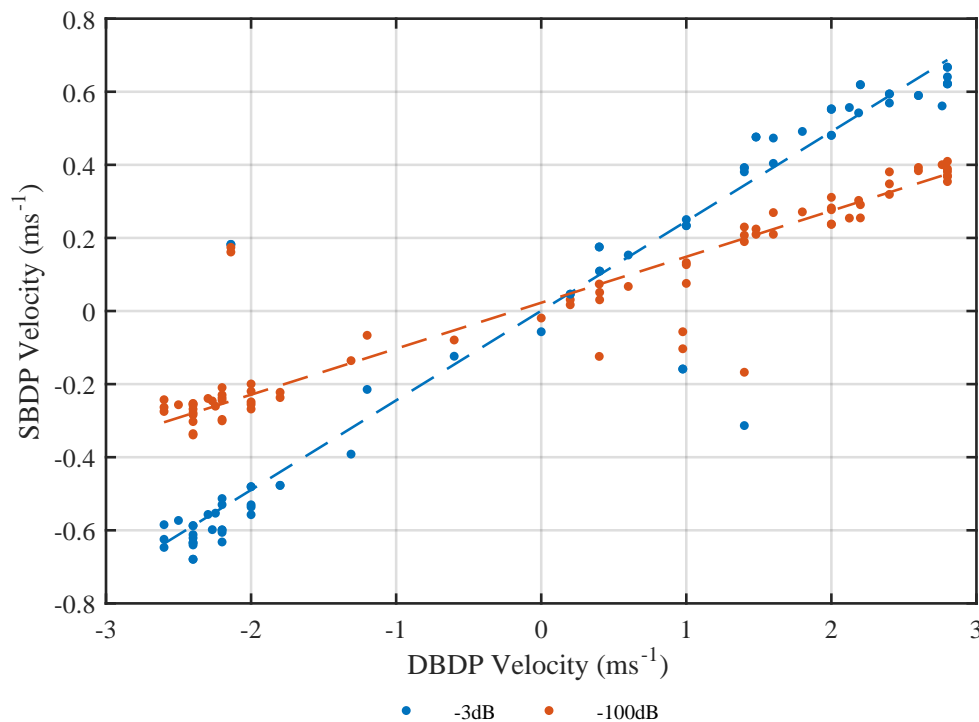


Figure 5.19: Comparison of bi-static angled LSNR mode SBDP velocity measurements with $\overline{u_{DBDP}}$.

co-located one in LSNR mode. A range of pulse offsets were used in these tests as given in Table 5.6.

Figure 5.19 shows the results across all the pulse offset settings at the intersecting beam, for the angled sensor of the consecutively measured LSNR and powered settings. The results show that the powered SBDP velocity measurements correspond to a component of the free-stream velocity. As this is an along beam measurement in a standard operating mode the associated uncertainty is low. The linear trend fitted to the data (excluding three evident outliers) had a gradient of 0.25 with an associated R^2 value of 0.96.

The measurements by the LSNR sensor in response to cross-talk, also shows a linear relationship to the flow. However, on a shallower gradient to the mean velocity. A shallower gradient was expected, as the -3 dB mode measures the along-beam component while the LSNR mode measures the component along the bisecting angle between it and the powered vertical sensor. Assuming that the vertical velocities are less than the horizontal component, the velocity measurement will decrease. A linear trend is again fitted (excluding 6 outliers) and has a gradient of 0.13 with a R^2 of 0.99.

A combination of the flow effects around the turbine nacelle and the distance of the upstream DBDP made direct comparisons for the flow components difficult for this instrument

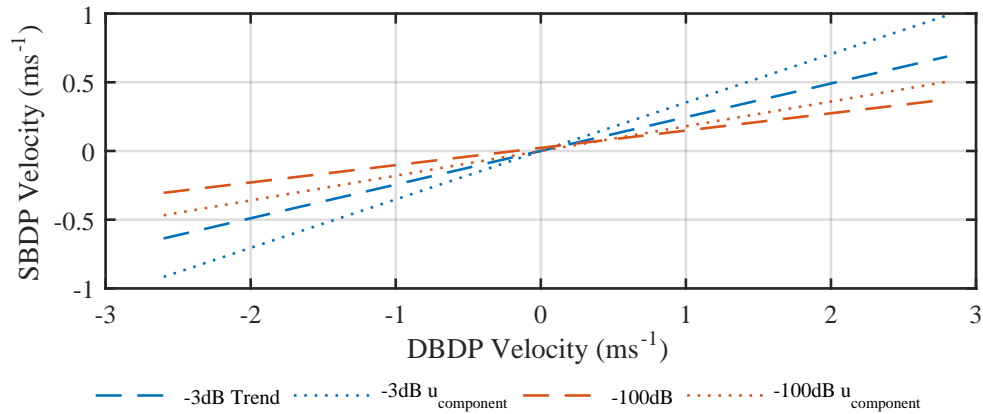


Figure 5.20: Expected component of \bar{u} along each angle against the value measured by an angled SBDP in both modes.

configuration. Thus, in this analysis the results from the two SBDP power settings are the primary comparison, with a reference DBDP used to give context to the ambient flow condition. Assuming only the streamwise flow component has a mean value significantly above 0 ms^{-1} then $u_{\text{component}} = \bar{u} \cdot \cos(90 - \phi) \cdot \cos(\theta)$, where ϕ is the pitch and θ the yaw to the onset flow.

The previously defined linear trends are plotted against the expected component of the free-stream velocity in Figure 5.20. It can be seen that the measured velocities underestimate the predicted component by 30.46 % and 29.44 % for the -3 dB and -100 dB sets respectively. The fact that the percentage under-estimations for both techniques are very similar is a positive indication for the LSNR technique. The under-estimation is likely due to the resultant velocity having a transverse component significantly greater than 0 ms^{-1} .

Having established that for certain angles LSNR mode could be used to measure a flow component via cross-talk, an investigation was made into the limits and maximum accuracy of the technique. Early trials of this technique focused on the blanking distance, which was varied to give the highest correlation and amplitude returns and increase the velocity component. Once a maximum was found this was ‘fine tuned’ by altering the pulse offset, with the results of this process detailed in this section. Figure 5.21 displays the amplitude and correlation returns for this ‘fine-tuning’ test. As can be seen the offset values were chosen such that the interference region is moving across the range, but with the maximum always within the 0.4 m bin.

The results of Figures 5.19 and 5.20 cover 7 different pulse offsets in 0.1 ms increments. Figure 5.22 subdivides this into the different offset values, fitting a linear trend for each. As these results are plotted against the expected flow component for this sensor orientation, the ideal result is a gradient of 1.

It is difficult to make an estimation of the accuracy of the standard deviation between the powered and LSNR results, given the different flow angles measured. It could be assumed that

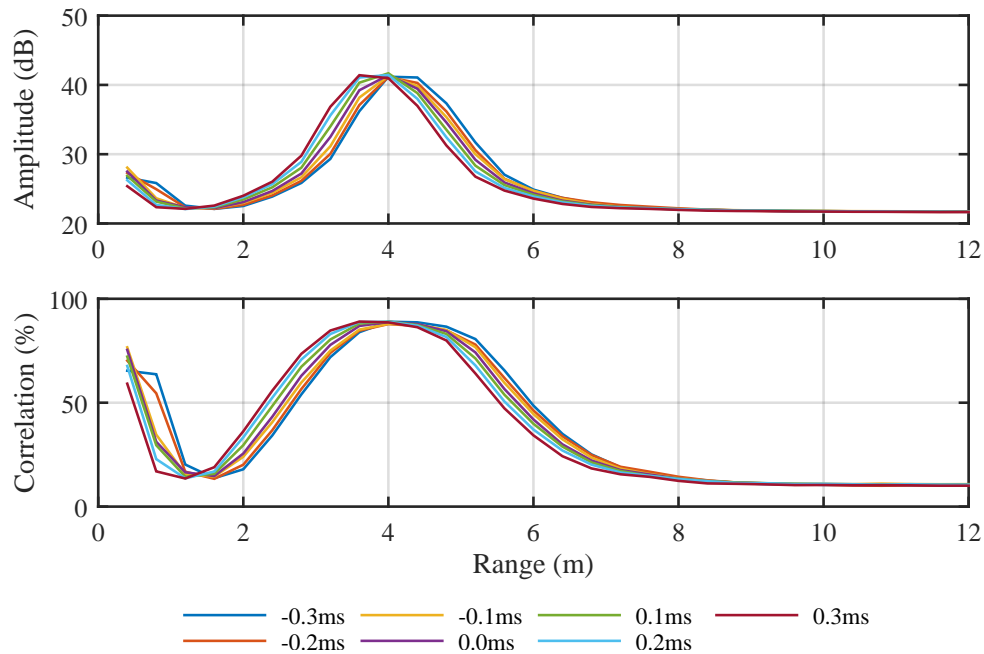


Figure 5.21: Amplitude and correlation returns for a range of pulse offsets for a receiving SBDP in a bi-static array configuration.

the flow fluctuations are isotropic but other results suggest this is a spurious assumption. Hence the instrument noise floor for each setting is assessed via the method of a double line fit to the spectrum as suggested by Richard *et al.* (2013) detailed in Chapter 2. Figure 5.23 gives the resulting gradient of component fit and instrument noise for each offset. It highlights that a -0.2ms offset provided both the lowest estimate of instrument noise and closest gradient to 1, but that there is no smooth curve from which turning points could be easily identified.

5.3.4 Mitigating cross-talk with ping offsets

It has been shown that an increased SNR and increased sensor separation will reduce the effects of cross-talk. However, as the instruments are equipped with the ability to offset the transmitting of the pulses it should be possible to co-ordinate them such that, for a given separation, they each ping during the processing time of the cycle of neighbouring instruments. Figure 5.24 presents the amplitude returns for three SBDPs in LSNR mode at three separations, for a range of ping offset values from the source SBDP.

Figure 5.24 shows that there is no variation in the amplitude response with increased pulse offset, other than where the peaks are flatter due to what is predicted to be related to the range gating effect. For the two nearest separations there are only 7 detectable spikes for 9 different offsets, the furthest offset also has a spike in the 0 ms (coincident) offset data set. However, none of the instruments show any sign of interference for offsets of 38.1 ms. This is due to the

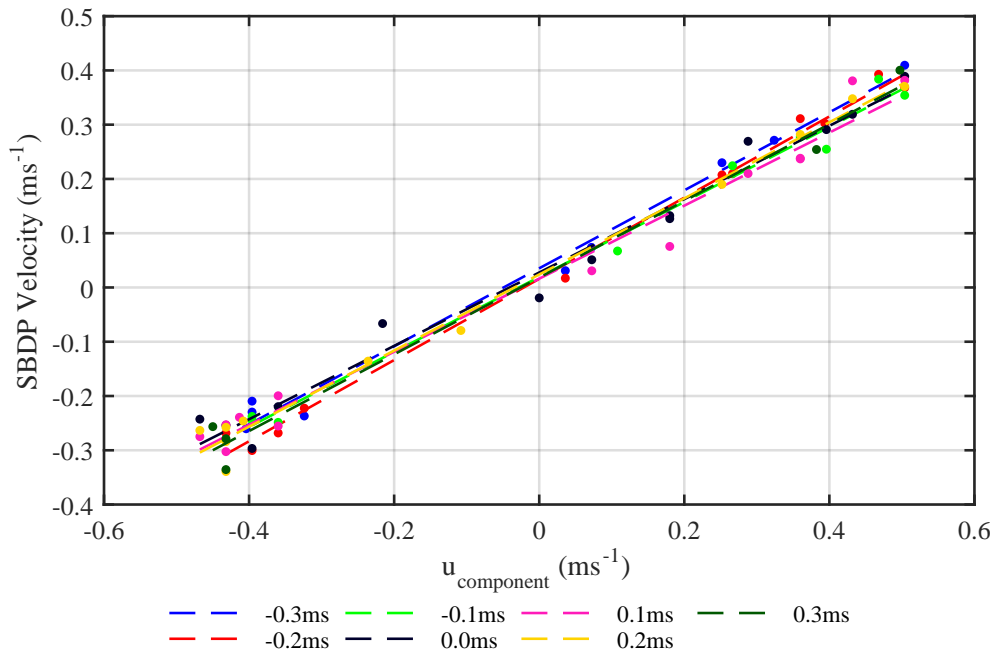


Figure 5.22: Measurement accuracy comparison of the measured and component velocities for a range of pulse offsets.

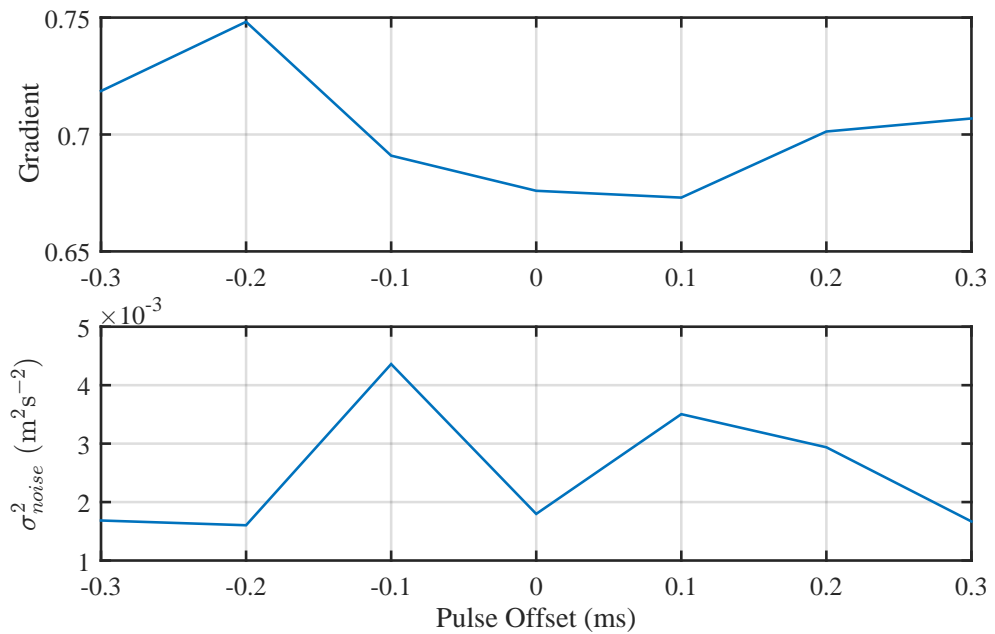


Figure 5.23: Resulting gradient of Figure 5.22 and noise variance of component measurement for a range of pulse offsets.

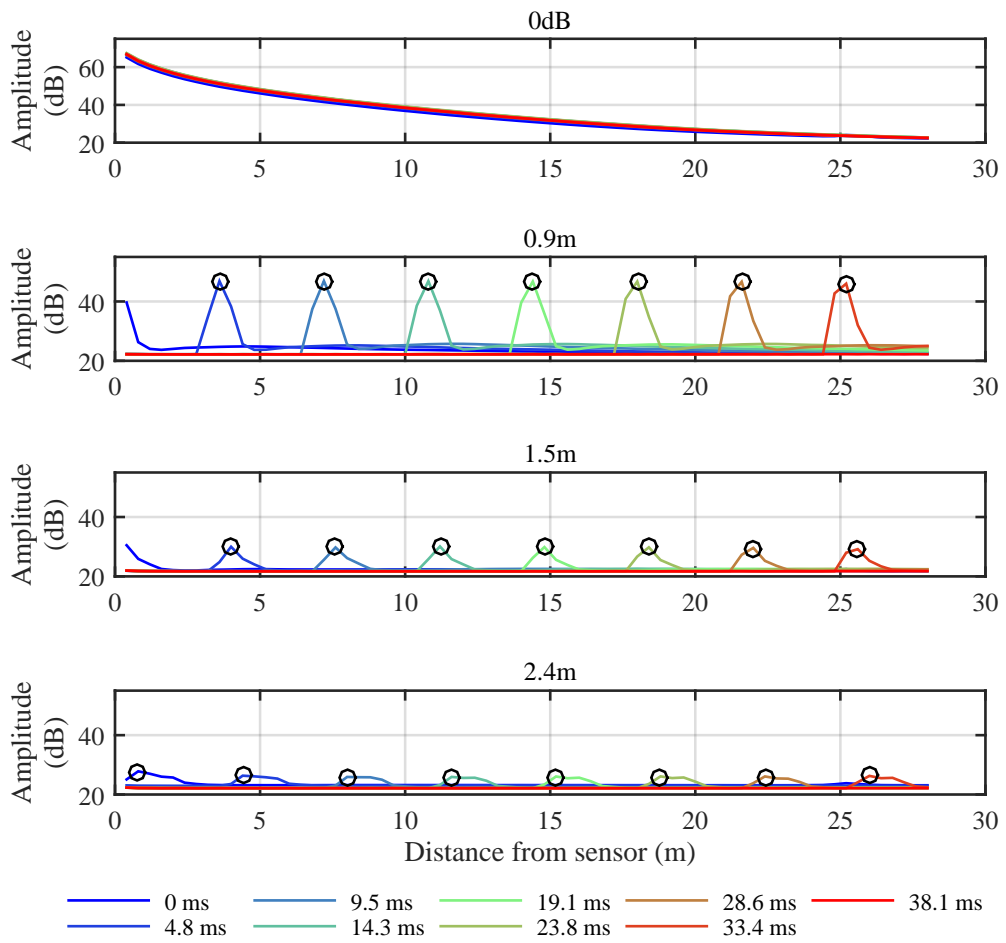


Figure 5.24: The effect of increasing the ping offset in the affected SBDPs at three separations.

instrument finishing its listen cycle for the furthest (28m) range bin by the time the ping from the source SBDP is transmitted.

A 3.6 m shift equates to a 7.2 m total distance travelled. Dividing 7.2 m by a speed of sound in water of estimated as 1490 ms^{-1} , means a travel time of 4.8 ms which equates to the offset increment. Hence the control mechanism is working as expected.

5.3.5 Surface reflections from vertical instruments

During the ReDAPT field measurement campaigns it was noted that the transverse sensors were showing interference at the extreme of their range. It was theorised that this interference might be due to reflections of pulses from vertically oriented sensors off the sea surface. A test was designed in order to quantify the effect of a vertically oriented SBDP on a Horizontal one.

Figure 5.25 presents the correlation returns for a horizontal SBDP and a vertical SBDP cycled through a range of power settings. It shows that as the power is increased in the vertical sensors there is an increase in correlation at the same bin in the horizontal sensor. Note that even at -100 dB the vertical sensor detects a discernible amplitude spike due to surface reflection. The range at which the interference occurs are roughly the same in both sensors, as they are mounted at the same depth thus the travel time from the sensor to the surface is equal. This can be mitigated with ping offsets, with a 4.8 ms offset moving the interference spike 3.4 m. Thus setting the vertical sensor to an offset of 5.3 ms will be enough to remove the interference spike from the sensors 28 m range in this setting.

The interference level in this case is small relative to the parallel and horizontal plane angle mounted configurations. Figure 5.26 shows the velocity readings by the horizontal SBDP. It shows a biasing towards zero consistent with other interference tests, but this was only significant for the highest two source instrument power settings.

5.3.6 Cross-talk from other acoustic sensor types on SBDPs

As the SBDPs all transmit an identically coded pulse at the same carrier frequency the likelihood of cross-talk affecting velocity measurements was relatively high. However, acoustic sensors come in a range of types as discussed in Section 2.6 thus it was desirable to assess the effect of different sensor types on the SBDPs. The AWAC has an identical carrier frequency of 1 MHz but transmits a narrowband, rather than broadband, pulse. Figure 5.27 illustrates the amplitude response of a vertically mounted SBDP, parallel to the AWAC at 0.9 m separation.

One of the notable changes from the SBDP cross-talk is that the interference location changes frequently. This is due to the lack of Precision Time Protocol (PTP) stamping in the AWAC, so its clock will drift compared with the SBDPs causing minor timing offsets. In addition for this test the SBD is sampling twice as fast as the AWAC (4 Hz and 2 Hz) respectively, thus the interference is not constantly present in every sample. In addition, the AWAC bin size and thus

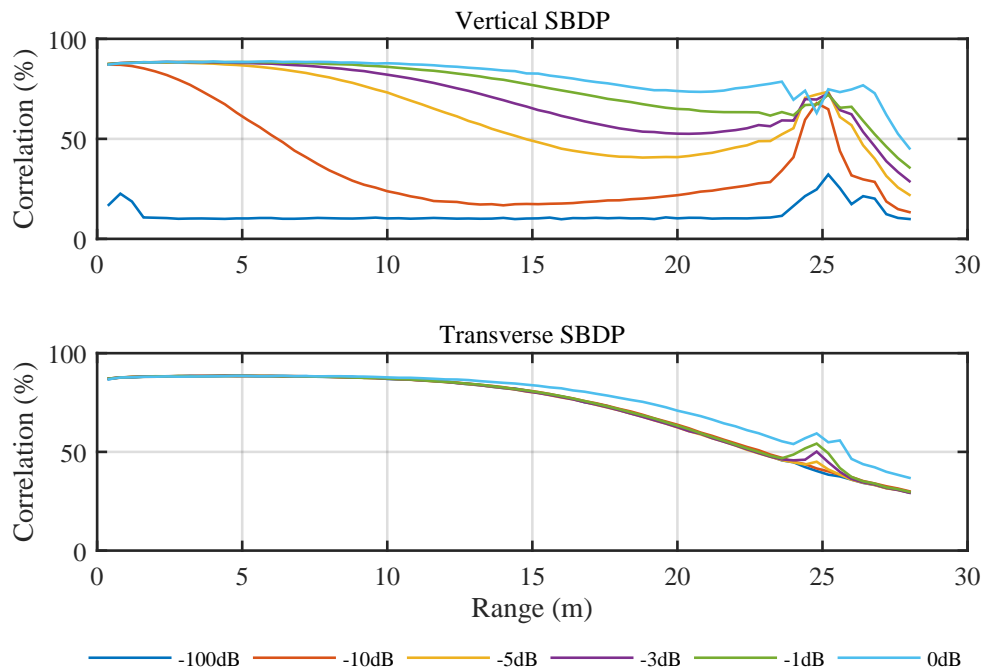


Figure 5.25: The correlation of co-pinging vertical and transverse SBDPs, with the vertical sensor being cycled through a range of power settings.

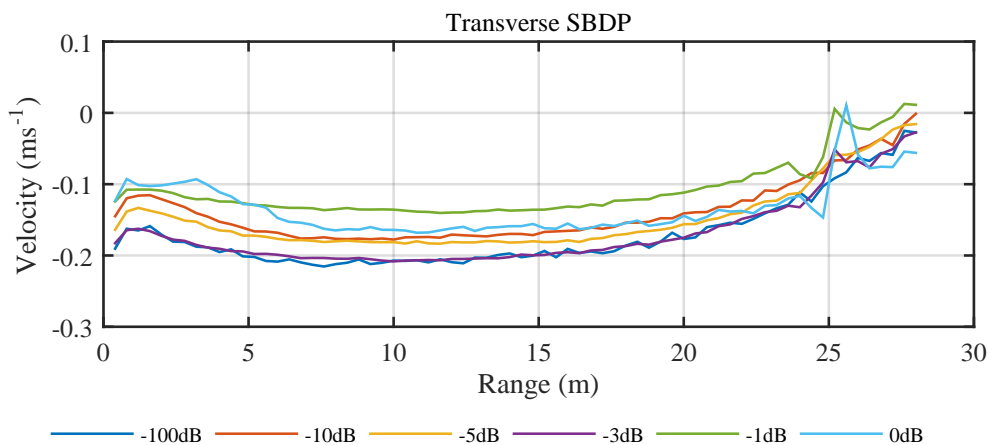


Figure 5.26: Velocity measurements by horizontal SBDP showing effects of surface reflections, for a range of power settings of the source vertical SBDP.

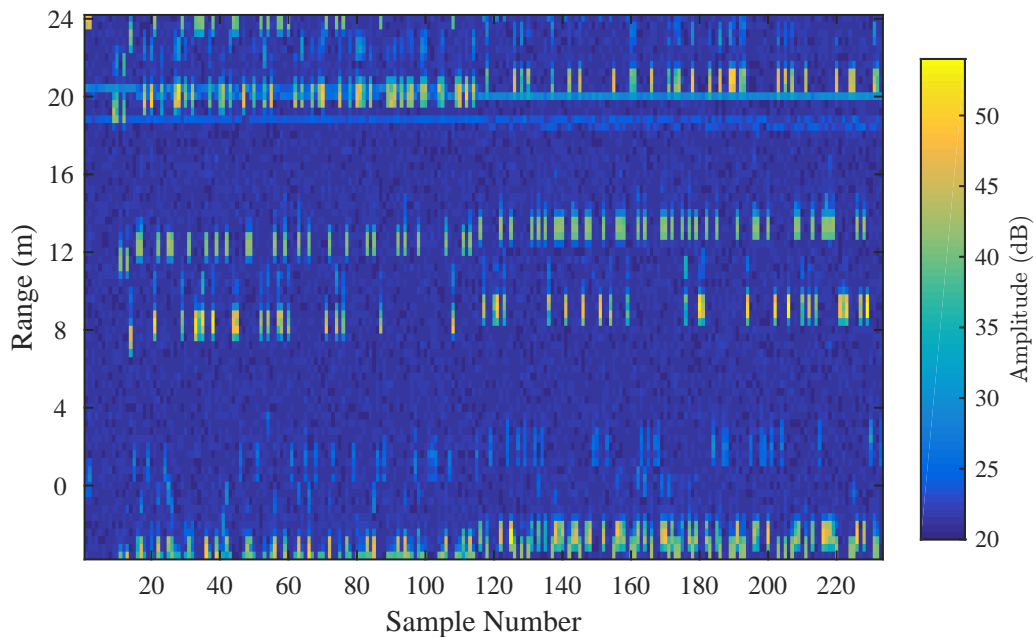


Figure 5.27: Amplitude returns for a SBDP set to LSNR mode, illustrating the complex effects due to a parallel oriented AWAC transmitting at full power.

pulse length were larger meaning one AWAC pulse is more than twice as long as that of the SBDP.

Figure 5.28 shows the equivalent graph for the SBDP switched to 0 dB power setting. Again the bands of interference are visible except where obscured by the high amplitudes near the instruments and at the surface reflections. As the vertical velocity measurements are very low it is difficult to discern the effects of a possible bias towards zero. However, Figure 5.29 illustrates the variation in velocity standard deviation with range up to 20 m. It is causing two spikes which coincide with the interference bands in Figure 5.28 at 7.6 m and 12.0 m range.

Figure 5.30 illustrates the spectral analysis of two range bins of the velocity measurements from figures 5.28 and 5.29. One at 4.0 m where there is minimal evidence of interference and one at 7.6 m coinciding with the largest standard deviation peak. The results show clear effects of additional energy centred at the 0.5 Hz range which is half the sampling frequency of the AWAC in this test.

A similar comparison was made with the effects of a long range Continental-SBDP. This sensor has a pulse frequency of 190 kHz and can take measurements over ranges of up to 200 m. The continental has much larger bins than the SBDP (2 m compared with 0.4m) thus one pulse from the continental will span 5 range gates of the SBDP. Figure 5.31 illustrates the average amplitude returns with range of SBDP_{RT} at 2 Hz in LSNR mode, with the Continental operating at 1 Hz mounted parallel to it. Here there is clear evidence of interference throughout the range,

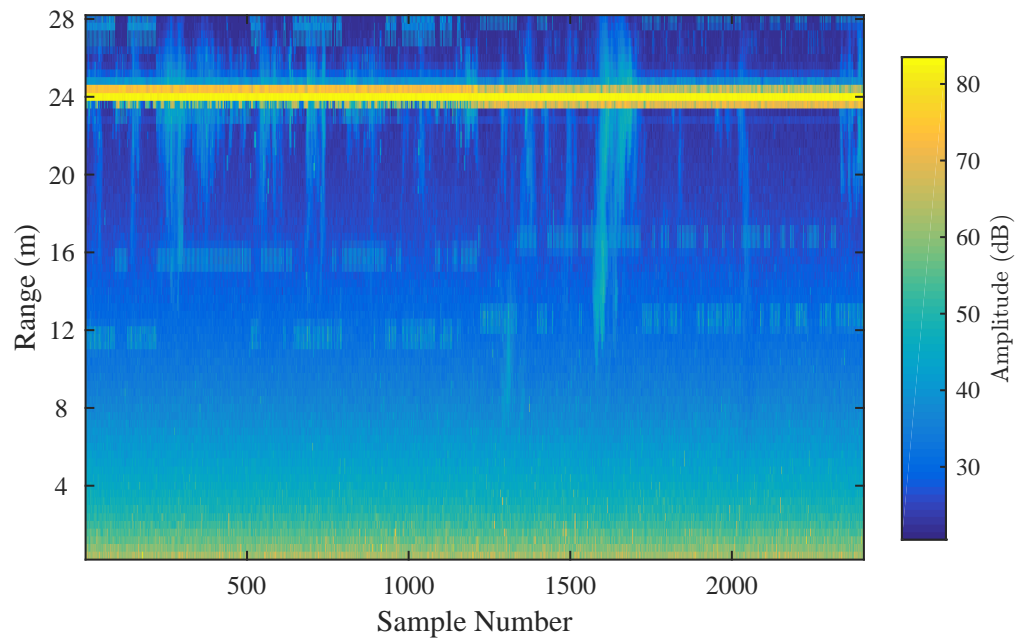


Figure 5.28: Amplitude returns for a SBDP set to 0 dB pulse power mode, illustrating the complex effects due to a parallel oriented AWAC transmitting at full power.

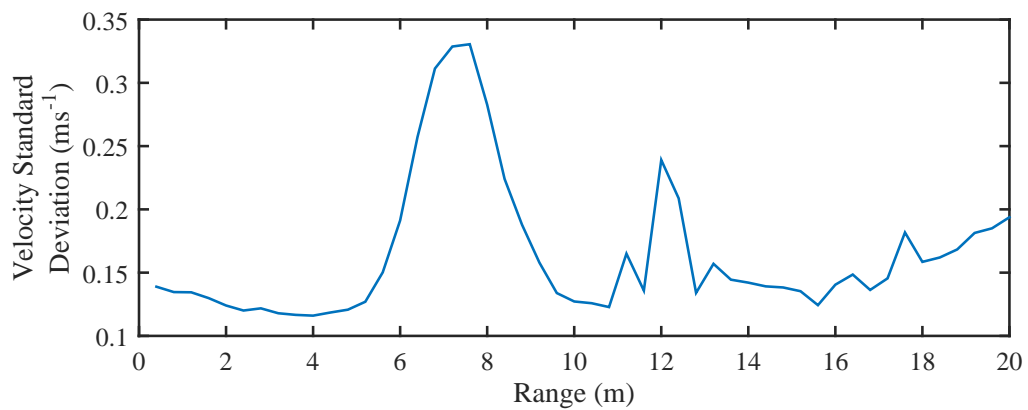


Figure 5.29: Standard deviation of velocity measurements at each range bin of SBDP, highlighting interference caused by the AWAC.

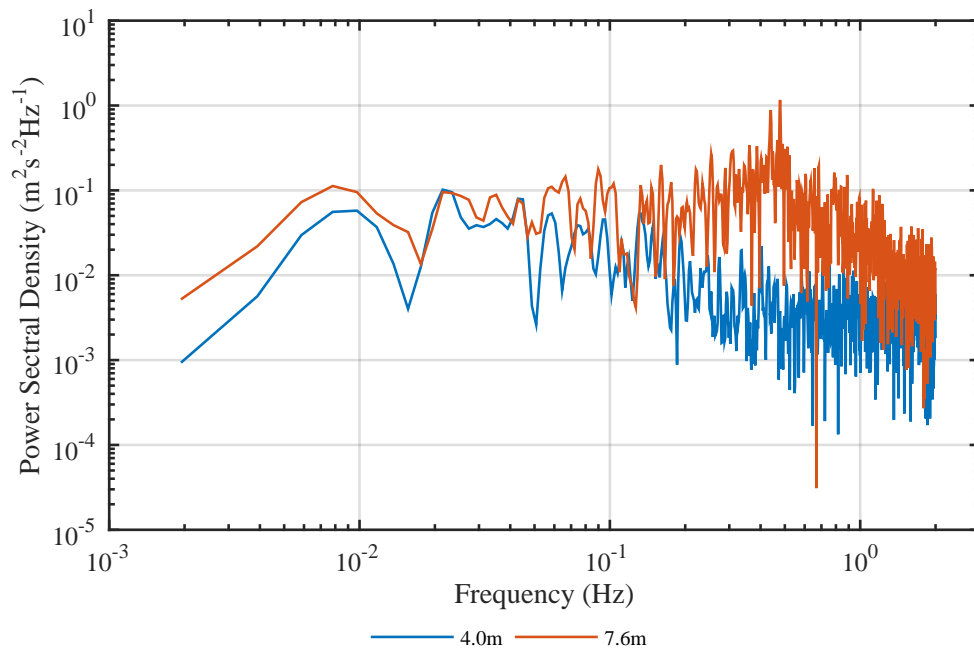


Figure 5.30: Power Spectral Density for an affected and non-affected range bin of the vertical SBDP due to interference from the AWAC.

rather than being limited to bands.

Assessing the effect when the SBDP is switched to 0 dB power setting, Figure 5.32 shows the velocity and its standard deviation with range. The velocity shows an improbable swing with range from positive for $x < 12$ m and negative for $x > 12$ m. The velocity standard deviation is low at the near region and increases beyond 8.0 m with a peak at 14.4 m range.

It is likely that the velocity readings of the SBDP are more reliable in the nearer range where its own signal strength is strong. Under this assumption the spectral content of two range-bins: 4.0 m (where the SBDP amplitude is relatively high) and 14.4 m (coinciding with the maximum velocity standard deviation range) are given in Figure 5.33. Neither signal shows evidence of the turbulent cascade but this is expected for the near slack water flow conditions at which this data set was collected. The energy content across the range of the 14.4 m sensor is visibly higher with a large spike at the 1 Hz range corresponding to the sample frequency of the Continental.

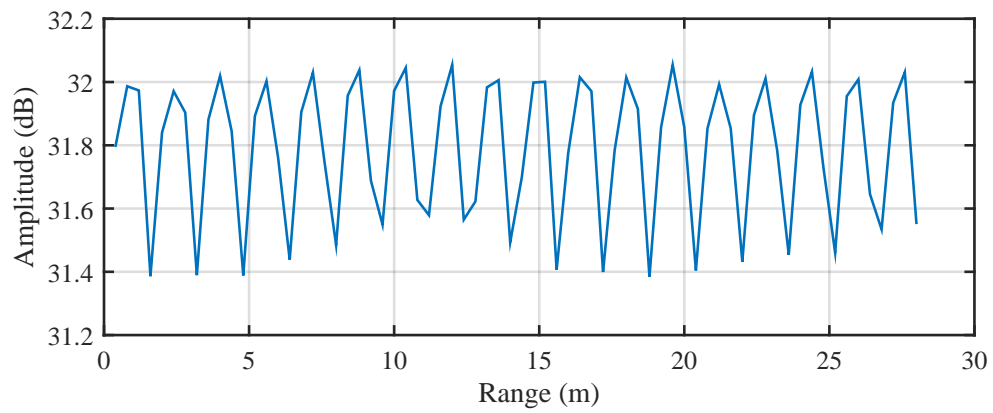


Figure 5.31: Amplitudes from SBDP set at 0 dB power setting, mounted parallel with a Continental-SBDP.

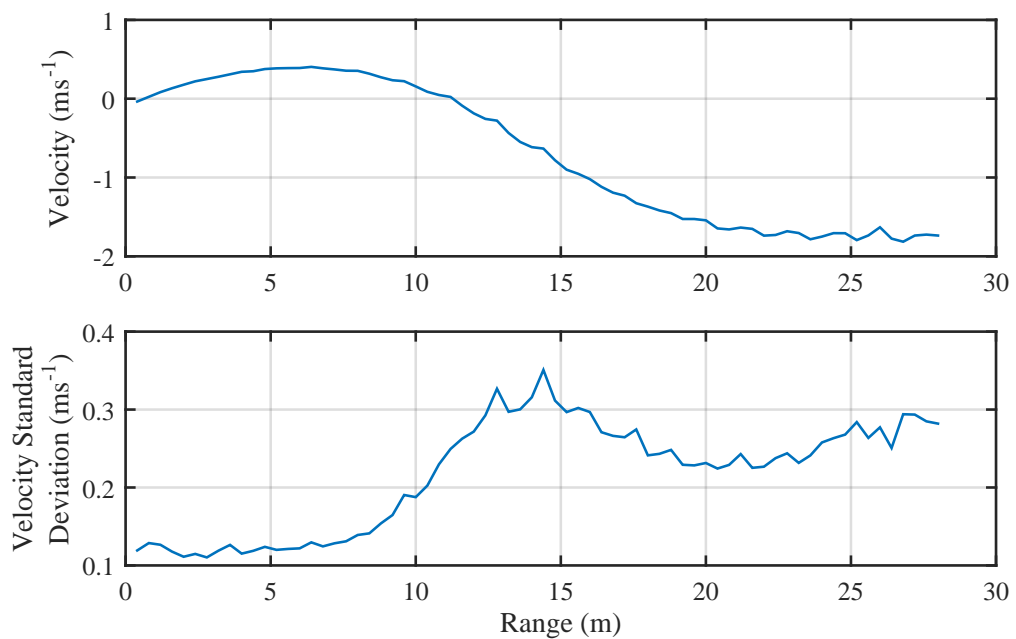


Figure 5.32: Standard deviation of velocities with range of SBDP set at 0dB power setting, mounted parallel with a Continental-SBDP.

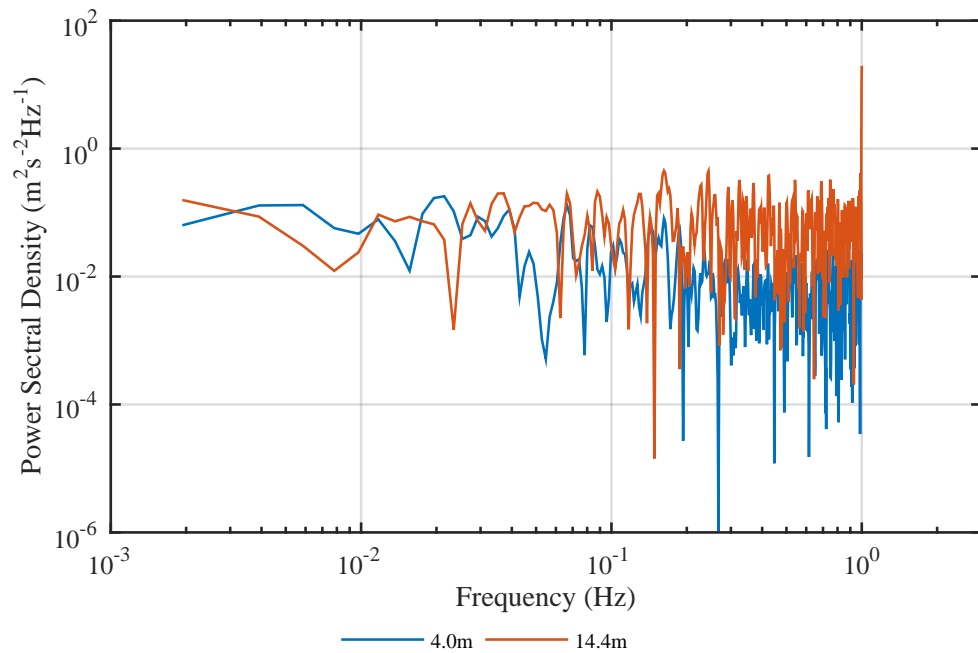


Figure 5.33: Power spectral density of SBDP set at 0 dB power setting at two range bins, mounted parallel with a Continental-SBDP. A spike at the Nyquist frequency and higher energy across the remaining frequency range is clearly evident in the 14.4 m range velocity measurements.

5.4 Discussion of Results

Overview

Previous knowledge of ultrasonic acoustic velocity sensors suggested that interference from one beam would adversely effect velocity measurements in another (Appell *et al.*, 1991). This chapter has presented clear evidence that acoustic sensors operating in < 4 m proximity will cause interference that will negatively affect velocity measurements. The evidence suggests that interference is at its strongest and most detrimental at the range corresponding to the period of the travel time of the pulse from the source sensor to the receiving sensor. There is evidence that interference exists beyond this range but as the amplitude of the interfering signal decreases significantly, the effects are negligible. Sensor users concerned about these effects in the far range should look for fluctuations in the instrument noise floor with range as evidence of cross-talk.

Effect of amplitude and SNR tests

The effects of interference in the velocity measurements has been shown to vary significantly with the amplitude of the spike caused by the cross-talk interference. For parallel sensors the result was a biasing of the velocities towards zero with a decrease in both mean and standard deviation. This effect was shown to decrease with signal to noise ratio. However, a high SNR of 0.9933 is needed to reduce the effects to a negligible level. This effect was only characterised for one offset configuration and separation and utilised a simplified assumption of the SNR. A more comprehensive study would reveal any variation in this rule of thumb with range and separation.

The amplitude in the receiving instrument for parallel sensors decreases with distance. With only four points to plot the fitted trend has a high level of uncertainty, but the amplitude would be expected to fall off as a function of distance squared as for a standard acoustic signal. There is also clear evidence that the amplitude of interference decreases with source power, however this appears more likely to be a linear relationship. This implies that power settings would need to be so low as to make the sensors ineffective over their designed range. Thus separation seems to be a better strategy to mitigate the effects.

Mitigating cross-talk with pulse offset

A more effective interference mitigation strategy is to use the pulse offset to ensure no instruments transit during a closely located instruments' listen cycle. The offset required is a function of the range of the receiving sensor:

$$T_{offset} = \frac{2 \cdot \delta y_{range} - \delta x_{separation}}{C} \quad (5.4)$$

where T_{offset} is the offset period, δy_{range} is the max range of the sensor, C is the speed of sound in water, and $\delta x_{separation}$ is the separation of the sensors.

Extensive use of this technique during the ReDAPT project lead to the discovery that there was a limit to the maximum offset that could be used before regular sensor errors occurred. This effect was most prevalent in the higher 4 Hz sample rate configuration where a maximum offset of around ~ 150 ms was possible. The next generation of SBDPs are expected to be more stable in this regard but will also offer higher sample rates which reduces the limit of the offset value that can be used for this technique.

In summary mitigation strategies for large numbers of sensor arrays should require all sensors to be linked over a PTP system but also make use of separation to maximise data gathering potential.

Effect of surface reflections

Section 5.2.2 showed that vertically mounted SBDPs caused reflections off the surface due to the change in medium, which was seen to adversely affect the measurements of the horizontal SBDPs. These effects were much weaker than those from parallel interference, although this would be expected to increase for sensors mounted in shallower depths. The location of the interference caused by these reflections will also be a function of depth and can be mitigated with a pulse offset.

Interference from other sensor types

Tests of the effect of cross-talk of different acoustic sensor types appeared to have a different effects from inter-SBDP cross-talk. Although the results were taken for slack water conditions which did not allow accurate assessment of mean velocity bias there was clear evidence that the affected areas caused increased velocity fluctuations in those regions. There are added complications with different sensor types with different sample rates and pulse lengths and the fact that these sensors are not PTP synchronised, causing the location of interference to drift and to be spread across the receiving SBDP range, rather than focused on a specific band.

The difference between the effects of the same sensor and those of different sensor types are not surprising. Different sensor types send out different coded pulses (with the SBDs being broadband and the others narrowband) and in this case different pulse lengths. No tests were carried out on the effect of the SBDPs on the other instrument types as it was deemed outwith the scope of this work. However, experience and visual observations of the data suggests they will also cause interference. The lack of PTP in the AWAC and Continental, makes these effects difficult to control and it is recommended that different types of sensors without PTP synchronization should not be operated in close proximity. If this is not possible, it is concluded that long range low frequency (and high pulse amplitude) sensors must be placed significantly far away from short-range devices if the latter are to operate effectively.

Cross talk in angled sensors

The angled sensors responded differently to cross-talk with evidence that they were measuring components of the flow velocity in the affected regions in LSNR mode. A clear correlation between the LSNR results in the affected bin was shown for a 23.2° sensor angle. Although the measured velocity was less than the estimated component from the DBDP upstream, the difference in results were similar (within 1.1 %) to the difference of the powered sensor which has a high level of reliability for mean velocity metrics. The same technique shows evidence of being possible at a sensor angle of 46.4° however there were too few data sets to assess its accuracy. There is little or no evidence of this phenomenon in the parallel sensors, thus there must be a relationship between accuracy and sensor angle. The optimum angle could be

inferred from work done on ADVs (Lohrmann *et al.*, 1994) or as part of a future project where sensor angle can be easily varied.

The results of pulse offsets in this mode showed that the highest gradient and lowest instrument noise value were both at an offset of -0.2 ms. The variance attributable to noise in this configuration was $1.61 \times 10^{-3} \text{ m}^2\text{s}^{-2}$ which is significantly lower than those of a standard SBDP, as presented in Figure 4.4. This suggests that lower than standard noise measurements may be taken with this method if it can be optimised.

In order to reduce uncertainty, future iterations of this experiment, measuring velocities by cross-talk in LSNR mode using angled sensors would include: a greater number of samples, a more rigorously measured sensor angle and repeatable and measurable flow conditions. An experiment where sensors could be mounted in a current tank of large enough dimensions to avoid significant boundary reflections, and velocities could be varied would be the ideal scenario.

This technique could be used as part of a focus beam sensor array. Work by Sellar *et al.* (2015) on the ReDAPT project has already focused on such a mounting configuration but utilising four SBDPs in a powered mode using pulse offsets to remove interference. The results showed high accuracy in resolving velocity vectors comparable with a standard DBDP. If the LSNR mode configuration could be used to resolve the same u , v and w vectors it would allow this same process but not require the period of time for 4 pulse offsets which is 0.25 seconds. As the processing time required by the instruments decreases the sample-rate will increase (as was the case in the latest iterations at the time of writing) limiting the maximum pulse offset that can be used. Some data was available to test this method and will form part of future work with this data.

5.5 Chapter Summary

This chapter has presented a comprehensive investigation of the indicators of, effects of and mitigation strategies for interference between acoustic Doppler sensors. It concluded that off-setting the pulses is the best form of cross-talk mitigation. If mitigation is not employed sensors will experience a band of interference that will render certain ranges of the instrument measurements unusable. Parallel and angled sensors as well as reflections from boundaries from all acoustic instrument types tested, adversely affected velocity measurements in the SBDPs.

With a strategy for mitigating inter-instrument interference, along with an understanding of other background noise characterised in Chapter 4, the confidence in the results of these instruments in the recommended configuration is enhanced. The following two chapters seek to

utilise data collected by the SBDPs, along with appropriate data from a seabed mounted DBDP to undertake a comparative study of the best practise measurements from both sensor types.

SBDP and DBDP comparison - Part A: Introduction and Data Preparation

6.1 Chapter Overview

This Chapter along with Chapter 7 investigate the metrics measured by an array of three Single Beam Doppler Profilers (SBDP) with one orientated along each Cartesian vector with a single Diverging Beam Doppler profiler (DBDP). The SBDPs are mounted at mid-depth on the turbine while the DBDP is mounted ~ 50 m upstream on a seabed gravity frame.

The aim is to assess the advantages and drawbacks of the SBDP array, compared with the current industry practise of a single DBDP. Chapter 6 gives an introduction to the potential advantages of a mid-depth SBDP array in this configuration. It also presents an overview of the DBDP data processing methodology. Chapter 7 presents the results of the comparison to give the best estimate of mean and turbulent flow metrics available from each sensor type.

In order to make an accurate comparison of two different types of sensor, the processing of measurements must be done so as to ensure appropriate data is selected and the most accurate metrics are calculated from each. The importance of accurate turbulence measurements at tidal energy sites has already been underlined in Chapter 2 and it is the goal of this work that the results of this chapter along with Chapter 7 will improve confidence in using SBDPs to capture these metrics.

Part A covers the following topics:

- Theoretical background;
- Data-set selection;
- DBDP velocity transforms;
- Instrument range bin selection for intra-instrument comparison;
- Defining DBDP noise correction curves;
- A discussion on appropriate ensemble averaging of measurements to reduce noise.

6.1.1 Motivation

The central aim of this thesis is to compare newly available SBDP sensors to the industry standard of seabed mounted DBDP. In order that this comparison is accurate the data selected for the comparison must be appropriate and the two instruments, installed on different mounting frames, must be aligned to a common axis. In addition, the issues relating to the velocity transform employed by the DBDP must be explored and minimised. This will allow the most accurate comparison between the resulting metrics processed by the two sensors.

6.1.2 Contribution

The data selection, processing algorithms, analysis and results are the sole work of the author unless specifically cited. The instrumentation set-up and data collection was a collaborative effort between the author and the project manager as discussed in Chapter 3. Here data was not collected specifically for this comparison, rather it uses data captured throughout the ReDAPT data campaigns.

6.2 Theoretical background

DBDPs have been common industry practise for measuring velocities at tidal energy sites as discussed in detail in Section 2.5. DBDPs come in various designs but most incorporate 3-4 transducers angled $15 - 30^\circ$ off vertical, with some devices also employing an additional vertical beam. The Fall of Warness site is approximately 45 m deep (dependent on location and tide) and the DBDP employed for this test was a 4 beam 600 kHz RDI Workhorse Sentinel, with the beams angled 20° off vertical.

DBDPs have two central issues when being used to measure the turbulent aspects of the flow:

- In order to resolve horizontal velocities from the angled beams the flow is measured at two separate locations, thus it is a required assumption that the flow is homogeneous over this range.
- The velocity transform required to convert the beam velocities to a Cartesian coordinate increases the random error in the outputs.

The spatial averaging required with a DBDP increases with range. At 45 m range the beam spread covers a diameter of 32.8 m and at hub height (which for the Alstom DeepGen iv device at the Wall of Warness is 20.8 m above the sensor) the spread is 15.1 m as illustrated in Figure 6.1. With a Reynolds number in the order of 10^7 (as calculated in Section 4.2.1) the site represents a fully developed turbulent flow (Crowe *et al.*, 2005). The magnitude of the integral lengthscales of turbulent flow in tidal channels are not well understood with Blackmore *et al.* (2011) running CFD simulations that predicted $1/3$ of the channel depth to be a good estimate. Guidance for the wind industry recommends that the characteristic lengthscale in the transverse

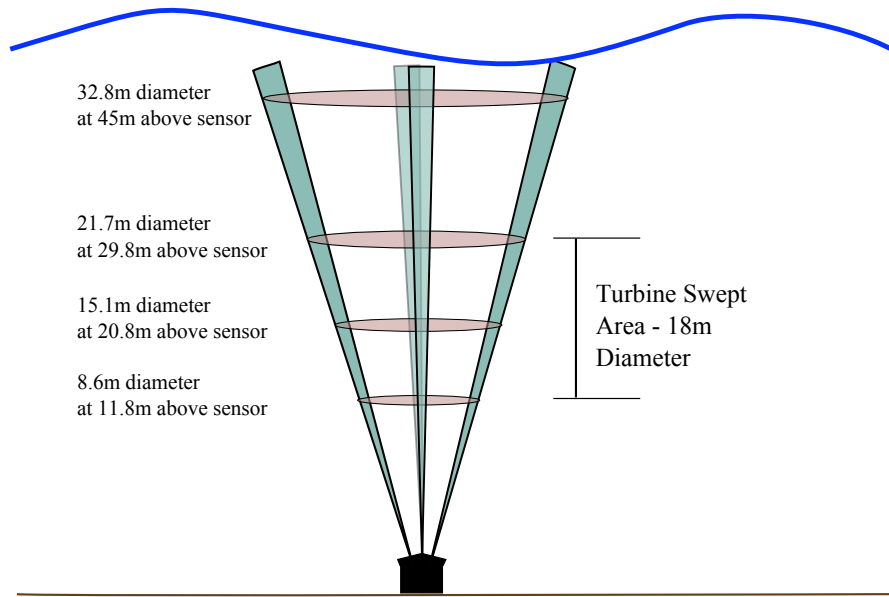


Figure 6.1: Illustration of increased spatial averaging of DBDP measurements with separation from the instrument.

should be 0.3 times this value and the vertical 0.1 times this value (DNV, 2002). For a 45 m channel that would indicate lengthscales of $\ell_x = 15m$, $\ell_y = 5m$ and $\ell_z = 1.5m$. These predictions are of similar values to recent field measurements taken by Thomson *et al.* (2014) in a 55 m deep channel in Admiralty inlet, North West coast of the USA.

Since the diameter over which a single value for a given depth is measured by the DBDP exceeds the expected size of the largest eddies in the flow for a large part of the water column, it is spurious to assume the flow is homogeneous over these scales. In addition, the transform from the original beam velocities increases instrument error as discussed in more detail in Section 6.4 (Nystrom *et al.*, 2002).

The transform of the beam velocities to the Cartesian velocity measurements is required as the beam velocities are of little use to device developers who are concerned with inflow to the device. DBDPs have the advantage of being able to measure this portion of the flow from a mounting point on the seabed. On the ReDAPT project the asset of the turbine allowed measurements in the swept area to be taken with SBDPs which removes the need for a velocity transform of the measurements and does not rely on large scale spatial averaging. However, the separate velocity components (u, v and w) will not be from a common measurement volume, nor do they form a pseudo-point as with the DBDP.

In order to assess if a Cartesian SBDP array could improve confidence in site characterisation metrics, a study utilising SBDPs mounted on the Turbine along the three Cartesian vectors,

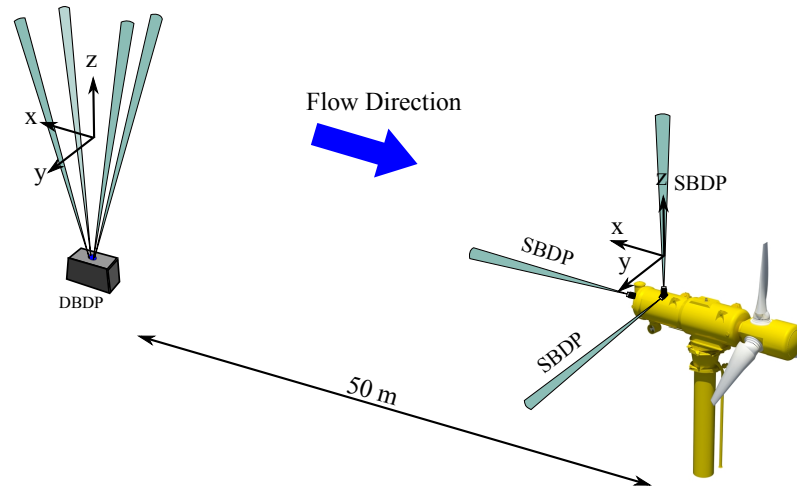


Figure 6.2: Illustration of the measurements from the two instruments.

x , y and z and an ~ 50 m upstream DBDP was employed. Figure 6.2 gives an overview of the instrument setup with the adopted common vector convention between instruments and Figure 6.3 illustrates the relative height of the turbine above the two main DBDP deployment locations. The orientation of all the SBDPs are shown in Figures 3.7 and 3.8 in Chapter 3. The SBDPs employed for this test were: SBDP_{RMS} sensor mounted on the rear frame of the turbine pointing rearwards along the axis of the turbine nacelle, SBDP_{VR} mounted on the top frame pointing vertically towards the surface and SBDP_{SMA} mounted on the top frame on the starboard side, parallel to the surface and normal to the other two sensors. The data from these SBDPs is then contrasted with that from the upstream North West DBDP for flood tide measurements.

6.3 Data Set Selection

The data used in this section was not collected as part of a specifically designed test. Data collected throughout the eight turbine deployments with their associated data collection campaigns was available for use. However, it was desirable to select a single deployment with the most appropriate data available for a single tide direction for each of the x , y and z comparisons. This was primarily due to uncertainty in the location of DBDP deployments which, although in the same location to within approximately 20m (see Sellar and Sutherland (2015) for more information of DBDP deployment locations), could introduce discrepancies in orientation and position, as well as reduce the effect of seasonal and tide-direction variations.

All the data collected during the project was averaged into 5 minute data sets and was stored in an internally designed database as described in Section 3.7. The database also includes information about the turbine orientation and operation as well as basic wave statistics, which

are contemporaneous with the velocity measurements. In order to extract an appropriate data-set, the database had to be searched based on specified criteria. The individual SBDP and instrument combination for each vector with the most data meeting those criteria was selected. This was done to minimise the effect of differences between individual sensors based on mounting location, as was discussed in Chapter 4. In addition, the site shows significant variation in mean and turbulence statistics between the ebb and flood tide. Thus, it was desirable to only select one tide in order to maximise the likelihood of metrics converging over a large number of samples. Once the data-set was selected from the 5 minute sets in the database, the original data corresponding to those sets were loaded for each sensor at the original sample-rate.

As described in Chapter 3 the instrumentation on the turbine was altered throughout the 8 turbine deployments. For this study each vector x, y and z is considered independently. The criteria for data selection of 5 minute data averages were:

1. Turbine not operating;
2. Turbine reversed to within 10° either side of the onset flow;
3. Estimated H_{m0} was < 1.5 m;
4. DBDP upstream of the turbine data available;
5. SBDP data available along the appropriate axis;
6. SBDP data not affected by excessive electrical noise or cross-talk.

For example: A Flood tide data set with the North-West DBDP as well as SBD_{RMS} on the rear of the turbine were selected for the x axis data set, as this deployment had the most data meeting these criteria for two individual instruments. Only data for the Flood tide was used within this study, as the flow characteristics are known to vary significantly between Ebb and Flood at this site (Sutherland *et al.*, 2013). The data sets selected for each direction are detailed in the relevant sections of Chapter 7.

In order to accurately compare metrics, fixed instrument settings were required throughout the data set. The data selection was refined to include the most prevalent settings with other data removed. The settings used are detailed in Table 6.1

Instrument	Power (dB)	Sample Rate (Hz)	Cell Size (m)	Blanking Distance (m)	Velocity Range (ms^{-1})
SBDP	0	2	0.4	0.4	4
DBDP	0	1 / 0.5*	1	2.1	5

* 0.5 Hz samplerate was the setting on the DBDP deployment used in the vertical comparison.

Table 6.1: SBDP and DBDP settings for comparison.

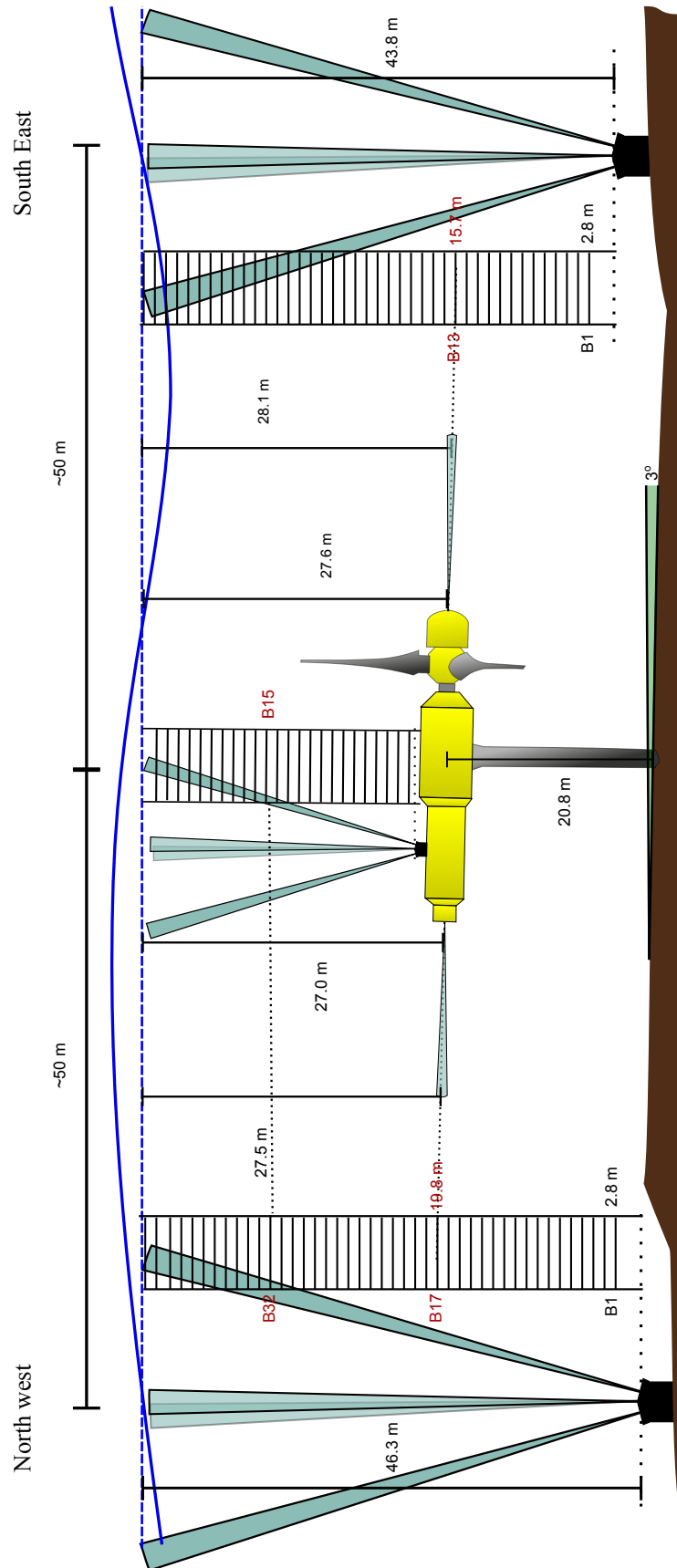


Figure 6.3: Turbine and DBDP measurement bin heights for comparison

6.4 DBDP Velocity Transforms

6.4.1 Introduction

DBDPs measure the ‘along-beam’ velocities, i.e. those along the orientation of a given transducer and thus the path of the acoustic pulse as discussed in Section 2.6. These velocities are of little use to device designers, who are concerned with the flow onset to the rotor plane. It is therefore desirable to define the flow in terms of the turbine orientation, thus metrics are usually defined as outlined in Section 2.7.4, with x along the nacelle, y normal to this and horizontal and z as vertical.

Two stages are required in order to achieve this velocity transform. The first is to transform the beam velocities into two pairs of one horizontal and one vertical velocity based on the planes of opposing DBDP beams. The second is to rotate these to account for the heading, pitch and roll of the sensor. The heading is normally adjusted such that two horizontal vectors are orientated to North and East, but here the aim is that they are rotated such that one is orientated along the same angle to the flow as the turbine and the other normal to this.

It should be noted that a fixed angle is used for direction to the turbine. The turbine can yaw to different angles to the onset flow, however, this is limited to closely aligned values by the data selection. It would be possible to adjust the heading to account for this variation but with the uncertainty of the meander of flow direction upstream of the turbine and its variation over the tide, a fixed angle was deemed the best option. In order to calculate this angle, a technique to align the flow velocities from the DBDP and turbine mounted sensors was required.

6.4.2 Transform definitions

The first phase of the DBDP velocity transform is from the beam velocities into a Cartesian co-ordinate system relative to the sensor’s transducers. This is done by calculating the resultant component of the velocities based on the geometry of the beam angle. Opposite facing beams are used in pairs, with each pair producing a horizontal and vertical component. As this produces two vertical estimates, this can either be used to provide an error velocity or a single vertical measurement can be calculated from the four beam velocities to increase the accuracy, as is done here.

The equations of this velocity transform are defined as:

$$vel_{h1} = \frac{1}{2 \sin(\beta)} \cdot (vel_{B1} - vel_{B2}) \quad (6.1)$$

$$vel_{h2} = \frac{1}{2 \sin(\beta)} \cdot (vel_{B4} - vel_{B3}) \quad (6.2)$$

$$vel_z = -\frac{1}{4 \cos(\beta)} \cdot (vel_{B1} + vel_{B2} + vel_{B3} + vel_{B4}) \quad (6.3)$$

where vel is a velocity in either the horizontal axis of the plane of beams 1 and 2 ($h1$) or 3 and 4 ($h2$) and z is the vector equidistant from all the beams (but not necessarily exactly vertical) (RDI, 2010). vel_{B1} is the measured velocity along beam 1, etc. and β is the beam angle from vertical, which in the case of the RDI 600 kHz Workhorse Sentinel in question, was 20° . Figure 6.4 illustrates these velocity vectors relevant to the instrument.

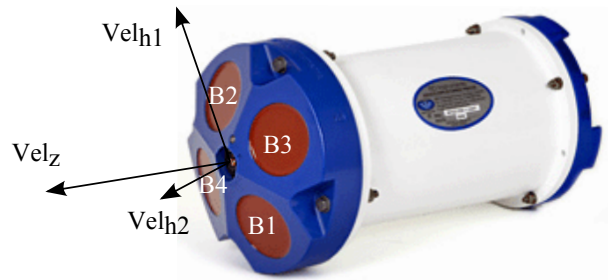


Figure 6.4: DBDP transform stage 1.

In order to rotate these instrument-relative metrics to those needed for the turbine, the heading angle between the turbine and the sensor is required to be known. The calculated angle from the DBDP to the turbine is then used to rotate the result, such that a heading of 0° is the heading best aligned with the turbine to the onset flow. In addition, the DBDP was mounted in a gimbal to mitigate for any offset angle of the gravity base from horizontal, thus small offsets in pitch and roll are still possible. An example of pitch and roll data is illustrated in Figure 6.5. The DBDP's internal pitch and roll sensor measurements are used to compute this transform.

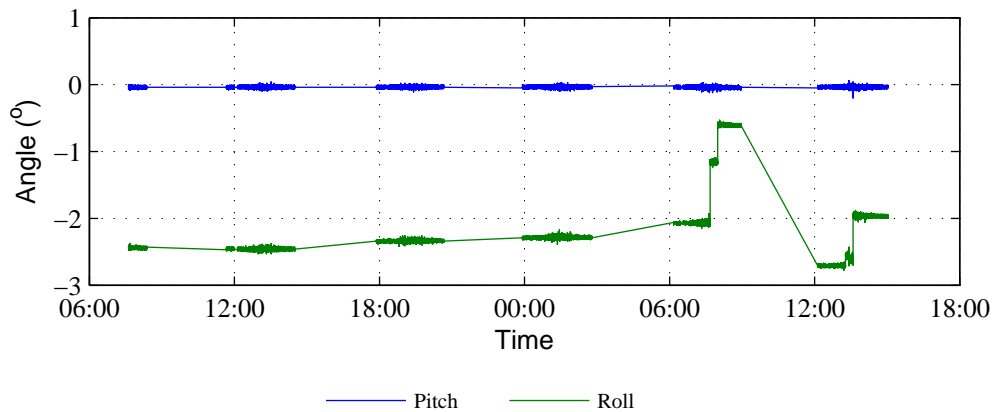


Figure 6.5: Example of DBDP pitch and roll measurements showing Flood data.

The rotation matrix is defined as:

$$T = \begin{bmatrix} -\cos(\theta)\cos(\psi) - \sin(\theta)\sin(\phi)\sin(\psi) & \sin(\theta)\cos(\phi) & \sin(\theta)\sin(\phi)\cos(\psi) - \cos(\theta)\sin(\psi) \\ \sin(\theta)\cos(\psi) - \cos(\theta)\sin(\phi)\sin(\psi) & \cos(\theta)\cos(\phi) & \cos(\theta)\sin(\phi)\cos(\psi) + \sin(\theta)\sin(\psi) \\ \cos(\phi)\sin(\psi) & \sin(\phi) & -\cos(\phi)\cos(\psi) \end{bmatrix} \quad (6.4)$$

where θ is the heading, i.e. the DBDP heading measurement with the heading to the turbine subtracted from it, ψ is the roll and ϕ is the pitch (RDI, 2010).

The velocities relative to the turbine co-ordinate system are then calculated via:

$$\begin{bmatrix} v \\ u \\ w \end{bmatrix} = T \cdot \begin{bmatrix} vel_{h1} \\ vel_{h2} \\ vel_z \end{bmatrix} \quad (6.5)$$

6.4.3 Angle to turbine

The locations of the turbine and of each DBDP deployment and thus the heading between them are known. However the heading of the DBDP was measured by the internal compass, which measures the angle from North, and is only accurate to around 5° (depending on the accuracy of the pre-deployment calibration). This meant the accuracy of results would be improved by verifying the flow angle through analysis of flow velocities between the DBDP and turbine mounted sensors. This was done by comparing the DBDP to the Acoustic Wave And Current (AWAC) sensor (a DBDP variant with three angled beams and one vertical beam), mounted on the top of the turbine. The AWAC was mounted in a fixed position, orientated such that its internally processed u velocity was orientated along the turbine nacelle without any post-processing rotation.

For each DBDP deployment a contemporaneous data subset was selected where the DBDP and the AWAC were both operating during flood tides with the turbine reversed to within 10° of the onset flow (mean turbine yaw angle of 141.7°) and the estimated H_{m0} was $< 1.5\text{m}$. Bin heights were selected such that the depths were equal and the AWAC measurements were suitably removed from both the turbine nacelle and the surface. These were AWAC bin 15 and DBDP bin 32. The DBDP 5 minute averaged beam velocities were then transformed for a range of turbine angles from 120° to 160° in 0.1° increments. For each angle the resulting transformed DBDP \bar{u} and \bar{v} velocities were plotted against the AWAC equivalent measurements. Figure 6.6 presents the gradients and R^2 values of the linear fits of these plots and Figure 6.7 shows an example of the one-to-one \bar{u} and \bar{v} inter-instrument comparison plots.

Figure 6.6 shows a difference in angle for the gradients closest to 1 and -1 in the x (139.3°) and y (146.5°) directions respectively of 6.2° . The y direction has a negative gradient due to the opposing positive direction conventions between the two instruments, but the physical direction

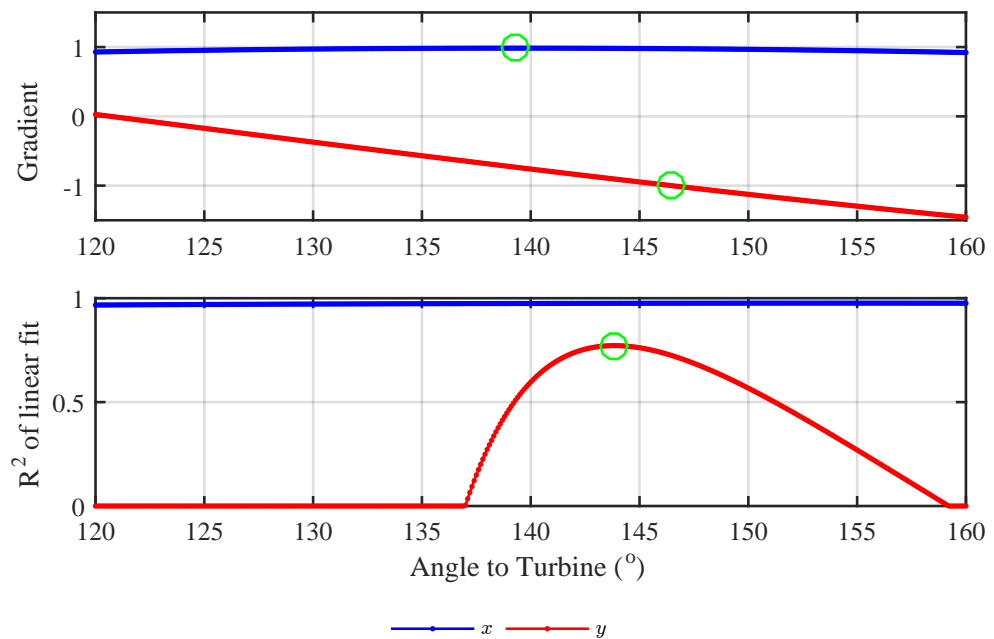


Figure 6.6: Gradients (top) and R^2 values (bottom) for linear fits of mean velocities for the NW DBDP and the AWAC for a variety of trial angles between DBDP and turbine. The green circles highlight the gradients closest to 1 and the highest R^2 of the v measurements.

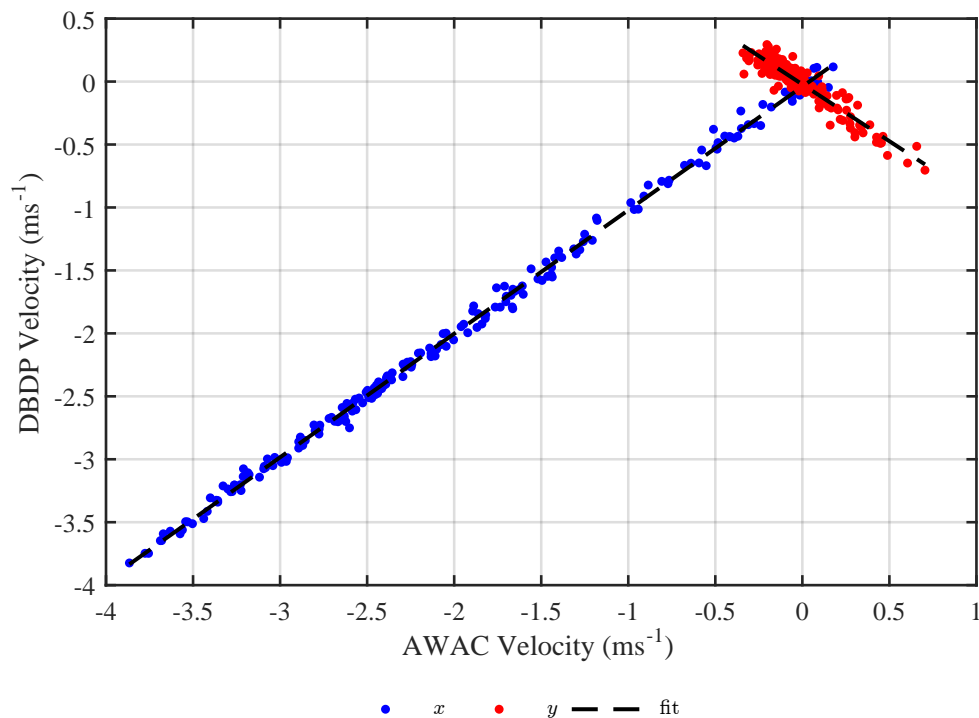


Figure 6.7: One to one mean velocity plot for a DBDP heading to turbine angle of 148.7° between DBDP and turbine using AWAC.

	x	y
Gradient	0.98	-0.90
R^2	0.98	0.77

Table 6.2: Gradients and associated R^2 values of linear fits for the heading to turbine angle given in Figure 6.7.

Direction	x	y	z
DBDP Deployment	NW 6 th	NW 1 st	NW 1 st
Angle to Turbine	143.8	140.52	140.52

Table 6.3: Turbine angles from alternate NW DBDP deployments.

is the same. This infers a relatively small change in direction over the separation between the two sensors. The \bar{u} measurements stay relatively close to 1 with an R^2 of > 0.97 throughout the range and thus were not used further to define the angle. However the R^2 values of the \bar{v} fit vary more significantly. Thus the median of the three angle values: the closest gradient to 1 for \bar{u} , the closest gradient to -1 for \bar{v} and the highest R^2 of the \bar{v} fit was selected as the most accurate representation of the angle to the turbine. The gradients and R^2 values for the chosen angle for this example are presented in Table 6.2.

Table 6.3 presents the chosen DBDP deployments and associated alignment angles for each basis vector used in the analysis.

6.4.4 Discussion

There is the option of including pitch and roll data as part of general quality control of data as some metrics, such as Reynolds Stresses, are particularly sensitive to this (Osalusi *et al.*, 2009). However, with the measured angles less than 3° this was not deemed necessary. As the tides change in direction and flow velocity, the resulting forces alters the frame position and/or gimbal angle within it (as seen in the roll in Figure 6.5). Over long deployments the gimbals tended to stiffen causing a ‘jerking’ rather than a smooth movement. The low amplitude higher frequency fluctuations are likely due to sensor noise. The stiffness of gimbals (and whether they are a preferable mounting option at all) remains a key challenge. An early DBDP deployment with an under-damped gimbal led to a large amount of low quality data due to extreme DBDP movement. If the technique used to align the sensor information is proved to be reliable, it could be utilised to calibrate an upstream DBDP for use in an active control system for a turbine to predict upstream velocities.

The spread of heading angles between the three methods used in its derivation presents a source of uncertainty. In the given example the one to one gradients of the x and y directions are separated by 7.2° , as the cosine of this angle represents a $< 1\%$ change in velocity magnitude the effect should be minimal. In addition taking the median of the three values should provide

the most accurate assessment of the tide direction. The method presented here was compared with alternate methods used in Sellar and Sutherland (2015) with a high degree of agreement in results.

6.5 Instrument Range-Bin Selection

6.5.1 Introduction

With the available instrument mounting locations it was impossible to achieve a common sample volume for the two instrument types for any of the measurements. However, in order to compare metrics, a range bin for each instrument had to be selected. With the SBDP mounted on the turbine, there are several effects that cause a variation in velocity measurements as a function of range. Near the turbine the flow is slowed due to friction and blockage effects of the nacelle and support structure, and at the far range as the pulse amplitude returns decrease, the velocity tends to zero as discussed in Chapter 4. Hence there is a ‘sweet spot’ in the middle range between these two effects, ideally with a stable flat range in the middle. In addition there is the possibility of spatial variation in the flow along the SBDP beam vector due to changing bathymetry and meander of flow direction. Similarly for the DBDP, the flow nearest the seabed would be the slowest and increases towards the surface due to the bottom boundary layer friction as discussed in Section 2.4.

6.5.2 Results

Streamwise velocities

Figure 6.8 shows how this was assessed for the rear facing SBDP for the x direction, with the selected bin highlighted with a red circle. The flow can be seen to increase with distance from the turbine, steeply over the first 10 bins (4.4 m) then there is a region of relative constant velocity from bins 15 to 40 (6.4 m to 10.4 m). Beyond this the noise tends to bias the velocity reading towards 0. Thus the bin of maximum velocity readings was selected as the ideal bin for uninterrupted flow which was bin 23, 9.4 m from the sensor.

For the two horizontal components of the DBDPs measurements there were two options for bin selection:

- Equal depth below the surface;
- Equal flow velocity.

For the flood tide (to which all the data analysis in Part B belongs) the upstream DBDP to the North West (NW) was used. As shown in Figure 6.3, bin 17, 19.8 m above the instrument was closest matched to the same depth below the surface.

In order to compute the equal flow speed, one-to-one plots of 5 minute mean velocities between the SBDP at bin 23 and the u component of the DBDP were made for each bin of the DBDP. Figure 6.9 shows the steady increase in gradient as the bin number (i.e. the height above the seabed) increases.

Figure 6.10 shows the relationship of these gradients with range, highlighting the point at which the two instruments give the best match, which is at bin 10. The difference in gradient between bin 10 which had the gradient the closest to 1 and bin 17 which has an associated gradient of 0.93 is significant at 7%. Bin 17 was selected due to the measurement in the rotor plane being deemed the more important factor. However, this introduces an additional uncertainty into the comparison of turbulence metrics measured by the two sensors.

Transverse velocities

For the SBDP in the transverse and vertical similar uninterrupted flow regions were seen. Beyond 5 m in the transverse direction the velocities were found to be relatively steady with range and thus the same bins were selected as for the streamwise.

Vertical velocities

The vertical velocities were found to be sensitive to surface wave fluctuation and thus bins were selected at an equivalent depth for the two sensors that were as deep as possible while avoiding turbine effects on the flow. Bin 15 of the SBDP (6 m above the turbine) and bin 25 of the DBDP (26.8 m above the instrument on the seabed) were selected for this purpose.

6.5.3 Discussion

A point of interest is the selection of the range bin of the DBDP, with the option of matched height rather than mean axial velocity. A 7% difference in mean flow speed is significant over these scales at the same height. Since the AWAC velocities were significantly better matched with only a 2% velocity deficit, one possible contribution to this difference is the SBDPs angle to the onset flow. The next nearest sensor (SBD_{RT}) matched the one-to-one plot at bin 15 of the ADCP. This suggests the SBDP used was at a significant angle to the flow. A 0.93 gradient corresponds to an angle of 21.6° to the resultant. However such a significant angle would be identifiable by eye thus it is likely paired with other contributions. These are expected to include, spatial variation in the flow over this range due to local depth and bathymetry, flow meander and noise in the SBDPs.

As discussed, it was that measurements where taken in the rotor plane that was the more important factor and thus bin 17 was selected. However, it should be noted that this disparity in mean velocity (which is likely due to spatial variability) will affect the turbulence metrics.

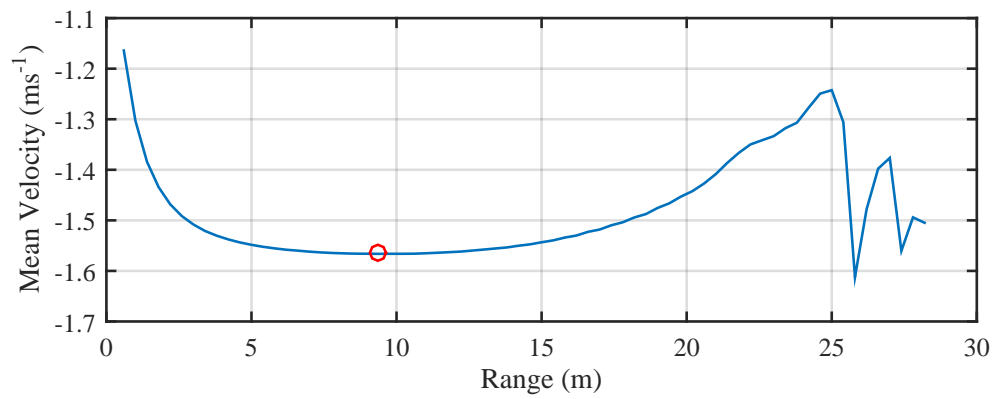


Figure 6.8: Bin Selection for SBDP in x direction, showing \bar{u} with range.

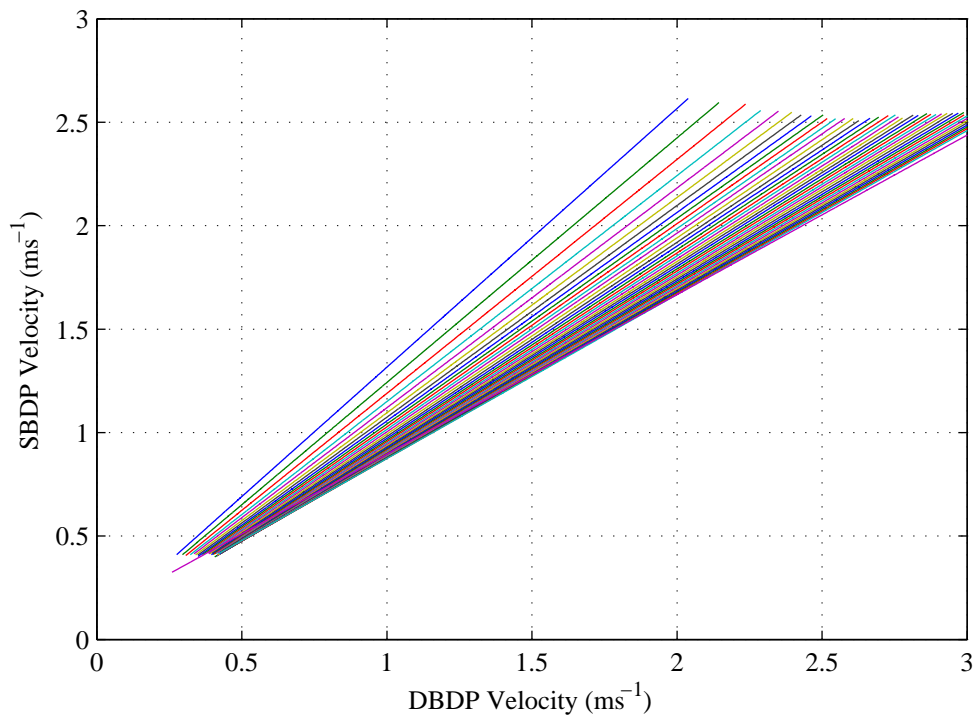


Figure 6.9: Illustration of increasing gradient of one-to-one velocity plots between SBDP and increasing bin number of DBDP.

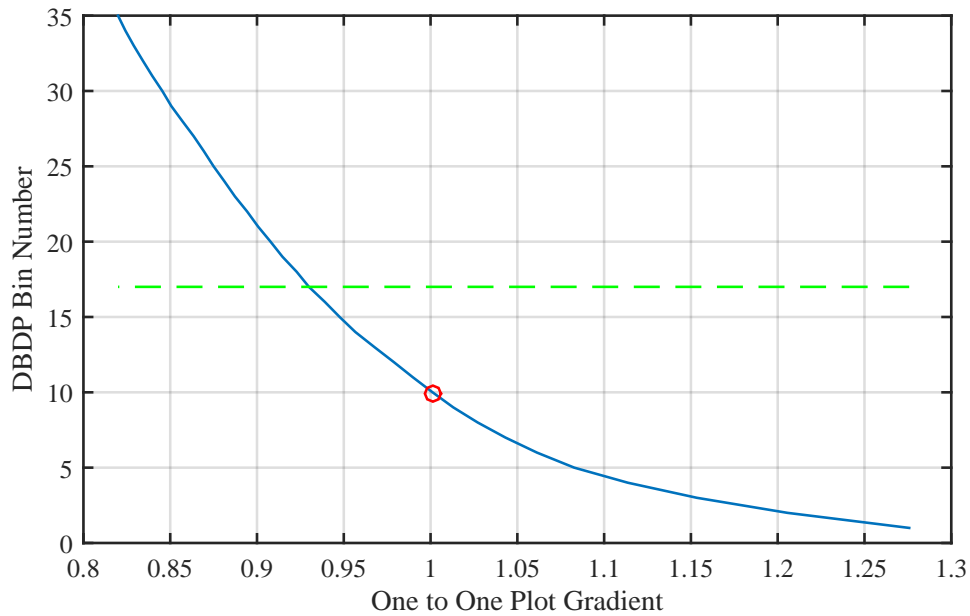


Figure 6.10: Gradients of one-to-one velocity plots between SBDP at bin 25 and u component of DBDP at a range of bins.

This variation does cast doubt on the scale of applicability of the frozen nature of turbulence in these environments. This is highlighted in the range of the axial SBDP which, although there is a relatively flat region, is still a definite curve with a defined minimum turning point. This means there is a constant variation in mean velocity which will likely be associated with a constant variation in turbulence metrics with range.

6.6 Defining DBDP Noise Variance to Axial Velocity Relationship

6.6.1 Introduction

As introduced in Chapter 4, acoustic sensors are inherently noisy technology and generally the variance due to random error increases as the sensor's sample frequency decreases or as required range increases (Gordon, 1996). As the turbulence intensity and Reynolds stresses are correctable for the contribution of random error, a DBDP noise variance curve must be defined in order to make the corrections. In addition, examination of the spectral content of the velocity fluctuations should allow observation of how well the DBDPs are capturing the structure of the turbulent flow.

6.6.2 Results

Effect of velocity transform

The same spectral method developed by Durgesh *et al.* (2014) and Richard *et al.* (2013) which was used to calculate the variance due to noise in Chapter 4 can be applied to the DBDPs. DBDPs introduce an additional challenge with this method due to the effect of the two stages of the velocity transform on the PSD. Figure 6.11 highlights this with an example for a $2.00 \pm 0.05 \text{ ms}^{-1}$ velocity bin data set, illustrating the PSD of the original beam velocities and those from the horizontal and vertical velocities after the two stages of the transform, to the two horizontal and a vertical and then rotated to u , v and w .

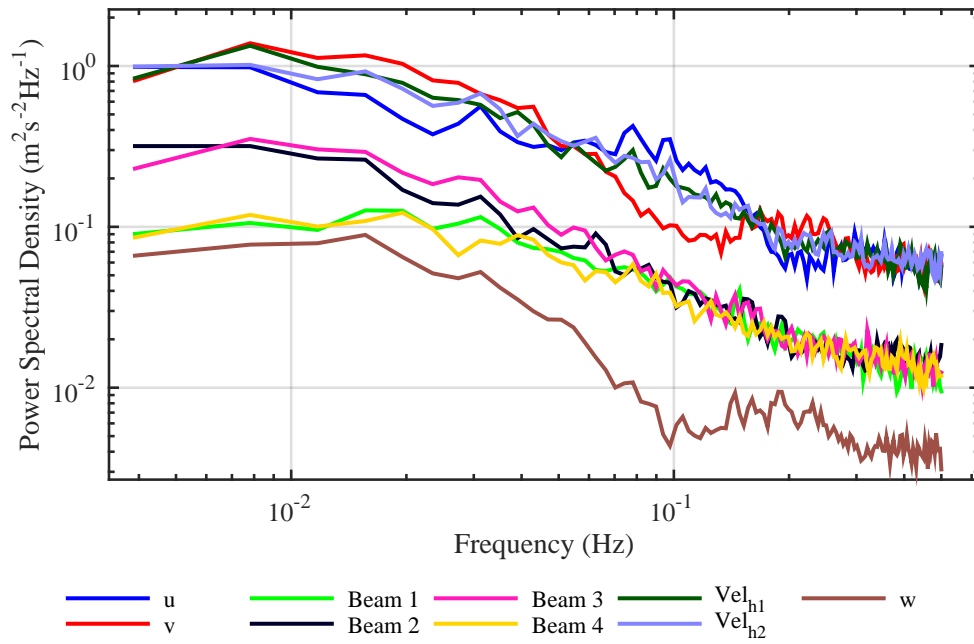


Figure 6.11: Example of the effect of the two stages of the velocity transform on the spectra and subsequent noise floor.

The two stages of the transform have two distinct effects. Firstly the transform from beam velocities to a Cartesian velocity set increases the energy across the frequency range. As part of this, the variance due to noise can be seen to increase proportionally. This effect is predictable due to the way noise is transformed with the velocities. The noise will increase as:

$$\sigma_{noise\ vel_h}^2 = \frac{\sigma_{noise\ beam}^2}{2 \sin(\beta)} \quad (6.6)$$

$$\sigma_{noise\ vel_z}^2 = \frac{\sigma_{noise\ beam}^2}{2 \cos(\beta)} \quad (6.7)$$

where $\sigma_{noise vel_h}^2$ and $\sigma_{noise vel_z}^2$ are the variances due to noise of the two transformed velocities, $\sigma_{noise beam}^2$ is the variance due to noise in the individual beams and β is the beam inclination angle from vertical (Lohrmann, 2015).

An interesting effect to note is the similar energies at the lowest frequencies for both the u and v estimates. It is expected that the largest coherent turbulent structures will appear in the streamwise direction (DNV, 2002; Thomson *et al.*, 2014), and thus that there will be more energy at low frequencies in the streamwise PSD than the transverse. This effect can be seen in Figure 6.11 with greater energy in Beams 2 and 3 compared with 1 and 4. However, this is not evident after the transform to horizontal and vertical velocities, as the higher values don't correspond to a beam pair. This in itself is an interesting result in terms of isotropy and homogeneity of the flow as the turbulent structures would expect to be similar across a beam pair as long as the velocity direction and turbulent structures do not change along that separation distance.

Additionally the vertical velocity has significantly lower energy across the frequency range than the other PSDs. This is expected as the turbulent structures in the vertical are expected to have the least energy associated with them, and the beam velocities (being a combination of vertical and horizontal velocities) would be expected to have an energy content between those of the components. However, this example highlights that the velocity transform doesn't capture the integral sub-range slope in the PSD of the vertical velocities. It is also clear that the noise estimate from the beam velocities suggested in Equation 6.7 should have a greater variance than the total of the resolved vertical velocity.

The second effect highlighted by Figure 6.11 is due to the heading correction. As the heading is rotated away from the beam pairs the spectral slope becomes uneven with the PSD based on u and v fluctuations alternatively increasing and decreasing at different frequency ranges. This effect is at a maximum at a rotation angle of 45° (and increments of 90°) as this is the furthest from being in-line with either beam pair. However, it can be seen that the overall energy level is not altered by this rotation, i.e. no additional variance is introduced.

Issues with DBDP spectra

There were issues encountered in applying the spectral fit method to the DBDP PSDs. Initially the noise values were found to be surprisingly low in the averaged PSD for each velocity range. These results were contrasted with the method of calculating an individual PSD for each 256 second data sub-set. The latter method showed a much greater spread of results compared with those in the SBDP and in Richard *et al.* (2013). Upon visual inspection of individual PSDs it was found that sharp dips in the results at high frequencies were causing the fit method to bias the noise floor low. As these spikes were evenly spread across the high frequencies in different samples, the effect of averaging them was to bias the average PSD unrealistically low at high

frequencies. Figure 6.12 gives an example for a PSD of an individual data subset, showing the unrealistically low noise floor.

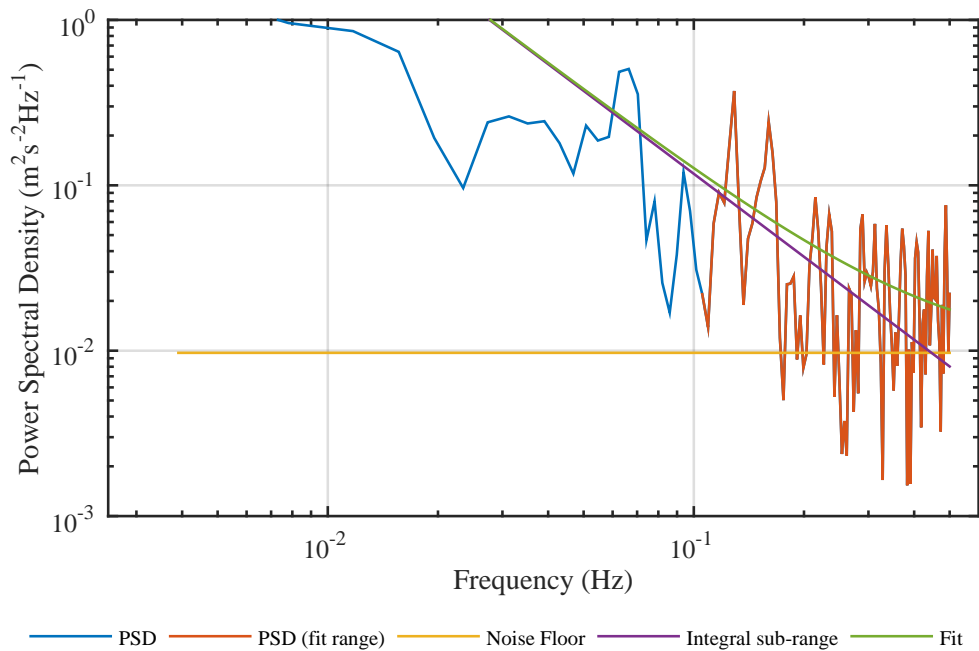


Figure 6.12: Example of the issues experienced with fitting to a DBDP PSD.

This issue was significantly worse in certain DBDP deployments compared with others. Thus the noise variance values calculated are calculated for a single DBDP with good data, with R^2 values of the fit used to track the quality of the data. This does remove the ability to compare seasonal variation in noise which would be expected to vary as scatterers in the water vary over the seasons, but will give the best estimate from the available data.

In order to assess whether the differences in noise floor are due to the samplerate (f_s), a test of down-sampling the SBDP data was undertaken. This involved omitting every 2nd data point to reduce to 1 Hz. Note that this is different to ensemble averaging across 2 points which would reduce instrument noise. Figure 6.13 shows the comparison for the $2.50 \pm 0.05 \text{ ms}^{-1}$ velocity range subset with the relevant noise floor variance values highlighted in Table 6.4. It shows that the σ_{noise} does increase inversely with the sample-rate but, at an equal sample-rate the SBDP still has a lower random error than the DBDP, with the noise variance $0.031 \text{ m}^2\text{s}^{-2}$ lower for this case.

In addition to the higher noise floor it highlights the generally shallower slope in the DBDP results. This suggests that there is more energy in the fluctuations in the DBDP horizontal velocity measurements but this is not due to turbulent fluctuations alone. This suggests that the slopes of the DBDP results will not be accurate but the noise floor is still valid as suggested by Richard *et al.* (2013).

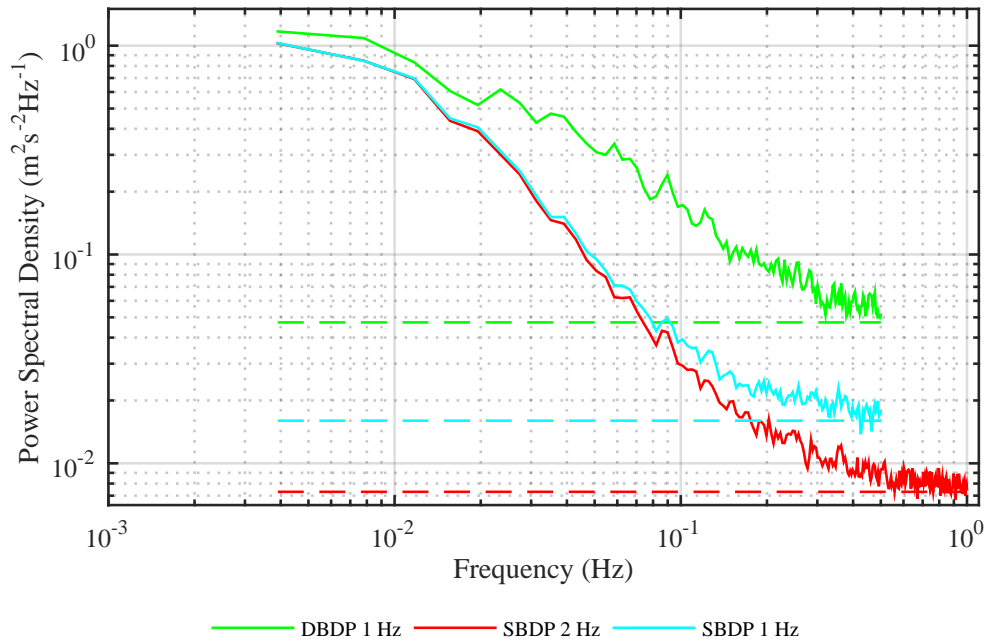


Figure 6.13: Comparison of spectra and noise floor for the streamwise SBDP data down sampled and the DBDP at the original sample-rate.

Instrument	Samplerate (Hz)	PSD value $\times 10^{-3}$ ($\text{m}^2\text{s}^{-2}\text{Hz}^{-1}$)	$\sigma_{noise}^2 \times 10^{-3}$ (m^2s^{-2})
DBDP	1	47.27	23.64
SBDP	2	7.30	7.30
SBDP	1	16.00	8.00

Table 6.4: Comparison of σ_{noise}^2 based on f_s for streamwise data from the SBDP and the DBDP.

Horizontal noise variance

In order to characterise the noise variance across the velocity range, a data set from the first North West DBDP was selected for flood tide measurements. Both un-rotated horizontal velocities and beam velocities were computed, with data subdivided into 256 second 50% overlapping subsets. These subsets are then divided based on axial velocity into bins centred on 0.55 ms^{-1} to 2.95 ms^{-1} each of 0.1 ms^{-1} width.

For each velocity range the relevant data sets are processed for a PSD as described in Section 4.2.1. For each 256 second sample-set a PSD is produced. For the beam velocities these are averaged across the 4 individual PSDs and likewise for the two horizontal estimates. Then for each velocity bin all PSDs are averaged giving one beam and one horizontal spectrum for each range bin. At this stage the least squares fit is applied and the variance due to noise calculated. The noise estimate in the horizontal based on the beam velocity PSD has to be multiplied by a factor of the beam inclination angle such that:

$$\sigma_{noise\ x}^2 = \frac{\sigma_{noise\ beam}^2}{2 \sin(\beta)} \quad (6.8)$$

where $\sigma_{noise\ x}^2$ is the horizontal noise variance, $\sigma_{noise\ beam}^2$ the beam noise variance and β the beam inclination angle. This fit has an associated R^2 goodness of fit value of 0.99.

Figure 6.14 shows the resulting noise variance and cut-off frequencies across the axial velocity range. The estimates by beam and horizontal methods are well matched with a mean difference of 6.05×10^{-4} between estimates. The R^2 goodness of fit was measured over the fitted region ($10^{-1.3}$ Hz to 1 Hz) for each velocity range, with the beam velocities giving the better mean fit (0.92 compared with 0.88) and thus they were used to fit a trend line.

The relationship between $\sigma_{noise\ x}^2$ and axial velocity for horizontal DBDP measurements from Figure 6.14 was then fitted to a two part relationship with a constant value for low flow speeds and a second order polynomial for axial velocities greater than 1 ms^{-1} , such that:

$$\sigma_{noise\ h}^2 = 20.62 \times 10^{-3} \quad \bar{u} < 1 \text{ ms}^{-1} \quad (6.9)$$

$$\sigma_{noise\ h}^2 = (6.01\bar{u}^2 - 11.11\bar{u} + 25.80) \times 10^{-3} \quad \bar{u} > 1 \text{ ms}^{-1} \quad (6.10)$$

This relationship can be used to calculate the variance for a given axial flow speed to correct horizontal turbulence metrics. Richard *et al.* (2013) measured noise variance of DBDPs in a velocity range of 0.2 ms^{-1} to 2 ms^{-1} and showed a relatively constant value of σ_{noise}^2 of $0.026 \text{ m}^2\text{s}^{-2}$ across this velocity range. In the results presented here, across the $< 2 \text{ ms}^{-1}$ range the values are slightly lower but also relatively constant with velocity. However, it is at speeds

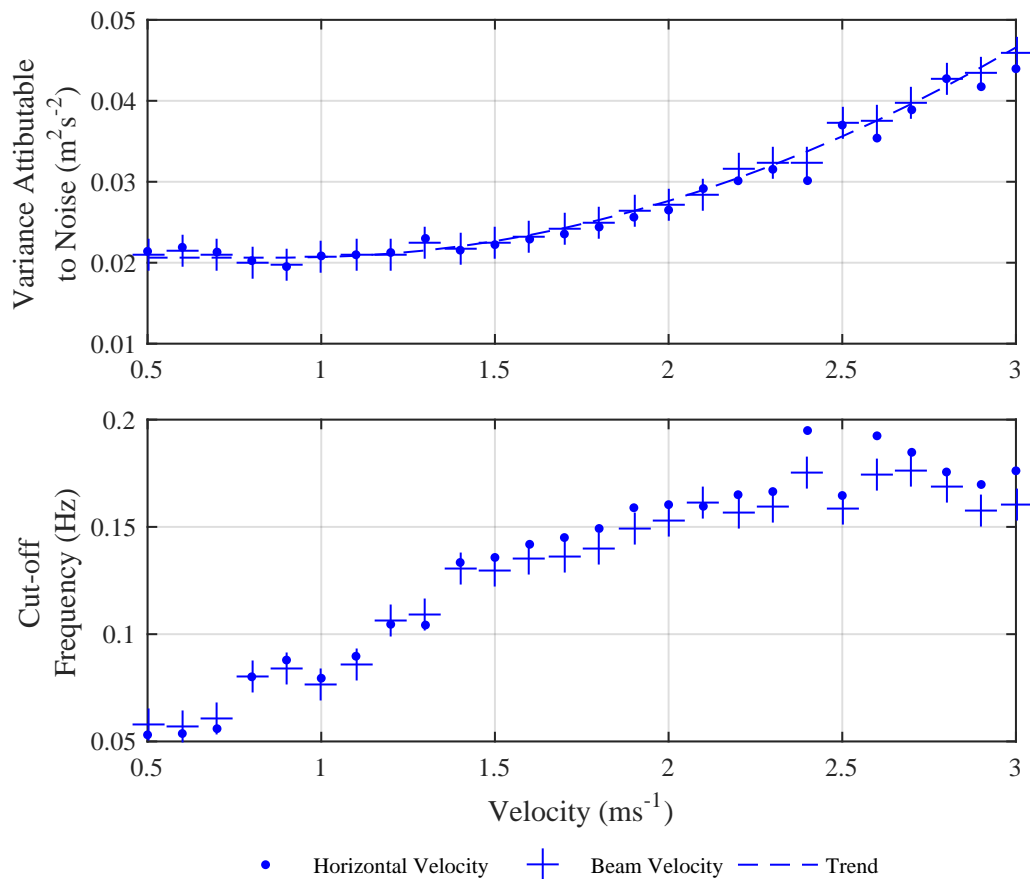


Figure 6.14: Relationship of DBDP noise variance and cut-off frequency with velocity.

above this where the power law becomes a more appropriate fit.

The Cut-off frequency shows an approximately linear increase that is well matched between the two methods. This indicates the effects of larger turbulent structures at higher flow speeds are being captured, as was the case for the SBDPs in Section 4.2.2.

Vertical noise variance

As discussed in Section 6.6.2 the DBDP vertical spectra were inappropriate for the fit method. The results presented in Figure 6.15, alongside the equivalent vertical spectra from the SBDP (in this example for a 2.65 ms^{-1} axial velocity) lend further evidence to this. Therefore based on the theory that the vertical DBDP noise variance should be less than the horizontal by a factor of $\sin(\beta)/\cos(\beta)$ (based on the beam transformation) was applied. This factor equates to 0.36 for the beam inclination angle (β) of 20° . Thus the vertical variance due to noise relationship with streamwise velocity is defined as:

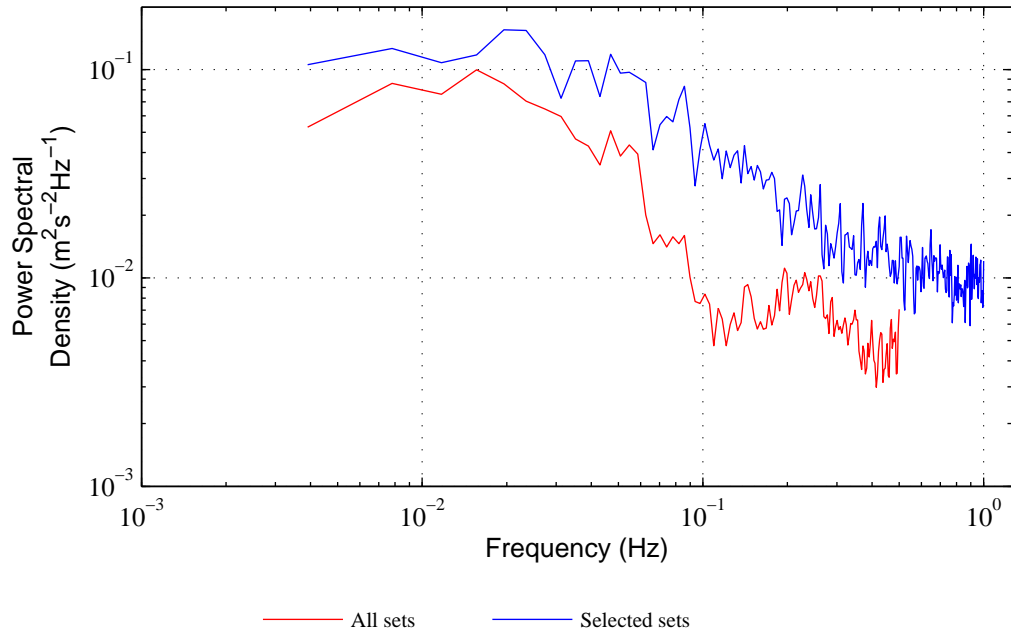


Figure 6.15: An example of the issues with DBDP vertical velocity from transform to compute the PSD, for 2.65 ms^{-1} axial velocity data set.

$$\sigma_{noise_z}^2 = (10^{-1.83}) \cdot (10^{0.15 \cdot \bar{u}}) \cdot \frac{\sin(\beta)}{\cos(\beta)} \quad (6.11)$$

However, as shown in Section 6.6.2 it is likely in the majority of cases that this value will exceed variance in the velocity sub-sets. In these cases, using Equation 4.4 to correct I cannot be used and values will go uncorrected.

6.6.3 Discussion

As the lines of best fit to the calculated noise variance with axial velocity shows variation around the fit, there is the option to bias the fit low to ensure device developers are not designing to ‘optimistic’ turbulence conditions. One option is to bias the fit so that it passes through the point furthest removed in the y axis. However, the work presented in Chapter 7 of corrected turbulence intensities from both a DBDP and a SBDP shows that the chosen method brings the results into good alignment.

With the data sets used to calculate these curves covering a wide range of flow conditions, it is possible there are additional drivers in the flow that affect this curve that have not been extricated. Further work focusing on a sensitivity study on the curve to flow acceleration (i.e. whether the flow is at peak or in the phase of ramping up or down) would be of benefit. Fur-

thermore, as several DBDP deployments produced spectra that did not fit well to the expected slopes, the ability to correct for seasonal variation was removed. As back-scatterers are partly composed of organic matter, seasonal variation in their density and thus the amplitude of pulse returns is expected to be high. In general it is recommended that where possible a noise curve is defined for each individual DBDP deployment.

One aspect of the PSD that has not been investigated is the windowing method used in FFT. The Hamming window employed is based on recommendations of previous work. Different window types will affect the accuracy of the resulting PSD and a full sensitivity study may suggest a method that improves the fit of the DBDP spectra to the curves, particularly at higher frequencies.

6.7 A Discussion of Averaging Options

6.7.1 Introduction

As discussed in Section 4.1 any measurement taken by an acoustic sensor is comprised of physical mean and fluctuating components as well as random and systematic error (see Equation 4.2). The two fluctuating components are very difficult to isolate as any given variation of a measurement around the mean value could be either the effect of a physical change or of noise, or a combination of the two. In Section 4.2.1 a method of measuring the random error and correcting the turbulence intensity was introduced. However, this is only a statistical correction and cannot be used to correct time series measurements.

One common method of reducing instrument noise is ensemble averaging. Here we define ensemble averaging as an average over either space or time (by one or more sensors) of a value that has stable mean and variance. Ensemble averaging will reduce the noise by a factor of:

$$\sigma_{noise\ corrected}^2 = \frac{\sigma_{noise}^2}{\sqrt{N}} \quad (6.12)$$

where σ_{noise}^2 is the variance due to noise and N is the number of values averaged. This relationship assumes that noise is both white with zero mean value and uncorrelated (Thomson *et al.*, 2010).

Thus there are trade-offs to consider with the averaging options in preparing two different instruments' data sets for comparison. Firstly the two instruments have different single range-bin sizes, thus there is an argument that it is appropriate to average over two bins of an SBDP so that the measurement lengths are closer to being equal while reducing the noise in the resultant SDBP data. Conversely it could be deemed preferable to highlight the benefits of increased spatial resolution. The same question can be raised with regard to the higher samplerate. As the SBDPs have the higher maximum samplerate and spatial resolution, as well as the

possibility to have two independent sensors measure roughly the same measurement length, the consequences of averaging on the turbulence metrics must be understood. All methods of ensemble averaging the velocity time series for processing turbulence metrics are a trade off between reduced noise and reduced resolution at the smaller scales at which turbulent motions are measured.

6.7.2 Effect of spatial averaging on metrics

Here an example is presented for a SBDP data set that has been ensemble averaged spatially to assess the effect on the turbulence metrics. This involves 88, 256 second sample sets for a mean upstream streamwise velocity (measured by the seabed mounted DBDP) in the 1.85 ms^{-1} to 1.95 ms^{-1} range. The data is centred around bin 23 as suggested by Section 6.5, with the bins either side of this being included incrementally to extend the included range by 1 bin each iteration. Data sets are then averaged along this range before being divided into 256 second sample sets and the metrics calculated for each sub-set.

As data is averaged and the fluctuation around the mean decreases, the (uncorrected) turbulence intensity value would be expected to drop. Conversely the autocorrelation coefficient will increase as the velocity data set tends towards a constant, thus the lengthscale value will increase. However, this will lose progressively more spatial information and eventually decrease the normally distributed fluctuations to zero. Thus a limit based on the physical phenomenon being measured, must be put on the spatial averaging. Here two limits are applied:

1. That I does not drop below the predicted noise corrected value as per Equation 4.4 and results of Section 4.2.1;
2. That the spectral slope accurately recommends the inertial sub-range slope up until the noise floor. I.e. that the low pass filter does not remove useful turbulence information.

Figure 6.16 illustrates the results of the effect of this spatial averaging on the mean velocity and turbulence metrics. Figure 6.16 illustrates the expected trends in metrics with spatial averaging; showing an increasing ℓ_x and a decreasing I_x for an increased number of bins averaged, while the mean velocity stays relatively constant across the range. The corrected I_x value of 8.03% is achieved averaging over 9 bins for this example, with an associated increase in lengthscale of 33.06 %.

Since there is a concern that spatial averaging over 9 bins (3.6 m), reduces the spatial resolution significantly, the effect on the PSD of averaging over this range must be investigated. Figure 6.17 illustrates the relationship of the PSD slope over a frequency range of 0.04 Hz to 0.3 Hz with the number of bins averaged. The closest result to the theoretical $-5/3$ slope is found averaging over 5 bins. Averaging more than 5 bins decreases the contribution of the spectral slope at higher frequencies beyond the expectations of theory. The lower plot in Figure 6.17 highlights this by providing the mean spectra across the samples for four spatial averaging ranges, 1 bin, 20 bins and the two suggested solutions of 5 and 9 bins. The most appropriate

spatial averaging range from these results is over 5 bins, centred on the turning point of velocity with range given in Figure 6.8. This gives a reduction in I_x of 10.50% and an increase in ℓ_x of 27.76%.

Effect of temporal averaging on metrics

The previous study was repeated for single bin (23) with a running average over the sample set. For this the data was processed into 282 second sample sets, so that the unevenly averaged edges could be trimmed after the running average was calculated. The full results of the effects on the metrics are not presented here as the results were similar as for the spatial averaging, which is an indication that frozen field hypothesis is valid at these scales of averaging. The key numbers were that the corrected I value was met at a running average over 5 samples (2.5 seconds) with an associated increase in length-scale of 36.60%.

The spectra slope over a frequency range of 0.04 Hz to 0.3 Hz was best matched to the theoretical value when averaging over 4 samples. However, a running average has an adverse effect on the high frequency end of the spectrum. This is highlighted in Figure 6.18 which shows a drop off of energy at the high frequency with a sinusoidal pattern. This indicates that temporal averaging is not appropriate in turbulence calculations.

6.7.3 Discussion

This example for the streamwise SBDP has shown spatial averaging to reduce I_x and increase ℓ_x while defining sensible limits for this process based on the physical processes in the flow. Temporal averaging is shown to adversely affect the high frequency content of turbulence and thus is not appropriate for this purpose. It should be noted that this analysis represents only one data set, in one orientation, at one flow speed and a further sensitivity study is required. Chapter 7 along with Sellar and Sutherland (2015) show that the spread in lengthscale values is high and the effect of averaging on the distributions also needs to be assessed. Sellar and Sutherland (2015) also highlights the effect of surface waves on ℓ_x and the limits on averaging in the presence of waves requires further investigation.

The goal of this chapter is not just to discern the most accurate turbulence metrics, it also has to consider the most accurate comparison between two different instrument types, with different beam orientations. As a full sensitivity study of turbulence metrics to averaging types was outwith the scope of this work, although spatial averaging shows promising results, a more conservative strategy for inter-instrument comparisons was preferred. There is still the issue of whether the two instrument types should be averaged over an equal range and thus if it is appropriate to average the DBDP bins vertically, when the vertical profile of \bar{u} is known to not have stable mean velocity with range, in order to compare a similar measurement length. In order to provide a robust comparison between the two sensors it was decided that only a single

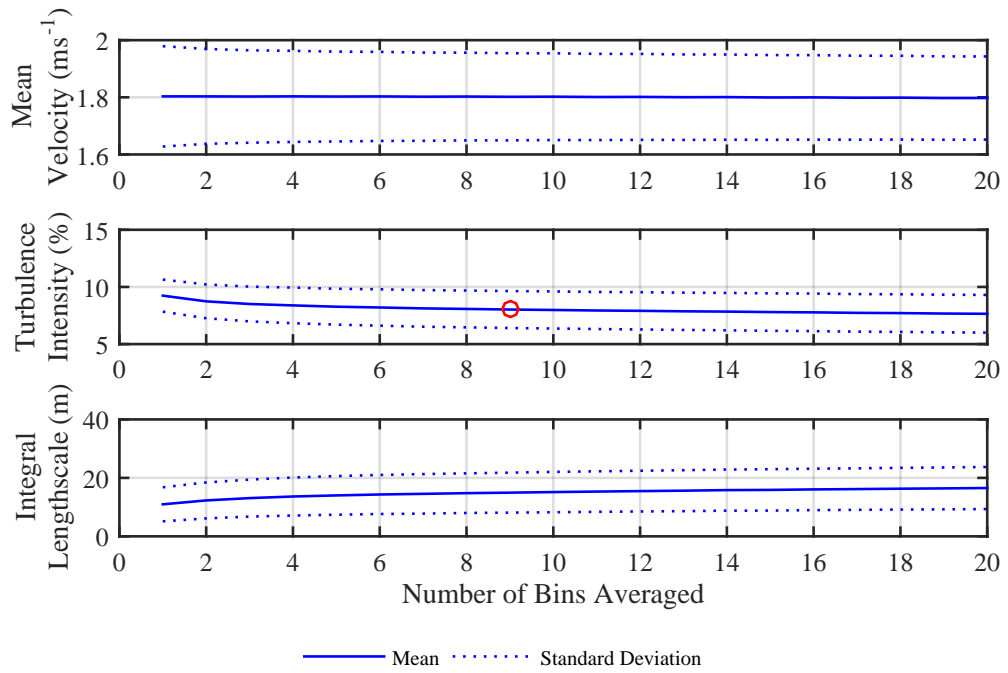


Figure 6.16: The effect of spatial averaging on SBDP measured metrics. The circle indicates the number of averaged bins that reduces I to the value corrected for variance due to noise.

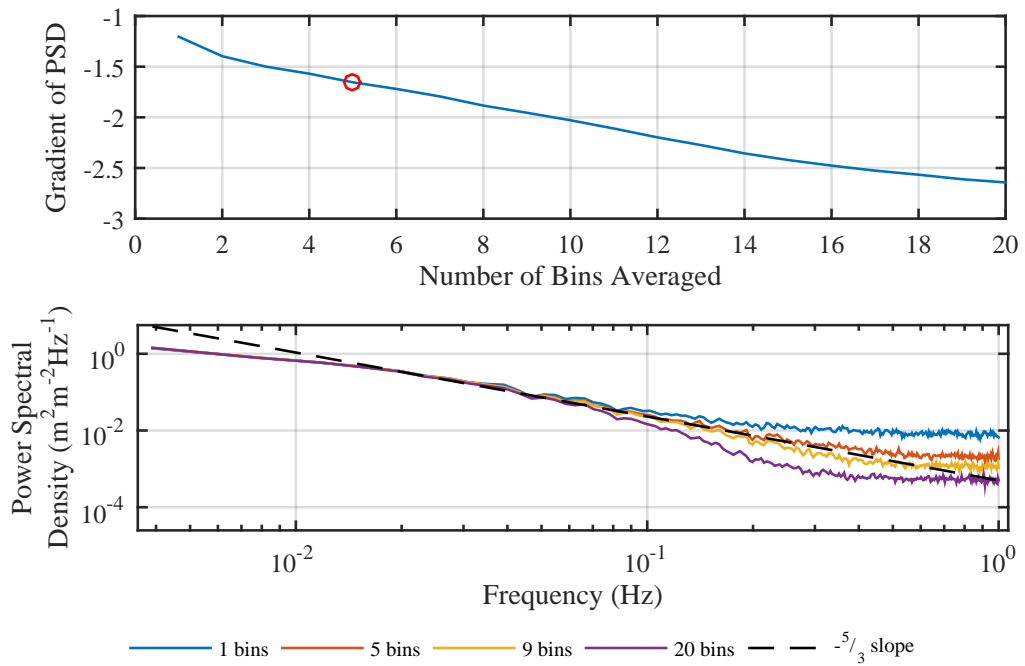


Figure 6.17: The effect of spatial averaging on the PSD. The circle indicates the number of averaged bins that represents the best estimation of the inertial sub-range slope.

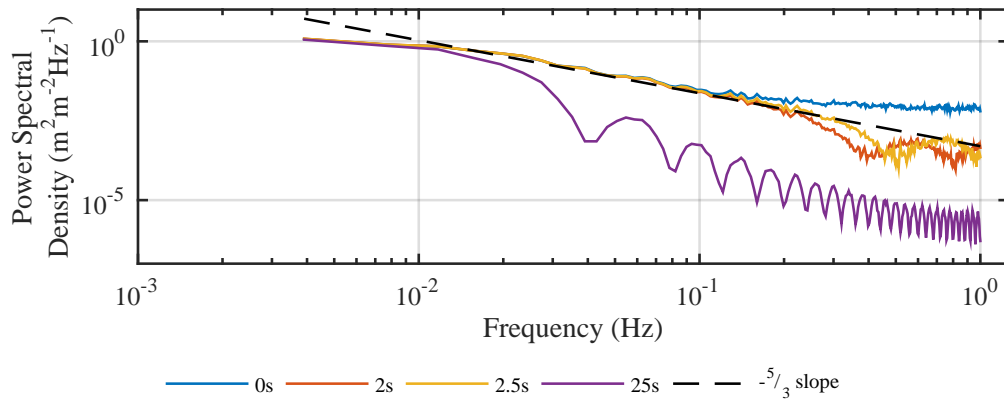


Figure 6.18: The effect of temporal averaging on the PSD.

bin would be used for the comparison in Chapter 7. However, the results of this section are still a valuable resource for best practise for processing turbulence metrics from the SBDPs.

6.8 Chapter Summary

This chapter has summarised the theoretical advantages of mid-depth mounted SBDP arrays over bottom mounted DBDPs and the motivations for a comparative study. In order to ensure an accurate comparison, a technique for aligning the DBDP measurements with those of the turbine mounted sensors has been presented along with the appropriate range bin selection. The variance attributable to noise is computed for horizontal and vertical orientations of a DBDP via the beam velocities to correct turbulent metrics for a range of flow velocities. These can be combined with those for the SBDP defined in Section 4.2.1. Finally a discussion of the advantages and issues with ensemble averaging velocity time series to calculate turbulence metrics is presented. The conclusion was that, although it would be advantageous for processing turbulence metrics from SBDP measurements, there is too much uncertainty for it to provide a robust comparison between two sensor types.

With the methodology for data selection for the instrument comparison defined, Chapter 7 presents the methodology for processing the turbulence metrics and the results for each Cartesian direction.

SBDP and DBDP comparison - Part B

Results

7.1 Chapter Overview

This chapter presents the results of a comparison study utilising three mid-channel depth SBDPs, normal to each other along the three Cartesian vectors with a single upstream DBDP. The results of this chapter, based on the data selection and alignment in Chapter 6, represent the most accurate metrics for comparison. First an overview of the method of calculating each metric is given. Then the results for each Cartesian direction is dealt with independently and a discussion of the results with respect to theory and previous work is presented.

7.1.1 Motivation

The motivation is firstly to highlight the advantages and disadvantages of the two sensor types in characterising turbulent flows. As highlighted in Chapter 2, accurate metrics are a key challenge to the ongoing development of the tidal industry. Secondly, the metrics from the SBDPs are the first mid channel depth mounted measurements taken from a stable structure with remote (range >0.1 m) sensors. They provide valuable insight into the nature of the flow in a tidal channel at the depth of the turbine rotor.

7.1.2 Author's contribution

The data selection, processing algorithms, analysis and results are the sole work of the author unless specifically cited. The instrumentation set-up and data collection was a collaborative effort between the author and the project manager as discussed in Chapter 3. Here data was not collected specifically for this comparison, rather it uses data captured throughout the ReDAPT data campaigns.

7.2 Methodology and Theory

The metrics selected to assess the performance of the two systems were: the mean velocities along each vector \bar{u} , \bar{v} and \bar{w} , the turbulence intensities (I_i), the turbulence dissipation rate (ϵ) and the integral lengthscale (ℓ_i) for each of the relevant velocity components (denoted by the subscripts x , y , z or i for a generic definition). In addition, analysis of the vertical-streamwise, Reynolds stress tensor using a smaller data sub-set is presented. These metrics were all calculated over a period of stationarity (T_{stat}) of 256 seconds, as discussed in Section 2.7. Although all the metrics included here have previously been defined in Section 2.7, the following section highlights the specifics of the methods used for this section.

Note that the term ‘axial’ is preferred to ‘stream-wise’ to describe properties of the x vector in this test, as all metrics are relative to the turbine nacelle, which may not always be aligned to the direction of maximum flow velocity which is known to vary over a 6.22 hour tidal cycle (Sutherland *et al.*, 2013). Section 6.4 discusses how this alignment angle is defined for this study.

Throughout, the metrics were binned into subsets based on the axial flow speed measured by the upstream DBDP, where each subset had a bin width of 0.1 ms^{-1} . Where trend lines are fitted to the data they are through the mean values for each velocity bin. This decision was made in order to reduce bias of turbulence metrics based on the most commonly occurring flow speeds. The axial flow speed is used as the varying parameter for all metrics (regardless of orientation), as the transverse and vertical velocities are consistently low and show little or no trend.

7.2.1 Mean velocity

The mean velocities along each vector are ensemble averaged over 256 second T_{stat} period, in order to reduce the associated random error.

7.2.2 Turbulence intensity

The definition for I along the individual velocity components was introduced in section 2.7. In these tests the metrics for each direction are not taken concurrently but are by definition normalised by a mean velocity. For consistency between the metrics, I values were normalised by the mean axial velocity (\bar{u}) measured by the upstream DBDP, denoted \bar{u}_{DBDP} , even for the axial measurements from the SBDP.

The turbulence intensity values are presented both before and after correction for instrument noise to highlight the effect of noise on the metrics using Equations 2.13 and 4.4. If the measured fluctuation is less than the noise variance estimate, then using Equation 4.4 to correct the noise will lead to an imaginary result; in these cases no correction is made. An alternative option would be to remove these instances (as done in Thomson *et al.* (2010)). However, as

there is no known scientific reason to attribute low fluctuations to error, this was seen as part of the natural fluctuation of turbulence measurements and values were not removed.

7.2.3 Turbulent kinetic energy dissipation rate

The dissipation rate was calculated from the Power Spectral Density (PSD) using the same least squares fit method as used to calculate the variance due to noise in Chapter 4. The PSD, as previous defined is:

$$S_{measured}(f) = C_i \cdot f^{-5/3} + N \quad (7.1)$$

where

$$C_i = 0.5 \cdot \varepsilon^{2/3} \quad (7.2)$$

and $S_{measured}(f)$ is the measured PSD, ε is the turbulent dissipation rate and f is the frequency. The 0.5 in Equation 7.2 is an empirical factor taken from Thomson *et al.* (2010). ε is then multiplied by the density of water (taken as 1024 kgm^{-3}) to convert it to a volumetric dissipation rate, with units of Wm^{-3} . It should be noted that in the case of the DBDP this method acts as an upper limit to the physical value of ε due to the uncertainty of the isotropic nature of turbulence, with the real values in the range of $0.65 < \varepsilon < \varepsilon^*$ where ε^* is the measured value (Lorke and Wüest, 2005). This does not apply to the SBDPs results.

ε can also be estimated via the structure function as defined in Equation 2.29. However, this can only be computed for the DBDP along the beam range and from work with micro-structure profilers, ε is known to vary with depth (Moum *et al.*, 1995) and this method obscures that variation. Thus this test was limited to the results of the same height between the two instruments using the spectral method.

7.2.4 Integral lengthscale

The integral lengthscale is defined qualitatively as the average size of the largest eddies in a turbulent flow (Pope, 2000). There are several methods of estimating this value as summarised in Section 2.7.4. These are: spatial auto-correlation, temporal autocorrelation and via the frequency of the peak of the PSD. Spatial auto-correlation requires an effective measurement range of around seven times greater than the scale being measured (O'Neill *et al.*, 2004) and thus was not practical for the streamwise scales. The Spectral slope method requires the fitting of the spectra to a spectral slope used for atmospheric turbulence. This was not used due to the fact that these spectra are yet to be proved conclusively to be accurate for tidal channels and the peaks of the PSDs were often difficult to define.

Here, the primary method used was temporal autocorrelation. However, the spatial correlation method is trialled for the transverse and vertical scales where the lengthscales are expected to be smaller (as discussed in Section 6.2).

De-trending of velocity data

Temporal correlation uses a de-trended time series velocity signal and is processed via the autocorrelation function. The correlation coefficient $R(\Upsilon)$ is calculated for a given temporal difference of lag (Υ) between the velocity measurements as defined in Equation 2.21, Section 2.7.

Two de-trending methods were considered, these were: constant (i.e. subtracting the mean value of the sample-set), and subtracting a linear fit. A second order polynomial fit was also initially considered but was rejected on poor goodness of fit results. A test of a data subset for a velocity range of 2.0 ms^{-1} to 2.1 ms^{-1} from a SBDP orientated towards the onset flow comprising 60 sample-sets, was used to trial these two methods. An example of a single 256 second sample-set from this velocity range subset is shown in Figure 7.1 with the resulting autocorrelation function in Figure 7.2 for the two methods. The constant de-trending method results in a higher standard deviation of 0.15 compared with 0.14 (linear). Figure 7.2 highlights the increased area under the auto-correlation up until the first zero crossing point via the constant de-trending method, which relates to a increased lengthscale value.

Table 7.1 summarises the effect of these two methods on the mean and standard deviation of ℓ_x for the whole data subset for the stated velocity range. Although the linear de-trend increased the values collected it also increased the standard deviation of ℓ_x and introduced maximum values that were greater than the depth of the channel. Results in the transverse with the spatial autocorrelation produced similar if less extreme results. A Linear method was adopted in all cases.

	$\bar{\ell}_x$ (m)	σ_{ℓ_x} (m)	Max Value (m)
Linear	10.72	5.23	27.26
Constant	15.41	9.49	59.19
Increase (%)	43.76	81.46	117.13

Table 7.1: Summary of the effect of de-trending on ℓ_x values.

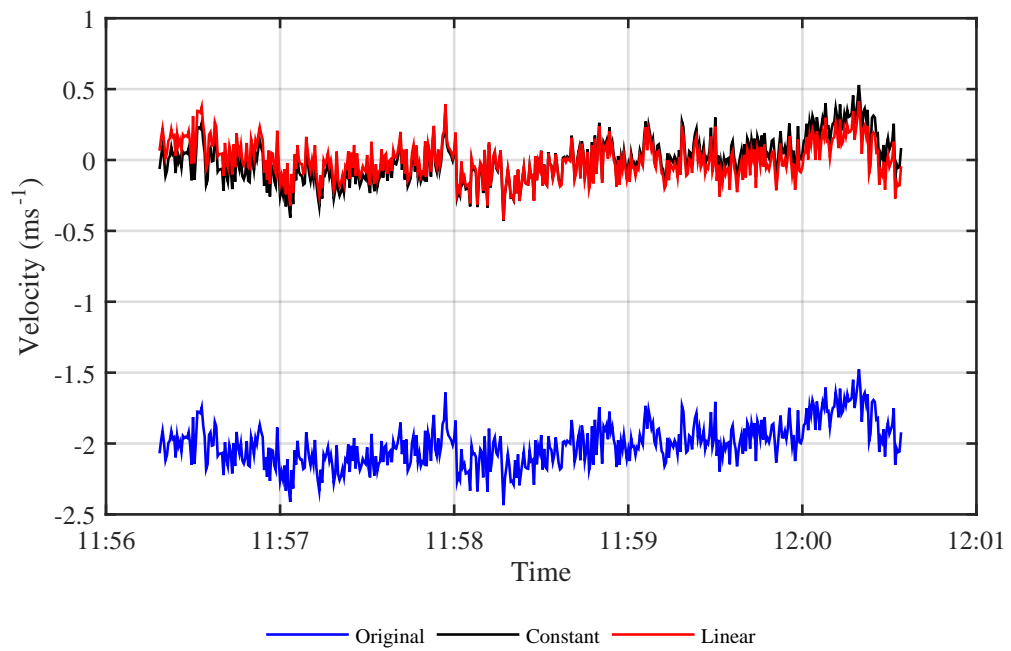


Figure 7.1: Example of de-trending methods of velocity time series data.

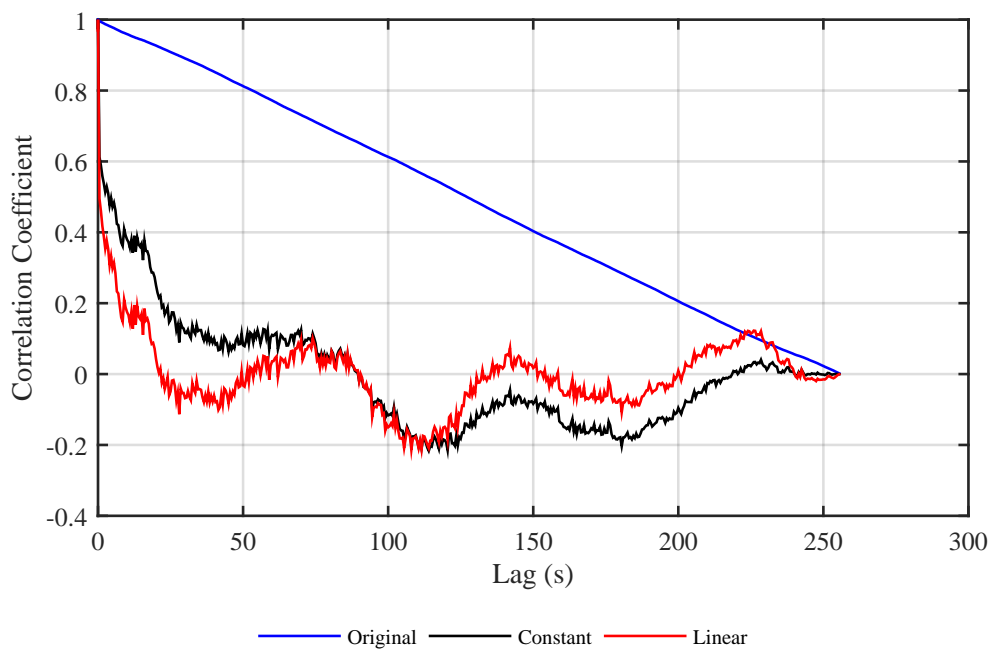


Figure 7.2: An example of the effect of de-trending method on the autocorrelation function.

Data processing for spatial autocorrelation

To calculate the transverse and vertical lengthscales via the spatial correlation method an ‘effective’ range for the SBDPs had to be defined. As discussed in Section 6.5, there are three regions of the SBDP’s velocity profile with range: the near region where flow slows as it approaches the turbine, the middle region representing the ‘free flow’ and the far region where the instrument’s signal is weak and velocity measurements are biased towards zero.

The use of noise dominated and turbine affected flow regions would bias ℓ estimations low. Bins 4 through 50 covering a 18.4 m range were selected after inspection of the data. This should in theory allow the resolution of integral lengthscales up to $18.4/7 = 2.6$ m. The data for these bins were subdivided into 256 second samples sets. For each time instance a lengthscale is calculated and then the mean value across the 256 second sample set is reported. The alternative method would have been to average the auto-correlation coefficients before calculating the area underneath but this was found to give unrealistically low values.

7.2.5 Reynold stresses

Reynolds stresses as discussed in Section 2.7.4 are a matrix of metrics that describe the shear stresses in the flow. Here, owing partially to a lack of appropriate data, only the vertical-streamwise tensor $\langle u'w' \rangle$ is calculated. For the SBDPs this requires two instruments and thus the assumption of homogeneous flow over a large volume, as is also the case for the DBDP measurements.

For the SBDP, Reynolds stress tensor was defined as:

$$\tau_{uw} = \langle u'w' \rangle \cdot \rho \quad (7.3)$$

where τ_{uw} is the Reynolds stress tensor for the vertical-streamwise pair, u' and w' are the de-trended velocity fluctuations of both instruments, averaged over a T_{stat} period and ρ is the fluid density.

Normal practise for estimates of Reynolds stresses from DBDP measurements is to compute directly from the beam measurements using the variance method, such that:

$$\tau_{uw} = \frac{\langle b_2'^2 \rangle - \langle b_1'^2 \rangle}{2 \cdot \sin 2\beta} \quad (7.4)$$

where b_1' and b_2' are the de-trended beam velocity time series and β is the transducer angle off vertical (Lohrmann *et al.*, 1990). This requires several assumption: firstly that the flow is

homogeneous across the horizontal beam spread and secondly that the opposite facing beam pairs are aligned with and normal to the resultant flow direction.

In addition, Equation 7.4 assumes that the DBDP is orientated perfectly vertical, whereas in reality this is never the case. Small angles of tilt can lead to large biases in Reynold stress estimates with Lu and Lueck (1999b) suggesting a 2° tilt could lead to a bias of up to 17%. Small values of tilt can in theory be corrected for by the following relation:

$$\tau_{uw} = \frac{\langle b_2'^2 \rangle - \langle b_1'^2 \rangle}{2 \cdot \sin 2\beta} + \phi(\overline{u'^2} - \overline{w'^2}) - \psi \overline{u'v'} \quad (7.5)$$

where ϕ is the roll angle and ψ is the pitch angle (Lu and Lueck, 1999b). However, this correction will only work for a fixed sensor, i.e. one that is not mounted in a gimbal, due to the uncertainty in the source of variation that time variant tilt angles introduces. Lu and Lueck (1999b) suggest that a non-rigidly mounted sensor can still effectively measure turbulence when the largest scales of motion are greater than the beam spread as the velocity field should be homogeneous over such scales. Section 7.3.1 along with results from a similar site (Thomson *et al.*, 2014) suggests the largest scales of motion are around 17 m after corrections. Assuming that a streamwise integral lengthscale of double the beam spread is sufficient for accurate results, this corresponds to a maximum beam spread of 8.5 m. For a angle inclination of 20° this is at a height of 12 m, which does not extend to the turbine hub-height in this case. This also does not account for the decreasing size of the maximum fluctuations nearer the boundary, thus the estimates from the gimbals mounted DBDP in these environments will likely be affected by this limitation.

Estimates of Reynolds stresses suffer from the same issues of Doppler noise as other turbulence metrics. If the noise variance in the opposing beam pair is not equal this can bias results of τ . Lu and Lueck (1999b) present a method for correction of this value. This requires the derivation of a noise variance value for each beam, for each range-bin for each T_{stat} sample set.

For the DBDP, the noise variance of the DBDP is removed from the horizontal beam variance:

$$\tau_{uw} = \frac{\langle vel_{beam2}'^2 - vel_{beam1}'^2 \rangle}{2 \cdot \sin 2\beta} - \frac{\sigma_{noise\ beam}^2}{\sin 2\beta} \quad (7.6)$$

based on Lu and Lueck (1999b) with the assumption that the individual beam variances are equal in magnitude but opposite in sign.

SBDPs represent a potential advantage as in theory no beam transformation is needed as the beams point along the primary axis. This assumes no off angle flow and any variation will be a source of error. Thus the Reynolds stress tensor can be computed directly from the contemporaneous fluctuations in the two sensors given in Equation 7.3.

In this case there is no need to correct for Doppler noise, as two independent measurements will mean noise is uncorrelated and therefore cannot bias the τ_{uv} value (Lohrmann *et al.*, 1990). The assumptions with this method are that: flow is homogeneous over these ranges, particularly that turbulence is not evolving over the streamwise separation, that turbine body is not affecting the turbulence within the selected range and that the sensors are perfectly aligned with the streamwise flow and vertical directions.

One of the main challenges in making this comparison was the identification of a suitable data set. This required two SBDPs (vertical and axial) and an upstream DBDP all measuring concurrently. The inclusion of the upward facing SBDP meant a low wave condition was required as well as that the AWAC not be operating to mitigate crosstalk issues. Finally the turbine needed to be reversed to a flood tide as per all the other data sets. This meant a data set of only 90 minutes was available for this comparison. Thus statistical variation for a mean axial velocity range were not possible and all the values from the data set are presented. This analysis represents only an initial insight into the use of SBDPs for this purpose.

Data processing basics

Data sets were selected as described in Section 6.3, with details of the quantity of the data and dates over which it was collected for each direction, given individually in the respective results sections. Once the original sample-rate data sets were loaded they were divided into 256 second sample-sets employing a 50% overlap where data was continuous to maximise the number of samples. Sample sets were contemporaneous across both instruments.

The DBDP velocities were transformed as described in the Section 6.4 such that the horizontal velocity directions were aligned and normal to the axis of the turbine nacelle. The range bins were selected as discussed in Section 6.5 and no spatial averaging of data was undertaken as discussed in Section 6.7.

7.2.6 Quality control

Quality Control (QC) was integrated into the data selection and loading process. Starting with the selection criteria as described in Section 6.3, then as data is loaded, data with instrument error codes, exceeding the velocity range or with non unique timestamps are removed. Velocity sets are visually checked for spurious data caused by database errors such as: interference from other instruments or incorrect turbine heading.

At the stage where data is divided into T_{stat} length subsets small gaps left by data removal are interpolated over. Gaps of up to and including three consecutive missing data points in the sample set were interpolated across using a cubic spline method. As this method produced spurious results when interpolating near the edges of a time series, data beyond missing values within three time-steps of the start or end of a time series were removed. Time series with more than three consecutive missing values were removed and not used in analysis.

7.3 Results

7.3.1 Axial metrics (x)

Data set

For the axial data comparison, data from SBDP_{RMS} along with the North-West DBDP (5th deployment) with the turbine reversed to the Flood tide was used. The data was collected over July 2014. This included 1317, 256 second sample sets. The data subset for both instruments is displayed in Figure 7.3, showing the u values measured by both instruments. Gaps exist where the requirements for the test were not met such as turbine orientation, instrument settings etc. The number of 256 second data sub-sets in each 0.1 ms^{-1} velocity range are presented in Figure 7.4.

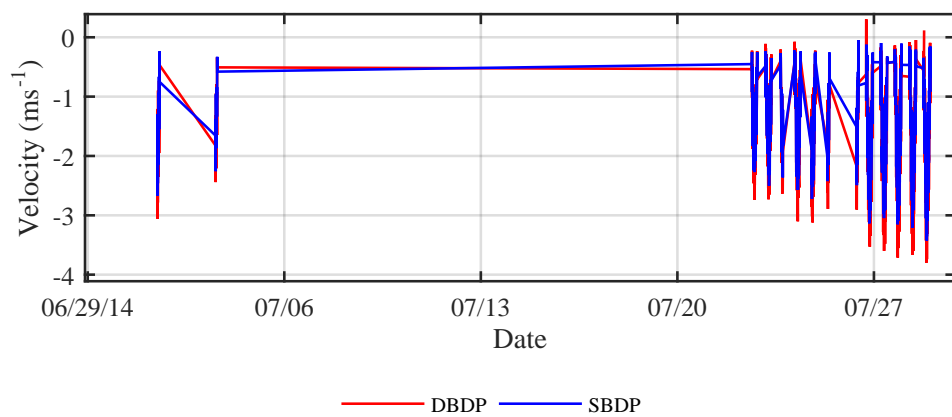


Figure 7.3: Selected samples for the SBDP and DBDP for the axial comparison study.

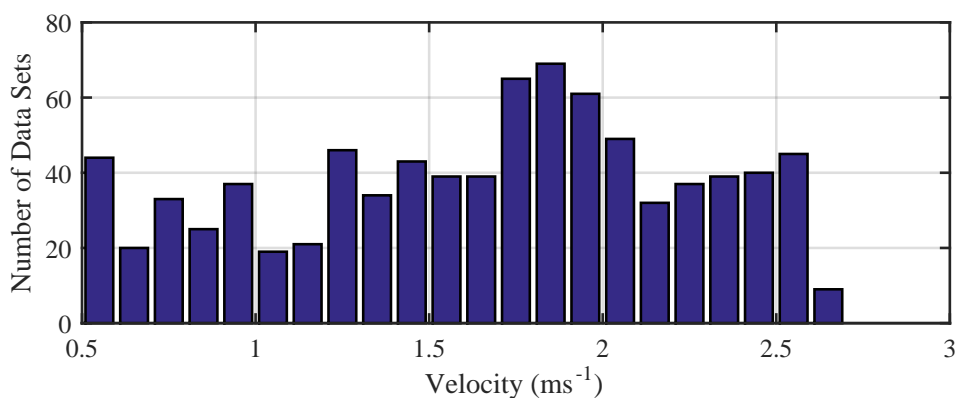


Figure 7.4: Histogram of streamwise data availability by mean DBDP velocity bin centres.

Velocity

Figure 7.5 shows the one to one plot of the T_{stat} averaged velocity (\bar{u}) reading for the SBDP and a linear fit of the data. The fit has an R^2 goodness-of-fit value of 0.99 and has a slope of 0.93 indicating that the DBDP velocities are biased high compared with the SBDP at hub height. This was expected from the work on bin selection in the Section 6.5. This bias is likely down to a combination of off angle velocities with the SBDP measuring a combination of the vertical and streamwise components, along with the spatial variation of velocity based on the change in depth over this range. The relationship between turbulence metrics with velocity and depth is difficult to quantify but the SBDP x direction turbulence metrics would be expected to be biased towards the lower y direction values.

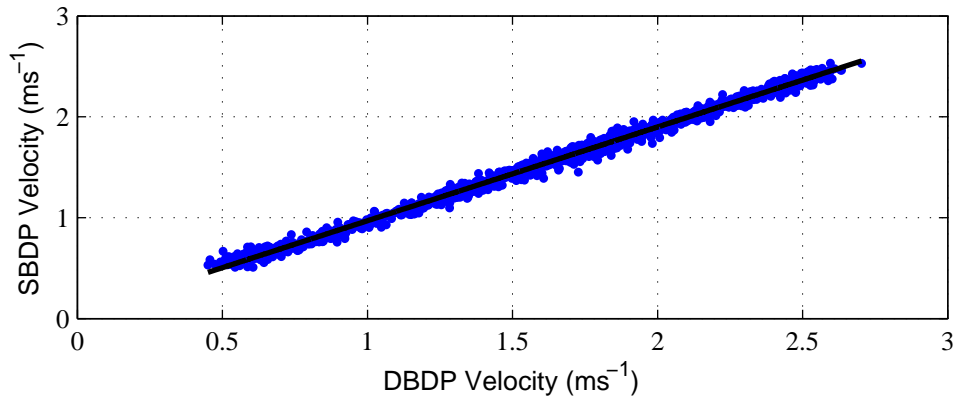


Figure 7.5: Comparison of contemporaneous \bar{u} measurements by the SBDP and the DBDP.

Turbulence intensity

The axial turbulence intensities (I_x) for the two instruments for each velocity bin are presented in Figure 7.6 for both uncorrected and corrected values. The correction is made using Equation 4.4 with individual noise variance estimates based on Equations 4.11 and 6.6. The large dots indicate the mean value and the small dots the standard deviation either side of the mean.

For the uncorrected values the average difference between the two instruments is 3.09 % and for the corrected values 1.97 %. Thus the correction reduces the value but there would appear to be residual variance in the DBDP even after correction, particularly at the lower flow speeds. A power law trend (being found to be the best fit type in the majority of $I(\bar{u})$ cases) was fitted by a leased squares method to the mean values of the corrected I values of both instruments resulting in similar slopes such that:

$$I_{xSBDP} = 8.69 \cdot (\bar{u}_{DBDP})^{-0.14} \quad (7.7)$$

$$I_{xDBDP} = 11.14 \cdot (\bar{u}_{DBDP})^{-0.40} \quad (7.8)$$

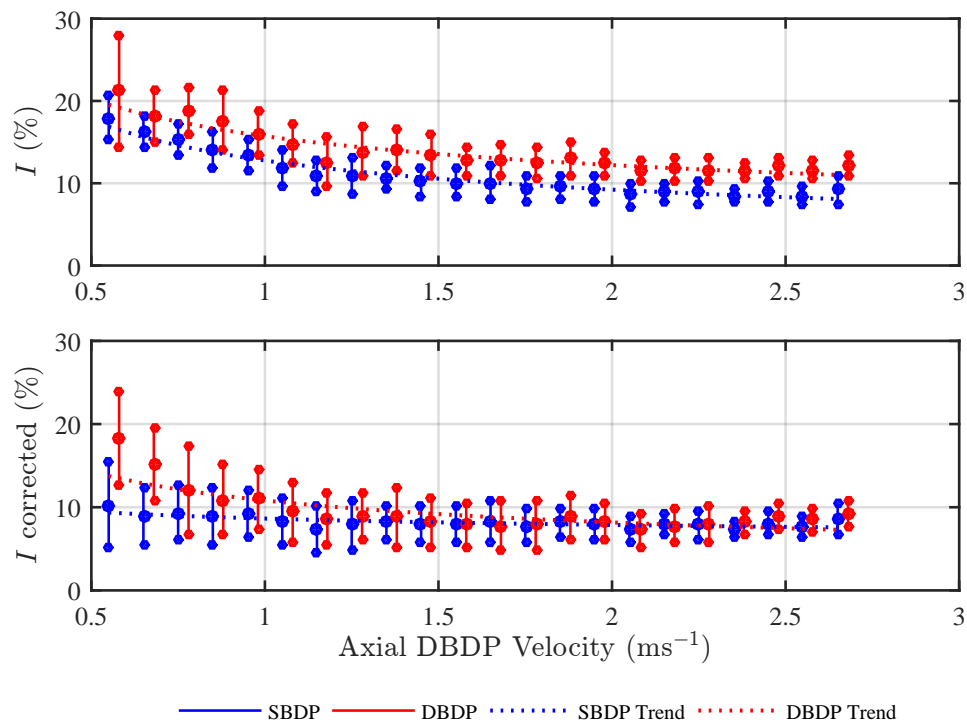


Figure 7.6: Comparison of the I_x values from the SBDP and DBDP. The large dots mark the mean values and the small dots the standard deviation about the mean for each 0.1 ms^{-1} velocity range. The top plot is the uncorrected values and the lower those corrected for the contribution of random error.

with R^2 goodness of fit values of 0.51 and 0.64 respectively.

The turbulence intensity is shown to decrease with axial velocity in both cases. At the lower velocities the fit is less satisfactory. The corrected values of I_x had standard deviations which were on average slightly higher in the DBDP I_x than those of the SBDP by 0.48 ms^{-1} . The standard deviation also decreases as velocity increases for both instruments. The correction of I_x brings mean values and standard deviations in close alignment, particularly at flow-speeds greater than 1 ms^{-1} , meaning that there is a high level of confidence in these values.

Turbulent kinetic energy dissipation rate

Figure 7.7 presents the estimates of the dissipation rate via the spectral fit method used for discerning the noise floor, for both instruments across the velocity range. The two instruments present similar gradients of 0.86 and 0.90 for the SBDP and DBDP respectively indicating that dissipation rate increases linearly with velocity. It is also evident that the value of ε measured by the DBDP is biased consistently high compared with that of the SBDP. The results for the SBDP match well with those measured by Thomson *et al.* (2010) at a similar site. As additional noise should not affect the result of the dissipation rate this result suggests there is an issue with

the curve fit method accurately identifying the $-5/3$ slope. This is due in part to the issues with the PSD fit method to this turbine deployment as discussed in Section 6.6.2. This suggests that the DBDP estimations using this method are not reliable, while the SBDP values match well with those at other sites (Thomson *et al.*, 2010).

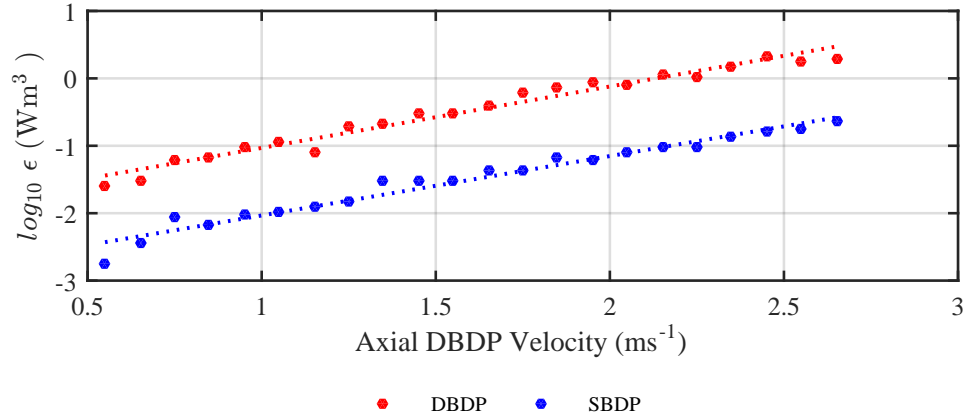


Figure 7.7: ϵ measurements from the two sensor types based on axial velocity measurements.

Integral lengthscale

Figure 7.8 illustrates the relationship between velocity (\bar{u}) and the axial integral lengthscale (ℓ_x) for the two instruments. The large dots indicate the mean value and the small dots the standard deviation either side of the mean.

The mean values were fitted to a base 10 logarithmic curve (found to be the best fit after trial of several curve types) of the form $\ell = a + b \cdot \log_{10}(\bar{u})$, where a and b are coefficients.

$$\ell_{xSBDP} = 4.99 + 18.95 \cdot \log_{10}(\bar{u}_{DBDP}) \quad (7.9)$$

$$\ell_{xDBDP} = 3.56 + 5.64 \cdot \log_{10}(\bar{u}_{DBDP}) \quad (7.10)$$

The slopes were a good fit of the mean data points for the specified range, with R^2 values of 0.95 and 0.85 respectively.

The SBDP data values of ℓ_x are generally higher than those of the DBDP with the disparity increasing with velocity to a difference of 7.41 m between mean values at the highest velocity range. The standard deviation also increases with velocity, up to 7.14 m for the SBDP and 4.36 m for the DBDP at the highest velocity range. Thus the mean value and spread were of similar magnitude. The maximum values also show large disparity with the largest SBDP value of 35.54 m and DBDP of 23.76 m. The SBDP results are closer to the expected values for a channel of this depth at high flow speeds with the DBDP underestimating them significantly (Blackmore *et al.*, 2011; Thomson *et al.*, 2014).

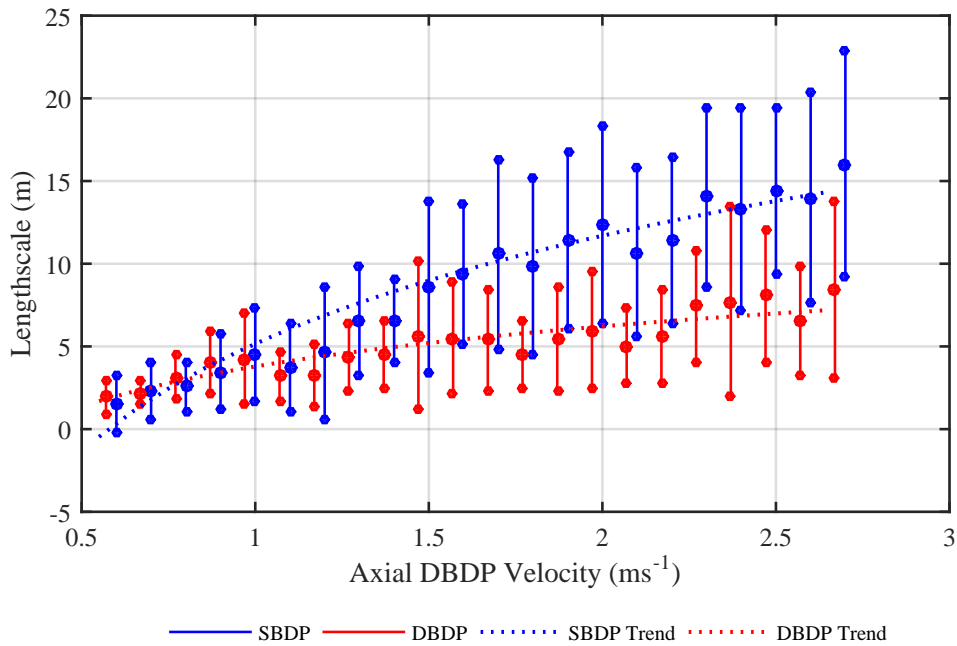


Figure 7.8: Comparison of ℓ_x calculated via temporal autocorrelation method on measurements by the SBDP and DBDP. The large dots mark the mean values and the small dots the standard deviation about the mean for each 0.01 ms^{-1} velocity range.

7.3.2 Transverse metrics (y)

Data set

For the transverse data set, SBDP_{SA} matched with the North-West DBDP from the first deployment, had the most data for the required conditions. This covered dates across February 2013 including 1331 256 second subsets and the data set used is illustrated in Figure 7.9, which plots the transverse velocity readings from the 2 sensors. Figure 7.10 shows the number of 256 second data sets in each velocity-range bin.

Velocity

Figure 7.11 presents the co-measured \bar{v} from both sensors. It illustrates that there is a much greater spread of measurements between the two instruments in the transverse than the stream-wise direction with a R^2 of 0.61. The gradient of the linear fit is 0.96. Figure 7.12 illustrates the relationship of \bar{v} with \bar{v}_{DBDP} . It shows that the results are relatively well matched across the velocity range.

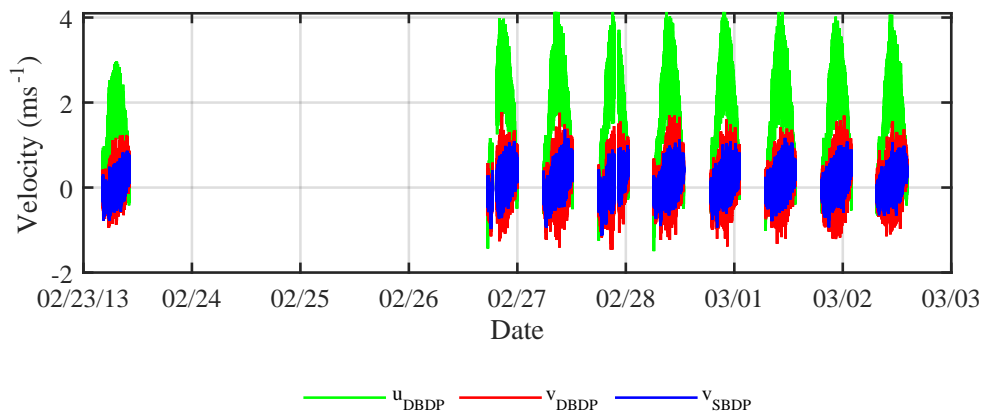


Figure 7.9: Selected samples for the SBDP and DBDP for the transverse comparison study.

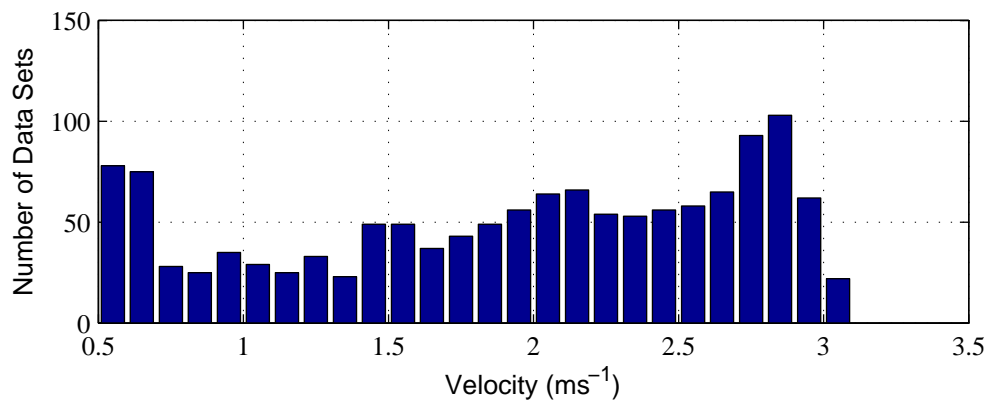


Figure 7.10: Histogram of transverse data availability by mean DBDP velocity bin centres.

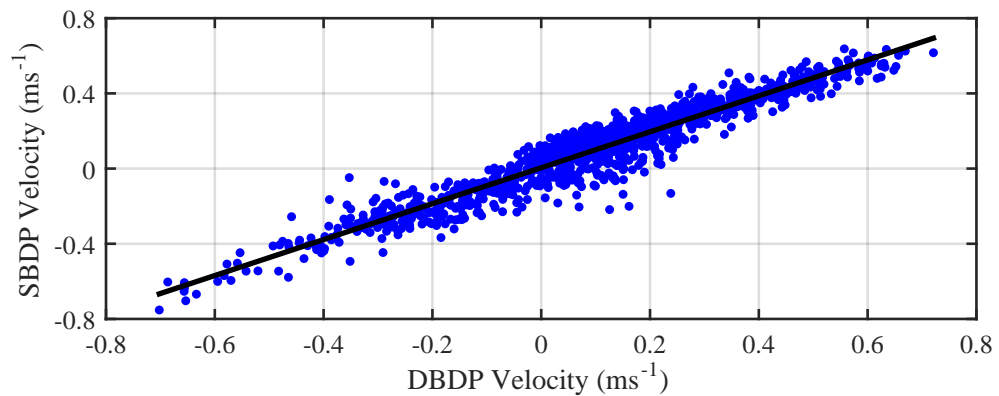


Figure 7.11: Comparison of contemporaneous \bar{v} measurements by the SBDP and the DBDP.

Turbulence intensity

Figure 7.13 shows the I_y values, uncorrected and corrected, normalised by \bar{u}_{DBDP} for both instruments. As with the streamwise data the SBDP shows a significantly lower value than the DBDP, with a mean difference of 6.46 % for the uncorrected and 4.48 % in the corrected case. This suggests that the horizontal noise relationship calculated for the DBDP is not correcting the transverse values as well as for the streamwise.

As with the axial case I_y decreases with increasing \bar{u}_{DBDP} . One notable aspect is the extremely high I values at low \bar{u}_{DBDP} . This is due at least in part to the method of calculating I by a u velocity with a fixed angle, when the resultant flow direction is changing over the course of the tide. These high I_y values are due to a high \bar{v} component with associated increased fluctuations. At the highest flow speeds the mean I_y values were 5.62 (SBDP) and 8.73 (DBDP) compared with the I_x values of 8.94 (SBDP) and 9.76 (DBDP) for the highest velocity range.

A power law trend was fitted to the mean values of the corrected SBDP and DBDP I values:

$$I_{ySBDP} = 8.54 \cdot (\bar{u}_{DBDP})^{-0.42} \quad (7.11)$$

$$I_{yDBDP} = 12.93 \cdot (\bar{u}_{DBDP})^{-0.35} \quad (7.12)$$

with an R^2 goodness of fit of 0.84 and 0.74, respectively.

Turbulent kinetic energy dissipation rate

Figure 7.14 presents the estimates of ε via the spectral fit method. As was the case with the axial analysis the results from the two instruments show similar gradients of 0.80 and 0.79 for the SBDP and DBDP, with the DBDP consistently biased high by 1.15 Wm^{-3} . The values are closely matched to those for the streamwise direction, with the latter being 7.9 % greater on average.

Integral lengthscale

For the transverse integral lengthscale ℓ_y the results of two methods are presented, one via the temporal autocorrelation converted via the assumption of frozen turbulence and one computed directly by spatial autocorrelation. The latter can only be processed for the SBDP as it requires a series of bins along the transverse axis. Figure 7.15 presents the results of the former for both instruments.

Here the two results for the two instruments are much better matched than in the axial case, with the DBDP producing the higher values for this orientation. The average DBDP result was 0.58 m greater than the SBDP. The mean values at the highest velocity bin (centred at 3.05 ms^{-1}) were 7.62 m and 6.57 m respectively. The mean values for both the SBDP and the DBDP across the velocity range were fitted to a power law such that:

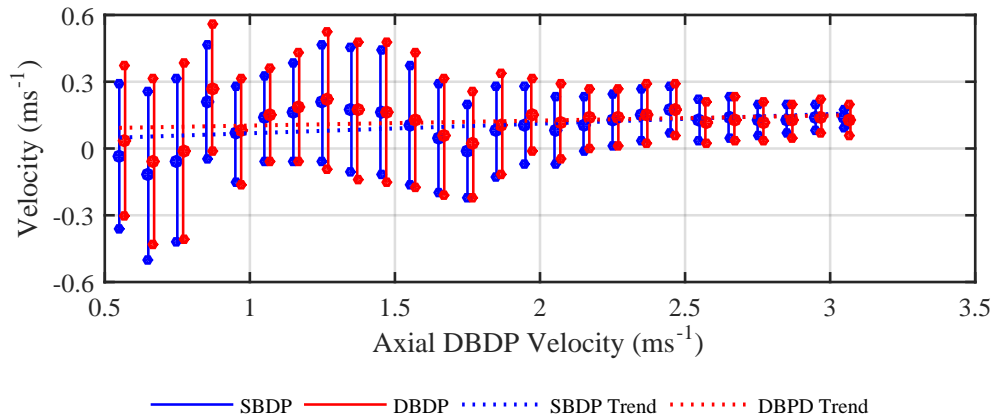


Figure 7.12: Distribution plot of \bar{v} measurements with axial velocity. The large dots mark the mean values and the small dots the standard deviation about the mean for each 0.1 ms^{-1} velocity range.

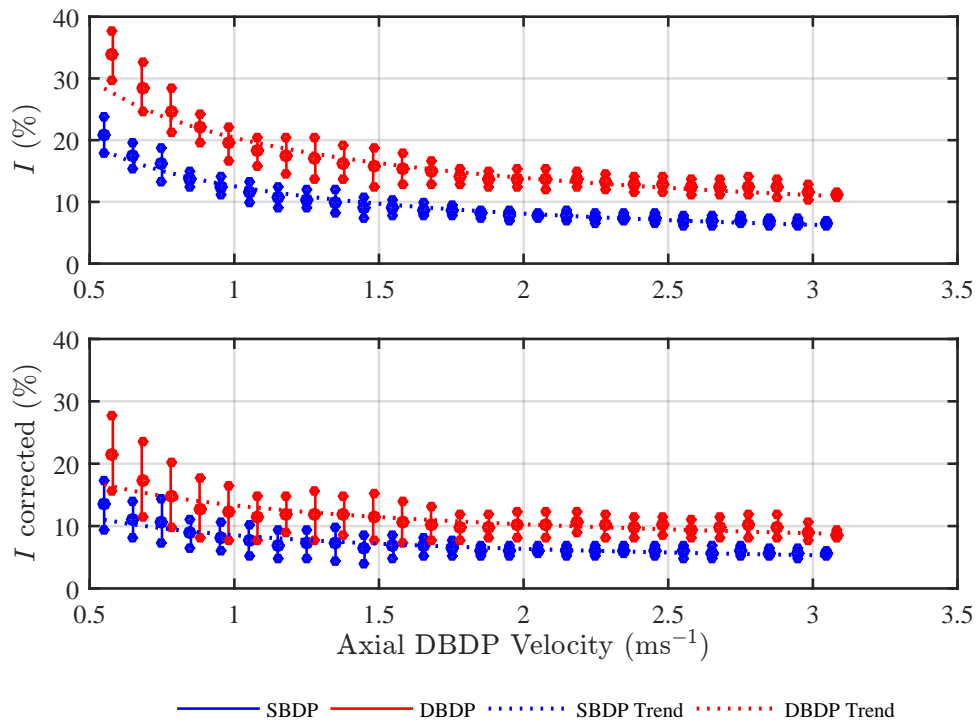


Figure 7.13: Comparison of the I_y values from the SBDP and DBDP. The large dots mark the mean values and the small dots the standard deviation about the mean for each 0.1 ms^{-1} velocity range. The top plot are the uncorrected values and the lower those corrected for the contribution of random error.

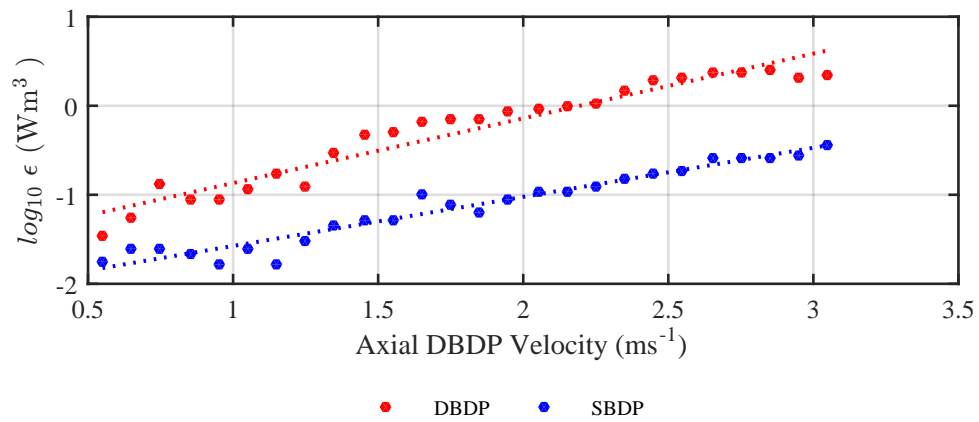


Figure 7.14: ε measurements from the two sensor types mounted in the traverse orientation.

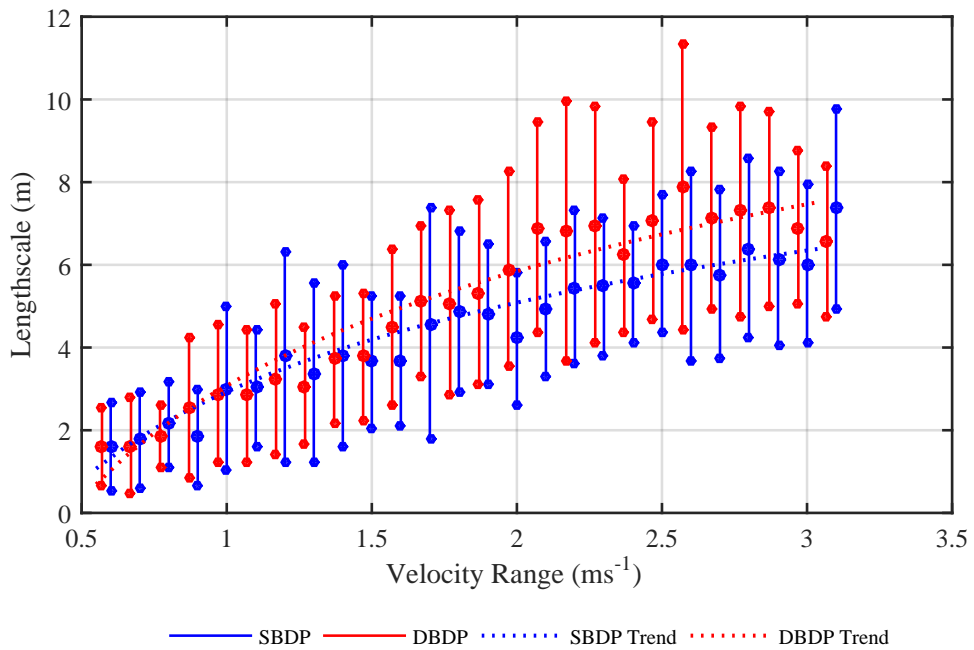


Figure 7.15: Comparison of ℓ_y calculated via temporal autocorrelation method on measurements by the SBDP and DBDP. The large dots mark the mean values and the small dots the standard deviation about the mean for each 0.01 ms⁻¹ velocity range.

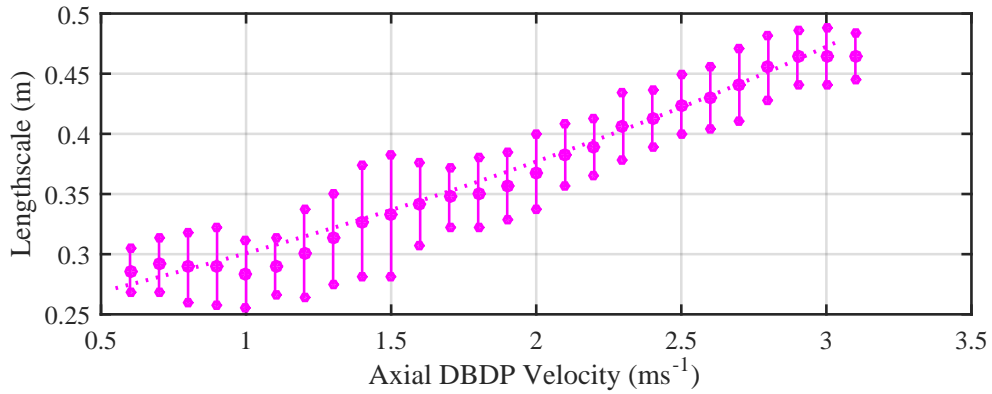


Figure 7.16: SBDP measurements of ℓ_y calculated via a spatial autocorrelation method.

$$\ell_{ySBDP} = 2.90 + 7.27 \cdot \log_{10}(\bar{u}) \quad (7.13)$$

$$\ell_{yDBDP} = 3.07 + 9.22 \cdot \log_{10}(\bar{u}) \quad (7.14)$$

with associated R^2 values of 0.93 in both cases.

Figure 7.16 presents the results from the SBDP of the alternative spatial autocorrelation method of calculating the Lengthscale. It is evident that the results are a factor of 10 lower throughout the velocity range than the temporal autocorrelation method. This limited value of results is likely an underestimation due to the limited effective range of the SBDP compared with the physical lengthscale values.

7.3.3 Vertical metrics (z)

Data set

The vertical velocities are considered in the same manner as for the x and y directions, here utilising data collected by SBDP_{VA} and the second North-West DBDP deployment over February 2013 with 478 available 256 second sample-sets, covering flood tide data only. The data set selected is shown in Figure 7.17. Figure 7.18 shows the number of 256 second data-sets in each velocity bin range.

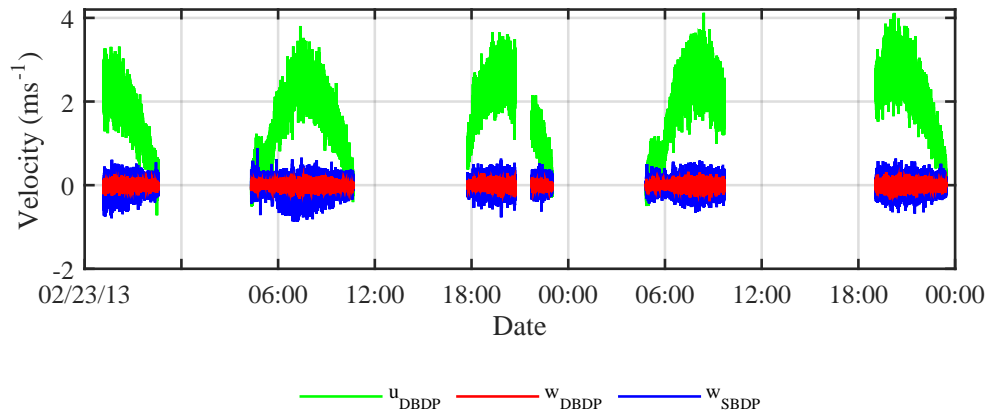


Figure 7.17: Selected samples for the SBDP and DBDP for the vertical comparison study.

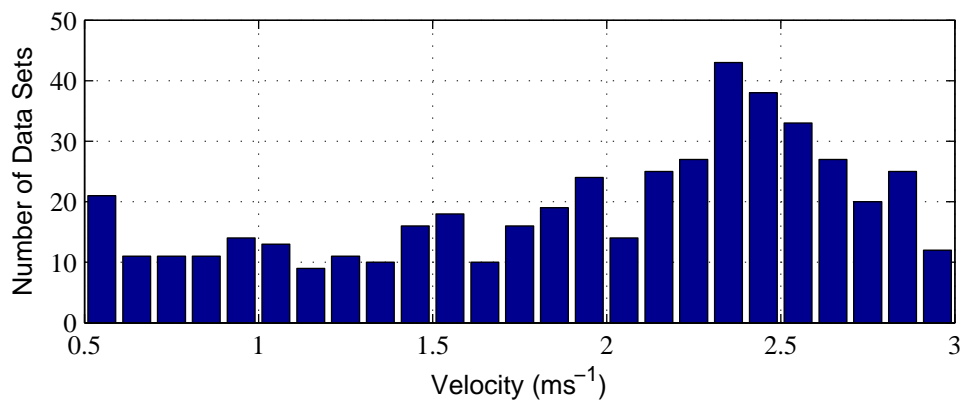


Figure 7.18: Histogram of vertical data availability by mean DBDP velocity bin centres.

Velocity

Figure 7.19 presents the one to one plot of co-measured \bar{w} from both sensors. The relationship is centred around the mean values of 0.01 ms^{-1} (DBDP) and -0.04 ms^{-1} (SBDP). Figure 7.20 illustrates the differences in the vertical velocities over the axial velocity range. The large dots indicating the means and the small dots the standard deviation around the mean. With no linear trend (like those seen in the streamwise and transverse) between the two sensors this indicates mean vertical velocities are poorly correlated between the two sensors.

Both sensors indicate a downward velocity as negative and a upward one as positive. Thus, both sensors show a mean downward trajectory but this is more significant in the SBDP, as can be seen as the axial flow speed increases. The values of the SBDP were expected to be positive due to the turbine's slope relative to the seabed which is known to be $\sim 3^\circ$ (see Figure 6.3). The DBDP is corrected for the pitch and roll of the sensor but vertical velocities could still occur due to bathymetrical features. Analysis of different data sets suggests this disparity was constant over all turbine and associated DBDP deployments.

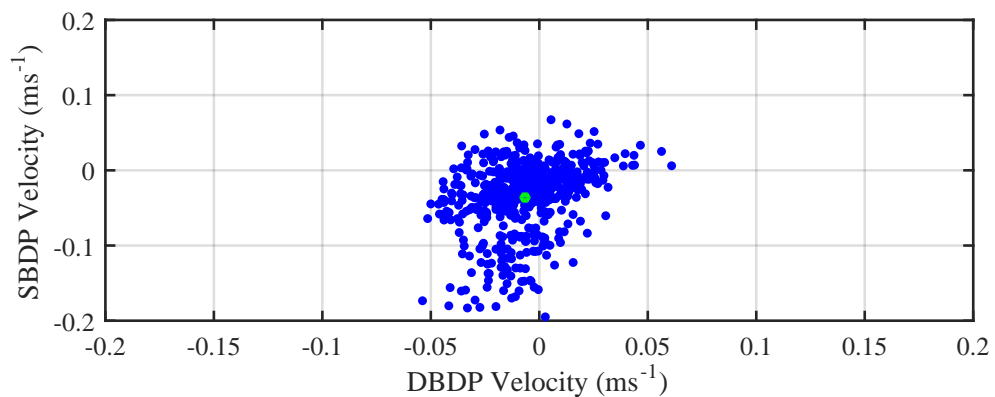


Figure 7.19: Comparison of contemporaneous \bar{w} measurements by the SBDP and the DBDP.

Turbulence intensity

The I_z values, uncorrected and corrected, for the two instruments are plotted in Figure 7.21. The SBDP I_y values are comparable to the axial results while the DBDP are significantly lower. This is the only orientation for which the SBDP has a greater fluctuation than the DBDP. This is in part due to the noise in the transformed DBDP velocity being less in the vertical as explained in Section 6.4. The correction causes the two estimates to converge with a difference in mean value of 1.92 %, reduced from 4.92 %. However the vertical fluctuations in the DBDP measurements are generally not corrected as they were lower than the estimated noise variance (as discussed in Section 6.6.2). At the highest velocities the mean I_z measured is 4.30 % (SBDP) to 2.75 % (DBDP).

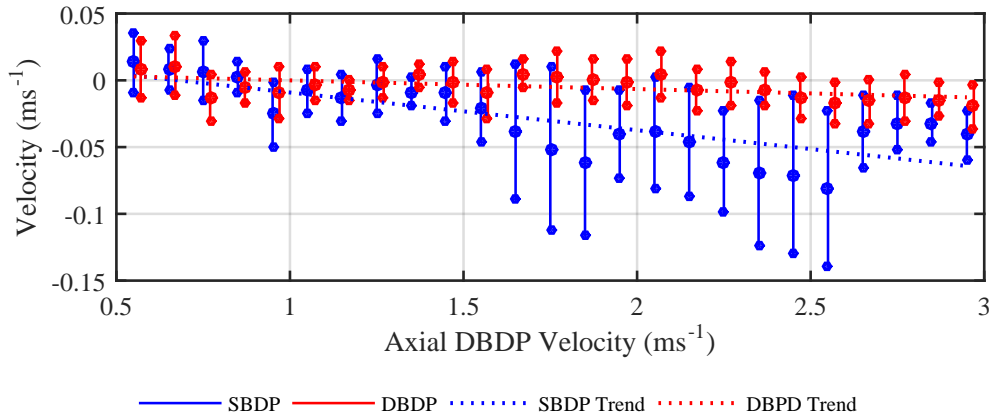


Figure 7.20: Distribution plot of \bar{w} measurements with axial velocity. The large dots mark the mean values and the small dots the standard deviation about the mean for each 0.1 ms^{-1} velocity range.

They show a similar log law relationship as the mean I_x and I_y results such that:

$$I_{z_{SBDP}} = 6.56 \cdot (\bar{u}_{DBDP})^{-0.41} \quad (7.15)$$

$$I_{z_{DBDP}} = 5.26 \cdot (\bar{u}_{DBDP})^{-0.66} \quad (7.16)$$

with an R^2 of 0.69 and 0.96 for the SBDP and DBDP respectively respectively.

In this case the primary cause for the differences between the two sensors is likely a small offset in the vertical SBDP based on the turbine and instrument mounting angle.

Turbulent kinetic energy dissipation rate

Figure 7.22 presents the calculation of ϵ via the two sensors. As discussed in Section 6.6 the DBDP spectral slopes were not well resolved in the vertical component. Thus, the results from the DBDP are not reliable. The SBDP, shows a similar gradient to the other orientations with a gradient of 0.73 for a least squares linear fit. Values were in a similar range to the other two directions with the vertical estimates being 3.46% higher than for the streamwise direction.

Integral lengthscale

Figure 7.23 presents the estimates of ℓ_z with \bar{u} for both instruments. In the vertical case it is the DBDP that gives the greater estimates of ℓ_z with a mean value of 5.53 m compared with 2.72 m (SBDP). The maximum value is also greater in the DBDP, 20.10 m compared with 10.54 m (SBDP). As the spectra (which are based upon a similar auto-correlation process) for the DBDP were unreliable there is increased uncertainty surrounding the DBDP ℓ_z results. The following least squares curve fits were applied to the mean values:

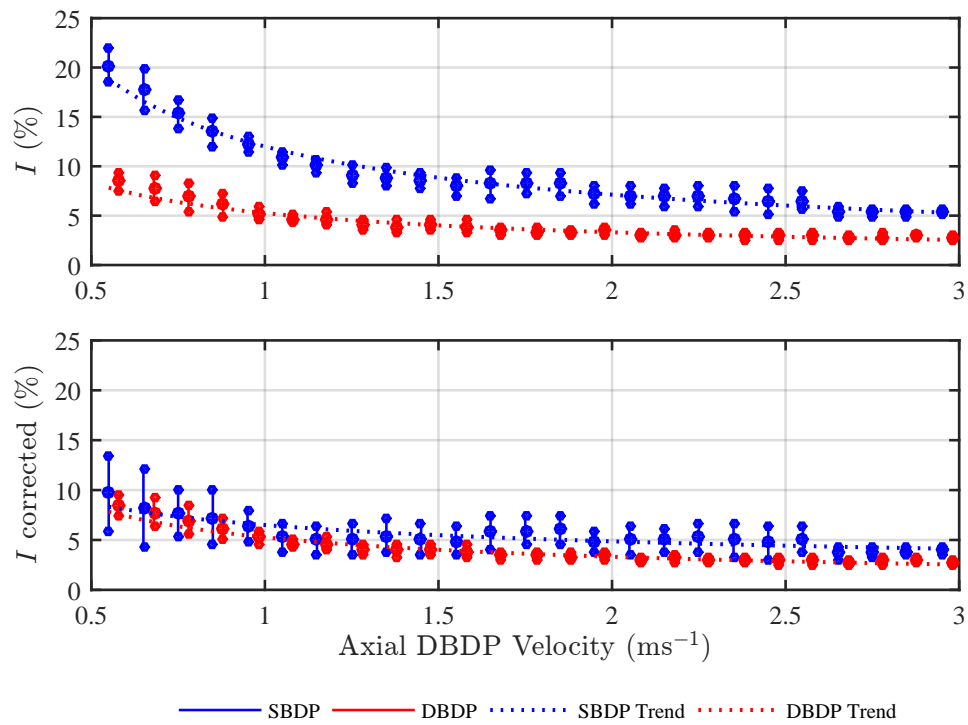


Figure 7.21: Comparison of the I_z values from the SBDP and DBDP. The large dots mark the mean values and the small dots the standard deviation about the mean for each 0.1 ms^{-1} velocity range. The top plot is the uncorrected values and the lower those corrected for the contribution of random error.

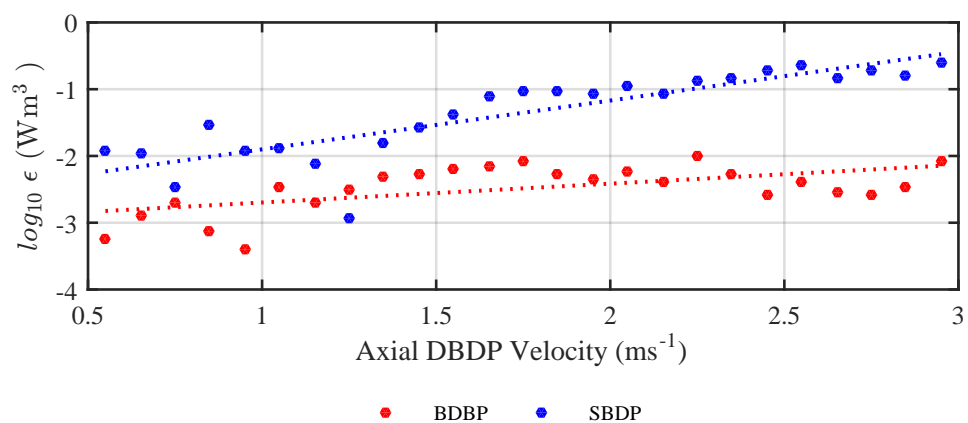


Figure 7.22: ϵ measurements from the two sensor types mounted in the vertical orientation.

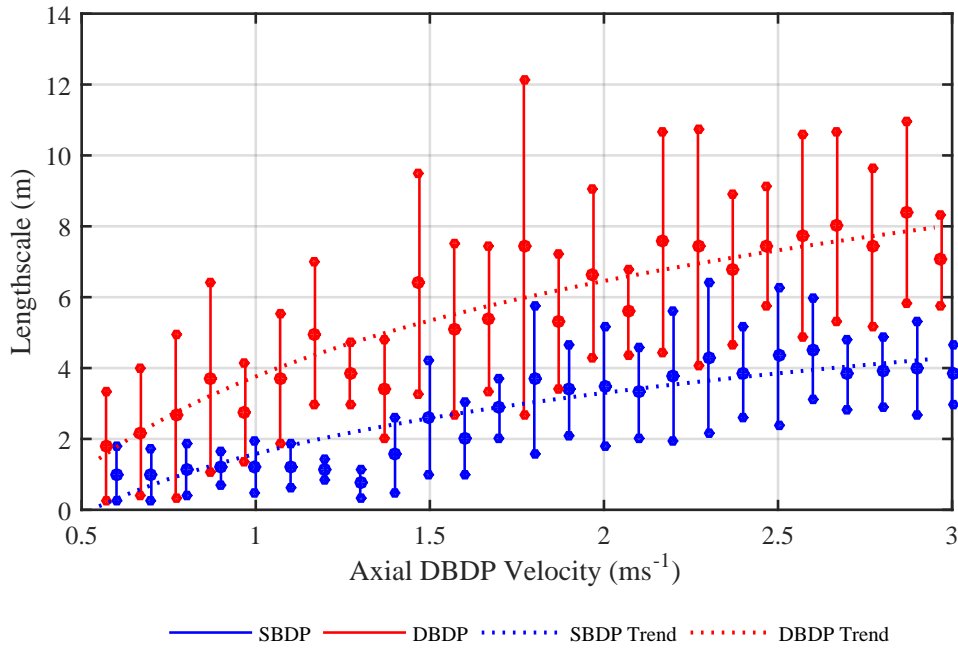


Figure 7.23: Comparison of ℓ_z calculated via temporal autocorrelation method on measurements by the SBDP and DBDP. The large dots mark the mean values and the small dots the standard deviation about the mean for each 0.01 ms^{-1} velocity range.

$$\ell_{zSBDP} = 1.52 + 5.70 \cdot \log_{10}(\bar{u}) \quad (7.17)$$

$$\ell_{zDBDP} = 3.77 + 8.94 \cdot \log_{10}(\bar{u}) \quad (7.18)$$

with associated R^2 goodness of fit values of 0.83 and 0.87.

Figure 7.24 illustrates the estimates from the SBDP via the spatial autocorrelation method. As in the transverse case these values are significantly lower than those measured by the temporal auto-correlation method.

7.3.4 Reynolds Stresses

The vertical-streamwise Reynolds stress tensor was calculated both by the DBDP and a pair of SBDPs orientated along the appropriate direction. As mentioned previously, due to the stringent requirements for the data for this test and that it was not specifically tested for during the data collection campaign only a limited data set was available covering approximately 90 minutes. Figure 7.25 presents the data set selected. Gaps appear where any of the instruments was not collecting data or a data sub-set failed QC procedures.

Figure 7.26 presents the results for the DBDP, calculated by the two beam pairs. Values corrected for bias due to mismatched noise variances in the beam pairs as given by Equation 7.6

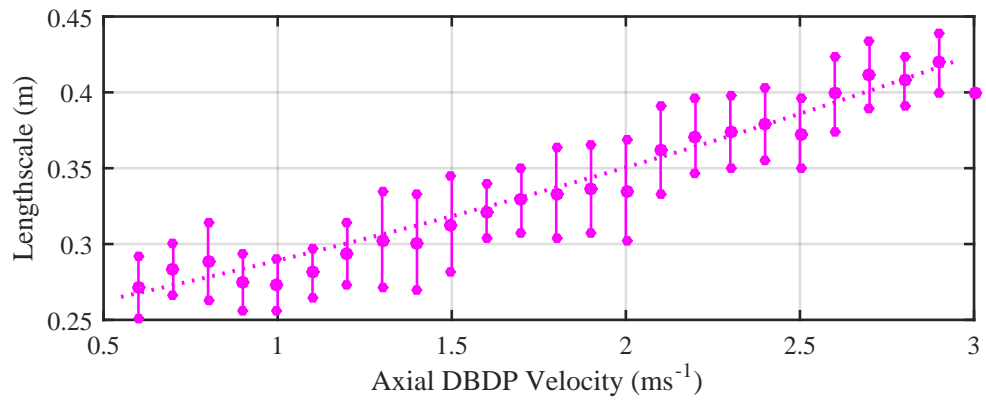


Figure 7.24: SBDP measurements of ℓ_z calculated via a spatial autocorrelation method.

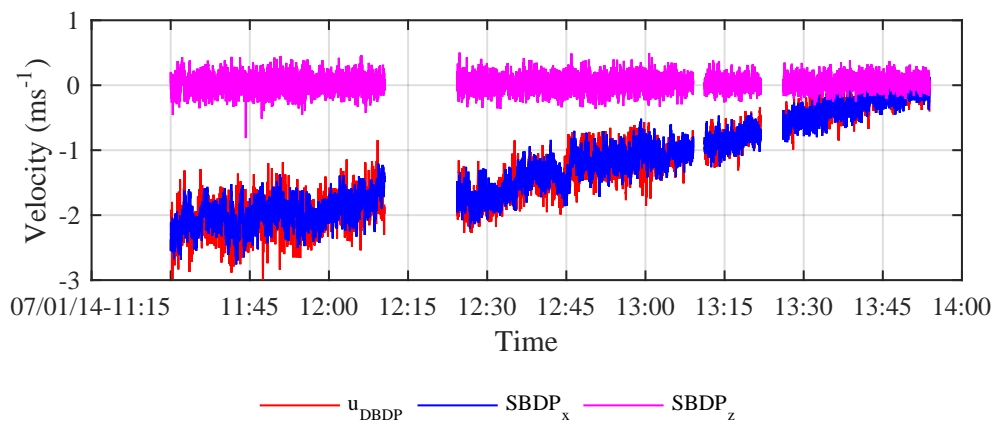


Figure 7.25: Data set matched across three sensors for τ_{uv} comparison.

are also included. As can be seen the correction can adjust the value lower or higher depending on which beam contained the dominant noise variance. For the streamwise-vertical tensor the average correction was 0.18 % of the original mean value at that depth bin.

As neither beam pair is exactly aligned with the x direction, with the heading for this deployment was 7° compared with a flow direction of 148° . A misalignment of 39° to the nearest beam pair. Thus the best estimate for the streamwise-vertical Reynolds stress tensor is from the Beam 3 and 4 pair which have the highest resultant velocity values for the majority of the depth. The dominant tensor changes to the beam 1 and 2 pair near the bottom which is evidence of the twist in the flow profile as detailed in Sutherland *et al.* (2013). It is expected that the beam pair most closely aligned with the flow would have the higher value. Togneri and Masters (2012) have showed the $\langle u'w' \rangle$ tensor to generally have greater magnitude than the $\langle v'w' \rangle$ tensor at a nearby site. In reality the $\langle u'w' \rangle$ would be expected to increase with increased alignment to the streamwise direction.

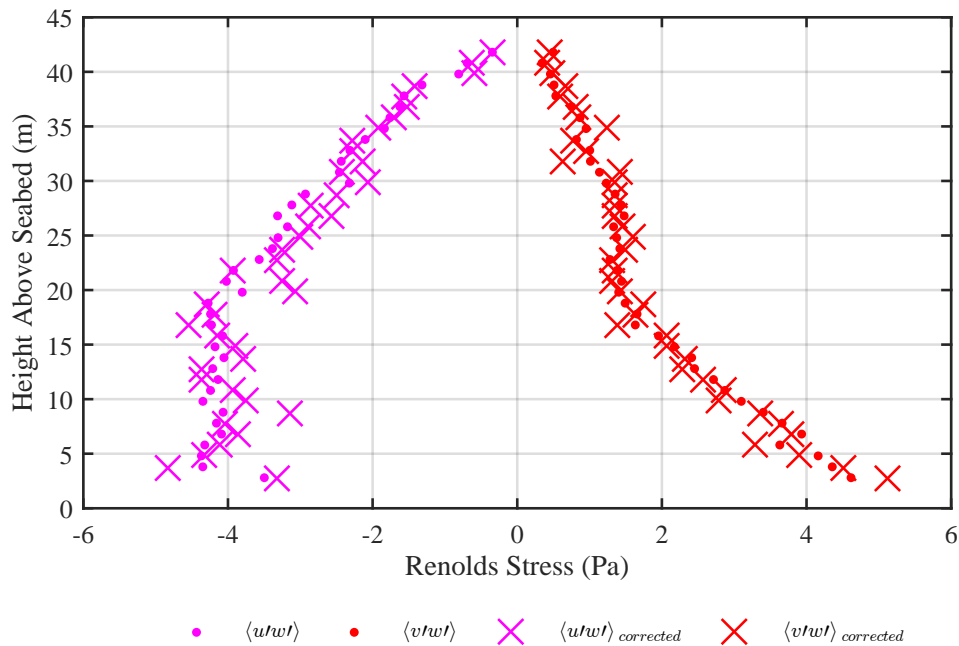


Figure 7.26: Estimates of the Reynolds stress two calculated via the beam-pair method and via $\langle u'w' \rangle$ from rotated DBDP velocities.

It can be seen in both tensors that the Reynolds stress is highest at the bottom boundary with values of greater than 4 Pa and decreasing to 0.4 Pa near the surface. These values are averaged over a range of axial flow speeds (with a mean value of 1.30 ms^{-1} at hub-height) and resulting turbulent conditions. The calculated values are similar to those collected around the Fall of Warness site for similar average flow speeds (Togneri and Masters, 2012; Osalusi *et al.*, 2009).

Figure 7.27 shows the equivalent results computed from the SBDP pair. Here the range is the

same for both SBDPs, noting that the spatial area covered between the independent measurement points is greater than this. The values increase with separation from the turbine over the first 2m and then fall off towards 0 Pa over the 20 m. The mean DBDP result at the equivalent height above the seabed is 3.00 Pa suggesting that the SBDP pair is underestimating this value.

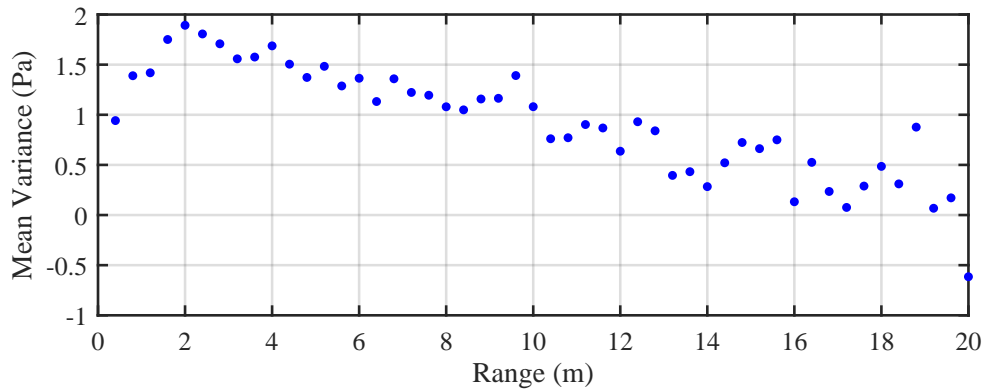


Figure 7.27: Reynolds stress estimates via a x - z SBDP pair averaged over all available flow speeds.

There is no reason the SBD pair needs to be restricted to the same range bin as is the case for the DBDP. In order to increase the values being underestimated by the SBDP pair, the bin for each individual sensor is varied to find the maximum τ_{uv} value (limiting the maximum range to 15 m range in the x and 5 m in the z to account for effective instrument range). The highest value was determined to compare to the DBDP. The vertical bin selected was 4 and the x was bin 5. Figure 7.28 shows the results from this comparison. It shows that even with this optimisation the SBDP still underestimates the DBDP values by a mean value of 2.7 Pa.

7.4 Discussion

When comparing two different instruments the aim is to conduct a fair comparison. This presents challenges in this case with the sensors mounted in separate locations in a spatially varying channel. Differences between measurements can be attributed to many things including sample rate, spatial sample volume, spatial variation, spatial averaging down to pulse processing algorithms within the instrument. Here the instruments are not co-located and use slightly different pulse processing techniques as developed by two different manufacturers and it is important to bear these facts in mind when contrasting the results from the two instruments.

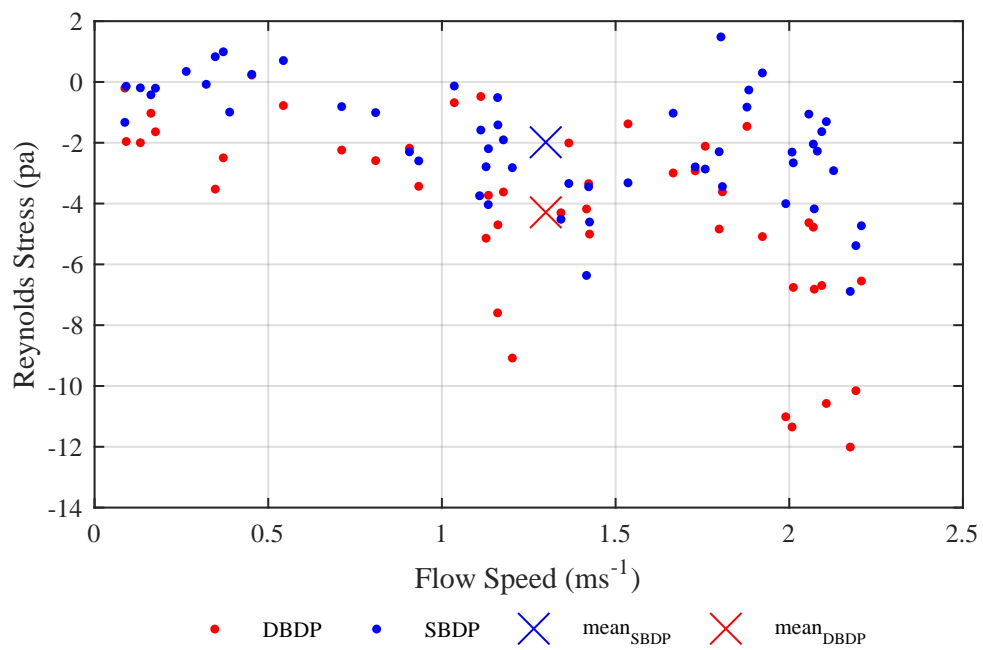


Figure 7.28: Hub height comparison of SBDP and DBDP Reynolds stress results across the available flow speeds.

Data selection and treatment

As one sensor is upstream of the other by 50 m there is an argument for offsetting the matched timestamps by $50/\bar{u}$. However at the highest 3 ms^{-1} flow speeds, this only equates to 16.7 seconds in a flow that is taken to be stationary over a period of 5 minutes.

Velocity

The one to one axial velocity plot showed a consistently higher velocity reading from the DBDP at the equivalent height above the seabed. As Figure 6.8 shows the SBDP velocity with range is a curve with a defined turning point, albeit a shallow one, it could be that the effective range of the SBDP does not reach the unimpeded flow ahead of the blockage effects of the turbine. However, with the turbine not operating in these tests a region of significantly slowed flow of >10 m seems high. More likely, is that the spatial variation upstream, due at least in part to the difference in channel depth, is enough to cause this disparity. The upstream DBDP is known to be in a shallower depth of channel which is expected to contribute to this velocity increase.

The velocities in the transverse direction presented in Figures 7.9, 7.11 and 7.12 were reasonably well matched with the SBDP showing marginally higher mean values and the DBDP the greater standard deviation, across the velocity range. Figure 7.12 shows that the standard deviation in both sensors is higher at the lower velocities as this will include values of \bar{v} that are both positive and negative as the resultant tide direction changes around the fixed angle used. At the higher flow speeds the standard deviation is low and the mean value of the transverse velocity close to zero as would be expected for this method. This suggests that the methodology for matching the flow angle was justified.

In the vertical direction the greatest disparity existed between the two sensor types for the velocity results. Here the mean value would be expected to be close to zero. Figure 7.19 shows that the one to one plot of \bar{w} was poorly matched with the results spread around a central downward mean value. The DBDPs are corrected for tilt angles where as the SBDP are not, it would be possible to multiply the SBDP vertical velocity results by $\cos(3)$, however this would not account for the magnitude of difference in vertical measurement between the sensors. For the DBDP the vertical velocities were of the order of 0.01 ms^{-1} which represents a negligible quantity. In the SBDP though maximum vertical velocities were in the order of 0.10 ms^{-1} , as shown in Figure 7.20. This lends further evidence to the suggestion that the flow at this site varies over these scales. It might be expected that the presence of the turbine would lead to a small upward trajectory of velocities, however the negative velocities mean a downward vertical velocity. This would suggest the upward trajectory due to the turbine is upstream and directly above the nacelle there is a down-welling as the flow is redistributed across the depth. The low fluctuations of the vertical velocities measured by the DBDP, compared with the horizontal velocities will in part be due to the four beam method employed in the

vertical velocity processing reducing the error, which is possible in 4 or more beam instrument configurations (Gordon, 1996).

Turbulence Intensity

For all three vectors the turbulence intensity falls off with axial velocity for both sensors as shown in Figures 7.6, 7.13 and 7.21. The goodness of fit of a power law trend-line for the corrected I values were wide ranging between 0.5 and 0.95, due in part to the fact that some curves were tending towards a constant value. The correction for noise brought the estimates between instruments closer in all cases indicating a good approximation of the noise contribution to I was captured.

The fitted power law slopes are only used in order to represent data where speeds are less than 1 ms^{-1} . At greater flow speeds a linear slope would be the best fit in all cases. This is due, in part, to relatively energetic flow around ‘slack water’, even if the mean value of the flow at those times is close to zero over a 5 minute period in the axial component, due to highly fluctuating direction. Normalising a high average perturbation by $\bar{u} \approx 0$ will produce very high I_x values. The I measurements in the axial and transverse (the more energetic flow directions) were both higher in the DBDP than the SBDP. This is at least partially due to instrument noise which has been shown in Sections 4.2.2 and 6.6, to be higher in the DBDP. This can be corrected for when calculating I , but is still evidence that the SBDPs provide a more reliable indication of the turbulent fluctuations.

Thomson *et al.* (2010) found that the uncorrected velocity standard deviations of an DBDP were roughly double that of an Acoustic Doppler Velocimeter (ADV). Thomson *et al.* (2012) also report I measurements with the DBDP velocities of similar magnitude to those reported here for a Puget sound in the US. Both site show evidence of a power law relationship with velocity at lower speeds, with I appearing to increase as a straight line for flow speeds $> 1 \text{ ms}^{-1}$, although this is not quantified in the report.

I values are often used in site characterisation but, as they vary with flow speed they are difficult to quantify as a single value for an individual site. As the I values have been shown to vary as a power law with the mean velocity, there is an asymptotic limit on the lowest I value. The I value associated with this asymptote may provide a useful single indicator of the turbulence magnitude for a given site.

Turbulence Kinetic Energy Dissipation Rate

The SBDP results showed similar curves for all three directions. As the dissipation rate should not vary with direction this is an indicator of accurate measurement which is in the same order of magnitude as found by studies at similar sites (Thomson *et al.*, 2010). The DBDP results were high compared with this for the transverse and streamwise but lower for the vertical. This is evidence that the spectral fitting method was not correctly capturing the integral sub-range part of the slope for the DBDPs particularly in certain DBDP deployments as discussed in Section 6.6.2. This is likely due to the inability of the DBDP to accurately capture the turbulent structures across the scales due to non-homogeneous flow and velocity transforms. It should also be remembered that the measurements using the spectral method and the DBDP represent an upper limit of the physical processing due to the uncertainty of isotropy content (Lorke and Wüest, 2005).

Integral Lengthscale

The axial integral lengthscale ℓ_x was shown to increase with \bar{u} in Figure 7.8. However the disparity in mean value between the instruments is large with a mean difference of 6.33 m. The SBDP data produced the larger values across the velocity range. At flow speeds $>2 \text{ ms}^{-1}$ the mean values are within 10% of the $\ell_x = Z/3$ predicted from modelling work (Blackmore *et al.*, 2011). The DBDP data however underestimates the lengthscale with mean value of 5.1 m for the fastest flow speed case. The spread of values in both instruments is wide with the standard deviation being 42% and 60% of the mean velocity at high flow speeds for the SBDP and DBDP respectively. ℓ_x is defined as an estimate of the largest size of eddies in the flow and thus a relatively large spread of data is expected compared with other metrics. Note that for streamwise lengthscales, the initial study of spatial averaging of velocity measurements as discussed in Section 6.7 suggests these values could be increased by as much $\sim 27.76\%$. However, further work is needed on the impact of distribution of values and appropriateness in transverse and vertical orientations.

The mean values measured by the SBDP can be compared with results by Kilcher *et al.* (2014), who found the lengthscale to increase with velocity up to around 17 m at 2 ms^{-1} . The data was collected using an ADV with an f_s of 16 Hz at a site in Admiralty Inlet on the North-West coast of the USA. The site has a water-depth of approximately 55 m deep which along with flow speeds in excess of 2 ms^{-1} , represents similar conditions to the Fall of Warness. An increase in the lengthscales is expected with an increase in depth however the values reported are still slightly higher than measured here. Data was also presented in Kilcher *et al.* (2014) for a shallower site in the East River which gave lengthscales of around 15 m at 2 ms^{-1} but with a much reduced spread of results. This indicates that deeper channels may have a greater spread of lengthscales.

The conclusions that can be drawn from these results are: that ℓ_x increases with \bar{u} at the Fall

of Warness as at other sites, and that the SBDPs are more accurate than DBDPs at resolving length-scales which underestimated them. This improvement is most likely due to the decrease in spatial averaging required by the SBDP. The SBDP lengthscale values can be further improved by spatially averaging data over an appropriate range, as discussed in Section 6.7. The logarithmic relationship with velocity implies an asymptote, indicating a physical limit on the size of eddies that can exist which is consistent with the restricted dimensions of the channel.

According to DNV (2002) transverse lengthscales should be approximately $0.3 \cdot \ell_x$ which, if using the mean ℓ_x value of 13.0 m representative of the highest flow speed, would be in the region of 4.3 m for the highest flow speeds presented here. With vertical lengthscales predicted to be $0.1 \cdot \ell_x$, this would be 1.3m compared with 4.1 m measured. There are very limited field measurements of the transverse and vertical lengthscales for comparison of turbulence. An estimate can be made using results by Thomson *et al.* (2014) of the spectra of turbulence along each vector, as the integral lengthscale is associated with the maximum turning point of the spectra. For the same Admiralty Inlet site the spectral estimates indicate a relationship more like $\ell_y = 0.5\ell_x$ and $\ell_z = 0.25\ell_x$. This is based on the spectral energy at the peak frequency being directly proportional to the associated ℓ_i .

The results from the temporal correlation method presented in Figure 7.16 give values that increase as a function of axial velocity with mean values of around 6.2 m from the SBDP and 7.8 m from the DBDP. The results of the spatial autocorrelation method were a factor of 10 lower, as was the case for the vertical results, and thus this method is deemed to be unsuitable for calculating length-scales. A few variations on the instrument range were compared to test if the results would increase but there was little improvement.

In the vertical direction the DBDP results were similar to the transverse with mean values at the highest flow speeds of 8.0m. The SBDP value was 5.1 m at the equivalent range. Examining the vertical, transverse and streamwise results the SBDP produced the values closest to the predicted $x : y : z$ size ratio at 1:0.33:0.32. The transverse values are slightly low compared with the streamwise, this could in part be due to an underestimation of the streamwise values due to noise. Since the DBDP size ratio is closer to 1:1:1, it is likely that this is due to the velocity transform being unable to appropriately distribute the scales from the individual directions.

The vertical values are slightly high which could be due to the flow round the turbine giving higher along beam velocity components as shown by the negative vertical velocity measurements. Also since the DBDPs overestimate in the transverse and vertical, it could be that a higher resolution will help resolve the smaller lengthscales and thus the SBDPs results are still biased high for these directions. It is also possible the $x : y : z$ size ratio predicted from wind measurements does not hold for tidal channels, although the evidence from these results, and Thomson *et al.* (2014), is that a similar ratio exists. These results also suggest that the SBDPs are capturing the scales of turbulent motion more accurately than the DBDP. This highlights a key advantage of Cartesian SBDP arrays mounted at mid-depth over DBDPs.

Reynolds Stress Tensor

The Reynolds stress tensor was based on a limited data set and thus has higher uncertainty compared with the other results. However the SBDPs results underestimate those computed by the DBDP beam velocities at the equivalent height. The noise correction for the DBDP caused only small corrections indicating that in the majority of cases the random error in opposing beams was of similar magnitude. The Reynolds stress calculation with the SBDPs employs readings over a large spatial area with instruments mounted on the rear frame 3m from those on the top. The results would be expected to increase with reduced separation as the flow is evidently not homogeneous over these scales. Additional sources of uncertainty include the angle of the rear sensor which is assumed to have been slightly off horizontal from work in Section 6.5 and the effect of the turbine on the flow. An alternative array arrangement of the SBDPs where spatial separation is minimised would likely significantly increase the accuracy of results.

7.4.1 Future work

Future work would include the repeat of these tests utilising a longer range single beam sensor to investigate several of the parameters including: variation of the axial velocity with range $u(x)$ and transverse lengthscales ℓ_y . A longer range sensor was available on the project but it suffered significantly from noise issues on the majority of deployments and was probably specified too much in favour of range at the expense of accuracy and spatial and temporal resolution. A 40 m to 60 m effective range at 2 Hz is suggested to resolve lengthscales of 6 m to 8 m by the spatial averaging method.

A study comparing the dissipation rates measured by the SBDPs with those measured by an ADV at equal depth would increase confidence in the SBDP result and indicate if the DBDP high result is a bias based on poor representation of the inertial sub-range in the PSD as suggested here.

The lengthscales in the axial and transverse were both shown to be sensitive to de-trending. In order to resolve the lengthscales with greater confidence using both auto-correlation methods and others such as the spectral slope turning point method, a full study is required including: signal filtering and analysis of the curve steepness of the correlation that may allow greater resolution of the lengthscales. A longer time series sample may also help uncover a greater correlation co-efficient at the lower lags if properly de-trended.

A further comparison study with an ADV would allow a sensitivity to noise analysis, as noise is known to bias correlations low. It is possible such a study would indicate empirical correction factors that could be applied to SBDPs in future site characterisation work, in order that their advantageous range over an ADV be utilised.

The Reynolds stress tensors require a larger data set to reduce uncertainty in the results. It is

clear that if SBDPs are to be used for this purpose the spatial averaging must be minimised. Use of a focus beam array such as in Sellar *et al.* (2015) would allow this along with increasing the separation of the measurement volume from the turbine body. In addition, the measurement of other Reynolds stress tensors would give more information about the turbulent processes at this and similar sites. An inter-instrument comparison study with ADV results would provide further confidence as with the other metrics.

With the benefits of SBDPs in site characterisation outlined, future work should extend the use of these sensors to other sites. Initially a study of the differences in results between Ebb and Flood tides at the Fall of Warness would reveal directional variations. Further drivers such as flow acceleration on the metrics could also be investigated. If the sensors could be mounted in such a fashion that they could be varied in vertical position in the water column while kept stable this would increase the understanding of the variation of these flow metrics with depth. Finally the sensitivity of metrics to the surface wave conditions remains a key area of study that SBDP arrays could be utilised in.

7.5 Chapter Summary

This chapter has highlighted the increased accuracy of the SBDP used in arrays mounted at mid-depth compared with a seabed mounted DBDP for the majority of turbulence metrics. This concludes the experimental and analysis chapters of this thesis. The final chapter seeks to summarise the findings and recommended future work.

Summary, Conclusions and Recommendations for Future Work

8.1 Chapter Overview

This thesis aimed to ascertain whether multiple single beam Doppler profilers (SBDPs) mounted at mid-channel depth would present advantages over the current industry practise of seabed mounted diverging beam Doppler profilers (DBDPs). Of particular interest was the ability of these sensors to capture the turbulence metrics of primary importance to device designers. This chapter summarises the key findings of this work, reviews the formal hypothesis and suggests future work which would further deepen and widen knowledge and improve confidence in these findings.

Each chapter is taken in turn with associated future work within each one. One generic comment that is worth reiterating as it pertains to all the results: these results were all taken in real sea conditions where spatial and temporal variation were high. This means the uncertainty of the results is in turn higher than those associated with a laboratory test where conditions can be consistent and repeatable as required. In addition, the industrial and collaborative nature of this project meant that the data required for this analysis was sometimes secondary to other requirements (such as operating the turbine), thus limited data sets were unavoidable in some cases.

8.2 Quantification and Mitigation of Noise in SBDP Measurements

8.2.1 Summary of Contributions to Knowledge

This chapter presented the relationship between noise variance and streamwise flow velocity for SBDPs mounted streamwise, transverse and vertical. The variation of noise with sensor orientation is within itself a critical finding which will allow the use of these sensors to accurately measure the turbulence intensity at tidal sites. Results presented in Chapter 7 showed that results from the two instruments converged using the correction, particularly at speeds of

primary importance, i.e. those above 1 ms^{-1} . This suggests the spectral method resulted in an accurate representation of the variance attributable to noise.

The novel use of the low signal to noise ratio mode highlighted the variation in sensor noise based on mounting location. LSNR results showed the noise in the SBDPs to be white in all but one case. As this is an important assumption in many turbulence corrections this highlights the value of this method. This was extended to a method to predict instrument bias but limited data and constant fluctuations of tidal conditions meant results were inconclusive.

Finally a mitigation strategy to reduce noise by altering grounding and power supply were investigated. This study involved a filtering capacitor and an isolated power conditioning transformer being applied to the DC input. As the grounding rod for the capacitor eroded, the tests were unable to utilise the remote relay switch between the two to assess their individual effects. However, there was evidence of improvement by this set-up as random error with range was reduced, improving the effective range of the sensor.

8.2.2 Future Work

A test of the effect of noise on both random and systematic error would require a set-up where the noise on the DC supply could be generated, characterised and controlled. Thus the effect of noise in the power supply on the measured velocity and QC metrics (amplitude return and pulse correlation) could be quantified. If use of acoustic instruments on commercial turbines is to prove a successful strategy in the future, understanding this relationship is an important step.

In addition a repeat of the grounding test, isolated from varying the DC input, would highlight the effect of this strategy. As different capacitor sizes filter different noise frequencies, the study should include a range of selectable capacitor sizes to determine the most appropriate for these instruments in this situation. It is important that such a test take place in water of appropriate salinity to replicate the grounding environment at sea.

8.3 Crosstalk Between Co-Located Acoustic Instruments

8.3.1 Summary of Contributions to Knowledge

There are several motivations for installing multiple acoustic sensors in close proximity, including: redundancy, assessment of cross-correlated lengthscales, small spatial scale variation, etc. Knowledge of how to identify and mitigate inter-instrument interference is vital if multiple sensors are to be used in close proximity in future site characterisation work. The interactions identified in this thesis can be summarised as:

- Cross-talk between instruments of the same type will cause velocity readings to bias towards zero in the affected region unless the angle created by the Beams is sufficient to

resolve the bisecting velocity. See below. In parallel sensors this can be identified by as a 6 bin increase in the value of the QC metrics.

- Where the sensors are angled such that the beams cross, the angle causes a widening of the affected band.
- Cross-talk from instruments of different types will show an increase in the standard deviation of the velocity measurements in the affected region. This can also be observed in the spectra of the velocity with an increase in energy at the frequency of the sample-rate of the instrument causing interference.
- Surface reflections can cause interference in the same manner as the transmitted pulse.

One interesting output of cross talk between sensors of different types is evidence that they could be used to create a bi-static multi-sensor system to measure velocities. With one sensor operating in normal power mode and one in LSNR mode results showed that if the pulses are correctly timed the velocity along the bi-secting angle can be measured.

The best mitigation strategy was found to be to utilise Precision Time Protocol (PTP) co-ordinated pulses. As the interference band is a function of separation between the sensors, by offsetting the subsequent transmit-receive cycle, the affected range is moved outwith the measured range of that sensor. The findings of this work can be used to position and setup sensors mounted in close proximity in future site characterisation work.

8.3.2 Future Work

One of the innovations to come out of the ReDAPT project is the development of a focused beam SBDP array as detailed in Sellar *et al.* (2015). This array configuration allows the SBDPs to resolve the velocities in three Cartesian Directions remotely, but employing far less spatial averaging than is the case for the DBDPs. Sellar *et al.* (2015) use four powered offsets utilising the pulse offset mitigation suggested by the work in Chapter 5. However, the system could be modified to a bi-static configuration with one central powered sensor and the four angled sensors in LSNR mode ‘listening’ for the reflection from the vertical sensor. As the instruments processing times decrease with new iterations of these devices, as was the case at the time of writing, the maximum PTP offset that can be used will decrease. If the bi-static method proved successful it would allow such an array to operate at higher sample rate. A full study should include the sensitivity of such a set up to beam angle, flow direction and range.

8.4 SBDP and DBDP comparison - Part A: Introduction and Data Preparation

8.4.1 Summary of Contributions to Knowledge

A methodology to align data from two mountings solutions to a common axis was presented. This proved successful for data comparison but could also be used in the future as part of an upstream monitoring system for active device control such as is done for wind turbines (Schlipf *et al.*, 2010).

The relationship of random error with velocity for the DBDP was characterised for three orientations along with the individual beam velocities. As was the case for the SBDPs the noise was seen to vary with velocity and these correction curves can be used to correct turbulence measurements. However, there is increased uncertainty in the DBDP curves as in measurements from certain deployments the PSDs showed sharp dips at high frequencies which reduced the effectiveness of the fit and biased noise floor measurements low.

In bin selection for the two instruments, significant variation of \bar{u} between the SBDPs and a DBDP at equivalent height above the seabed over a 50m range was highlighted. This could be due to a number of phenomenon, but, as the AWAC matches the ADCP to a high degree there SBDP misalignment is a likely factor. However, the SBDP utilised had by far the most data meeting selection criteria for comparison.

A study of a case study ensemble averaging streamwise SBDP data to improve accuracy of turbulence metrics, found that temporally averaging was not appropriate for generating turbulence metrics due to effects at the high frequency range of the spectra. Although it is still a valid method to define a mean velocity. Averaging spatially across the range over 5 bins (2m) was found to reduce turbulence intensity close to the noise corrected value and increase mean estimates of ℓ_x by 27.76% and improved the accuracy of the slope of the inertial sub-range. As the mean results in Section 7.3.1 were slightly lower than expected from theory this method may prove to increase the accuracy. However the spread of ℓ_x results was high and an extensive sensitivity study is required to improve confidence in the method.

8.4.2 Future Work

One issue that arises investigating instrument velocity measurements with range and inter-instrument comparisons at different locations is the range of applicability of the frozen field hypothesis (as described in Section 2.4.1). This hypothesis is a key assumption in turbulent flow analysis, particularly in calculating the integral lengthscales via the integral timescale. Studies for atmospheric turbulence have utilised cross-correlation functions along the primary flow direction to measure the range over which eddies are correlated above a value 0.9 (Schlipf *et al.*, 2010). An initial piece of work by the author into this, found that the effective range

of the SBDPs was not sufficient to accurately calculate the applicable range of the hypothesis. A sensor with a longer range such that there was a long stable region would be required. The longer range Continental device was also investigated but in that case the instrument noise was too high, biasing correlation results low. The use of an intermediate range sensor with lower noise may be sufficient for such a study. Alternatively, a series of sensors placed at intervals along the primary flow direction would be required to fully capture the evolution of the turbulent structure.

In addition, there was evidence of significant sensor misalignment to the flow. For future turbine mounted acoustic instrument site characterisation it is recommended that improved sensor alignment systems/methods be utilised.

A full study on spatial averaging in both SBDPs and DBDPs across key turbulence metrics would improve confidence in results. This should include sensitivity to: streamwise velocity, sensor orientation and surface waves.

8.5 SBDP and DBDP comparison - Part B Results

8.5.1 Summary of Contributions to Knowledge

The site characterisation results compared between the two instruments for the Flood tide at the Fall of Warness are reported in each Cartesian direction. The key discoveries are:

- The turbulence intensity is initially higher in the DBDP, but after correction for variance due to noise, there was better agreement between the two instruments.
- Turbulence intensity decreases as a power law. However, a linear fit is generally appropriate for axial flow speeds greater than 1ms^{-1} .
- Use of SBDPs to calculate the turbulent kinetic energy dissipation rate were within 8% of the same values across the flow speeds for all orientations and matched well with other studies. The DBDPs were unable to resolve the values with results biased high, this was understood to primarily be due to lack of a clear integral sub-range slope for the line of best fit procedure to find.
- Lengthscales calculated by the SBDPs were closer to theory and results from other sites than the DBDPs for all directions. The evidence suggests that the DBDP gave similar results for all axes suggesting that the spatial averaging and/or the velocity transformation mean it is unable to resolve the scales in the individual orientations.
- The effective range of the SBDPs was not sufficient to resolve the lengthscales by the spatial autocorrelation method.
- The SBDP pairs measurement of the vertical-streamwise Reynolds stress tensor underestimated values compared to the DBDP beam measurements and to other studies. This is likely due to the large scale spatial averaging required in this sensor mounting

configuration. However, due to the limited data set this result has increased uncertainty compared with the other findings of this chapter.

In summary the SBDPs have less random error in the time series and can resolve integral lengthscales that DBDPs can not. Turbulence intensity (when corrected for noise) values appear to be similar in both cases. More accurate estimates of ϵ measured by the SBDPs but with the SBDPs in this array arrangement unable to resolve the streamwise-vertical Reynolds stress.

8.5.2 Future Work

A study to expand on the Reynolds stress calculations of the SBDPs is needed to improve confidence in this method. Ideally if an array of three SBDPs mounted along the Cartesian axes is to be used, it should be more closely mounted with a DBDP in close proximity on the seabed for comparison. There is also the option of including a downward facing vertical beam to investigate the measurements nearer the seabed. However, a converging beam array such as that presented in Sellar *et al.* (2015) would significantly reduce the spatial averaging required and thus is likely to improve results. A dataset incorporating enough 5 minute samples for each 0.1 ms^{-1} data set in order to capture the statistical variation is required to define the metric for a range of flow conditions. Furthermore additional Reynolds stress tensors could be captured to reveal further information about the stresses in the flow.

A more detailed study into the best method to calculate the integral lengthscales of the flow and to validate spectra of turbulence for tidal channels would be of great value to the industry and scientific community. A sensitivity study of lengthscale values to alternate method of calculation, such as the spectral fit method and the fitting of autocorrelation curves with autoregressive moving average (ARMA) models, would add value to the work included in this thesis. Alternate methods of calculation should feature in the study of lengthscale sensitivity to averaging methods discussed in Section 8.4.2.

A study comparing the dissipation rate captured by the SBDPs to the structure function via the DBDPs (as introduced by Wiles *et al.* (2006)), would provide further confidence in the SBDPs to resolve this quantity. However, this would require a robust estimation of the variation of ϵ with depth. In addition, a comparison study of a SBDP with an ADV (with its higher sample rate and subsequently lower random error) would also help quantify the effect of instrument noise on this metrics.

With the exception of the vertical SBDP the SBDP array is unable to quantify the metrics as a function of depth, which is an important relationship in a tidal channel. The pyramid array proposed in Sellar *et al.* (2015) with controllable beam angles would be one option to explore this. However, that array configuration still requires a velocity transform. An experimental set-up where a orthogonal SBDP array could be varied in height to characterise this variation would reveal information about turbulent structures with depth.

8.6 Review of the Hypothesis

The formal hypothesis of this work stated that: “Single beam Doppler sensors used in arrays mounted at mid-channel depth will reduce uncertainty in turbulent flow metrics at tidal energy sites compared with standard seabed-mounted diverging beam Doppler profilers.”

The ability of these arrays configured to minimise instrument noise to measure the turbulent metrics has been demonstrated. This covered a comprehensive set of metrics with the SBDP array measuring length-scales and dissipation rates with significantly greater accuracy than a seabed mounted DBDP, as well as having reduced noise in time series measurements and similar results in turbulence intensity and Reynolds stress methods. Thus, the evidence suggests the hypothesis was correct. It is hoped that this work will contribute to the use of these sensors in future site characterisation work, improve confidence in turbulence metrics and ultimately assist the tidal industry to move forward.

Bibliography

- ABPmer. Atlas of UK Marine Renewable Energy Resources: Technical Report. (May):181, 2008.
- Afgan, I., Ahmed, U., Stallard, T., Afgan, I., Ahmed, U., and Stallard, T. MD 1.4 CFD Simulations of a Full-Scale Tidal Stream Turbine : Comparison Between Large-Eddy Simulations and Field Measurements. Technical report, 2014.
- Alstom. Alstom's 1MW tidal stream turbine installed in Scotland achieves 1 GWh power production, 2014. URL <http://www.alstom.com/press-centre/2014/12/>.
- Alstom. Alstom tidal stream turbines. URL <http://www.alstom.com/products-services/product-catalogue/power-generation/renewable-energy/ocean-energy/tidal-energy/tidal-power/>.
- Anderson, J. *Fundamentals of Aerodynamics*. McGraw-Hill Education, 5th edition, 2010. ISBN 0073398101.
- Andritz Hydro Hammerfest. Tidal Turbine getting ready to feed the grid, 2012. URL <http://www.hammerfeststrom.com/news/08-02-2012-tidal-turbine-getting-ready-to-feed-the-grid/>.
- Appell, G., Bass, P., and Metcalf, M. Acoustic Doppler current profiler performance in near surface and bottom boundaries. *IEEE Journal of Oceanic Engineering*, 16(4):390–396, 1991. ISSN 0364-9059. doi: 10.1109/48.90903.
- Atlantis. Atlantis Resources Corporation connects 1MW tidal turbine to the national grid, 2008. URL <http://atlantisresourcesltd.com/media-centre/>.
- Beauchamp, K. *Transforms for Engineers, A guide to Signal Processing*. Clarendon Press, 1 edition, 1987. ISBN 0-19-856174-1.
- Black & Veatch. Phase II - UK Tidal Stream Energy Resource Assessment. Technical Report 0, 2005.
- Blackmore, T., Batten, W., Harrison, M., and Bahaj, A. The Sensitivity of Actuator-Disc RANS Simulations to Turbulence Length Scale Assumptions. *European Wave and Tidal Energy Conference*, pages 390–399, 2011.
- Bowden, K. and Howe, M. Observations of turbulence in a tidal current. *Journal of Fluid Mechanics*, 17(2):271—284, 1963.

- BP. Statistical Review of World Energy June 2014. Technical Report June, 2014.
- Brumley, B. H., Cabrera, R. G., Deines, K. L., and Terray, E. A. Performance of a Broad-Band Acoustic Doppler Current Profiler. *October*, 16(4):402–407, 1991. ISSN 03649059. doi: 10.1109/48.90905.
- Burton, T., Jenkins, N., Sharpe, D., and Bossanyi, E. *Wind Energy Handbook*. 2011. ISBN 0471489972.
- Carbon Trust. UK Tidal Current Resource and Economics Study. Technical Report July, 2011.
- Çengel, Y. and Turner, R. *Fundamentals of thermal-fluid sciences*. McGraw-Hill, 2nd edition, 2005. ISBN 007-123926-X.
- CIA. *The World Factbook*. 2014. URL <https://www.cia.gov/library/publications/the-world-factbook/rankorder/2241rank.html>.
- Clark, T. H. E. Turbulence in Marine Environments (TiME): A framework for understanding turbulence and its effects on tidal devices. *In review*, 2015.
- Crowe, C., Elgar, D., and Roberson, J. *Engineering Fluid Mechanics*. John Wiley & Sons, 8th edition, 2005. ISBN 0-471-66161-9.
- DECC. Overarching National Policy Statement for Energy (EN-1). Technical Report July, 2011.
- Diels, H. *Doxographi graeci*. De Gruyter, 1879.
- DiMassa, D., Magnell, B., and Lund, J. Effects of temporal and vertical variability of echo amplitude on ADCP selection and performance. *MTS/IEEE Oceans 2001. An Ocean Odyssey. Conference Proceedings (IEEE Cat. No.01CH37295)*, 2:922–929, 2001. ISSN 01977385. doi: 10.1109/OCEANS.2001.968240.
- DNV. *Guidelines for Design of Wind Turbines*, volume 29. 2nd edition, 2002. ISBN 8755028705.
- Durgesh, V., Thomson, J., Richmond, M. C., and Polagye, B. L. Noise correction of turbulent spectra obtained from acoustic doppler velocimeters. *Flow Measurement and Instrumentation*, 37:29–41, 2014. ISSN 09555986. doi: 10.1016/j.flowmeasinst.2014.03.001.
- EMEC. Facilities : EMEC: European Marine Energy Centre, 2015. URL <http://www.emec.org.uk/facilities/>.
- Emery, W. and Thomson, R. *Data analysis methods in physical oceanography*. 2nd edition, 2001.

- Evans, P., Armstrong, S., Wilson, C., Fairley, I., Wooldridge, C., and Masters, I. Characterisation of a Highly Energetic Tidal Energy Site with Specific Reference to Hydrodynamics and Bathymetry. In *European Wave and Tidal Energy Conference*, 2013.
- Fondriest. Conductivity, Salinity & Total Dissolved Solids - Environmental Measurement Systems, 2015. URL <http://www.fondriest.com/environmental-measurements/parameters/water-quality/conductivity-salinity-tds/>.
- Gooch, S., Thomson, J., Polagye, B., and Meggitt, D. Site Characterization for Tidal Power. In *OCEANS 2009, MTS/IEEE Biloxi - Marine Technology for Our Future: Global and Local Challenges*, pages 1–10, 2009.
- Gordon, R. L. *Acoustic Doppler current profiler: Principles of operation, a practical primer*. 1996. ISBN 6196951459.
- Grant, H. The Large Eddies of Turbulent Motion. *J. Fluid Mech*, 4(02):149–190, 1958.
- Grant, H., Stewart, R., and Moilliet, A. Turbulence spectra from a tidal channel. *J. fluid Mech*, 12:241–268, 1962.
- Hansen, J. E. and Sato, M. Earth's Climate History: Implications for Tomorrow. Technical Report July, Earth Institute, Columbia University, 2011.
- Harding, S., Thomson, J., Polagye, B., Richmond, M., Durgesh, V., and Bryden, I. Extreme Value Analysis of Tidal Stream Velocity Perturbations. In *European Wave and Tidal Energy Conference*, 2011.
- ICIS. Power Index Q4 2014 analysis: wholesale prices finish 2014 11% lower year on year Highlights Price moves in 2014. Technical report, 2015.
- IPCC. *Climate Change 2013 - The Physical Science Basis*. Cambridge University Press, Cambridge, 2014. ISBN 9781107415324. doi: 10.1017/CBO9781107415324.
- Karsten, R. H., Flaherty-Sproul, M. O., McMillan, J. M., Culina, J., Trowse, G., and Hay, A. E. Analysis of Tidal Turbine Arrays in Digby Gut and Petit Passage, Nova Scotia. *4th International Conference on Ocean Energy*, 2:1–6, 2012.
- Kilcher, L. F., Thomson, J., and Colby, J. Determining the spatial coherence of turbulence at mhk sites. In *Proceedings of the 2nd Marine Energy Technology Symposium*, pages 1–7, Seattle, 2014.
- Knauss, J. A. *Introduction to Physical Oceanography*. Prentice-Hall, 1978. ISBN 0-13-493015-0.
- Kolmogorov, A. A refinement of previous hypotheses concerning the local structure of turbulence in a viscous incompressible fluid at high Reynolds number. *J. Fluid Mech*, 13 (01):82–85, 1962.

- Le Houérou, H. N. Climate change, drought and desertification. *Journal of Arid Environments*, 34(2):133–185, 1996. ISSN 01401963. doi: 10.1006/jare.1996.0099.
- Le Quéré, C., Peters, G. P., Andres, R. J., Andrew, R. M., Boden, T., Ciais, P., Friedlingstein, P., Houghton, R. a., Marland, G., Moriarty, R., Sitch, S., Tans, P., Arneeth, A., Arvanitis, A., Bakker, D. C. E., Bopp, L., Canadell, J. G., Chini, L. P., Doney, S. C., Harper, A., Harris, I., House, J. I., Jain, a. K., Jones, S. D., Kato, E., Keeling, R. F., Klein Goldewijk, K., Körtzinger, A., Koven, C., Lefèvre, N., Omar, A., Ono, T., Park, G.-H., Pfeil, B., Poulter, B., Raupach, M. R., Regnier, P., Rödenbeck, C., Saito, S., Schwinger, J., Segsneider, J., Stocker, B. D., Tilbrook, B., van Heuven, S., Viovy, N., Wanninkhof, R., Wiltshire, A., Zaehle, S., and Yue, C. Global carbon budget 2013. *Earth System Science Data Discussions*, 6:689–760, 2013. ISSN 1866-3591. doi: 10.5194/essdd-6-689-2013.
- Legrand, C. Assessment of Tidal Energy Resource. Technical report, Black and Veatch, EMEC, 2009.
- Leishman, J. G. Challenges in modelling the unsteady aerodynamics of wind turbines. *Wind Energy*, 5(2-3):85–132, April 2002. ISSN 1095-4244. doi: 10.1002/we.62.
- Lhermitte, R. and Lemmin, U. Probing water turbulence by high frequency Doppler sonar. *Geophysical Research Letters*, 17(10):1549, 1990. ISSN 0094-8276. doi: 10.1029/GL017i010p01549.
- Lohrmann, A. Introduction to AD2CP turbulence measurements, 2015.
- Lohrmann, A., Hackett, B., and R\oed, L. High resolution measurements of turbulence, velocity and stress using a pulse-to-pulse coherent sonar. *Journal of Atmospheric and . . .*, 7 (1):19–37, 1990.
- Lohrmann, A., Cabrera, R., and Kraus, N. Acoustic-doppler velocimeter(ADV) for laboratory use. In *Fundamentals and advancements in Hydraulic Measurements and Experimentation*, pages 351–365, New York, 1994.
- Lorke, A. and Wüest, A. Application of coherent ADCP for turbulence measurements in the bottom boundary layer. *Journal of Atmospheric and Oceanic Technology*, 22(11):1821–1828, 2005. ISSN 07390572. doi: 10.1175/JTECH1813.1.
- Lu, Y. and Lueck, R. G. Using a broadband ADCP in a tidal channel. Part I: Mean flow and shear. *Journal of Atmospheric and Oceanic Technology*, 16(11 PART 1):1556–1567, 1999a. ISSN 07390572. doi: 10.1175/1520-0426(1999)016<1568:UABAIA>2.0.CO;2.
- Lu, Y. and Lueck, R. G. Using a Broadband ADCP in a Tidal Channel. Part 2: Turbulence. *Journal of Atmospheric and Oceanic Technology*, 16(11 PART 2):1568–1579, 1999b. ISSN 07390572. doi: 10.1175/1520-0426(1999)016<1568:UABAIA>2.0.CO;2.

- MacKay, D. *Sustainable Energy-without the hot air*. UIT Cambridge Ltd., 2008. ISBN 9780954452933. URL <http://www.dspace.cam.ac.uk/handle/1810/217849>.
- Marsh, G. Wave and tidal power – an emerging new market for composites. *Reinforced Plastics*, 53(5):20–24, June 2009. ISSN 00343617. doi: 10.1016/S0034-3617(09)70220-6. URL <http://linkinghub.elsevier.com/retrieve/pii/S0034361709702206>.
- MCT. World’s first commercial-scale tidal power system feeds electricity to the National Grid | Marine Current Turbines, 2008. URL http://www.marineturbines.com/3/news/article/10/world_s_first_commercial_scale_tidal_power_system_feeds_electricity_to_the_national_grid__.
- MCT. Project Background | SeaGeneration. URL <http://www.seageneration.co.uk/background.php>.
- Meehl, G., Zwiers, F., Evans, J., Knutson, T., Mearns, L., and Whetton, P. Trends in extreme weather and climate events: issues related to modeling extremes in projections of future climate change. *Bulletin of the American Meteorological Society*, 81:427–436, 2000.
- Milne, I. A., Sharma, R. N., Flay, R. G. J., and Bickerton, S. Characteristics of the turbulence in the flow at a tidal stream power site Characteristics of the turbulence in the flow at a tidal stream power site. *The Royal Society A*, 2013.
- Moum, J. N., Gregg, M. C., Lien, R. C., and Carr, M. E. Comparison of Turbulence Kinetic Energy Dissipation Rate Estimates from Two Ocean Microstructure Profilers, 1995. ISSN 0739-0572.
- Nichols, R. H. Turbulence models and their application to complex flows. Technical report, University of Alabama at Birmingham, NASA, 2001.
- NOAA. Paleoclimatology Program - Perspective on Abrupt climate Change, 2015a. URL <https://www.ncdc.noaa.gov/paleo/abrupt/data2.html>.
- NOAA. ESRL Global Monitoring Division - Global Greenhouse Gas Reference Network, 2015b. URL <http://www.esrl.noaa.gov/gmd/ccgg/trends/weekly.html>.
- Nortek-AS. Aquadopp HR-Profiler, 2015a.
- Nortek-AS. Continental 3D Current Profiler Datasheet, 2015b.
- Nortek-AS. Vectrino Data Sheet, 2015c.
- Nylund, S. email, (nortag:163958) single beam doppler - midas debugging enquiries, 30/08/2013, 2013a.
- Nylund, S. email, grounding issues, 05/04/2013, 2013b.

- Nystrom, E. a., Oberg, K. a., and Rehmann, C. R. Measurement of Turbulence with Acoustic Doppler Current Profilers - Sources of Error and Laboratory Results. *Hydraulic Measurements and Experimental Methods 2002*, pages 1–10, October 2002. doi: 10.1061/40655(2002)55.
- O’Neill, P., Nicolaidis, D., Honnery, D., and Soria, J. Autocorrelation Functions and the Determination of Integral Length with Reference to Experimental and Numerical Data. In *15th Australasian Fluid Mechanics Conference*, volume 1, pages 1–4, 2004.
- OpenHydro. Press release 10. (April):1–4, 2008.
- Osalusi, E., Side, J., and Harris, R. Structure of turbulent flow in EMEC’s tidal energy test site. *International Communications in Heat and Mass Transfer*, 36(5):422–431, May 2009. ISSN 07351933. doi: 10.1016/j.icheatmasstransfer.2009.02.010.
- Petit, R. J., Raynaud, D., Basile, I., Chappellaz, J., Ritz, C., Delmotte, M., Legrand, M., Lorius, C., and Pe, L. Climate and atmospheric history of the past 420,000 years from the Vostok ice core, Antarctica. *Nature*, 399:429–413, 1999. ISSN 0028-0836. doi: 10.1038/20859.
- Phoenix-Contact. Url: <https://www.phoenixcontact.com/online/portal/gb?1dmy&urile=wcm2014>.
- Piping-engineering.com. Flow Meter Types Based on Measurement Techniques. URL <http://www.piping-engineering.com/flow-meter-measurement-techniques-types.html>.
- Polagye, B. L. *Hydrodynamic effects of kinetic power extraction by in-stream tidal turbines*. PhD thesis, 2009.
- Pope, S. *Turbulent flows*. Cambridge University Press, 2000.
- Rahmstorf, S. Projecting Future Sea-Level Rise. *Science*, 315(January):368–370, 2007. ISSN 00368075. doi: 10.1126/science.1135456.
- RDI. RiverRay. URL <http://www.rdinstruments.com/riverray.aspx>.
- RDI. ADCP Coordinate Transformation, 2010.
- Reynolds, O. On the Dynamical Theory of Incompressible Viscous Fluids and the Determination of the Criterion. *Philosophical Transactions of the Royal Society A: Mathematical, Physical and Engineering Sciences*, 186:123–164, January 1895. ISSN 1364-503X. doi: 10.1098/rsta.1895.0004.
- Richard, J.-B., Thomson, J., Polagye, B., and Bard, J. Method for identification of Doppler noise levels in turbulent flow measurements dedicated to tidal energy. *International Journal of Marine Energy*, 3-4:52–64, December 2013. ISSN 22141669. doi: 10.1016/j.ijome.2013.11.005.

- Richter, J. *The Notebooks of Leonardo da Vinci*. Dover, New York, 1970.
- Rockland Scientific. rocklandscientific.com. URL <http://rocklandscientific.com/>.
- Sarpkaya, T. and Isaacson, M. *Mechanics of Wave Forces on Offshore Structures*. Van Nostrand Reinhold Company Inc, 1981. ISBN 0-442-25402-4.
- Schlipf, D., Trabucchi, D., Bischoff, O., Hofsäß, M., Mann, J., Mikkelsen, T., Rettenmeier, A., Trujillo, J. J., and Kühn, M. Testing of Frozen Turbulence Hypothesis for Wind Turbine Applications with a Staring Lidar. In *15th International Symposium for the Advancement of Boundary Layer Remote Sensing (ISARS)*, volume 12, page 5410, 2010.
- Scottish Government. Energy in Scotland: Get the facts, April 2003. URL <http://www.gov.scot/Topics/Business-Industry/Energy/Facts>.
- Scottish Government. *2020 Routemap for Renewable Energy in Scotland*. 2011. ISBN 9781780452715.
- Sellar, B., Harding, S., and Richmond, M. Enabling high-resolution velocimetry in energetic tidal currents using a convergent-beam acoustic Doppler profiler. *In review*, 2015.
- Sellar, B. G. and Sutherland, D. R. J. MD 3.8 - Tidal energy site characterisation at the fall of warness, emec, uk. Technical report, 2015.
- Sherwood, S. C. and Huber, M. An adaptability limit to climate change due to heat stress. *Proceedings of the National Academy of Sciences of the United States of America*, 107(21): 9552–9555, 2010. ISSN 0027-8424. doi: 10.1073/pnas.0913352107.
- Smith, S. W. *The Scientist and Engineers Guide to Digital Signal Processing*. California Technical Publishing, 2nd edition, 1999. ISBN 0-9660176-6-8.
- SMV-Tec. Hotwire Systems. URL <http://shop.svm-tec.com/en/Conditions-of-Use>.
- SonTek. Argonaut-ADV for shallow water flow monitoring, 3D Doppler Technology. URL <http://www.sontek.com/productsdetail.php?Argonaut-ADV-6>.
- Stacey, M. T., Monismith, G., and Burau, J. R. Measurements of Reynolds stress profiles in unstratified. *Journal of Geophysical Research*, 104:933–949, 1999.
- Stock-Williams, C. and Gunn, K. MD5.2 Fall of Warness 3D Model Validation Report. Technical report, E.ON, 2012.
- Surachit. Tides Wikipedia. URL <http://en.wikipedia.org/wiki/Tide>.
- Sutherland, D. R. J., Sellar, B. G., Harding, S. H., and Bryden, I. Initial Flow Characterisation Utilising Turbine and Seabed Installed Acoustic Sensor Arrays. *European Wave and Tidal Energy Conference*, pages 1 — 8, 2013.

- Taylor, G. The spectrum of turbulence. *Proceedings of the Royal Society of ...*, 164(919): 476–490, 1938.
- Taylor, J. R. *An Introduction to Error Analysis*, volume 101. University Science Books, 2nd edition, 1997. ISBN 093570275X. doi: 10.1121/1.418074.
- Thomson, J., Polagye, B., Richmond, M., and Durgesh, V. Quantifying turbulence for tidal power applications. In *MTS/IEEE Seattle, OCEANS 2010*, number 4, 2010. ISBN 9781424443321. doi: 10.1109/OCEANS.2010.5664600.
- Thomson, J., Polagye, B., Durgesh, V., and Richmond, M. C. Measurements of Turbulence at Two Tidal Energy Sites in Puget Sound, WA. *IEEE Journal of Oceanic Engineering*, 37(3): 363–374, 2012.
- Thomson, J., Kilcher, L. F., and Harding, S. F. MULTI-SCALE COHERENT TURBULENCE AT TIDAL ENERGY SITES. In *Proceedings of the 5th International Conference on Ocean Energy*, pages 1–6, Halifax, Nova Scotia, 2014.
- Thorpe, S. *The Turbulent Ocean*. Cambridge University Press, 2007. ISBN 978-0521676809. doi: 10.1017/CBO9780511819933. URL http://www.tos.org/oceanography/archive/19-3_smyth.pdf<http://books.google.com/books?hl=en&lr=&id=Ax2d94PODgIC&oi=fnd&pg=PR11&dq=The+Turbulent+Ocean.&ots=Mc0hNULvMG&sig=1ZbIPp680JtMi5ySkKeR2ZfXskw>.
- Togneri, M. and Masters, I. Comparison of marine turbulence characteristics for some potential turbine installation sites. In *4th International Conference on Ocean Energy*, pages 6–11, 2012.
- Topper, M. B. R. Guidance for Numerical Modelling in Wave and Tidal Energy. Technical Report March, 2010.
- UK Parliament. Search Results Energy trends section 5: electricity. Technical report, 2014.
- UK Parliament. Climate Change Act 2008, 2008.
- UK Parliament. The UK Low Carbon Transition Plan. Technical report, 2009.
- Valeport. *Model 803 Operating Manual*. 2001.
- Valeport. Model 106 Current Meter Datasheet, 2015. URL <http://www.valeport.co.uk/Products/CurrentMeters.aspx>.
- Visbeck, M. Sea Surface Conditions remotely sensed by Upward-Looking ADCPs. *Journal of Atmospheric and Oceanic Technology*, 1(2):141–149, 1995.

- Voulgaris, G. and Trowbridge, J. H. Evaluation of the Acoustic Doppler Velocimeter (ADV) for Turbulence Measurements. *Journal of Atmospheric and Oceanic Technology*, 15(1):272–289, 1998. ISSN 0739-0572. doi: 10.1175/1520-0426(1998)015<0272:EOTADV>2.0.CO;2.
- Way, S. and Collier, W. MD6.6 Initial Validation of Tidal Bladed Modelling of the TGL 500kW Tidal Turbine. Technical report, DNV - GL, 2012.
- Way, S. and Thomson, M. MD6.1 Site Characterisation and Design Basis Report. Technical report, DNV - GL, 2011.
- Wiles, P. J., Rippeth, T. P., Simpson, J. H., and Hendricks, P. J. A novel technique for measuring the rate of turbulent dissipation in the marine environment. *Geophysical Research Letters*, 33(21):L21608, November 2006. ISSN 0094-8276. doi: 10.1029/2006GL027050.
- Yellow Maps. Digby NS Free Topo Map Online. URL <http://www.canmaps.com/topo/nts50/topomap/021a12.htm>.
- Yu, X. Y. X. and Gordon, L. 38 kHz broadband phased array acoustic Doppler current profiler. *Proceedings of the IEEE Fifth Working Conference on Current Measurement*, pages 53–57, 1995. doi: 10.1109/CCM.1995.516150.
- Zeebe, R. E. Time-dependent climate sensitivity and the legacy of anthropogenic greenhouse gas emissions. *Proceedings of the National Academy of Sciences of the United States of America*, 110(34):13739–44, 2013. ISSN 1091-6490. doi: 10.1073/pnas.1222843110.